THESIS ON NATURAL AND EXACT SCIENCES B168

Properties of ZnO-nanorod/In_2S_3/$CuInS_2$ Solar Cell and the Constituent Layers Deposited by Chemical Spray Method

ERKI KÄRBER

TUT
PRESS

TALLINN UNIVERSITY OF TECHNOLOGY
Faculty of Chemical and Materials Technology
Department of Materials Science
Laboratory of Thin Film Chemical Technologies

Dissertation was accepted for the defense of the degree of Doctor of Philosophy in Natural and Exact Sciences on 26 March 2014

Supervisors: Dr. Malle Krunks, Leading Research Scientist,
Department of Materials Science, Tallinn University of Technology

Dr. Arvo Mere, Senior Research Scientist,
Department of Materials Science, Tallinn University of Technology

Opponents: Dr. Yaroslav Romanyuk, Laboratory for Thin Films and
Photovoltaics, Swiss Federal Laboratories for Materials Science
and Technology (EMPA), Switzerland

Dr. Ilmar Kink, Institute of Physics, University of Tartu, Estonia

Defense of the thesis: 7 May 2014 at 14.00
Lecture hall: VII-226
Tallinn University of Technology, Ehitajate tee 5, Tallinn

Declaration: Hereby I declare that this doctoral thesis, my original investigation and achievement, submitted for the doctoral degree at Tallinn University of Technology, has not been previously submitted for any academic degree.

Erki Kärber

European Union
Regional Development Fund

Investing in your future

ISSN 1406-4723
ISBN 978-9949-23-600-8 (publication)
ISBN 978-9949-23-601-5 (PDF)

LOODUS- JA TÄPPISTEADUSED B168

Keemilise pihustuse meetodil sadestatud ZnO-nanovarras/In_2S_3/$CuInS_2$ päikesepatarei ja selle koostisosade omadused

ERKI KÄRBER

TTÜ
KIRJASTUS

TABLE OF CONTENTS

LIST OF PUBLICATIONS

The thesis is based on the following publications, which are referred to in the text by the Roman numerals **I–VI**:

I. **E.Kärber**, K.Otto, A.Katerski, A.Mere, M.Krunks. (2014). Raman spectroscopic study of In_2S_3 films prepared by spray pyrolysis. Materials Science in Semiconductor Processing, *in press.*

II. **E.Kärber,** A.Abass, S.Khelifi, M.Burgelman, A.Katerski, M.Krunks. (2013). Electrical characterization of all-layers-sprayed solar cell based on ZnO nanorods and extremely thin CIS absorber. Solar Energy 91, 48–58.

III. **E.Kärber**, T.Raadik, T.Dedova, J.Krustok, A.Mere, V.Mikli, M.Krunks. (2011). Photoluminescence of spray pyrolysis deposited ZnO nanorods. Nanoscale Research Letters 6(359), 1–7.

IV. **E.Kärber**, A.Katerski, I.Oja Acik, V.Mikli, A.Mere, M.Krunks. (2011). Effect of H_2S treatment on properties of $CuInS_2$ thin films deposited by chemical spray pyrolysis at low temperature. Thin Solid Films 519, 7180–7183.

V. M.Krunks, **E.Kärber**, A.Katerski, K.Otto, I.Oja Acik, T.Dedova, A.Mere. (2010). Extremely thin absorber layer solar cells on zinc oxide nanorods by chemical spray. Solar Energy Materials and Solar Cells 94(7), 1191–1195.

VI. M.Krunks, T.Dedova, **E.Kärber**, V.Mikli, I.Oja Acik, M.Grossberg, A.Mere. (2009). Growth and electrical properties of ZnO nanorod arrays prepared by chemical spray pyrolysis. Physica B: Physics of Condensed Matter 404(22), 4422–4425.

Copies of these articles are included in APPENDIX A.

AUTHOR´S CONTRIBUTION

The author´s contribution to papers included in the thesis is as follows:

I. Optical measurements (Raman spectroscopy) of the sprayed In_2S_3 films, analysis of the results, major role in writing.

II. Electrical (I-V-T, C-f-T, EQE) measurements of the sprayed $ZnO_{NR}/In_2S_3/CuInS_2$ solar cell, analysis of the results, major role in writing.

III. Part of the optical measurements (photoluminescence) of the sprayed ZnO nanorod layers, analysis of the results, major role in writing.

IV. Optical measurements (Raman spectroscopy) of the sprayed $CuInS_2$ films, analysis of the results, major part of writing.

V. Electrical measurements (EQE) of the sprayed $ZnO_{NR}/In_2S_3/CuInS_2$ solar cell, analysis of the results, minor role in writing.

VI. Electrical (C-V) measurements of the sprayed ZnO nanorod layers, analysis of the results, minor role in writing.

LIST OF ABBREVIATIONS

ALD	Atomic Layer Deposition
AM1.5	Air Mass coefficient at 1.5 atmosphere thickness
CA	Cu-Au ordering
CH	Chalcopyrite
CBD	Chemical Bath Deposition
CIS	$CuInS_2$
CISe	$CuInSe_2$
CGSe	$CuGaSe_2$
CIGSe	$Cu(In, Ga)Se_2$
CIGSSe	$Cu(In, Ga)(Se, S)_2$
CZTS	Cu_2ZnSnS_4
CZTSSe	$Cu_2ZnSn(S, Se)_4$
CZTSe	$Cu_2ZnSnSe_4$
CSP	Chemical Spray Pyrolysis
CVD	Chemical Vapor Deposition
CuSCN	Copper(I) thiocyanate
EDX	Energy Dispersive X-ray Spectroscopy
E_g	Optical bandgap
ETA	Extremely thin absorber
FF	Fill factor
FWHM	Full Width at Half Maximum
ILGAR	Ion-Layer-Gas-Reaction Process
ITO	Indium tin oxide
n	Ideality factor
J_{SC}	Short circuit current
PV	Photovoltaic
SEM	Scanning Electron Microscopy
ZnO_{NR}	ZnO nanorod layer
T_S	Temperature of the surface of the substrate
TCO	Transparent Conductive Oxide
V_{OC}	Open circuit voltage
XRD	X-Ray diffraction
η	Power conversion efficiency

INTRODUCTION

> "I'd put my money on the sun and solar energy. What a source of power!
> I hope we don't have to wait until oil and coal run out before we tackle that."
> — Thomas A. Edison (1847–1931)

The energy flux from the sun is practically inexhaustible. Effectively, the solar irradiation is the source of renewable power sources like hydropower, wind power and waves, biomass and fossil fuels. The use of renewables, coupled with energy efficient technologies, transport, consumption, reuse and recycling leads to sustainability. Solar energy can be converted to electricity via solar thermal collectors or photovoltaic cells (PV cells). The latter are devices that directly convert light to electricity, with heat as an undesirable side product as opposed to an intermediate product.

In a stack of semiconductor layers that constitute a PV cell, the absorber material receives the most attention. The I generation solar cells use a high-quality, no-defect silicon-wafer based absorber that yield high cell efficiencies, however, at the cost of energy- and time-consuming technology. The II generation of PV cells uses less material, or materials with a lower quality, examples of which are cadmium telluride, thin film silicon, organic dye or chalcopyrite as the absorber material. The thicknesses of the absorber layers or absorber/window composites vary from a monomolecular layer up to a few micrometers, hence the term thin-film PV. The II generation of solar cells can further reduce cost by the use of low-cost technologies. Among such, the chemical spray pyrolysis (CSP) is an attractive method that boasts a high source-to-material conversion efficiency.

In the current thesis, the $CuInS_2$ chalcopyrite absorber material properties are studied separately from, and, as the constituents of a $ZnO/In_2S_3/CuInS_2$ solar cell, all prepared by the CSP. The ZnO optical window layer is prepared as a continuous thin film, or, as a layer of vertically standing nanorods (ZnO_{NR}). I characterize the unconventional $ZnO_{NR}/In_2S_3/CuInS_2$ solar cell with an extremely thin absorber (ETA) and its constituent layers. I describe the non-idealities of the sprayed cell hand-in-hand with the properties of the constituents, mainly based on publications [II] and [V] with expanded discussion and explanations. In [II] we investigated the cell with a focus on the absorber material, whereas in [V] we analyzed the cell output as a function of In_2S_3 thickness, and, at varied ZnO_{NR} lengths.

Additionally, the main results of materials′ studies [I, III, IV, VI] relevant to the solar cell operation are discussed. In [III] we presented the photoluminescence of the sprayed ZnO_{NR}, in [VI] the electrical properties of the ZnO_{NR} and in [IV] the effect of post-deposition annealing on the absorber quality; in [I] the prospect of the CSP method for preparation of In_2S_3 as a candidate for intermediate band solar cell absorber application [I].

1. LITERATURE OVERVIEW

1.1. Solar energy conversion

1.1.1. Photovoltaic conversion and materials

The basic requirements for a solar cell are – a strong absorber, a heterojunction of the absorber with an optical window material and ohmic contacts [1]. The central part of a solar cell is the heterojunction – an intimate contact between two electrically dissimilar materials. The light-to-electricity conversion process relies in the extraction of energy, as voltage and current, from the irradiated junction via the photogenerated carriers in materials. The carriers are separated with the help of a potential gradient that is asymmetric for carriers of different type; whereas such gradient for carriers is intrinsic to such a materials′ interface and can be described in terms of electrical or chemical potential, for conventional and excitonic solar cells, respectively [2].

In a conventional inorganic solar cell, as opposed to an excitonic solar cell, the gradient is described as the *built-in* electric field in the depletion region of the *pn*-junction (where *p* stands for hole-conductor and *n* for electron-conductor). Additionally, the completed cells with the electrodes have to be *band-aligned* for efficient carrier extraction [3-10]. The use of absorber-*buffer*-window structures emphasizes the need for energy band alignment in the structure since the cells with window-absorber alone, without the buffer, are not always as efficient. The very thin buffer layer, if present, is an electrically active part of the p-absorber/n-(buffer/window) heterojunction [11].

A diverse selection of semiconductor materials have been used to make a single pn-junction: monocrystalline materials (Si, GaAs), thick polycrystalline materials (p-Si), thin polycrystalline materials (p-CIS, p-CISe, p-CIGSe, p-CZTS, p-CdTe; n-CdS, n-TiO_2, n-In_2S_3), thin amorphous materials (a-Si:H, a-SiGe:H, a-SiC:H) to name a few relevant inorganic materials. A pn-junction can be formed as a single homojunction (p-Si/n-Si), as a single type II heterojunction (CIS/(In_2S_3/ZnO); CIGSe/(CdS/ZnO); CdTe/CdS), p-i-n junction (p-Si:H/i-Si:H/n-Si:H) or a multijunction (a stack of pn-junctions) [12, 13] and as a Schottky junction (metal-semiconductor junction), among others. In a heterojunction, the narrow-gap part of the junction is the light absorber (usually p-type) while the wide-gap part is the optical window (n-type).

1.1.2. Thin film solar cells

An affordable solar cell is made by a simple, preferably low-temperature technology in a small number of steps; using materials from sources that are abundant in nature and non-toxic; and treatments that do not involve toxic or explosive gases. While the first generation of solar cells complies with most conditions, the technology for producing monocrystalline wafer based solar cells need a high energy input at several device fabrication steps, lack the ability for a monolithic interconnection (no ′wires′, no soldering-strips connection), ultimately yielding an expensive solar cell [14, 15].

A solar cell could be labeled as a *macro*-electronic device as opposed to micro-electronic component, hence, the trade-off has to come in the form of lower material quality when aiming large-area and low-cost in PV [16]. The second generation of solar cells offers competition to the monocrystalline silicon technology in sense of close-to-comparable efficiencies at a significantly lowered cost [17]. Such thin film solar cells use less and lower quality material at cheaper production costs [12, 18, 19].

Unlike with the crystalline silicon, that has an indirect bandgap and requires absorber thicknesses of several hundred micrometers; the use of absorber material with a direct bandgap and a high absorption coefficient allows to use the minimal amount of material (a few micrometers) for every watt of energy conversion. The thin film chalcopyrite CIGSe cells have the highest efficiencies of the thin film technologies [14, 15, 17, 20]. Due to the low availability of indium and gallium, hence the high cost, alternative absorbers have been developed with aluminium instead of gallium as a replacement for CIGS, or zinc and tin instead of indium (CZTS, E_g=1.45 eV; CZTSe, E_g=1.05 eV; and alloys) as a replacement for CIS [14, 21].

While the conversion efficiencies of solar cells based on first generation mono- and multicrystalline silicon has reached up to 25% and 20.4%, respectively [20, 22], the II generation polycrystalline chalcopyrite cell record show a remarkable 20.8% for CIGSe and 12% for the CZTSSe absorber based solar cells [20], on a lab scale. The CZTSSe compounds are also investigated in the Department of Materials Science, Tallinn University of Technology, and applied in the so-called monograin solar cells that show efficiencies above 5% [23].

Although the CIGSe record cell still uses CdS buffer layer by CBD, an efficiency of 16.1% has been achieved with CIGSSe absorber and spray-ILGAR deposition of In_2S_3 buffer layer, surpassing efficiencies on reference cells with CdS by spray-ILGAR [24]. By non-vacuum printing method of CIGS on a flexible aluminium foil, followed by CdS by CBD, an efficiency of 17.1% has been achieved [25]. The thin film silicon (a-Si) cells are at efficiencies above 10% [20].

As a general trend, when compared to the lab cells (with a smaller area) the PV modules in mass production lag in efficiency, showing 22.9%, 18.5% and

15.7% for mono-Si, poly-Si and CIGSe, respectively [20]. The production *average*, in turn, naturally lags the production records. Due to the intensive research, and the interest in PV record cells, tables of highest efficiencies are renewed regularly (twice a year) with details on the cell sizes and measurement conditions, the latest issued early in 2014 [20].

1.1.3. Semiconductor sensitized solar cells

The SSSC (semiconductor-sensitized solar cell) is a conceptual offspring of the DSSC (dye-sensitized solar cell) concept, whereas the dye has been replaced with an inorganic sensitizer, that is, an inorganic absorber material [26, 27]. These cell types, SSSC and DSSC, sensitize a wide bandgap window material with an inorganic semiconductor or an organic semiconductor (dye), respectively, or even both [4]. The advantages of the SSSC are considered to be a greater stability of the inorganic sensitizer, and a wider range of optical absorption [28-31]. However, since the extensive study of DSSC-s predates that of SSSC-s, the efficiencies of the latter are generally inferior, with causes still under discussion. Nevertheless, large improvements have been predicted for the SSSC performance [28, 32, 33].

In a dye cell, the organic absorber layer (dye) is restricted to a thickness of a monomolecular layer. The working principle of the dye cell is to extract the energy of the photoinduced exciton at the donor-acceptor materials interface, as opposed to the extraction of energy by separation of photoinduced and thermally dissociated free carriers pairs in the absorber of SSSC. Besides the DSSC, other *excitonic* cell types include: planar or three-dimensional (bulk-heterojunction) cells based on conjugated polymers and fullerenes as the electron donor-acceptor pair [2, 34]; polymer-inorganic hybrids where the inorganic component has replaced the fullerene and act as the electron acceptor [18], two-terminal inorganic-(inorganic-polymer) hybrid-tandem cells [4], polymer cells based on a triple junction [35]. Also, planar heterojunctions formed by two inorganic materials based on colloidal nanocrystals may share similarities with the excitonic cells in sense of carrier extraction and the band model [31]. For the excitonic cells, the rationale of using bulk instead of a planar junction is similar to that between thin film and ETA cell and relates to the small exciton diffusion length. The hybrid solar cells combine the advantages of organic and inorganic semiconductors: the polymers absorb light and transport holes while the inorganic component is the electron transporter. The hole-conductor can also act as an absorber in hybrid cells such as TiO_2/Sb_2S_3/P3HT where the P3HT hole-conductor doubles as a light absorber [4]. Numerous possibilities have been explored, for example, four- or two-terminal tandem cell that uses thin film chalcopyrite cell as the bottom cell and dye cell as the top cell [30].

The ETA (extremely thin absorber) cell is a recent concept introduced by professor Könenkamp et. al. with CIS and CdTe as the first absorber candidates [26, 29, 33, 36-38]. The ETA (extremely thin absorber) cell is a type of the SSSC that uses a *continuous* absorber material in a *solid-state* [27, 28] as opposed to a quantum-dot SSSC or a nanocomposite SSSC, where the absorbing semiconductor or the window material is in the form of *particles* [29, 32, 33], or, as opposed to any SSSC concepts that use a *liquid* electrolyte [28]. In contrast to a DSSC or a SSSC with a liquid electrolyte, the ETA cell uses a solid-state hole-conductor instead of an electrolyte. Thus, to avoid using the expression SS-SSSC (solid-state SSSC), we use the shorter expression ETA solar cell.

Followingly, some examples of successful inorganic and hybrid SSSC cells, including ETA cells, are presented without being exhaustive. The survey is summarized below in Table 1.

The use of recently emerged organic-inorganic hybrid materials with perovskite-like structure as an absorber material yield cell efficiencies as high as 14.1% when used as a sensitizer in TiO_2. This solid-state hybrid record cell uses spiro-MeOTAD hole-conductor, and is entirely deposited by solution based methods [20, 39]. The dye-sensitized cells itself and polymer based (organic) cells are at efficiencies above 10% [20].

The feasibility of a cheap solar paint process has been explored, using TiO_2 or ZnO nanoparticles covered by a thin CdS or CdSe absorber layer, yielding cells with 1.1% efficiency by fast one-step-coating with a SILAR-like process [40].

Solar cells based on mesoporous TiO_2 impregnated with Sb_2S_3 absorber by CBD and covered by an organic hole-conducting polymer (P3HT) reach conversion efficiencies above 5% with a maximum EQE of 80% [4]. A similar organic-inorganic hybrid approach using TiO_2/Sb_2S_3/spiro-MeOTAD cell design shows above 3% efficiency with a maximum EQE nearly 90% [41]. Another experiment with a TiO_2/Sb_2S_3/CuSCN cell design reaches 3.4% [42]. For the TiO_2/Sb_2S_3 interface an In(OH)S buffer layer has been used, while ZnS has been used for the ZnO/Sb_2S_3 interface [27, 41]. Other choices for absorber materials have been CdTe, $Cu_{1.8}S$, Se, InP and FeS_2 by CBD as the most common choice with post-deposition annealing as a preferable route [27, 43, 44], and CdSe by electrodeposition [26].

Solid-state cells based on Sb_2S_3 absorber have reached efficiencies 3.4%, 3.1%, 4.9% and 6.3% when used in tandem with CuSCN, spiro-MeOTAD, P3HT and the PCPDTBT as hole conductors, respectively, in a mesoporous TiO_2 structure [45].

For the ZnO/In_2S_3/CuSCN cell by wet chemical methods, an efficiency of 3.4% has been reported [46]. Nanocomposite TiO_2/In_2S_3/CIS cells based on chemically sprayed CIS have reached conversion efficiencies around 7% [29].

Table 1. A selection of inorganic and hybrid semiconductor-sensitized solar cells with efficiencies above 3%. The cells are based on ZnO nanorods or mesoporous TiO_2 window layer.

Structure	Conversion efficiency, %	Year	Reference
$ZnO/In_2S_3/CuSCN$	3.4	2008	[46]
$TiO_2/In_2S_3/CIS$	7	2008	[29]
$TiO_2/Sb_2S_3/CuSCN$	3.37	2009	[42]
TiO_2/Sb_2S_3/P3HT	5.13	2010	[4]
TiO_2/Sb_2S_3/spiro-MeOTAD	3.1	2010	[41]
$TiO_2/Sb_2S_3/CuSCN$	3.7	2010	[47]
$ZnO/In_2S_3/CIS$	4.17	2010	[48]
$TiO_2/Sb_2S_3/CuSCN$	3.4	2012	[45]
TiO_2/Sb_2S_3/ spiro-MeOTAD	3.1	2012	[45]
TiO_2/Sb_2S_3/P3HT	4.9	2012	[45]
TiO_2/Sb_2S_3/ PCPDTBT	6.3	2012	[45]

An extensive list of hybrid cells based inorganic nanostructured materials or nanocrystals (CdSe, CdS, CdTe, Si, PbS, TiO_2, ZnO, ZnS) and various polymeric donors is published by Wright [18]. A recent overview of the all-solid-state inorganic ETA cells with reasonable efficiencies was published by Hodes and Cahen [27] featuring mainly cells based on the $TiO_2/In(OH)S/Sb_2S_3/CuSCN$ structure. A review on semiconductor quantum dot sensitized nanostructures can be found by Rühle [49]. A comprehensive review of ETA cells has also been published by Dittrich et al. [33] underlining the many complex obstacles and the need for fundamental research in the field of nanostructured inorganic solar cells.

1.1.4. Extremely thin absorber (ETA) solar cell

As with the II generation solar cells, the rationale of the ETA cell is to minimize material bulk, by the use of a high absorption coefficient material that allows minimizing material thickness. In a thin film cell, a CIS absorber thickness of about 2 μm is sufficient to absorb most of the incident light with energies above the E_g [50]. However the ETA concept has even more ambition to decrease the absorber thickness down to a few hundred nanometers or less [3, 27]. Instead of a relatively thick absorber layer (1–3 μm) with a high electronic quality, such as thin film CIGSe that provides a long diffusion length in the order of 0.1–1 μm for carriers [11, 16, 50, 51], the concept of the ETA justifies the use of very low quality materials since the carriers do not have to diffuse over a significant length in the ETA material [19, 27, 43]. Once the diffusion length has reached absorber thickness, the impact of carrier lifetime has a marginal effect on the device performance [52].

At the same time, the low absorption ability of a single ETA layer is compensated by using a multiple ´folding´ of the ETA such that the optical thickness remains similar to that of the thick absorber [19, 33, 53]. The folding of the ETA is achieved via the use of optically transparent materials such as meso- or nanoporous TiO_2 [3, 4, 29, 36, 41, 42], ZnO nanorods [48, 54-56] or ZnO nanowires [26, 44]. A concept similar to where ZnO vertical structures are used, was already published as a patent in 1978 titled "Solar cell comprising semiconductive whiskers" [57]. A few detailed examples of state-of-the-art ETA cells follow further below.

Despite the complications in modeling the ′three-dimensional′ ETA cell, we share the majority of the deficiencies, and hence the models developed with the second generation solar cells: imperfect crystallinity of the absorber; poor minority carrier lifetime; carrier separation that may rely on electric field strength; interface recombination; grain boundaries that act as recombination surfaces or shunt paths; highly resistive or non-ohmic contacts.

The conventional thin film chalcopyrite cell may need to ′engineer′ the bulk material by grading the bandgap throughout the absorber thickness, up to the inversion of the conductivity type at the pn interface, by the use of different Cu-In-Ga-Se deposition profiles [15]. In an ETA cell, grading is neither required nor applicable because the bulk material responsible for absorption and transport has been minimized. In this sense, a cell that follows the ETA concept could have an advantage by decreasing the complexity that arises from producing materials with graded properties. Furthermore, in principle, the efficiencies of the photon absorption and carrier transport are decoupled in an ETA cell, from the aspect of the absorber material. This will be discussed in the following section.

Maximum theoretical efficiency of an ETA cell

Here, further details on the ETA cell are provided, mainly based on a model and valuable discussion by Taretto and Rau in 2004 [19].

In a conventional cell, the carrier collection length L_C in the absorber should exceed thickness d of the absorber (i); whereas the d should be close to the inverse of the absorption coefficient α of the absorber, that is, close to the penetration depth (ii), thus $L_C > \alpha^{-1}$. For the ETA cell, condition (ii) is relieved, since we have adapted the multiple folding technique to compensate for the poor absorption [19].

Condition (i) still applies for the very-low-quality extremely-thin absorber, i.e. the collection length L_C (sum of the depletion layer width and the diffusion length) should exceed the absorber layer thickness [50, 58]. Out of these components, the depletion layer width is of higher importance compared to the diffusion length in the ETA cells where carriers are rather driven by drift than diffusion, unlike in thin film chalcopyrite cells [50]. The trivial way to suit condition (i) is to drastically reduce the absorber thickness [19]. Simultaneously, the decrease in the absorber thickness reduces the total amount of grain boundaries that the carriers have to confront [59].

A parallel-connected ′single-gap multi-junction′ cell has been used to model an ETA cell [19]. According to simulations, an ETA cell with $CuInS_2$ absorber, has an optimized structure with no more than 6 cells in parallel with a single absorber thickness of around 20 nm predicting efficiencies up to 15% [19]. This value does not account for optical reflection losses at the front surface of the cell as well as series and shunt resistances, thus, it is an upper estimate – an output of an ideal case. The study [19] also reveals that the use of 7 versus 2 cells stacked perpendicularly to incident light yield only a minor improvement in the expected efficiency. That is, a very complicated structure may not be needed for a reasonable gain of efficiency, compared to a classical solar cell. The use of the optimum number of cells and the optimum absorber thicknesses requires very low diffusion lengths of L_D>10nm to reach efficiencies above 15% while the minimum required $CuInS_2$ absorber thickness W is 15 nm (thus the diffusion length L_D need only satisfy $L_D > 1/2 \cdot W$ with respect to the absorber thickness W). Below this value of critical absorber thickness, the *tunneling* recombination is major contributor that severely limits the cell′s efficiency [19, 53]. Likewise, built-voltages V_{bi} that reach very high values (and reach the limit $q \cdot V_{bi} \approx E_g$ set by the absorber bandgap energy) may not be desirable at a very low absorber width, due to a very high electric-field across a thin absorber and, as a result, a significant tunneling effect [19, 53].

In case of added light *trapping* ability, no more than just one $CuInS_2$ absorber layer with a width of 20 to 40 nm may be required (the simulations were performed assuming absorber carrier density of $\sim 3 \cdot 10^{11}$ cm^{-3} that determines the width of the depletion layer). In other words, the number of absorber layers required is significantly reduced up to an order of magnitude in case light trapping is used in the ETA cell [19, 53]. In other words, the light-trapping capability in a cell reduces the number of required absorber layers (perpendicular to the incident light). In fact, the latter is what we expect of the sprayed $ZnO_{NR}/In_2S_3/CuInS_2$ solar cell– a *light-trapping assisted single-absorber layer structure* (further in §1.2.5 Rationale of $ZnO_{NR}/In_2S_3/CuInS_2$ solar cell by spray).

The study [19] further found that the use of an absorber with very high absorption coefficient, such as $CuInS_2$, has an advantage in the ETA configuration when compared to the use of an absorber with a somewhat lower absorption coefficient, such as CdTe, reducing the required number of layers by a factor of two. Additionally, by a simple use of light-trapping, the total absorber thickness can principally be reduced to a order of magnitude smaller than the inverse of the absorption coefficient, even without the use of multiple folded layers [19].

1.1.5. Third generation solar cell

A first generation PV cell could be described as ′high efficiency at a high cost′ while the second generation cell as ′lower efficiency at a reasonable cost′, both of which are in production on a large scale. The third generation aims ′high efficiency at a low cost′. Most certainly, each of the technologies within the generations will have certain advantages dependent on the requirements for a specific application.

The second generation cells that use a single absorber material (the foundation of single junction solar cells) are fundamentally limited to a conversion efficiency below 33%, that is, below the Shockley-Queisser limit at one sun [60, 61]. Only photons with energy equal to or higher than E_g can be used to photovoltaic conversion. The efficiencies of the cells are thus limited by losses due to transmission of photons with energies below the bandgap ($h\nu<E_g$), and due to thermalization of the excess energy of the carriers created by photons with energies higher the bandgap ($h\nu>E_g$).

The technologies that seek to overcome that theoretical limit are called the third generation PV that apply a modification of the materials or a conversion of the incident light, for a highly efficient absorption of the polychromatic solar spectrum [12, 13]. However, they are expected to do so at easy materials processing and at a low cost of materials.

One of these concepts rely on materials that, upon modification, have an ability to absorb multiple sub-bandgap photons to create an electron-hole pair [14]. Such absorbers have a narrow delocalized energy band, at one third of the bandgap, introduced by doping beyond Mott transition with a suitable element [13, 62]. The theoretical efficiency limits for cells utilizing such a material are 48% and 63% for one-sun and for the maximum solar power concentration (46 050 suns), respectively [13, 14]. The feasibility of this intermediate band absorption concept has been proven for In_2S_3:V [63] and predicted in SnS_2:V [64]. These materials contain octahedrally coordinated sites with In or Sn, that are suitable locations for dopants.

A third generation solar cell will most likely take advantage of nanostructures [14]. The light-trapping capabilities, has been shown to be very important to support weaker absorption processes e.g. when impurity-introduced subgap defect levels are used to enhance the photocurrent [65].

1.2. Introduction to chemical spray deposition, $ZnO_{NR}/In_2S_3/CuInS_2$ solar cell and relevant thin film semiconductors

1.2.1. Chemical Spray Pyrolysis

The pioneering work on chemical spray pyrolysis is by Chamberlin and Skarman in 1966 on CdS films for photovoltaics [66]. The CSP is a non-vacuum chemical technique that has basically no limitations on substrate type, size or its surface profile. The CSP has been used to grow oxides; binary, ternary and quaternary chalcogenides and superconducting oxide films [67, 68]. The CSP method allows in-situ doping of the films by introducing precursors of dopants in the spray solution. The CSP technique is now widely used in industrial large-area-coating processes.

In a spray deposition process the precursor solution in the form of aerosol is directed to a hot substrate, via the help of an inert carrier gas like nitrogen or compressed air. In the pneumatic CSP process, the carrier gas itself by Venturi effect induces the formation of the aerosol of the precursor solution. Other techniques to form the aerosol droplets may used for specific advantages, e.g. to achieve smaller droplets with a narrow size distribution, or more control over the trajectory of the droplet [67]. The use of non-reactive carrier gas could be advantageous when contamination by oxygen is a problem, however, a turbulent flow will always entrain ambient air into the spray cone [68].

In the flowing aerosol, the solvent evaporates while dissolved reactants form the desired product – a process that should preferably occur on the substrate. Thus, the lowest growth temperature of the thin film by CSP is set by the decomposition temperature of the precursors used. Other decomposition products, if any, have to be volatile at the temperature of deposition. Hence, it is clear that in a CSP process the optimization of the setup with respect to the precursors used play an important role. The critical factors that affect thermal processes are temperature of the substrate, nozzle-to-substrate distance and velocity of the carrier gas.

Higher solution flow rates (ml/min) may have to be used to compensate the need for solutions with a low concentration of precursors (mol/ml), thus retaining the overall high feeding rate (mol/min) needed to obtain a reasonable deposition period and sustain the overall low cost of the method. In general, smooth films with columnar grains can be expected at low concentrations and low solution flow rates [68]. The total amount of solution that reaches the substrate at a constant flow rate depend on the size of the substrate with respect to the width of the spray cone near the substrate that, in turn, is dependent on the nozzle-to-substrate distance. Other factors that affect the solution amount reaching the substrate is the volatility of the solvent and the droplet size, speed and angle of incidence (the momentum) of the droplets in the atomized solution [29, 67, 68]. As an example, the air column above the heat source is expected to affect to droplet behavior due to convection.

The choice of the heat source is critical as well, e.g. infrared heaters induce a rapid response, whereas a massive hotplate possesses a high heat capacity and thus thermal inertia. A solid flat hotplate will be in thermal contact with as low as 1% of the substrate [68] whereas a liquid-metal heat-bath produces a much better wetting ability and thermal homogeneity of the substrate.

The molar ratio of precorsors which may or may not correspond to the anion/cation ratio in the final product, is also known to be a critical factor that affects film stoichiometry and quality [68]. As with the physical evaporation method, the choice and purity of precursors is a very important aspect of CSP

[69]. The crystallinity of the substrate will affect films′ growth via the amount of nucleation sites present. Aqueous solvent is mostly used in view of the low cost. When considering the use of e.g. alcohols as a solvent: “spraying flammable liquids on a heated surface can be exciting, if not dangerous” as expressed by Mooney [68].

1.2.2. Zinc oxide

ZnO is an optically transparent material (mineral name: zincite), with a direct bandgap of 3.37 eV at 300K. In sense of the atomic arrangement, the wurzite polymorph is the most stable at room temperature and atmospheric pressure. The wurzite has a hexagonal lattice with a=3.24 Å and c=5.19 Å. In the two sublattices of Zn^{2+} and O^{2-} each zinc ion is surrounded by four oxygen ions (tetrahedral coordination) and vice versa. Zinc oxide is an amphoteric oxide. ZnO has an n-type electrical conductivity due to strong compensation of native donor defects (V_O and Zn_i) or due to hydrogen incorporation; the growth of p-type ZnO has remained challenging [70].

The use of nanostructures in the form of ZnO nanorods is advantageous for devices that demand a large specific surface area such as gas sensors, catalysts, light emitters, optical sensors and solar cells. Transparent metal-oxide nanostructures, such as ZnO nanorods, can be used as an electron acceptor in the organic absorber based solar cells [18], in excitonic solar cells such as the dye sensitized solar cell [71]; in the extremely thin absorber (ETA) cells (further in §1.1.4 Extremely thin absorber (ETA) solar cell); and, as an antireflection coating in thin film solar cells.

The presence of *undoped* ZnO has a significant influence on the pn junction of a solar cell. A cell based on an asymmetrical n^+p or even an n=p junction will have a significant advantage over p^+n junction (in case p absorbs the light) [7, 10]. The depletion width is the smallest when no i-ZnO (intrinsic ZnO) is present, and increases with the thickness of the i-ZnO when present in the cell [72]. Likewise, the presence of the i-ZnO in the cell is known to induce a much higher electric field when compared to the use of absorber/buffer alone [52, 73]. In case ZnO is present, the ZnO/In_2S_3/CuSCN cell has been reported to improve its carrier transport when compared to that when ZnO is absent [27]. Another study states that ZnO_{NR} play a major role in the photoresponse of the cell because the depletion layer at the surface of the rods help to transfer the charge quickly to the center of the nanorods [74]. Also, the defect density of the interface states determined by C-f measurements may be correlated with how much the depletion layer extends into the ZnO window layer [75].

The ZnO is material that has been vastly investigated. For solar cells with the extremely thin absorber (ETA), low cost methods such as electrochemical deposition [26, 38, 44, 76], chemical bath deposition [54, 74], hydrothermal growth method [77] have been used to grow ZnO nanorods.

In this work, a simple CSP method is used to grow the ZnO nanorods. The possibility to grow ZnO nanorods by CSP using zinc chloride or zinc acetate as precursors was investigated by Dedova, Krunks et. al. [78-81]. The length and the aspect ratio, the surface coverage and the morphology of the nanorods can be varied by the use of different precursor type and concentration in solution, different growth temperature, solution acidity, density of nucleation centres on the substrate, additives in the spray solution, and reaction time. The initiative work on ZnO_{NR} growth by spray pyrolysis by Dedova, Krunks et. al. (in Laboratory of Thin Film Chemical Technologies, Department of Materials Science, Tallinn University of Technology) focused on optimization of precursor and growth conditions, phase composition and morphology.

1.2.3. Indium (III) sulfide

The β-phase of In_2S_3 is the most stable phase at room temperature and up to 420°C. The β-In_2S_3 has a body-centered tetragonal lattice with $a=b=7.619$Å and $c=32.32$Å [82], and a primitive unit cell that consist of 40 atoms, in which 75% of the indium (12 out of 16 atoms in the unit cell) is expected to fill the octahedrally coordinated sites, whereas the rest of the indium is in the tetrahedrally coordinated interstitial sites of the sulfur sublattice [83]. However, one third of the available six tetrahedral sites remain un-occupied in an ordered manner to preserve stoichiometric lattice without introducing any dangling bonds. Thus, a large concentration of vacancies is a natural part of the β-In_2S_3 lattice [63, 82, 84]. The cation vacancies in β-In_2S_3 are ordered, whereas in the cubic α-In_2S_3 they are not. At room temperature an excess of indium up to 40.1% absolute in β-In_2S_3 is possible at the expense of higher disorder, resulting in a mixture of α-In_2S_3 and β-In_2S_3. When above 40.5% of In is in the lattice of indium sulfide, only the α-In_2S_3 is expected [85]. Phase diagram including other In-S phases (In_6S_7, InS) can be found in [86].

The width and nature of the bandgap of In_2S_3 has been a matter of dispute [82, 87]. The width of the In_2S_3 bandgap has been well shown to correlate with the content of impurities, such as copper or sodium; and with the content of oxygen that, in turn, is influenced by the deposition method, precursors and conditions used [82, 87-89]. The first optical transition of a single phase β-In_2S_3 is an indirect 2.0 eV transition. The films are visually perceived with a color between red and yellow.

Independent of the cell design, any layer that obstructs the light from reaching the absorber should be either decreased to a minimum thickness, chosen with a highest possible E_g value, or both, to increase transmittance [51]. Additionally, an indirect bandgap would be preferable. An estimation of 2% is assigned to losses due to the absorption in the CdS buffer layer [58]. A buffer layer with a 10–50 nm thickness would be desired, however a very thin layer may lead to a lower V_{OC} and FF due to possible shunting through buffer pinholes as in case of the conventional substrate type CIGSe cells with CdS or In_2S_3 buffers [14, 90]. The CdS has a bandgap of 2.4 eV, whereas the In_2S_3 has a smaller gap of 2.0 eV with an indirect transition [87]; thus the In_2S_3 is expected to have a smaller absorption coefficient, suitable for PV application.

The In_2S_3 has been attractive for replacing the CdS in thin film photovoltaic cells that use chalcopyrite as absorbers materials, due to health concerns at the chemicals use, processing and recycling of the cell [14, 82, 88]. The advantages and disadvantages of the use of alternative buffer materials (oxides, sulfides, selenides of zinc or indium) and technologies have been reviewed [5, 88, 91]. For cells based on CIGSSe absorber, the In_2S_3 has been shown to be a viable alternative buffer layer when prepared by the spray-ILGAR, yielding cell efficiencies 16.1%, similar to reference cells where CdS by CBD was used [90]. Cells that use CIS as an absorber have also been grown on a copper tape using wide-gap p-type CuI as the buffer layer between the absorber and ZnO window layer [92].

In a conventional thin film cell, the buffer layer is introduced in the cell to improve lattice match between the wide-gap ZnO window and the narrow-gap chalcopyrite absorber [52, 82, 91]. The buffer reduces the amount of defects at the window-absorber interface, thereby reducing the probability for non-radiative recombination [12, 91]. The buffer thickness, however, should be kept at the minimum thickness in order not to introduce significant optical losses or series resistance [37] or tunneling in case of the ETA cells [46]. Especially in the case of wide bandgap absorbers (such as the CIS used in this thesis) the role of buffer layer is substantial, an absence of buffer layer lead to poor solar cell performance due to unfavorable band-alignment [7, 9].

Another strong reasoning for the use of buffer layer is, however, simply to prevent chalcopyrite deterioration when exposed to air [52, 73] or to re-establish beneficial surface conditions after the required air-annealing [16]. Yet another explanation that predict to bring profit, in particular to the ETA design, is the introduction of two interfaces (n-type/buffer and buffer/p-type) instead of only one (n-type/p-type), which, dependent on the choice of materials would increase the activation energy of recombination, even without affecting the interface state density [10]. The role of the buffer may also be simply a nucleation enhancer for the absorber deposition [27]. A list of potential advantages has been proposed in favor of the use buffer layer in the substrate type cells [6, 16, 91]. However, the presumed advantages cannot simply be reasoned for the use in a superstrate type ETA cell, where the semiconductors layers are ordered reversely, are not flat and have a very high specific surface area, when compared to the conventional substrate type cell.

Various methods have been used to grow In_2S_3 such as atomic layer deposition (ALD), physical vapor deposition (PVD) [91], thermal evaporation, radio-frequency sputtering (RF), metal-organic chemical vapor deposition (MOCVD), spray ion layer gas reaction (spray-ILGAR) [93], chemical spray pyrolysis (CSP), chemical bath deposition (CBD), spin coating [82], electrochemical deposition (ECD), and other.

For In_2S_3:V films, the realization of the intermediate band absorption (further in §1.1.5 Third generation solar cell) has been reported, especially aiming the photovoltaic application [63]. In here, the vanadium as a dopant should occupy the octahedrally coordinated cation sites to introduce a non-local band of electronic states in the lattice.

Ultrasonic spray pyrolysis has been used to deposit In_2S_3 buffer layer for the CIGSe solar cells [94, 95]. The In_2S_3 in this thesis have been grown by pneumatic CSP. The deposition and the formation chemistry of In_2S_3 thin films when grown by CSP using $InCl_3$ and $SC(NH_2)_2$ at varied molar ratios as starting chemicals have been investigated in-depth by Otto, Krunks et. al. (Laboratory of Thin Film Chemical Technologies, Department of Materials Science, Tallinn University of Technology) [96-99].

1.2.4. Copper indium disulfide

The $CuInS_2$ (mineral name: roquesite) has a tetragonal crystal structure, a primitive unit cell with 8 atoms and a bandgap of 1.5 eV with a direct transition [14, 100, 101] and an absorption coefficient $\alpha(\lambda)$ of 10^5–10^4 cm^{-1} in the range of 400–900 nm [102]. The CIS has a tetragonal lattice with $a=b=5.523$ Å and $c=11.118$ Å.

The ABX_2 (where A, B – cation, X – anion) is a highly compensated compound that allows 12 type of intrinsic defects, covering all possible vacancies, interstitials and antisites; and associated defect complexes [29]; even more, a spontaneous formation of large amounts of defects are preconditions for compound stability [16, 103]. Crystals that are stable at large stoichiometric variations, while showing long-range order, are known as ordered vacancy compounds [104], reported to exist in CISe compounds. The CIS can be n-type when the main donor (V_S and In_{Cu}) defects dominate, or p-type when the main acceptor (V_{Cu} and Cu_{In}) defects dominate, dependent on deposition conditions.

The crystalline structure of CIS varies between two common polymorphs: chalcopyrite (CH), and sphalerite at high temperatures [105]. The CH is thermodynamically most stable at room temperature; two metastable polytypes exist: CA (Cu-Au ordered) phase and CP (Cu-Pt ordered) [104, 106] that only differ in the cation sublattice. The CP is the least stable, while the equilibrium CH phase (tetragonal) and disordered CA phase (cubic) are stable at room temperature, can coexist as separate domains and have a neglible difference in the bandgap [106, 107]. In the ABX_2 chalcopyrite each anion X is tetrahedrally coordinated by two atoms A and two atoms B, while each cation is coordinated by four anions X. The A_2B_2 coordination is preserved in both CH and CA.

Quasi-binary (copper sulfide – indium sulfide) diagrams are used to describe a ternary compound, such as the $CuInS_2$. A phase diagram of the Cu-In-S system reveals another ′In-rich′ ternary $CuIn_5S_8$ that is stable at room temperature and Cu_xS compounds that can also co-exist with $CuInS_2$ [108].

The use of CIS high-temperature sulfurization is reported to increase the Cu/In ratio, a decrease of V_S as an undesirable n-dopant and increased ordering of cations in the crystals [105, 107], increase of the crystallinity and stoichiometry, less contaminants like oxygen or residues like chloride, but no differences in morphology [101], polytype CA to CH transformation [107, 109, 110] and $CuIn_5S_8$ to $CuInS_2$ transformation [109-111].

The virtues of the ABX_2 compounds are: the ability to dope via native defects, due to low formation energy of V_{Cu} that introduces a shallow acceptor level; structural tolerance, that is, stability at a large off-stoichiometry and their structural defects have a low impact due to $2V_{Cu}^{-}$ and In_{Cu}^{2+} donor-acceptor cluster that is electronically neutral, thus, these defects are passivated [112] while the complex itself has a zero or negative formation energy [5]. The use of $CuInS_2$ has been studied by NASA as the material with optimum bandgap for the AM0 (outside the atmosphere) conditions since polycrystalline materials outperform the single crystal devices in terms of radiation resistance whereas the CIS seem to outperform the CIGSe alloys [105]. Another advantage of the CIS is that the sulfur compound is less toxic to produce than the selenium compounds, especially when deposition is carried out in air, as is the case for CSP where aerosols in air are used. The high mobility of Cu is believed to act in favor of defect relaxation in the chalcopyrites, including resistance to radiation damage, thus yielding a highly stable compound [14].

In case of CIS grown by aerosol-assisted CVD, the (112) orientation parallel to substrate has been noted as preferable, in which case the least amount of In-rich secondary phases was present in the CIS films [105]. Suitable conditions to achieve the (112) orientation was a temperature of 400°C or the use of post-deposition annealing [105]. The authors also expect splitting of the (200)/(004) and the (116)/(312) diffractions in case of the chalcopyrite structure, a phenomena that is not present in the diffractograms of the sphalerite structure [105, 113]. Because sphalerite is a non-equilibrium phase at room temperature, splitting could be taken as a quality indicator. The sprayed CIS with good stoichiometry when grown from S-rich solution, for use as a sensitizer in a mesoporous TiO_2 cell, is also reported as to show (112) orientation [114].

The solar cells that use chalcopyrites as an absorber material have reached very high efficiencies, whereas the cells deposited using vacuum-based three source (Cu-In-Ga-Se) co-evaporation have remained superior when compared to lower cost alternatives [14, 15]; the CIGS cells that are based on rigid glass substrates are with conversion efficiencies above 20% whereas cells that are based on lower cost polyimide substrates have been shown to ~19% [15]. Entirely solution-processed method, that uses toxic hydrazine as solvent, yield CIGS cells on glass that show above 15% efficiencies [115]. Thin film solar cells based on $CuInS_2$ absorber grown by sputtering of Cu and In followed by sulfurization have reached efficiencies up to

11.4% with V_{OC}=729.4 mV, FF=71.7 %, J_{SC}=21.83 mA/cm^2 on a cell area 0.511 cm^2 [116-119] or even 12.2% for a cell with an antireflection coating and CIS by co-evaporation [120].

Vacuum methods use high-cost equipment and yield low throughput. Non-vacuum methods such as spraying, printing and electrochemical deposition in conjunction with post-deposition heat-treatment realize low-cost and high-speed production. Methods, such as ILGAR [36], CSP [101, 114] and other low-temperature chemical methods [121] have been used for fast and low cost CIS deposition. Also chemical vapor deposition (CVD) [105] and atomic layer deposition ALD [111] has been used to grow CIS.

The use of pneumatic CSP for deposition of CIS films, and the formation chemistry has been investigated by Krunks et. al. (Laboratory of Thin Film Chemical Technologies, Department of Materials Science, Tallinn University of Technology). They used $CuCl_2$, $InCl_3$ and $SC(NH_2)_2$ as precursors and growth temperatures 320-380°C, KCN-etching to remove Cu_XS, and the effect of thermal treatment in vacuum at 500°C or H_2S-containing atmosphere (400-500°C) to the structure and electrical resistivity of CIS films [122]. They further investigated the use of copper-rich solutions when sprayed at 360°C, and thermal annealing at 500°C of the sprayed low crystallinity films in the presence of intentionally deposited Cu_XS layer [123]. They also investigated the phase composition of the CIS films deposited at 370°C and after thermal annealing at 525°C [110]. The carrier density and the electrical resistivity has been reported for CIS films deposited at 370°C and after thermal treatment at 530°C in H_2S atmosphere followed by slow or fast cooling [124]. Finally, the chemical composition of sprayed CIS films deposited at low temperature of 250°C, with no post-deposition heat treatment in H_2S, was reported [125].

1.2.5. Rationale of $ZnO_{NR}/In_2S_3/CuInS_2$ solar cell by spray

Cost issues

Low-cost CSP can be used to deposit the window/buffer/absorber components of the cell. Low cost methods are of tremendous interest to solar cell community and of high importance to the use of solar energy at a very large scale. While the deposition rate for a 1.8 µm thick amorphous silicon cell is five hours [14], the whole $ZnO_{NR}/In_2S_3/CuInS_2$ stack by spray can be deposited in about an hour at most.

For the high efficiency thin film chalcopyrite cells, the deposition of the CdS buffer by low-cost CBD interrupts the otherwise in-line vacuum process, thus consuming time and energy. [24]. The $ZnO_{NR}/In_2S_3/CuInS_2$ cells can be deposited as all-layers-by-spray on a conductive substrate in a fast process which could easily be extended to a simple low-cost in-line production.

The concept of extremely thin absorber (ETA) and the use of simple spray pyrolysis technology diminish any cost, availability or supply issues concerning the use of *indium* as a constituent of the solar cell. The use of toxic elements has been avoided since the use of Se is questionable when open environments are used, such as the CSP setup here.

The thickness of the whole $ZnO_{NR}/In_2S_3/CuInS_2$ stack may be in the order of 1 μm, while e.g. thin film silicon cell can be decreased to minimum of 50 μm [14]. The thicknesses of the CIGSe cells are 1 to 3 μm, CdTe cells are 4 to 10 nm thick [126]. As a case in point, when a-Si is used in an ETA configuration on top of ZnO_{NR}, absorber thicknesses can be reduced to 150–200 nm [77, 127].

Width of the bandgap of the absorber

The use of an absorber with a relatively wide bandgap, such as the CIS with 1.5 eV should in principle allow higher voltages at the expense of lower currents, when compared to cells with a lower bandgap. The maximum voltage V_{OC} will unavoidably be lower from that expected of a cell with an absorber with a bandgap of E_g and $qV_{OC}<E_g$ is inevitable due to thermodynamic losses [60] whereas the losses would be relatively smaller in a cell with a higher bandgap absorber. Additionally, a wide bandgap cell is less affected by transmission losses due to free-carrier absorption in the TCO window layers. When used in a tandem configuration, a wide gap absorber is desirable as the top cell that situates on the narrow-gap bottom cell [30, 59]. Ideally, a cell with a wide-gap absorber such as CIS, instead of e.g. CISe, would suffer less at higher temperatures due to a potentially larger V_{OC} and thus benefit from a lower thermal coefficient of the cell efficiency [11].

Substrate vs. superstrate configuration of solar cells

In a *superstrate* cell design the deposition order of the layers has been reversed (glass/ITO/window/buffer/absorber) when compared to that in a conventional *substrate* design where the absorber is deposited on an opaque material and the cell is covered with a transparent material (glass or polymer) [51]. Although the efficiencies of the superstrate type chalcopyrite thin film cells have reached ~13% efficiency, the substrate configuration where the buffer layer is deposited onto the absorber outperform the superstrate type with >13% efficiencies [14]. In case of the CdS/CdTe solar cells, the superstrate configuration yield cells with *higher* efficiencies, compared to the use of substrate design [14].

In the superstrate design, the $CuInS_2$ absorber will be deposited onto the In_2S_3 buffer layer that, in turn, is situated on a ZnO window and a TCO (transparent conductive oxide) layer. The choice in favor of the superstrate design is inevitable since ZnO_{NR} has to be pre-grown and can only be subsequently sensitized by the $CuInS_2$ absorber. We start with the growth of ZnO_{NR} having the highest growth temperature; proceed with that having an intermediate growth temperature (In_2S_3); while the subsequent absorber has to suffer the use of the lowest growth temperature as well as restrictions on annealing conditions. As a virtue in case of the *superstrate* design, the glass substrate is simultaneously the front side encapsulant that is exposed to the sunlight, whereas for the back-side a less durable material can be used to seal the cell, such as a polymer [68].

Role of ZnO_{NR} light scattering layer for increasing absorption ability of solar cell

The ZnO nanorod layer used in the superstrate type $ZnO_{NR}/In_2S_3/CuInS_2$ solar cell aims to ′fold′ the absorber layer and thus decrease the losses associated with poor absorption due to transmission, when compared to a single absorber layer perpendicular to the incident light. Additionally, the ZnO_{NR} is basically an antireflection aid that relies on the *scattering* the incident light as opposed to classical coatings based on interference of the incident light [128]. Moreover, ZnO_{NR} as a part of the sprayed cell is not a conventional textured coating for antireflection since the ZnO_{NR} layer is a vital and integrated part of the cell that also defines the thickness of the sprayed cell. In a ZnO_{NR} layer the multiple reflection events extend the photon path and the probability for photon absorption [129]. The light-trapping due to ZnO_{NR} has been shown to suppress losses due to reflections of photons with >2.5 eV (<500nm) and <2.25 eV (>550 nm) while longer rods show better antireflective properties, as reported for cell that uses a:Si:H absorber [77]. Strong enhancement of long-wavelength part of the spectrum has also been noted when increasing the nanorod lengths in a $ZnO_{NR}/In_2S_3/CuSCN$ cell by wet chemical methods [54]. The growth of ZnO_{NR} as a scattering layer is much cheaper from that when top-down approaches are used, such as etching of inverted pyramids on pre-grown silicon wafers; and less expensive from that when time-consuming vacuum-based techniques, such as reactive-ion etching are used to texture a surface, in order to decrease reflections and to increase absorption in the silicon based cells [14].

Front contact

A pair of electrically conductive leads is required to extract carriers from a solar cell. The outermost conductive layers should be metal or a highly-doped semiconductor, whereas the inner conductors should preferably be energy-selective (charge selective) conductors, which extract either holes from the valence band of the absorber, or electrons from the conduction band of the optical window material. The outer electrodes of the cells in present thesis are not deposited by CSP. Commercial ITO on glass, that is, tin doped indium oxide (In_2O_3:Sn) sputtered on soda-lime glass has been used as the transparent conductive substrate as the front contact (on the side that is facing the sun). In the long run, ITO should be preferably be replaced if possible by lower cost TCO alternatives. Popular alternatives are e.g. ZnO:Al, ZnO:In and SnO_2:Sb [14].

Back contact

The cell studied in the thesis uses neither a hole-conductor nor a metallic contact/back-reflector. A reflective back-contact is expected to boost the light-trapping factor by increasing the path length of the incident light by multiple reflections, however shadowing effect should be avoided due to the non-transparent metal [3]. In the studied cell, the CIS absorber itself acts as the hole-conductor. Although the use of a separate hole-conductor might not turn out to be critical, it could be of benefit to certain ETA cell designs dependent of materials used, and the porosity in the general meaning (spacings, gaps etc.). For example, a transparent hole-conductor that penetrates the gaps and pores of the nanostructure is especially advantageous to avoid shadowing effects in a highly structured layer [3]. In this thesis, speculations concerning the lack or the possible use of a hole-conductor are mostly avoided. For future development, the issues concerning the metallic back-contact and the possible use of a hole-conductor need a thorough revisit.

Previous studies on the sprayed $ZnO_{NR}/In_2S_3/CuInS_2$ and observations

There is very little knowledge about the all-layers-sprayed ETA cell based on ZnO nanorods and extremely thin CIS absorber. Previous work on the all-layers-sprayed $ZnO_{NR}/In_2S_3/CuInS_2$ has been on the general characterization of the cells at standard conditions [130] and on the effect of titania barrier layer on the cell performance [131]. Basic measurements had indicated higher current and lower voltages when compared with a flat analogue cell with compact ZnO; and an open-circuit voltage much lower than expected. We observed several phenomena, such a violation of the shifting approximation and cross-over effect of the current-voltage curves, and photosensitivity of shunt-conductance. The explanations were not complete or satisfactory, it was unclear which of the non-idealities was the dominant source of the frequently observed and significant anomalies.

1.3. Characterization methods of thin films and solar cells

1.3.1. Solar cell characterization

The route for developing a solar cell is to identify the main losses. There are factors that limit the voltage, factors that have an effect on the current, and optical losses. Optical losses can be evaluated from EQE, any deviation from an ideal transport mechanism of carriers reflects in the shape of the I-V curve. To distinguish the influence of each of the factors is not an easy task if a number of them occur simultaneously [92, 132]. For example, at a large enough series resistance (R'_S) and shunt-conductance (G'_{SH}) the ideality factor will be significantly overestimated, thus, the quality of the junction will be significantly underestimated, unless corrected for. The correction for R'_S and R'_{SH} will potentially reveal the properties that are intrinsic to the junction and to the absorber [51]. Obviously, the numerical values of the parasitic effects are just as valuable. After all, the properties of the devices have to be traced back to the properties of the constituent materials.

The opposite route, that is, evaluation of the physical properties of the component materials followed by applying a junction theory may not in reality lead to the expected device. For example, the carrier lifetime measurements on bare absorber films cannot be directly correlated to those made in the final device due to the fast charge separation [52, 73]. Another cause is that in reality the interface of the heterojunction device turns out to be much more complex than predicted by the idealized, although widely accepted, physical models [1]. Many of the available model used for thin film characterization cannot be considered more than approximation, with parameters extracted only as effective rather than an absolute realistic measure [7]. Nevertheless, if used with caution, the models can successfully be used to quantitatively compare a batch of samples.

Characterization of solar cells with low quality absorber cannot always follow the standard textbook model for crystalline silicon [7, 51]. As a prominent example, the restriction especially concerns the capacitance-voltage (C-V) profiling method for estimating the built-in voltage or carrier density in an absorber with e.g. significant interface states [133] or deep traps [134, 135]. For determination of the carrier density in the possibly non-uniform bulk material of the defect-rich polycrystalline or amorphous materials, the drive-level-capacitance-profiling (DLCP) method, insensitive to interface states, has been developed [51, 75, 136, 137]. Other methods, such as J_{SC}-V_{OC} method at varied illumination intensities, can only be conditionally applied [92]. Likewise, in most cases, the processing of the chalcopyrites has been empirical, and without strong knowledge on the identity of the active defects [1, 16, 112]. Causes of the deviations from idealized models are: the inability to predict all inaccuracies in a solar cell production, e.g. a non-uniform distribution of the concentration of defects and impurities; as well as macroscopically non-homogeneous materials; such, that the cell behavior may be described as ′beyond intuition′. An interesting case of empirical development is the, still disputed, relevance of the buffer layer.

Current-voltage characteristics

The analysis of the I-V curve, and extraction of the relevant parameters within, is an indispensable tool. The dark-light set of the I-V measurements, performed in dark, and at the conventional AM1.5 white light illumination (100 mW/cm^2) at room temperature (25°C) and at perpendicular incidence, is the common solar cell evaluation tool.

I-V curve of an ideal solar cell can be fitted with a single exponential (Shockley diode) equation. The idealized solar cell can be treated as a constant current generator in parallel with a diode, with the current independent of the voltage across the cell; as opposed to a battery that is idealized as a source of constant voltage independent of the current through the battery.

A *realistic* cell has deviations from the ideal diode model. Thus, an important step of the I-V analysis is to distinguish any of such parasitic effects (ohmic resistance and shunts) that are significant and interfere with the analysis of the diode; and if applicable, to determine the dominative parasitic effect [51]. The DC (direct current) equivalent circuit that describes a solar cell has a current source, a pn junction diode and a shunt resistor in parallel, along with a resistor in series. The shunts are basically unwanted stray currents; the discussion on effects of the series resistance on solar cell measurements go back to the early days of solar cells development [138]. The series resistance of the cell must also be taken as a possible source of interference in the interpretation of the admittance spectra [94, 139, 140].

The efficiency of the cell in the maximum power point of the I-V curve reflects the available portion of power available for conversion, out of a given energy flux in the form of photons incident on the cell. Other important data points extracted from the I-V plot are the current I_{SC} at short-circuit conditions of the cell, and the voltage V_{OC} at open circuit conditions. The fill factor FF reflects how the I-V curve resembles the *shape* of the I-V curve of an idealized solar cell with FF of 100%. The FF reaches from a minimum of 25%, up to 90% in high-efficiency GaAs cells. The FF is truly a compound characteristic; it characterizes the deviation of the I-V shape when compared to an ideal case; reflects significant carrier collection losses due to recombination and parasitic effects in the realistic cells, whereas generally the analysis and the value of FF does not differentiate one non-ideality from another.

Other non-idealities that are expected to interfere with the I-V analysis include material properties that are dependent on irradiance (including illumination dependent parasitic effects) and voltage dependent effects. For example, a deviation from the approximation of the constant current source $J_L = f(V)$ might be caused by field-dependent current collection when relatively thick absorbers are used [51]. Violation of the shifting approximation, by which the dark-curve does not translate to the light-curve by simply shifting the I-V data in the vertical axis direction, may have various reasons. The cross-over of the dark and light I-V curves is yet another non-ideality with several possible causes proposed [5]. Defect metastability dependent on illumination or voltage bias is another example [75, 135, 137]. These are only a few phenomena that complicate the cell analysis; and may have different causes in different cells [5, 51].

The details on the I-V analysis are presented in the Experimental section (§2.3.1 Current-voltage characteristics). The standard I-V measurements, the illumination and temperature dependent I-V measurements can provide a wealth of information, however, cautious interpretation and a constant look for non-consistencies in the analysis is advised, the extraction of diode parameters is difficult due to the presence of parasitic effects, and depend on the method that was used for calculation.

External quantum efficiency spectroscopy

The external quantum efficiency is the spectrally resolved photoinduced current (photocurrent) of a solar cell at short-circuit conditions. The unitless EQE is given by the short-circuit current density J_{SC} ($A \cdot m^{-2}$) and the light intensity P ($W \cdot m^{-2}$) incident on the solar cell [40]:

$$\mathrm{EQE}(\lambda) = \frac{hc}{q\lambda} \cdot \frac{J_{SC}(\lambda)}{P(\lambda)} \tag{1}$$

More simply, EQE is the ratio of the number of carriers collected $N_e = J_{SC}(\lambda)/q$ at the electrodes, to the number of photons $N_{ph}(\lambda) = P(\lambda)/\frac{hc}{\lambda}$ incident on the cell; where $\frac{hc}{\lambda}$ is the energy of a single photon as function of wavelength λ.

For practical I and II generation solar cells, the EQE is lower than unity (EQE<1) [61]. The incident spectra $N_{ph}(\lambda)$ will be lossy due to reflections and absorption in materials that cover the absorber layer, particularly the In_2S_3 buffer as also shown in [V]. Likewise, at the location of photon absorption, the number of photoinduced carriers will always exceed that collected externally at the electrodes. Ultimately, the efficiencies associated with different loss mechanisms add up:

$$\mathrm{EQE} = \eta_{abs} \cdot (\eta_{diff} \cdot \eta_{sep} \cdot \eta_{tr} \cdot \eta_{cc}) \tag{2}$$

where η_{abs} is the photon absorption efficiency and latter represent losses due to low electron-hole diffusion lengths (η_{diff}), poor electron-hole separation (η_{sep}), recombination at carrier transport (η_{tr}) and deficiencies in the charge collection (η_{cc}) process [18, 34]. The magnitude of η_{abs} describes the ability for photons to reach the absorber, as a function of wavelength; whereas the term in brackets (internal quantum efficiency) may have a dependence on irradiance as well as voltage bias. The photons that do reach the absorber can be estimated as follows:

$$\eta_{abs} = (1 - R_F) \cdot (1 - A_{TCO}) \cdot (1 - A_b) \cdot (1 - T_{CIS}) \tag{3}$$

where R_F is the reflectance of the front surface, A_{TCO} and A_b are the absorption in the TCO and in the buffer layer, and T_{CIS} is the transmittance of the CIS absorber, all functions of wavelength [51]. The last factor $(1 - T_{CIS})$ has been added due to incomplete absorption of light in the single ETA layer (§1.1.4. Extremely thin absorber (ETA) solar cell), and due to the fact that back-reflectors (metallic back-contacts) have not been used in the cell of the present study.

Incomplete light trapping is considered one of the main weaknesses of solar cells, a deficiency that deserves attention in the PV research [60]. We strike T_{abs} by the use of ZnO nanorod layer, in the superstrate type $ZnO_{NR}/In_2S_3/CuInS_2$ solar cell, which aims to decrease the losses due to incomplete light trapping [II]. The losses due to factor A_b are explored in [V]. Other losses described in [II, V] are the recombination, the shunt-conductance and the series resistance.

The integration of $\mathrm{EQE}(\lambda)$ over the incident wavelengths $\mathrm{N}(\lambda)$ should give an estimation of J_{SC} at AM1.5 conditions, that is, at ′full sunlight′ [18, 34, 51, 61]. However, when the carrier collection efficiency is a function of irradiance (as shown in [II]) or a function of the spectrum shape, then the expected J_{SC} will likely differ from that measured at AM1.5; and in EQE has to be accounted for experimentally by using a white light bias [51]. Thus ideally, $\mathrm{EQE}(\lambda)$ is independent of the ′shape′ of the incident spectrum, however, only up to a certain extent in realistic cells, such as the cells in here [II, V]. Unfortunately, in [V] this phenomenon received little attention and discussion.

As a remark, the silicon solar cells have been shown to give EQE>1 in the ultraviolet region, explained by the inverse-Auger-emission (impact ionization) of a carrier due to relaxation of a high energy carrier (a hot carrier) [141]. However such a phenomenon of ′carrier multiplication′ is considered marginal for a perspective use in the silicon cells [14]. On the other hand, PbSe nanocrystals have show quantum yields up to 700% [142]. The CIGSe cells with the highest efficiencies reported have shown EQE 90–95% between 500 and 900 nm [17].

Capacitance-frequency characteristics (admittance spectroscopy)

Admittance spectroscopy (AS) uses alternating current (ac) to probe the response of electronically active states introduced by defects in material bulk and at interfaces of the depletion layer of the pn-junction, that is, states within the band-bending region [51, 75, 135, 143]. Although capacitance measurements are the main method to evaluate deep states (traps), the AS is an advanced technique for thin film solar cell characterization, and the interpretation of the results is not trivial [75]. When used alone, the AS may not help much, but a combination with other measurements is very powerful approach to attack cell deficiencies.

Monocrystalline silicon does not have any specific features in the capacitance-frequency C-f plot in range of 1Hz to 1 MHz and above. However, the lower quality absorber materials and interfaces in thin film solar cells may have a capacitance plateau C_{LF} at low-frequencies (i), followed by a decay of the capacitance (ii), and a high-frequency capacitance plateau C_{HF} (iii). Defect levels do not respond to frequencies that correspond to C_{HF}.

The *magnitude* and the *steepness* of the step (ii) in between C_{LF} and C_{HF} speak of the total amount of defects and the width of the band of defects, respectively. It is common for thin film cells′ capacitance to decay over many decades of frequency, that corresponds to a continuous energetic distribution of defects as opposed to defects that introduce a single energy level [92, 133]. The C_{LF} may not be independent of the frequency, carrying information of a possible tail of states.

Still, there are several phenomena that may interfere with such an interpretation, and careful analysis is advised [90, 94, 126]. Voltage dependence of admittance may reveal metastability of defects, to assist in distinguishing between defect states in bulk from those at interfaces, or other sources of capacitance [51, 58, 75, 94, 136]. The temperature dependent admittance measurements of a voltage biased cell may allow to distinguish interface from bulk, or to distinguish presence of discrete states from a distribution of deep states. For example, the inflection point of the C-f decay from C_{LF} to C_{HF} is not expected to shift with bias in case of single energy levels in bulk are involved [5, 133, 135], while a shift is expected in case of the interface states. Still, when a high defect density at the interface states tend to energetically fixate the Fermi level, then no shift in the inflection point is expected [5, 75, 135]. That is because the admittance method is only sensitive to defect states with energies that coincide with the Fermi level [135, 144]. Followingly, a broad distribution of defects, when determined by admittance, has to be of bulk origin and cannot be attributed to the interface, when Fermi level is fixed with respect to the bands [144]. Alternatively, elaborate experiments with C-f measurements in conjunction with sample annealing could be used, whereas bulk states are not expected to shift upon annealing; or empirically, by observing changes of admittance having replaced a layer [75] or changed its thickness [135] in the cell structure.

The ac model of solar cells has two elements, a capacitance in parallel with a frequency dependent resistance. The cell is measured at zero bias or at a moderate reverse bias. Possible changes in sample, due to the probing current, are avoided since in the AS the use of only a small ac signal keep the sample at equilibrium conditions [75].

1.3.2. Semiconductor thin film characterization

The fundamental building block in a crystalline solid is referred to as the *unit cell* that contains a fixed number of atoms. The unit cells line up to form a regular *lattice* that constitutes as the basis of a crystalline solid. Solid materials are said to be amorphous (glassy) when they lack any short-range regularity, that is, a lack of short-range order. Long-range order, on the other hand, starts with the smallest monocrystalline unit – the *crystallite* that has a significant importance in materials studies. Dependent on the crystallite size (CS), materials could be classified as multicrystalline (CS>1mm), polycrystalline (>1µm), microcrystalline (>1µm), nanocrystalline (<1µm) and amorphous (no long-range ordering). By this classification, the submicronic films examined in this thesis are nanocrystalline.

The crystallites meet at a boundary – an interface that contains crystallographic defects in the form of intrinsic point defects and dislocations. The defects are due to a lattice mismatch between the crystallites of different orientation with respect to each other. The size of the crystallite depends, for one, on the growth speed of the solid phase determined by the method of choice and conditions used [1]. Thus, the defects tend to accumulate at the crystallite boundaries during growth of the film. The crystallites′ size (and stoichiometry) can be further increased by using post-growth heat-treatment (in a controlled atmosphere). In this view, in the limit of small crystallites, a solid is amorphous when the volume fraction of grain boundaries reaches 100%.

The semiconductor thin films are solids that are mostly expected to consist of a single phase of a crystalline material. However, the films usually contain secondary phases, phases with stacking disorder, and residues of the precursor in the form of reacted or unreacted products [82]. The existence of secondary phases affects the growth and the properties of polycrystalline solids, and prevents building long-range order.

The single-phase material thus forms *grains* – units of polycrystalline material, separated and yet held together by amorphous boundaries that may contain unwanted phases or voids [8, 101]. Since the grain boundaries induce carriers′ recombination in PV materials, large grains with less boundaries are beneficial [1, 11, 21, 44, 58, 73]. At least, *columnar* grains that extend throughout the absorber thickness are preferred [59, 68, 145] since the grain size along the substrate may have little or no effect on carriers collection [146]. Ultimately, the effect of defects on recombination is also determined by whether net charge is present at the location of recombination [7, 10, 59, 147]. As one example, discussed earlier, the defects in CIS bulk tend to be charge-compensated due to defect-pairing. Charges at grain boundaries and interfaces, on the other hand, may be present [10, 59].

A variety of methods are popular for characterization of thin film solar cell materials [1]. In the thesis, X-ray diffraction (XRD), Raman spectroscopy, photoluminescence, and scanning electron microscopy (SEM) were used to a large extent.

The arrangement of atoms in the thin solid films was determined by *X-ray diffraction* [I, III, IV] for characterization of the long-range order of the crystal. Since symmetric (Bragg-Brentano) measurement regime was used, crystalline planes that are parallel to the substrate are detected [1]. Information on phase composition, crystallinity and crystallite size, the type of lattice and the unit cell parameters, and preferential orientation of the crystallites with respect to the substrate were extracted from the diffractograms. The phase analysis relies on comparison of the peaks observed with those of the diffractograms published by the International Centre for Diffraction Data (ICDD).

Raman spectroscopy [I, III, IV] was used to evaluate the phase composition and quality of the films, and to differentiate between polytypes. The latter are a result of different stacking sequences of otherwise identical atomic layers (packing polymorphism). Raman spectroscopy is a valuable tool for characterization materials vibrational properties, and has been proven as essential method for the investigations of thin film chalcopyrite absorber materials. The method relies on the inelastic scattering of light by lattice thermal fluctuations. The position and the width of Raman peaks are sensitive to structural factors like stress, structural defects, disorder and the presence of secondary phases that all speak of the possible degradation of material quality [148, 149].

Photoluminescence spectroscopy allows to analyze the energetic distribution of defects in a semiconductor, thus to evaluate the quality of the material by measuring the emission spectra of radiative recombination. The peak energy and linewidth of the spectra were mainly evaluated to extract useful information. Low temperature measurements were used to ´freeze´ non-radiative recombination. Photoluminescence measurements require the radiative emission to dominate the non-radiative recombination. Thus a good PL spectrum, in essence, speaks of a relatively pure material.

Scanning electron microscopy (SEM) is used for high resolution imaging of surfaces, can be used to estimate the grain size in the thin films, and to check existence of cracks or voids.

1.4. Summary of literature review and aim of the study

The development of solar cells could be divided into three categories. The first generation focused on materials quality alone. The second generation focused on the overall rationalization and optimization of the cell design by introducing new materials such as defect-rich semiconductors and organic semiconductors; new cell designs such as nanocomposites and hybrid cells; and new technologies. The third generation focuses on the efficient use of incident light by photonic enhancements. The sprayed $ZnO_{NR}/In_2S_3/CuInS_2$ solar cell based on nanorods has perspective to incorporate third generation photovoltaic ideas, such as the intermediate band concept. The spray method itself has a huge potential in sense of the reduction of the cost of thin films and devices.

Based on literature review, following conclusions are drawn:

1. The extremely thin absorber based solar cells use either ZnO nanorod or mesoporous TiO_2 as the window layer, while several buffer and absorber layer candidates have been tested worldwide using various deposition methods. Among these, the all-layers-sprayed $ZnO_{NR}/In_2S_3/CIS$ is unique. Our previous papers on the sprayed $ZnO_{NR}/In_2S_3/CIS$ solar cell are mainly descriptive, with cell output reported at standard conditions only. Several anomalies occur with the cell (violation of the shifting approximation and cross-over of the I-V curves, lower than expected bandgap of the absorber, and lower than expected open-circuit-voltage) that need attention. There are no reports on electrical characteristics at varied measurement conditions.

2. The formation, composition and morphology of CIS thin films are well-studied when deposited by spray at temperatures above 300°C. The chemical composition when deposited 300°C has been reported. There is no report for

structural studies of low temperature films, and the effect of post-deposition annealing of the CIS structure.

3. The formation chemistry, and the optimum deposition parameters of sprayed In_2S_3 have been well-studied. There are many reports with In_2S_3 applied as buffer layer in thin film solar cells. Additional optical absorption is present, when vanadium is introduced in the octahedral cation sites of In_2S_3 due to intermediate band effect. There are no experimental reports by Raman on the structural ordering of the sprayed In_2S_3 films.

4. The effect of varying deposition parameters on the morphology of sprayed ZnO_{NR} has been reported. There are no reports on crystalline quality and electrical properties of ZnO_{NR} deposited by spray.

Based on the conclusions of literature overview, this thesis has the following aims:

1. To extensively characterize the all-layers-sprayed $ZnO_{NR}/In_2S_3/CuInS_2$ solar cell and, if possible, to state the causes of the prominent anomalies that are observed. The shortfalls might be the cell design, materials used, as well as preparation conditions and so forth.

2. To determine structural properties (crystallinity, stoichiometry, phase composition) of CIS films when grown by spray on glass at lowest possible growth temperatures, and when annealed at varied duration in sulfur containing atmosphere. If applicable, to link results to solar cells´ studies.

3. To determine structural properties, in particular indium to sulfur coordination, of indium sulfide films when grown by spray on glass at varied growth temperatures and when annealed in sulfur containing atmosphere, using aqueous or alcoholic precursor solvent. To draw relevant links to solar cells´ studies.

4. To study the morphology, crystalline quality and carrier concentration in ZnO nanorods when grown by spray at varied substrates and at varied growth temperatures. To provide further discussion in relation with solar cells´ studies.

2. EXPERIMENTAL

2.1. Deposition of thin films and layers

2.1.1. Chemical Spray Pyrolysis

We used pneumatic CSP. The spray solution (that contains precursor and solvent) is forced through a stainless steel nozzle using ca 6 L/min flow of compressed air. The nozzle is stationary and tilted with respect to the substrate. The resulting aerosol is directed towards a heated substrate. The solvent evaporates primarily in the vicinity of a heated substrate while the precursor materials decompose to form the resulting thin film, whereas the solvent and residues of the precursor materials are expected to evaporate. The presence of circular formations on some of the thin films, in the order of tens of micrometers, hint the characteristic size of the spray droplets, which may or may not reach the substrate dependent of deposition conditions.

The substrate is situated on a rotating tin bath with a temperature controlled by a thermostat. The temperature of the substrate surface is as much as 50°C lower with respect to the temperature of the tin bath due to heat gradient in the substrate. Most of the cooling, however, is due to the flowing carrier gas. Whenever possible, actual surface temperatures are reported that were measured by a thermocouple during the spray process. However, the true temperature of the idealized pyrolysis process in the reaction zone near the substrate surface would be difficult to determine.

2.1.2. Zinc oxide nanorod layers

The ZnO nanorods grow from the dissolved zinc chloride in an aqueous or alcoholic solution that was sprayed onto the heated substrate. An ITO covered glass was used for solar cell application [II, V] and for the optical and electrical studies of single ZnO_{NR} layers [III, VI]; alternatively a soda-lime glass (microscope slide) with 25 cm side lengths and 1 mm in thickness was used [III]. The ZnO nanorod layers were deposited at substrates with a surface temperature in between 480°C and 550°C. The resulting nanorods were with a length of 500–1000 nm and a diameter of 100–300 nm, dependent on deposition conditions. More details in the respective papers.

2.1.3. Indium (III) sulfide thin films

When grown onto the ZnO nanorods for solar cell application [II, V] the In_2S_3 was grown by CSP as a double-layer using aqueous precursor solutions with pH=5 and another with pH=3 to avoid dissolving the ZnO_{NR} substrate which was kept at ca 300°C [48, 130]. As precursors, $InCl_3$ and thiourea $CS(NH_2)_2$ with molar ratio of 1:3 [II, V] or 1:6 [I] were used. In the solution, the precursors form an indium-chloride-thiourea complex as an intermediate compound that decomposes to form the In_2S_3 [96]. When grown onto glass or borosilicate as single layers at temperatures of 205–320 °C, the films were n-type, uniform in thickness, with no pinholes and adherent to the glass substrates. After deposition, the films grown onto borosilicate glass were heat-treated for 30 min at 500°C; subjected to flowing gas in proportion of 5% H_2S (99.99% purity) and 95% N_2 (99.999% purity); followed by cooling to room-temperature at a rate of ~25 °C/min [I]. More details in the respective papers.

2.1.4. Copper indium disulfide thin films

The $CuInS_2$ thin films were grown in air by CSP from aqueous solutions containing $CuCl_2$, $InCl_3$ and thiourea $CS(NH_2)_2$ as precursors with molar ratio Cu:In:S of 1:1:3 [II, IV, V] or 1.1:1:3.1 (Cu-rich) [IV] in the solution using $[In^{3+}]$=2 mmol/l. In the spray solution, copper-chloride-thiourea and indium-chloride-thiourea complexes are formed that decompose thermally at temperatures above 200°C [150]. As a result, the corresponding metal sulfide phases, In_2S_3 and Cu_XS, are formed, which then react to form the $CuInS_2$ [150]. For solar cell application [II, V] acidic solutions with pH=3 were sprayed onto the window/buffer substrate kept at ca 270°C [II] or 300°C [V].

When deposited as separate layers [IV], borosilicate substrates were kept at 250±5 °C [IV]. The as-deposited films were etched in KCN (potassium cyanide) to remove Cu_XS phase that had segregated on the surface of the $CuInS_2$ film. The etching is highly selective and does not affect $CuInS_2$ [50]. The samples were annealed at 530°C in a mixture of 95% N_2 (99.5% purity) and 5% H_2S (99.99% purity) gas atmosphere for 5–60 minutes. For annealing, the samples were heated up in 5 minutes and cooled down with a rate of ~25 °C/min. More details in respective papers.

2.2. Characterization of thin films

A summary of the techniques used for the characterization of thin films prepared by the CSP is presented below in Table 2.

2.2.1. X-ray diffraction

X-ray diffraction patterns [I, III, IV] were recorded in Tallinn University of Technology on Rigaku Ultima IV apparatus using monochromatic Cu K_α radiation (λ=1.5406 Å, 40 kV at 40 mA) and equipped with silicon line detector D/teX Ultra, in 2θ (Bragg-Brentano) regime, using 2θ step of 0.04 deg, counting time 2–10 seconds per step, and sample rotation. Crystal phases were identified using files issued by JCPDS (Joint Committee on Powder Diffraction Standards). Crystallite size and lattice constants were calculated using Rigaku PDXL Version 1.4.0.3

software; NIST (National Institute of Standards and Technology) external standard (LaB_6) was used to determine the instrumental peak broadening. The lattice spacings were calculated using the Bragg formula. The crystallite size was calculated using the Debye-Scherrer method and a Scherrer constant of 0.94 [1, 44], using the full width at half maximum (FWHM) of the XRD peak with highest intensity, corrected for instrumental broadening.

2.2.2. Raman spectroscopy

The Raman spectra of the In_2S_3 films [I], ZnO_{NR} layers [III] and CIS films [IV] were measured in three characteristic sample locations at a backscattering configuration and at room temperature using confocal micro-Raman spectrometer HORIBA Jobin Yvon LabRAM HR800 using λ=532 nm (2.33 eV) laser excitation. The power density was kept sufficiently low to prevent excessive heating of the sample area of ca 100 μm^2, during 100 seconds of data acquisition. At 5 mW laser power and a spot diameter of 10–20 µm the excitation intensity is less than 10^4 W/cm^2. For CIS, this excitation intensity is an order or two lower in magnitude than that reported as safe for probing CIS without thermal side-effects [100, 148]. The Raman peak analysis is based on Lorenzian-fitting. The penetration depth, by definition, is the inverse of absorption coefficient at incident wavelength, thus, about 100 nm for CIS.

2.2.3. Energy Dispersive X-ray spectroscopy

Energy Dispersive X-ray spectroscopy was used to evaluate the elemental composition of In_2S_3 films [I], ZnO_{NR} layers [III] and CIS films [IV] using Oxford Instruments PentaFet x3 spectrometer with INCA Energy EDS system, at the Zeiss EVO-MA15 scanning electron microscope that operated at an accelerating voltage of 7 kV. Spectra were measured at four characteristic locations. The EDS analyses were made by Dr. Valdek Mikli in Tallinn University of Technology.

2.2.4. Scanning electron microscopy

The scanning electron microscopy (SEM) images were used to evaluate ZnO nanorod length [V, VI] and solar cell structure [V] using cross-sectional views; and to evaluate the surface morphology using the top-view images [III, VI]. We used Zeiss EVO-MA15 microscope [III, V, VI] and Zeiss HR FESEM Ultra 55 [V]. The SEM analyses were made by Dr. Valdek Mikli and Dr. Olga Volobujeva in Tallinn University of Technology.

2.2.5. Capacitance-voltage scans

Capacitance-voltage (C-V) scans at ac testing voltage of 20 mV and frequency of 10 kHz (guidelines for selection of frequency in [140]) were used to evaluate carrier density in ZnO nanorod (ZnO_{NR}) layers using AUTOLAB PGSTAT 30 [VI]. We formed a metal-semiconductor junction by using a mercury droplet to contact the ZnO_{NR}, and used I-V scans to verify the presence of a rectifying junction. The carrier density was calculated using a linear section in the $1/C^2$-V plot and the Mott-Schottky equation [136]:

$$n = \frac{2}{q\varepsilon_1\varepsilon_0(A_1)^2} \cdot \frac{1}{\frac{d(C^{-2})}{dV}} \qquad (4)$$

Here q is the electron charge, ε_1=8.5 is the relative permittivity of ZnO, ε_0 is the electric constant ($\varepsilon_0=8.85\cdot10^{-12}$ F/m), A_1 is the ZnO_{NR}/Hg contact area and C is in units of $F\cdot cm^{-2}$. Area A_1 is calculated according to a model introduced in [VI]:

$$A_1 = \frac{C_0L - \varepsilon_0A}{\varepsilon_0(\varepsilon_1 - 1)} \qquad (5)$$

Here C_0 is the capacitance at reverse bias (C_0=const) obtained from the $1/C^2$-V plot, L is the thickness of the ZnO_{NR} layer (the length of the nanorods), and A is the macroscopically measured (visually determined) ZnO/Hg interface area.

2.2.6. Photoluminescence

For evaluation of ZnO_{NR} crystal quality we measured photoluminescence at room temperature (T=300K) and at T=10K in a closed-cycle He cryostat (Janis). We used He-Cd laser (325 nm) as the light source with an excitation intensity ~0.5 mW/mm^2. The emission of luminescence in the energy region of 1.45–3.45 eV was dispersed by a computer-controlled Carl Zeiss SPM-2 monochromator (f=40cm) equipped with a prism and detected by FEU-79 photomultiplier coupled with a lock-in amplifier. [III, VI].

2.2.7. X-ray photoelectron spectroscopy

For the sprayed CIS films [IV], we measured X-ray photoelectron spectroscopic (XPS) spectra on a Kratos AXIS Ultra DLD X-ray Photoelectron Spectrometer. Analysis was carried out with monochromatic Al K_α X-rays (1486.6 eV) operating at 15 kV and 225 W. We used Ar^+ ion sputtering (4 kV, 20 mA) for the depth profiling to obtain information of the film bulk composition. The XPS analyses were made by Mati Danilson (MSc) and Dr. Atanas Katerski in Tallinn University of Technology.

Table 2. Methods used for characterization of thin films.

Properties	Method	Apparatus	Ref.
Phase composition, crystallite orientation, crystallite size	XRD	Rigaku Ultima IV	[I, III, IV]
Phase composition, crystal order	Raman	HORIBA Jobin Yvon LabRAM HR800	[I, III, IV]
Morphology, ZnO_{NR} length, film thickness	SEM	Zeiss EVO-MA15 Zeiss HR FESEM Ultra 55	[III, VI] [V]
Elemental composition	EDX	Oxford Instruments INCA PentaFet x3 spectrometer	[I, III, IV]
Carrier density	I-V, C-V	AUTOLAB PGSTAT 30	[VI]
Crystal quality	Photoluminescence	′Home-assembled′	[III, VI]
Chemical state of elements	XPS	Kratos AXIS Ultra DLD	[IV]

2.3. Characterization of solar cells

A summary of the techniques used for the characterization of solar cells prepared by the CSP is presented below in Table 3.

2.3.1. Current-voltage characteristics

Current-voltage (I-V) scans were used to evaluate the open-circuit voltage (V_{OC}), short-circuit current (J_{SC}), fill factor (FF) and solar cell efficiency (η) of the sprayed solar cells using the four-point-probe technique on the AUTOLAB PGSTAT 30 in Tallinn University of Technology [V], Oriel class A solar simulator 91159A in Tallinn University of Technology [V], or on the computer controlled KEITHLEY 236 Source Measure Unit in Electronics and Information Systems department (ELIS), Ghent University [II]. The I-V curves were measured with the cell in dark and under a standard white light with an illumination intensity of 100 mW/cm^2 (AM1.5) [II, V]. In [V] a calibrated photodiode was used measure the flux of a 300W halogen-tungsten light source. For the temperature-dependent I-V scans (I-V-T) the solar cells were placed on a cold-finger in a N_2-cooled cryostat [II]. The analysis of the I-V scans is based on the commonly used diode model [51, 55, 56, 92, 151] as follows:

$$J = J_0\left(\exp\left(\frac{qV^*}{nkT}\right) - 1\right) + \frac{G_{sh}}{A}V^* - J_L \qquad (6)$$

Here J_0 is the saturation current density at reverse bias, J_L is the light current generated in the cell under illumination, $V^* = V - J \cdot R_S A$ is the voltage across the pn junction of the cell, A is the cell area defined by back-contact, and kT/q is the thermal voltage. The non-idealities here that are not present in the idealized diode model, are series resistance R_S, shunt-conductance G_{sh} and the diode ideality factor n>1.

The area-invariant characteristic $R_S \cdot A$ ($\Omega \cdot cm^2$) was evaluated by fitting of the I-V curves using the above diode model (6). As a more convenient approach, $R_S \cdot A$ was evaluated by using linear section of I-V curve at large enough forward voltages, and calculated using the inverse slope in this I-V region:

$$R_S' = R_S \cdot A = (dI/dV)^{-1} \cdot A \qquad (7)$$

The series resistances when evaluated by fitting or by using (7) were similar, though small variations could be expected. A similar approach was used to calculate the area-invariant shunt-conductance G_{SH}/A (S/cm^2) by using linear part of the I-V curve in the reverse bias region:

$$G_{SH}' = G_{SH} \cdot A^{-1} = (dI/dV) \cdot A^{-1} \qquad (8)$$

Commonly, the R_S and G_{SH} are already the area-normalized quantities, the corresponding Ohm´s law treat current density J in A/cm^2 rather than current I in amps. In the thesis, the area-normalized quantity is indicated with an accent (R_S' and G_{SH}') to avoid possible confusion.

The ideality factor n is herein assumed to be voltage-dependent. A characteristic value is extracted at the local minima of the semilogarithmic plot of the I-V curve at a bias voltage range of 0.35–0.5 V, as follows:

$$n(V) = \frac{q}{kT} \cdot \frac{d(V^*)}{d(\ln I)} \qquad (9)$$

Here the diode voltage is corrected for series resistance via $V^* = V - J \cdot R_S'$. Whenever possible, fitting to the diode model (6) was used instead.

Taking into account that $J_0 = J_{00} \cdot \exp(-E_A/nkT)$ [51, 151] where J_{00} is weakly dependent on temperature; the open-circuit conditions ($J_0 = 0$) in the diode model (6) yield the open circuit voltage V_{OC} as follows [11, 16, 51, 55, 56, 152]:

$$V_{OC} = \frac{E_A}{q} - \frac{nkT}{q} \cdot \ln\left(\frac{J_{00}}{J_{SC}}\right) \qquad (10)$$

Using relation (7), the extrapolation of the open circuit V_{OC} to a temperature T of 0 Kelvin V_{OC} ($T \rightarrow 0K$) should yield the activation energy E_A/q (eV) of the saturation current J_0. Also, from here, it is evident that V_{OC} depend on J_{SC} and thus is expected to increase logarithmically with the light intensity; and that the saturation current J_0 has to be minimized to maximize cell output.

The light-to-electricity power-conversion efficiency η of a solar cell is calculated at the maximum power point of the I-V curve of the cell:

$$\eta = \frac{(I \cdot V)_{max}}{I_{IN} \cdot A} \qquad (11)$$

Here I_{IN} (W/m^2) is the irradiance incident on the cell, and A is the cell area.

The fill factor FF<1 of a solar cell is defined as:

$$FF = \frac{(J \cdot V)_{max}}{J_{SC} \cdot V_{OC}} \qquad (12)$$

with the short-circuit-current as J_{SC} and the open-circuit voltage as V_{OC}.

2.3.2. External quantum efficiency

By external quantum efficiency EQE spectroscopy we measure the spectral sensitivity of a solar cell in the short-circuit conditions. The EQE spectra was measured in the spectral region of 1.0–3.5 eV (1240–355 nm) by using a computer-controlled SPM-2 monochromator (Carl Zeiss-Jena, f=40 cm), and a 100W halogen lamp with calibrated spectral intensity as the light source for excitation [V]. The EQE is calculated as follows:

$$EQE = S_{ref}(\lambda) \cdot \frac{1240}{\lambda} \cdot \frac{I_c(\lambda)}{I_{ref}(\lambda)} \cdot \frac{A_{ref}}{A_c} \qquad (13)$$

where $S_{ref}(\lambda)$ is the spectral sensitivity (in units of A/W) of the calibrated reference detector, $I_c(\lambda)/A_C$ is the current density (A/m^2) of the investigated cell and $I_{ref}(\lambda)/A_{ref}$ is the current density of the reference detector when illuminated, whereas the quantum efficiency is unitless 0<EQE<1.

Determination of the bandgap of the absorber

The bandgap E_g of the absorber was estimated using an EQE spectrum of a solar cell and the following relation:

$$EQE \approx A(E - E_g)^{1/2}/E \qquad (14)$$

The relation (14) is valid for a direct transition near the bandgap energy $E \approx E_g$, where E is the photon energy and A is independent of E [153]. Thus, an extrapolation of the linear part of $(EQE \cdot E)^2$ vs. E plot up to the horizontal axis where $(EQE \cdot E)^2 = 0$ give the bandgap energy E_g.

2.3.3. Admittance spectroscopy

Capacitance-frequency-temperature (C-f-T) measurements, using 20K steps for temperature T, were used to evaluate the energetic distribution of defect density in the $CuInS_2$ absorber material of the sprayed solar cell using computer controlled HP 4192A LF Impedance Analyzer in Electronics and Information Systems department (ELIS), Ghent University. We evaluated the distribution of the defect density using a method proposed by Walter et. al [144]. For the x-axis, the frequency is converted to energetic distance E_ω from absorber band edge [144]:

$$E_\omega = kT \cdot \ln\frac{2\nu_0}{\omega} \tag{15}$$

where ν_0 is the attempt-to-escape frequency, and ω is the angular frequency $\omega = 2\pi f$. The criteria for choosing the numerical value of the parameter ν_0 is the best overlap of the scaled derivatives when plotted at varied temperatures [75]. A scaled derivative of the capacitance was used on the y-axis, as proposed by Decock et.al [94]:

$$-\frac{1}{w}\frac{dC}{d\omega}\frac{\omega}{kT} \tag{16}$$

where $w=\varepsilon\varepsilon_0/C$ is the depletion width of the pn-junction of the solar cell, and C is in units of F/cm^2.

Table 3. Methods used for characterization of solar cells.

Property	Method	Apparatus	Ref.
Spectral response, bandgap of absorber	EQE	′Home-assembled′	[II]
		′Home-assembled′	[V]
Open circuit voltage, short circuit current (fill factor, conversion efficiency)	I-V	KEITHLEY 236	[II]
		AUTOLAB PGSTAT 30	[V]
		Oriel class A solar simulator 91159A	[V]
Recombination mechanism	I-V-T	KEITHLEY 236	[II]
Quality of absorber material	C-f-T	HP 4192A LF Impedance Analyzer	[II]

3. RESULTS AND DISCUSSION

3.1. Characteristics of the sprayed $ZnO_{NR}/In_2S_3/CuInS_2$ solar cells

Two superstrate type cells were analyzed: the *flat* $ZnO/In_2S_3/CuInS_2$ cell and the *structured* $ZnO_{NR}/In_2S_3/CuInS_2$ cell. The *flat* cell with a continuous ZnO thin film and extremely thin absorber serves no other purpose that to act as a reference cell for measurements´ analysis. A sketch of the *structured* cell is presented in Figure 1.

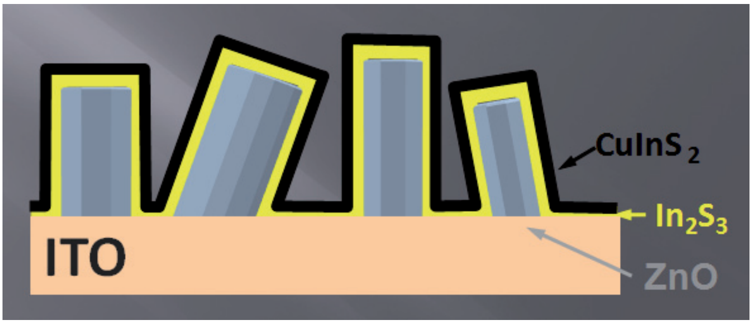

Figure 1. A sketch of the structure of the $ZnO_{NR}/In_2S_3/CuInS_2$ solar cell deposited by spray sprayed onto ITO. The $CuInS_2$ absorber is covered with graphite paste (not shown). The SEM images of partially completed ZnO_{NR}/In_2S_3 cell (Figure 17) and of the completed cell (Figure 21) follow later near the relevant discussion. Further SEM images and an EBIC (electron beam induced current) image of the structure can be found in [130] and in [V] (Appendix A).

3.1.1. Series resistance

The R'_S values for the *flat* cell were roughly 2–3 Ωcm^2 while for the *structured* cell the R'_S was 2–4 Ωcm^2 (Figure 2). Thus similar values of R'_S were present at standard illumination, while at low illumination the *structured* cell shows higher values of R'_S.

These resistances are so-called lumped values that include contributions from all the layers and barriers in between the external contacts, including spreading resistance of the front and back electrode, contact resistance and the bulk resistance of the whole $ZnO/In_2S_3/CuInS_2$ stack. The contribution of each factor yet remains to be explored.

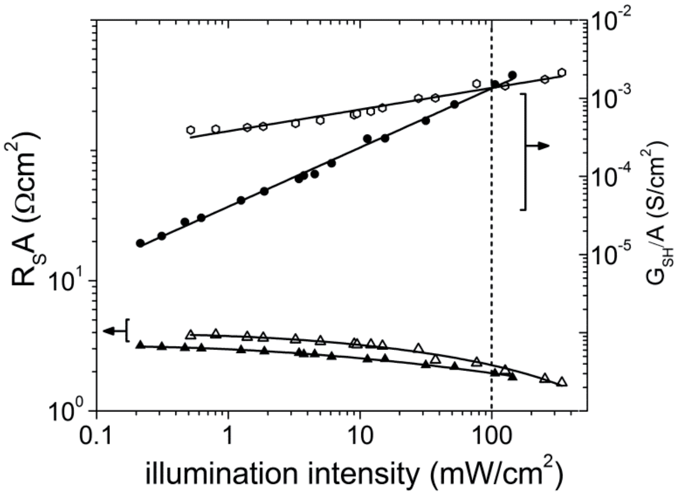

Figure 2. Series resistance *R′$_S$* (left scale, triangles) and shunt conductance *G′$_{SH}$* (right scale, circles) of the *structured* $ZnO_{NR}/In_2S_3/CuInS_2$ cell (empty symbols) and of the *flat* $ZnO/In_2S_3/CuInS_2$ cell (filled symbols) at varied irradiance. The structured cell has 3% conversion efficiency and flat has 2% efficiency at A.M.1.5 (indicated by the dashed line) [II].

The R′$_S$ could be a major factor that limits the output of the sprayed cell herein. For high-efficiency devices, only values below 0.4 Ωcm^2 can be neglected [58]. Values ~1 Ωcm^2 can only be accepted in case of a reasonable V$_{OC}$ [16]. For example, the record CZTSSe thin film cell with an efficiency of η>11% has an R′$_S$ of 0.4 Ωcm^2 [21]; whereas the record CIGSe cells (η>20%) show R′$_S$ below 0.5 Ωcm^2, down to 0.23 Ωcm^2 at a cell efficiency of 20.3%.

The series resistance of ETA cells does not seem to be a routinely reported characteristic. For the TiO_2/In_2S_3/CIS nanocomposite solar cell with 2.8% efficiency, a value of 5.5 Ωcm^2 has been reported in dark that decreased to 2.6 Ωcm^2 at illumination [154, 155]. An ETA solar cell with a ′singly folded′ absorber layer, such as the sprayed cell should, in fact, give an advantage with a smaller R′$_S$ compared to any design with a higher degree of absorber corrugation. However, we see that there is a lot of room for an improvement.

It could be that a lack of carrier-selective-conductor suppresses the maximum potential of the all-layers-sprayed cell, thus a suitable hole-conductor should be included in the cell for development [33]. For the ETA cells, inorganic, such as CuSCN [26, 27, 33, 44, 93] and organic materials such as small molecule spiro-MeOTAD [39, 41] or P3HT polymer [4] have been successfully used to extract holes from the absorber material. In general, due to the folded nature of the ETA cell, the hole-conductors should be wide bandgap materials; that is, optically transparent materials to avoid partial shadowing of the tilted ETA layers (Figure 1)

[3]. The p-conductor should be stable and should not introduce significant electrical resistance to the cell. A requirement when using a hole-conductor, as with any other layer, is to ′wet′ the absorber uniformly, so that carriers are replenished uniformly [32]. Other factors that induce local non-uniformities, and thus lateral variations in the local saturation current density, may be: fluctuations in the composition, stress and strain, grain boundaries, significant variation in crystallite sizes [151]. The issues regarding possible inhomogeneities are discussed followingly.

Inhomogeneities, and the effect of intentionally introduced series resistance

Another concern is the likely inhomogeneities in the sprayed cell, such as pin-holes or different local thicknesses of consituent layers, and inhomogeneities of the properties of the materials (grain boundaries, strain, concentration of impurities and intrinsic defects, stoichiometry deviations). Such fluctuations become more severe in a solar cell as the thicknesses of the component layers decrease, especially in the limit where grain sizes are comparable to the total layer thickness.

For a homogeneous device, an R'_S of up to 0.5 Ωcm^2 is acceptable, after which the cell is expected to suffer from ohmic losses [151]. At first it may seem counter-intuitive, but for a device with inhomogeneities it has been shown that there is a specific optimum R'_S larger than 0.5 Ωcm^2 that maximizes the cell efficiency [151]. That is, for a given inhomogeneity, larger R'_S is needed to inhibit losses due local increase of the recombination (′weak-diodes′), at the expense of a small reduction of the current of the whole cell, thus ′protecting′ the open circuit voltage of the entire device [72, 151]. The problem is somewhat similar to parallel-connected solar cells or modules, where upon inhomogeneous illumination the whole array suffers deterioration, despite the availability of cells with a higher output.

Such a concept has already been applied, although empirically, in the CIGSe cells where the low resistivity TCO is covered with a higher resistivity intrinsic ZnO layer. The use of such a bilayer is an example that the intentionally introduced series resistance may, in fact, improve the cell performance [151]. Likewise, such a bilayer could be used for decreasing shunts due to pin-holes in the CdS buffer layer [14]; and to act as a protection against front contact short-circuiting with the absorber or the hole conductor in the back-side of the ETA cell [27, 37, 44, 114]. The latter, short-circuiting, seems to be a conceptual drawback in cells that use a solid-state hole-conductor, in contrast to cells that are based on liquid electrolyte, and good performance may be expected only when the compact intrinsic layer has been introduced on top of the TCO [27, 49]. The use of an all-solid-state approach, nevertheless, seems to be somewhat more attractive, compared to the use of electrolyte, due to easier sealing [29, 49] and long-term stability [38, 156] of the solid state cell.

Obviously, the cell resistances that are calculated for the sprayed ETA cell, are above acceptable (Figure 2), and should not be allowed to further increase even if the cell suffers inhomogeneities. A likely source of inhomogeneities is the coverage of the substrate by the isolated ZnO nanorods, thus creating suitable ′hot-spots′ for short-circuiting in between the nanorods. For example, by increasing the buffer layer thickness of a cell with a poor output (V_{OC} of 100 mV, FF of 30%) the gaps in between the ZnO nanorods were filled with the buffer material, and the cell output improved to a V_{OC} of 463 mV and FF of 54%, see Figure 3a. However when the buffer layer thickness was further increased, a slight decrease of the J_{SC} was observed due to the increased series resistance [V].

In essence, the thicker buffer layer eliminates the shunts (evident at reverse bias; Figure 3a). In other words, it seems that the added In_2S_3 on top of ZnO_{NR} acted as an intentionally introduced resistive ′superstrate′ layer that increased the V_{OC} and eventually resulting in minor decrease of the J_{SC}.

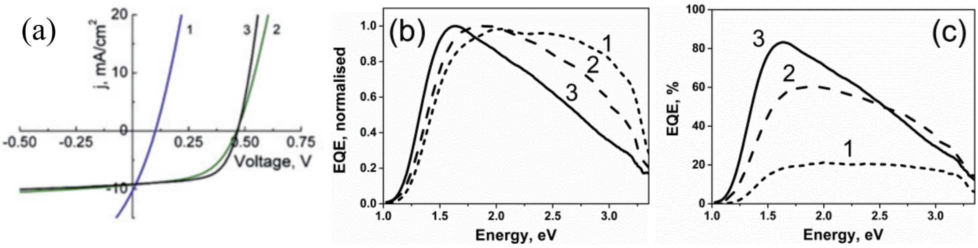

Figure 3. J-V curves **(a)** and EQE spectra **(b, c)** of the sprayed $ZnO_{NR}/In_2S_3/CuInS_2$ solar cell at increased buffer thicknesses (1–3). The FF of the J-V is small due to shunts ((**a**), curve 1), while the relative optical losses are smaller when using a thinner buffer as seen from curve 1 of **(b)** [V].

Despite the suitable gap-filling ability of the sprayed buffer layer, the photosensitivity of the buffer (further in §3.1.2 Shunt-conductance) significantly increases the conductivity of these shunt-paths (presumably due to the presence of the gaps in between the ZnO nanorods), and thus cannot be approved for the use as a ′gap-filler′ in the present cell configuration. Due to absorption in the buffer, any material with a wider bandgap than that of the In_2S_3 would be more suitable for further experiments.

3.1.2. Shunt-conductance

The sprayed *flat* cell shows G'_{SH} values roughly 10^{-5}–10^{-3} S/cm^2 and the sprayed *structured* cell shows G'_{SH} of $4 \cdot 10^{-4}$–10^{-3} S/cm^2 (Figure 2). Shunt-resistances above 5000 Ωcm^2, thus, shunt conductances G'_{SH} below $2 \cdot 10^{-4}$ S/cm^2 can be neglected as estimated for the high efficiency thin film cells [58]. The possible effect of voltage dependent collection, which might interfere with the G'_{SH} calculation and analysis, is most likely neglible as discussed further below (under the subheading *Possible effects of ′Voltage dependent collection′*).

Although the G'_{SH} seem close to acceptable at low illumination intensity, the significant photosensitivity of the shunts by several orders of magnitude is worrying. For example, a thin film cell with an efficiency of 15.5% shows 0.05 mS/cm^2 and 0.2 mS/cm^2 as values of G'_{SH} in dark and light conditions, respectively, thus varying only by a factor of four, with no difference in the series resistance of 0.2 Ωcm^2 [51]. For the TiO_2/In_2S_3/CIS nanocomposite solar cell with 2.8% efficiency, the G'_{SH} is 0.3 mS/cm^2 in dark that increases to 5.1 mS/cm^2 when the cell is illuminated [154, 155]. Thus, a significant photosensitivity is also present with the nanocomposite cell, a cell that differs only in the window layer. As discussed followingly, the In_2S_3/CIS interface is the likely cause of the photosensitivity.

One possibility for large leakage current is In_2O_3 on grain boundaries when precursors of CIS have been sprayed in air [101]. However we do not expect a high photoconductive behavior in this case; and secondly, the formation of metal-oxide has only been observed if grown at approximately 350°C or higher [119, 150, 157]. As shown for the CGSe cells, another possibility for large shunt currents is the presence of degenerate p-type Cu_XSe inclusions in the absorber or buffer of the Cu-rich samples or regions [8]. An excess of Cu seems to be a suitable explanation, explained as follows.

The most likely factor to affect the G'_{SH} of the sprayed cell in such a manner could be the presence of In_2S_3:Cu layer [V]. That is, the buffer layer could have been unintentionally doped with copper during the absorber preparation. This process can be expected if Cu_XS binaries are available. Indeed, the existence of secondary phases can be expected as in the CSP process the CIS forms from binary sulfides (Cu_XS, In_2S_3) [150, 158] and sprayed CIS films, especially those grown at temperatures below 300°C may contain residues of nonreacted binary sulfides [159]. As will be shown (§3.2.1 Structural properties of $CuInS_2$ thin films) an copper-containing extra phase is present in the CIS films when prepared at close to comparable conditions (250°C) as those in the solar cells (270°C).

The assumption of In_2S_3:Cu layer is supported by the fact that a lower photosensitivity of the G'_{SH} is present in the *structured* cell, despite showing higher values of G'_{SH} (Figure 2), when compared to the behavior of the G'_{SH} of the *flat* cell. Such a phenomenon is likely to be explained by a lower growth temperature of an absorber when deposited onto lengthy ZnO nanorods which extend to a further distance above the substrate. Hence, lower diffusion rate of Cu is likely when the CIS is grown onto ZnO_{NR} as opposed to a flat ZnO, assuming similar substrate temperatures. We have shown for *flat* cells in [160] that lowering the CIS growth temperature from 320°C to 250°C results in a decrease of the cross-over effect. For solar cells with CIS grown at 250°C, no cross-over was observed. Most likely, the diffusion rate of Cu into the buffer layer is significantly reduced at lower CIS deposition temperatures. Additionally, the effective bandgap is lower in the structured cell (further in §3.1.3 Ideality factor, and §3.1.4 Copper diffusion into buffer layer). The lowered E_g was, at the time [II], attributed to a higher defect density in the *structured* cell or to the presence of a secondary binary phase such as Cu_XS. Both factors also support a lower growth temperature of the absorber of the *structured* cell.

Another phenomena that speak of the possible buffer photodoping is that there is a *very low* EQE for the cell with the thickest buffer layer (Figure 3c) whereas at AM1.5 the J_{SC} of the cell is *similar* to J_{SC} in cells with thinner buffers (Figure 3a). Such an anomaly can be attributed to the presence of a barrier for photocurrent at low light intensity whereas at AM1.5 the buffer photodoping lowers the barrier [5]. Alternatively, a large number of microshunts can the cause such anomaly [5] – a phenomena that we cannot exclude either.

When compared to the *flat* cell, the *structured* cell has higher shunt-conductance even at low levels of irradiance (Figure 2). Possible explanations are: the presence of the gaps between the nanorods (i), higher absorption ability and thus higher photosensitivity of the structured cell (ii) or highly conductive Cu_XS residues (iii). The latter two (ii, iii) require that that In_2S_3:Cu is physically the photosensitive shunt path, while (i) is independent of the phenomena of copper diffusion. All these factors may contribute to the deterioration of the output of the *structured* cell. Additionally, it is worth mentioning that the ′bottom′ of the nanorods is in fact the first part of the ZnO_{NR} which the light ′sees′ when traveling through the cell, allowing any anomalies (discontinuity of films, photoconductivity) to have the maximum effect at the ′bottom′ of the nanorods. Further discussion follows in §3.1.5 (Open-circuit voltage) and §3.1.4 (Copper diffusion into buffer layer).

Possible effects of ′Voltage dependent collection′

The purpose of the following discussion is to show that the voltage dependent collection effect is most likely rejectable in the studied cells and had little or no effect on the determination and the critical analysis of the G'_{SH}.

Voltage dependent collection of the light-generated current $J_L(V)$ is a non-ideality that causes $-J_L$ to gradually diverge from that at zero bias (J_{SC}). It mainly affects the fill factor by increasing the slope of the I-V curve and thus it might interfere with the accurate determination of G'_{SH}. The $J_L(V)$ affects mainly the FF of the cell. The voltage dependent collection is commonly seen in polycrystalline material devices that rely on carrier diffusion. The small minority carrier lifetime in the polycrystalline absorber lead to a drift-aided current collection [51]. Hence, bias voltage will likely have an effect on the carrier collection if the absorber layer is significantly thicker than the depletion width.

The G'_{SH} is generally assumed to be ohmic. Thus, if the *dark* I-V is ′well-behaved′ and the *light* G'_{SH} does not have a voltage dependence, then the voltage dependent collection evident in the *light* I-V curve is usually assigned to the effect of voltage dependent light-current $J_L=f(V)$ as opposed to $G'_{SH}=f(V)$ [51]. In other words, evaluation J_L minus J_{dark} allow to judge the voltage-dependent behavior. Such is the usual case for devices with a relatively thick absorber material.

A method to distinguish the dominant non-ideality is to plot a batch of J(V)+J_{SC} curves at varied illumination intensities, and to compare the evolution of the I-V shape with that obtained from simulations [161]. Although a simple approach, in reality the evaluation may not turn out to be that straightforward, as was the case for the sprayed cell (not shown). Yet another method is to use EQE with a voltage bias on the cell. At a sufficient reverse bias, the depletion layer should extend throughout the absorber, carriers are collected without transport losses throughout the absorber thickness, and the QE reaches an *optically limited* maximum. A comparison of the optically limited maximum QE with that at zero bias (short-circuit) should give an idea of the magnitude of the voltage dependent collection [51, 115].

For the sprayed cell, when comparing EQE at 0V with that at reverse bias, no difference in the collection of carriers occurs in the low energy region (Figure 4a). However, a minor increase is present in the higher energy region >2eV, that is, improvement in the absorbing region of the buffer layer. This led to speculate that the thin absorber layer is already depleted at 0V and the further reverse bias might expand the depletion layer into the buffer layer. After all, a near or full depletion of the low quality absorber, and a complete collection of carriers throughout the absorber, is what we expect of the ETA cell concept.

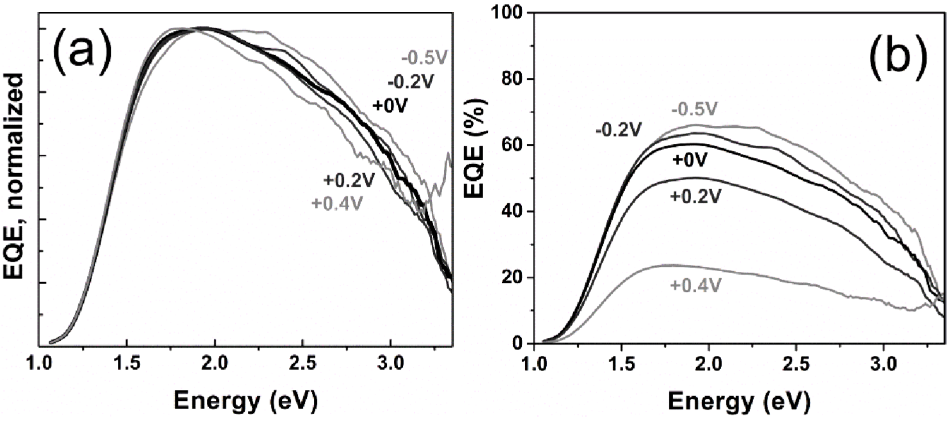

Figure 4. (a): Normalized EQE spectra as a function of bias voltage (-0.5 to 0.4 V) of the $ZnO_{NR}/In_2S_3/CuInS_2$ cell. **(b)**: Absolute EQE(V) spectra [162]. The results are discussed in the text.

Likewise, at a forward bias up to 0.4 V (near the flat-band conditions, V_{OC}=463mV) there is no relative loss in the low-energy region versus that at energies >2eV (Figure 4a). The observation provides some confidence that the voltage dependent collection at forward bias is likely to be neglectable, when compared to the current losses due to the G'_{SH} (with or without the illumination dependency of G'_{SH}).

The EQE in Figure 4a,b was measured with a lock-in amplifier using low-intensity monochromatic incident light in near-to-dark ambient conditions.

Thus, the effect of the photosensitivity to the continuous AM1.5 spectrum via the G'_{SH} was involuntarily excluded. For the same reason the integral of EQE is not expected to correlate with the J_{SC} at a significantly higher illumination of 1 sun. The morale is, when the EQE measurements of a cell with photosensitive parameters should reflect the short-circuit output at AM1.5 light, one should include unchopped white light bias to the EQE measurements to simulate the material properties at AM1.5 illumination [51, 163]. More precisely, the EQE measurements should be labeled as ′apparent quantum efficiency′ (AQE) whenever measured differently from the *one sun, zero bias* conditions [164]. At the early stage of studies, in [V], these considerations received no attention.

The analysis of the voltage dependence of the EQE would have more certainty in case the cell materials itself were ′immune′ to illumination effects. According to our assumption, however, the buffer layer is photosensitive. Therefore, the G'_{SH} is expected to influence the EQE owing to additional absorption in the buffer layer due to the photoexcitation of electrons from the shallow levels introduced by In_2S_3:Cu [165]. Further experiments would be needed, and possibly realistic simulations, to account for all factors that influence the cell behavior.

In case of the CdTe cells, the photoconductivity of CdS leads to a higher effective doping density, widens the depletion layer and by that influences the collection efficiency $J_L(V)$ [51, 164]. Thus, it may seem that buffer photodoping may not be a negative factor at all, at least for cell with a *thick* thin film polycrystalline absorber. However, in case of an ETA cell, stronger electric fields may not result in higher efficiencies due to increased probability of carrier tunneling. Due to the tunneling enhanced recombination, high ideality factor (n>2) could be expected. Indeed, such was the case for the sprayed ETA cell (Figure 5a). However, carrier tunneling as a recombination mechanism is not the only source of ideality factors larger than 2, discussed followingly (§3.1.3. Ideality factor).

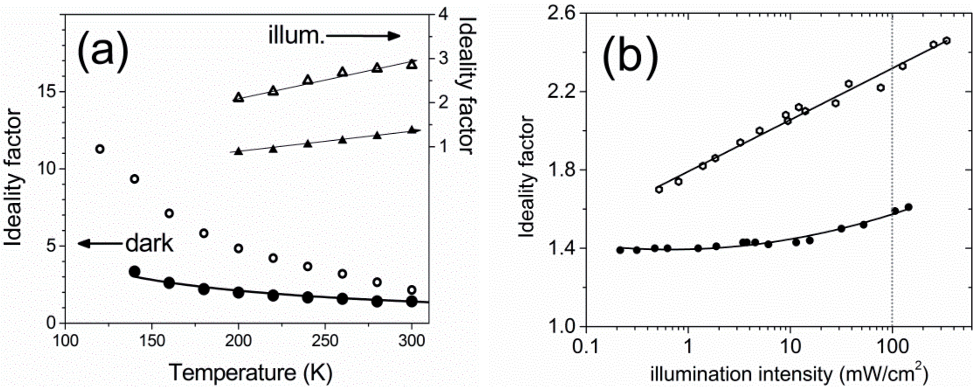

Figure 5. The ideality factor of the *structured* cell (open symbols), and that of the *flat* cell (solid symbols) with the cell in dark and at ~100 mW/cm^2 irradiation as a function of temperature **(a),** and at varied illumination intensity **(b)**. In dark, the temperature dependent ideality factor of the *flat* cell is fitted with a model of tunneling enhanced interface recombination (a, lowest curve) [II].

3.1.3. Ideality factor

A single value of the ideality factor (n) may not be reliable when isolated from a series of samples, other measurements on the same cell, or variance in the technology. However, the extensive amount of measurements at varied illumination; the comparison of the ideality factors with those of the reference cell; and a consistency with parameters like the shunt-conductance, should raise confidence in the following analysis. The analysis of the saturation current has been omitted due unsatisfactory precision when calculating J_0 from the I-V curves.

Illumination dependent ideality factor

The ideality factors were corrected for series and shunt influence, in order to characterize the diode separately from other non-idealities. The *flat* cell had an ideality factor of 1.4–1.6 at varied illumination whereas the *structured* cell have significantly higher values of 1.7–2.5 (Figure 5b). A typical n of a ′decent′ cell lies in the range of $1.3<n<2$ [51], thus, the *structured* cell deviates significantly from the expected behaviour.

In general, the ideality factor n is introduced formally to account for a number of possible influences that causes deviation from the ideal model with n=1. An inverse of n is called the transfer factor ($\beta=n^{-1}<1$ [132]), hence a smaller ideality factor accounts for a larger ′transfer′ of the current through the cell, or equivalently – reduced losses in the cell due to recombination.

The ideal diode consider thermal activation (thermionic emission above any barrier present) of carriers with no tunnelling; drift and diffusion for carrier transport; and radiative recombination via bulk states in the quasi-neutral region. The factors that give a negative contribution to this idealized carrier transport mechanism are non-radiative recombination in the space-charge region (depletion regions on both sides) of the pn junction, via interface states, grain boundaries; due to tunneling through defect states, e.g. at interfaces or grain boundaries; and effects of spatial inhomogeneities, to name a few. Hence, the ideality factor will remain an ambiguous ′compound characteristic′ if not further investigated. Likewise, n is expected to be voltage dependent when different non-idealities dominate in a different range of bias voltages, yielding different transport mechanisms to dominate in different voltage regions.

Diode ideality factors higher than two, such as in the case of the *structured* cell, could be expected in case significant spatial non-uniformity is present, as shown in the case of absorber E_g fluctuations as modeled in a cell [151]. The *structured* cell show much lower absorption edge of 1.3 eV compared to the expected E_g of 1.5 eV in the absorber of the *flat* cell, as determined from the EQE measurements (Figure 6b). The lowered E_g was attributed to a higher defect density in the *structured* cell and the likely presence of a secondary phase in the CIS absorber material [II]. Thus, spatial variations of the effective E_g cannot be excluded in the absorber of the *structured* cell. Another reasoning of the differences in E_g is discussed in the next section (§3.1.4. Copper diffusion into buffer layer).

A possible solution for reducing the effect of inhomogeneities on cell output was discussed (§3.1.1. Series resistance) based on reference [151]. However, according to [151] even the deliberately introduced series resistance does not have a significant effect on the reduction of recombination, thus high ideality factors can still be expected of devices with large inhomogeneities in the material properties, despite the V_{OC} being ´saved´. Therefore, any inhomogeneities in the structured cell, if present, should have an effect on the cell´s ideality factor. Ideality factors >1, and thus, the non-ideal recombination along with an increase in the saturation current is expected to predominantly take its toll on the V_{OC} [58], further in (§3.1.5. Open-circuit voltage).

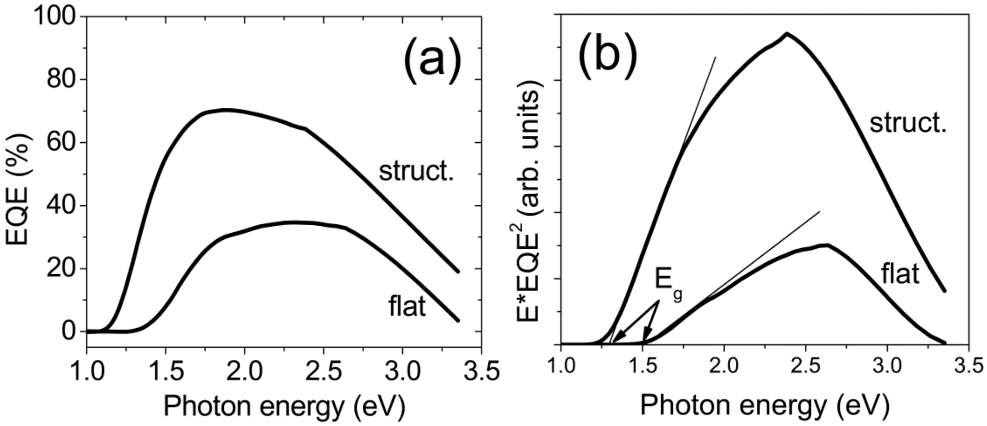

Figure 6. **(a)** EQE of the *structured* and the *flat* solar cells grown by the CSP method. The structured cell show improved photon absorption. **(b)** Modified EQE plot according to [153], give a bandgap estimation of 1.3 eV (*structured*) and 1.5 eV (*flat*) of the absorber materials, at T=300 K. The relative gain of the current is larger at lower photon energies (< 2.5 eV) [II].

Temperature dependent ideality factor

For an ideal cell, with recombination only in the quasi-neutral region, the ideality factor is 1. Ideality factors up to 2 are expected when recombination at midgap states in the depletion regions contribute to the current in the cell [50, 166]. The presence of a temperature dependence of n and ideality factors larger than 2 at low temperatures are an indication of tunneling contribution to the recombination [9, 50, 90, 92, 167].

For the n(T) of the *flat* cell in dark (Figure 5a), a characteristic tunneling energy of E_{00} = 36.4 meV was extracted from n(T) fitting using the relation $n=E_{00}/kT$ for tunneling enhanced interface recombination [92]. The structured cell show an even steeper n(T) relation (Figure 5a), whereas the available models for tunneling recombination [5, 168, 169] were not suitable for describing the n(T) behavior here: an example that the textbook formulas available for the analysis of a thin film cell may not suffice for the ETA characterization. It seemed reasonable though to assume that the tunneling contribution to the recombination is yet higher in case of the *structured* cell [152]. An increased defect density, such as in the absorber of the *structured* cell (as deduced from admittance measurements, in §3.2.1. Structural properties of $CuInS_2$ thin films) is likely to cause enhancement of the tunneling assisted recombination [100].

The recombination due to tunneling currents in ETA cell have been predicted early on, and are associated with the high electrical field present in the ETA cells [19]. The high fields limit the $CuInS_2$ absorber thickness to a minimum of 15 nm [19]. Despite that the expected thickness of the absorber in the *structured* cell is a multiple of that, the *local thickness* may still vary and affect the tunneling contribution, as shown for a similar cell design prepared by spray-ILGAR [46]. Indeed, uniform local thicknesses of the absorber layer, in other words a conformal coating of the structured window layer, is a critical step for the ETA design [3, 33, 44, 46, 54].

The required absorber thickness to activate the tunneling-controlled recombination is as high as 120 nm at short-circuit conditions, whereas at forward voltage bias the carrier lifetime will be less influenced by the tunneling processes [19]. Thus, a voltage dependent collection is not entirely excluded in our ETA cells; as a manifestation of such a contribution could be the ′second diode′ at a low voltage bias [9, 92], also observed for the sprayed cells herein. A ′bump′ at low voltages could be also be expected in case of a distribution of interface defect states at the heterojunction [133]. The analysis and possible origin of such a diode was omitted due to unsatisfactory fitting results, possibly due to the strong G'_{SH} contribution at low voltage bias.

In fact, the carrier tunneling is so ′intrinsic′ to the ETA concept that very high built-in voltages V_{bi} of the junction should not be a goal, in order to avoid the critical field-strength that triggers the carrier tunneling processes [19]. The high V_{bi} could, conversely, lead to a lower carrier collection in the ETA solar cell. According to theoretical modeling [19, 53], when the absorber has very low carrier diffusion lengths (less than 10 nm), or at the lower limit of ETA cell absorber thicknesses (15 nm for $CuInS_2$), a maximum V_{OC} may be reached at the internal V_{bi} as low as ¾ of the E_g/q whereas larger V_{bi} lead to a small decrease of the V_{OC} due to tunneling, restricting the cells below 10% efficiency. However, at larger diffusion lengths above 10 nm, a higher V_{bi} may lead to a higher V_{OC} up to a point where $E_g/q=1$ is fulfilled.

A demand for a higher quality absorber (with higher diffusion lengths) would somewhat conflict with the ETA concept. However, a more uniform local thickness of the absorber may indeed be required to maximize the potential of the CIS absorber with an E_g of 1.5 eV and to boost the efficiency of the sprayed ETA cell studied in the thesis. The potential of the bandgap E_g of the CIS, versus the activation energy E_A of the barrier determined experimentally, is discussed further below (§3.1.5. Open-circuit voltage). Still, to successfully assess the possible variance of the local absorber thickness, major influences such as the speculated photosensitivity should be eliminated as a priority.

3.1.4. Copper diffusion into buffer layer

An absorption edge of 1.3 eV was determined in the *structured* cell whereas in the *flat* cell the absorption edge at 1.5 eV coincides with the bandgap of the CIS absorber (Figure 6b). *Ex-situ* optical transmittance data (not shown) of the flat CIS layers show a bandgap of ~1.5 eV, which we expect from *both* cells. In this section, we present a *speculation* that might explain the lowered bandgap in the structured cell.

In the In_2S_3 material at the In_2S_3/CIS interface, two ternary compounds can form ($CuIn_5S_8$ or $CuInS_2$) dependent on the rate of Cu diffusion into the buffer. The crystalline structure of indium sulfide tolerates copper atoms until the composition reaches 1:5:8 ($CuIn_5S_8$), whereas for higher copper contents, the chalcopyrite $CuInS_2$ is formed [170]. The $CuInS_2$ is expected to form as low 200°C; and favorably when the concentration of the diffused copper in the In_2S_3 buffer is higher compared to that needed for the formation of $CuIn_5S_8$ [82, 88, 170]. The diffusion of copper into the In_2S_3 buffer layer may lead to the formation of n-type $CuIn_5S_8$ spinel even at temperatures as low as 130°C, or, while annealing the whole solar cell [24, 82, 88, 170, 171]. The $CuIn_5S_8$, also a vacancy-compound like the In_2S_3, is material with a bandgap value of 1.31 eV [84, 172].

In the structured cell, the absorption edge was at 1.3 eV, as determined from EQE (Figure 6b). The lower limit of EQE (Figure 6b) is determined by any material with the smallest bandgap in the cell from where carriers are efficiently collected. Thus, the formation of $CuIn_5S_8$ at the expense of the In_2S_3 buffer could serve as an explanation for the lowered absorption edge in the structured cell. As for the *flat* cell that shows the expected bandgap of 1.5 eV, a the higher effective growth temperature of the absorber (discussed in §3.1.2 Shunt-conductance), and hence, expectedly higher rate of Cu diffusion may lead to the formation of $CuInS_2$ in the In_2S_3 at the absorber/buffer interface. The formation of $CuInS_2$ at the expense of buffer material, thus, leaves the effective E_g unaffected in the *flat* cell as evaluated from EQE (Figure 6b). In this view, we find some confirmation to the proposal that the growth temperature of the absorber in the structured cell is somewhat lower than in the flat analogue (discussed in §3.1.2 Shunt-conductance).

In the conventional high-efficient substrate type CIGSe cells, an inversion of absorber conductivity to n-type at the junction interface is advantageous, explained by the smaller energetic distance between the conduction band and the Fermi level and, thus, a decrease of the probability of minority carrier recombination at the interface [7, 10]. For the substrate cells, the In-rich intermediate layer between the absorber and the buffer is considered favorable due to the higher E_g of 1.2–1.3 eV [173] of the n-type $CuIn_3Se_5$ compared to the CIGSe with an E_g of 1.15 eV. However, in the sprayed ETA cell herein, the smaller bandgap of 1.3 eV in front of the CIS with an E_g of 1.5 eV would interfere with the optimum cell design in sense of light absorption. Thus, the In_2S_3:Cu ′diffusion layer′ should be avoided.

The Cu:In molar ratios were 1:1 in the precursor solutions of both the flat and structured solar cell. The proposed formation of $CuIn_5S_8$ in the buffer of the *structured* cell is expected to ′consume′ *less* copper (Cu/In ratio is 1/5 in $CuIn_5S_8$ compound) when compared to that required to form the $CuInS_2$ (where Cu/In ratio is 1/1) in the buffer of the flat cell. Thus, the unreacted Cu_XS is likely to be higher in the absorber of the structured cell. This speculation finds support in further discussion (§3.1.5 Distribution of defect density in absorber).

3.1.5. Distribution of defect density in absorber

The energetic distribution of defects in the absorber material of solar cells based on ZnO_{NR} or flat ZnO (Figure 7) were determined from admittance measurements [II]. A similar band of states is present at ca 200 meV for both cells, whereas the *structured* cell shows higher values along the vertical axis, a tail of states reaching toward midgap, and an additional band at ca 100 meV. Thus, the absorber, when grown onto the ZnO_{NR} seems to be of lower quality when evaluated by the admittance technique. A higher content of unreacted binaries, such as the Cu_XS, is likely to cause a higher defect density in the absorber of the *structured* cell.

The existence of the Cu_XS compound in CIS films when grown at 250°C will be shown (§3.2.1 Structural properties of $CuInS_2$ thin films). For the solar cells here, the window/buffer was kept at a somewhat elevated temperature of 270°C [II] or 300°C [V] when growing the CIS. The latter temperature agree with the optimum temperature found for spray of CIS onto TiO_2 [114] and with the CIS sprayed onto In_2S_3 [160] for solar cells application. For temperatures 350°C and higher, metal-oxide phase is present in addition to Cu_XS [119, 157], or chemical reaction at buffer/absorber interface may be expected [114].

A higher content of degenerate p-type Cu_2Se precipitates have been well correlated experimentally with higher doping densities, higher defect densities at interface, higher internal fields and a higher tunneling probability in the case of Cu-rich CGSe substrate type cells [8, 174, 175]. The Cu excess has also been noted to result in Cu_XS precipitation in case of the spray-ILGAR deposited CIS films [119]. The Cu_XS may not appear as a continuous film but in the form of islands when it has segregated on the film surface [50, 107] which is obviously a non-desired feature, considering the requirement of both homogeneity, as well as the absence of secondary phases to begin with. We note that irregular surface morphology was present in the CIS films grown from Cu-rich solutions [123]. In a conventional CIGSe cells the Cu-rich material result in a cell with a dominating interface recombination, whereas in the case of Cu-poor material recombination in bulk is prevailing, explained by widened absorber bandgap at the absorber/buffer interface in the latter case [175, 176]. We note that for the sprayed cell, the behavior of the ideality factor indicated a higher tunneling contribution to interface recombination in case of the *structured* versus the *flat* cell (Figure 5a) which seems to be consistent with that reported by the cited authors, in case Cu-binaries are to blame.

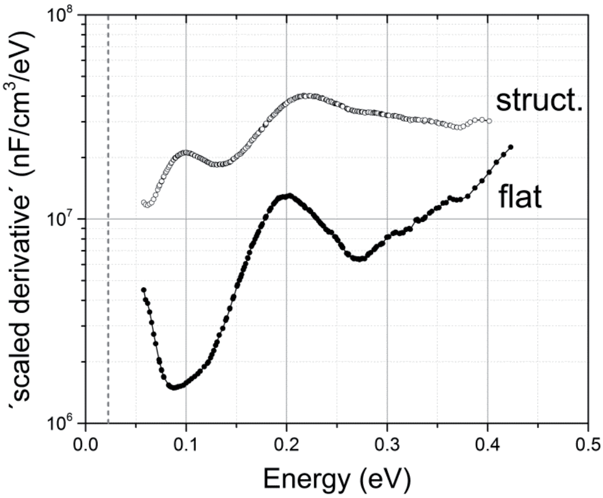

Figure 7. In the vertical axis – a magnitude that is proportional to the defect density in the absorber of the *structured* and *flat* cell. The plot is fused from spectra recorded from $3 \cdot 10^2$ to $5 \cdot 10^5$ Hz and temperatures 100–360 K at 0 V bias. The dashed line at ca 26 meV indicates kT at room temperature. [II]. In [29] the 0.2 eV states above the valence band have been attributed to Cu_{In} deep acceptor.

The substrate temperatures were kept approximately similar when the absorber of the *flat* and the *structured* cell was grown. Thus, the lower quality of the absorber (based on Figure 7) when grown onto ZnO_{NR}, as opposed to a flat window/buffer substrate, could be attributed to a lower growth temperature, as also speculated earlier (3.1.2. Shunt-conductance).

The exact spatial location of the defect densities manifested in Figure 7 yet remains unsolved. To detect states deeper than 0.4 eV in the bandgap higher temperatures than 360 K or frequencies lower than 10^2 Hz are required, that may be inaccessible due to sample itself or instrumental restrictions. A maximum sensitivity to the deep states is obtained at full depletion of the absorber, that is, at a sufficient reverse bias if needed.

Defect states in absorber bulk states seem to be the rational conclusion for explaining the features of Figure 7, considering the fact that broad defect bands are present (in Figure 7) and that no change in the C-f inflection frequencies were observed for a biased cell (not shown). Conversely, the I-V analysis (3.1.5. Open-circuit voltage) tends to indicate significant recombination due to interface states. Ultimately, if significant tunneling contribution is present at carrier recombination

(Figure 5a), there may be no sense to distinguish between interface and bulk recombination [167]. Clearly, the interpretation of admittance of a biased cell is not as straightforward as it would seem at first glance, and additional experiments are needed to confirm any speculations.

The higher density of defects, a broader distribution of defects, and the additional defect band in case of the structured cell is expected to reduce the V_{OC} as compared to the *flat* cell. The V_{OC} will be discussed followingly (§3.1.5 Open-circuit voltage).

3.1.5. Open-circuit voltage

The $V_{OC}(T)$ of the sprayed cell, as a function of irradiance, is presented in Figure 8. Ideally, one expects $qV_{OC}(\rightarrow 0K)=E_g$. Clearly, the qV_{OC} extrapolation to temperature of 0K is lower than the bandgap energy E_g=1.5 eV of the CIS absorber used.

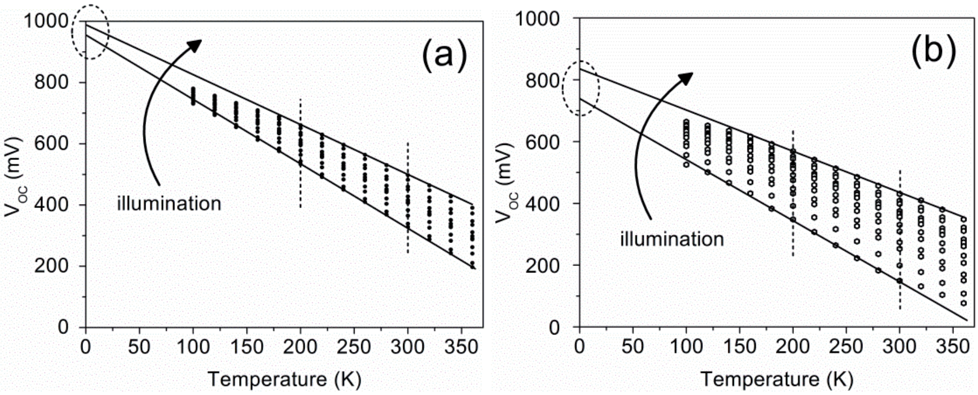

Figure 8. The V_{OC} of the *flat* **(a)** and the *structured* **(b)** cell versus measurement temperature of the cell, as a function of irradiance in between 0.5 . . 100 mW/cm^2. The extrapolation to 0K give the E_A of 950–990 meV and 740–830 meV, for the *flat* and the *structured* cell, respectively [II].

Cells that use materials with inhomogeneous compositional properties (discussed in §3.1.1. Series resistance) suffer from a decrease of the V_{OC} due to fluctuations of the saturation current (J_0) whereas ideality factors can be above 2 (discussed in §3.1.3 Ideality factor). Any fluctuations in the absorber bandgap cannot be excluded at our present knowledge of the sprayed cell (§3.1.3 Ideality factor). Furthermore, the presence of gaps in between the nanorods could introduce fluctuations. Other possibilities that have *not* been explicitly shown to exist in the sprayed cell (but not disproved either) are: discontinuity of the absorber in the gaps at the ′bottom′ of the nanorods; thickness variations or even pin-holes of the absorber; poor coverage of buffer with absorber; or poor wetting of the absorber with the back-contact – all which could be expected at some level.

However, the observation $qV_{OC}(\rightarrow 0K)<E_g$, as also seen from Figure 8, has been mostly attributed to the effect of recombination at interface [5, 7, 11, 50, 59,

152, 167] as usually reported for the cells with much thicker absorber when compared to the thickness of ETA and systematically observed in the cells that use CIS absorber. The analysis of the sprayed ETA cell seems to confirm the presence of interface states. Namely, the activation energy E_A of 740 . . . 830 meV of the *structured* cell lies further away from the expected 1.5 eV when compared to the E_A of the *flat* cell with E_A of 950 . . . 990 meV [II]. Thus, a higher specific surface area of the structured cell seems to show lower E_A as expected. Likewise, when increasing the length of the ZnO nanorods from 500 to 700 nm, the V_{OC} of the respective solar cell decreases from 428 to 334 mV and, despite of the increase of J_{SC} from 11.4 to 13.0 mA/cm^2, the efficiency decreases 2.9% to 1.9% (Table 4). A larger interface could be an explanation for this deterioration, as also presumed for ZnO_{NR}/a-Si:H cells with similar behavior [77]. Design-rules have been discussed that could reduce the amount of interface recombination, even if the high defect densities cannot or will not be avoided at interfaces [11, 59, 177].

However, at the same time, the G'_{SH} at illumination increases nearly twice when using rod length of 700 instead of 500 nm (Table 4). This suggests that the longer rods seem to allow more stray currents, and that a higher interface recombination may not be the only factor to blame. One explanation is that the longer ZnO nanorods induce additional absorption (due to a higher scattering ability, Figure 6) and thus ′assist′ to the photodoping of the buffer layer when considering the assumption of the photosensitive In_2S_3:Cu layer. Another explanation could be that the longer rods may have more Cu_XS residues that act as shunt paths (in §3.1.4. Copper diffusion into buffer layer, and §3.1.5 Distribution of defect density in absorber). For both cases, the primary cause is the available Cu_XS residues. Also, for the spray-ILGAR deposited ZnO_{NR}/In_2S_3/CuSCN superstrate ETA solar cell, the shunt resistance was reported to decrease from 4000 Ωcm^2 in a cell with a compact ZnO substrate and 0.8% efficiency, down to 400 Ωcm^2 in a cell with 2.4% efficiency where ZnO_{NR} substrate layer was used with nanorod lengths of 3.3 μm [54]. However, no explanation was provided for the large photosensitivity of the shunt-conductance.

Table 4. The length of ZnO nanorods versus the output of the respective solar cell at one sun [V].

Type	L, nm	V_{OC}, mV	J_{SC}, mA/cm^2	FF, %	η, %	G'_{SH}, mΩ/cm^2
FLAT	0	463	5.2	61	1.5	1.5
A	~500	428	11.4	60	2.9	3.5
B	~700	334	13.0	43	1.9	6.0
C	~1000	265	10.5	33	0.95	17

Additionally, when we compare the E_A (Figure 8) with the respective absorption edge of the cells (1.5 eV and 1.3 eV as calculated for the *flat* and *structured* cell, Figure 6), then the variance between E_A and E_g is *similar* for both cells, around 0.5 eV. Obviously, such an observation does not disprove the existence of interface states and interface recombination, but suggests to further study the variance between E_A and E_g for both cells.

In fact, according to Taretto and Rau [19], the surface recombination at the absorber interfaces is of second-order importance in the $CuInS_2$ based ETA cells, whereas the *tunneling* current through defects dominates the recombination. Indeed, as determined from n(T) (in § 3.1.3. Ideality factor) the tunneling enhanced interface recombination is likely to be the limiting factor in dark conditions (Figure 5a, below). However, at illumination the n(T) behavior was qualitatively different (Figure 5a, above): an increase in the temperature led to an increase of the ideality factor with $n<2$, indicating thermal activation of the saturation current [152]; and a similar tendency for the *structured* cell, however, with $n>2$. As noted, $n>2$ could be expected in case of significant non-homogeneities in the cell [151]. Thus, for both cells, a different recombination mechanism limits the cell current when in dark or at illumination. Similar results have been reported for the substrate type chalcopyrite solar cells with CdS buffer: a significant increase of the ideality factor and a change in the recombination in cells that use $CuInS_2$ absorber [50, 100]; whereas the change of the dominant recombination type upon light exposure is only present in case of the CIS or CIGS (sulfides) and not observed in cells with CIGSe, CISe or CGSe absorbers (selenides) prepared by the two stage sequential process [9, 11, 152, 178]. A study on CIGS cells indicated that an increase of irradiance resulted in an increase of the ideality factor (as is also observed in Figure 5b); an effect that was attributed to the increase/redistribution of charge-density at the interface and subsequent changes in banding of the energy bands; ultimately activating the contribution of interfacial states for recombination [179]. Finally, since tunneling mechanism involves states in the bandgap, an illumination dependent recombination mechanism (as hinted by Figure 5b) could be expected, since the occupation of these states change when the material is irradiated [9, 179].

Curiously, the J_{SC}-V_{OC} technique (not treated in Experimental section) that yields the I-V curve without the series resistance effects, show ideality factors lower than 2 that increase linearly with the temperature (not shown), unlike that seen for the *structured* cell in Figure 5a where $n>2$. In the case of voltage-dependent collection $J_L(V)$ one could expect the ideality factors to be overestimated [51]. However, the possibility of $J_L(V)$, although not entirely rejected, was discussed earlier as an unlikely phenomenon (§3.1.2 Shunt-conductance). Similarly, the inability to compensate either $R_S^{'}$ or $G_{SH}^{'}$ on the slope of the I-V curve, could lead to an overestimation of the ideality factor. Therefore, values presented here (Figure 5) are, at most, an upper bound to the estimation of the slope of the I-V curve, of the ideality factor, and of the magnitude of recombination.

The fact that the $V_{OC}(T\rightarrow 0K)$ does not converge at a temperature of 0K (Figure 8a, b) is a combination of the effect of n as a function of temperature (Figure 5a); but even more likely due to n as a function of illumination intensity (Figure 5b) – that in turn could be traced back to the tendency of the G'_{SH} for both cells (Figure 2) and thus to problems associated with the speculated In_2S_3:Cu layer.

Since the model requires a temperature-independent ideality factor [167], a deeper interpretation of the V_{OC}(T→0K) values are thereof ′out of scope′.

3.1.6. Cell output (J_{SC}; V_{OC}; FF; η) at varied irradiance

The J_{SC} of the *structured* and the *flat* cell increase with the intensity of the incident light (Figure 9a), as expected. When compared to the J_{SC} of flat cell, a higher J_{SC} in the *structured* cell can be attributed to higher absorption ability due to the scattering ability of the ZnO_{NR} in the structured cell.

Additionally, the smaller bandgap 1.3 eV in the structured cell also makes a significant contribution to the increase of the J_{SC} as seen from the EQE spectra (Figure 6). Possible causes of the decrease in the bandgap were discussed (§3.1.2, §3.1.3, §3.1.4). Despite the current gain near the absorption edge, the diffusion of copper should be eliminated to reduce photoconductivity of the shunts (§3.1.2), and, due to the unfavorable bandgap sequence of the speculated $In_2S_3/CuIn_5S_8/CIS$ stack (§3.1.4).

The behavior of the V_{OC}, the FF and the η is worrying for both cells, although the effect is more drastic for the *structured* cell. We would expect a steeper increase of the FF and the V_{OC} at increased light intensities, although the η (Figure 9d) of the *structured* cell still remains higher at AM1.5 owing to the high J_{SC}. The most likely cause of the ′lazy′ V_{OC} (Figure 9b) is the behavior of the ideality factor that shows higher values at higher illumination intensities (Figure 5b). In particular for the *structured* cell, a significantly higher recombination rate is expected at higher illumination intensity because n increases sharply at 2 mW/cm^2 irradiance (Figure 5b).

An increase of the V_{OC} should correlate with an increase in the FF [5, 92]. At low irradiance, a simultaneous and a significant discrepancy in FF (Figure 9d) of the cells, and of the V_{OC} of the cells (Figure 9b), can be observed; a tendency similar to that observed in the case of illumination dependent G'_{SH} (Figure 2). Followingly, since J_{SC} is not a dominant contributor to the efficiency at low irradiances, the efficiency of the cells shows a ′crossover′ at 2 mW/cm^2 (Figure 9d) and the *structured* cell loses the advantage it had at AM1.5 in sense of the cell efficiency. However, at AM1.5, where the G'_{SH} are similar for both cells, a smaller variance of the FF is present. The absorption ability of the *structured* cell remains higher even at low illumination, according to the behavior of G'_{SH} (Figure 2); hence, at low illumination intensities we could attribute the low performance of the *structured* cell to the illumination dependent G'_{SH}. Alternatively, a higher concentration of highly conductive Cu_XS in the absorber of the structured cell may be to blame (§3.1.4 Copper diffusion into buffer layer, and §3.1.5 Distribution of defect density in absorber).

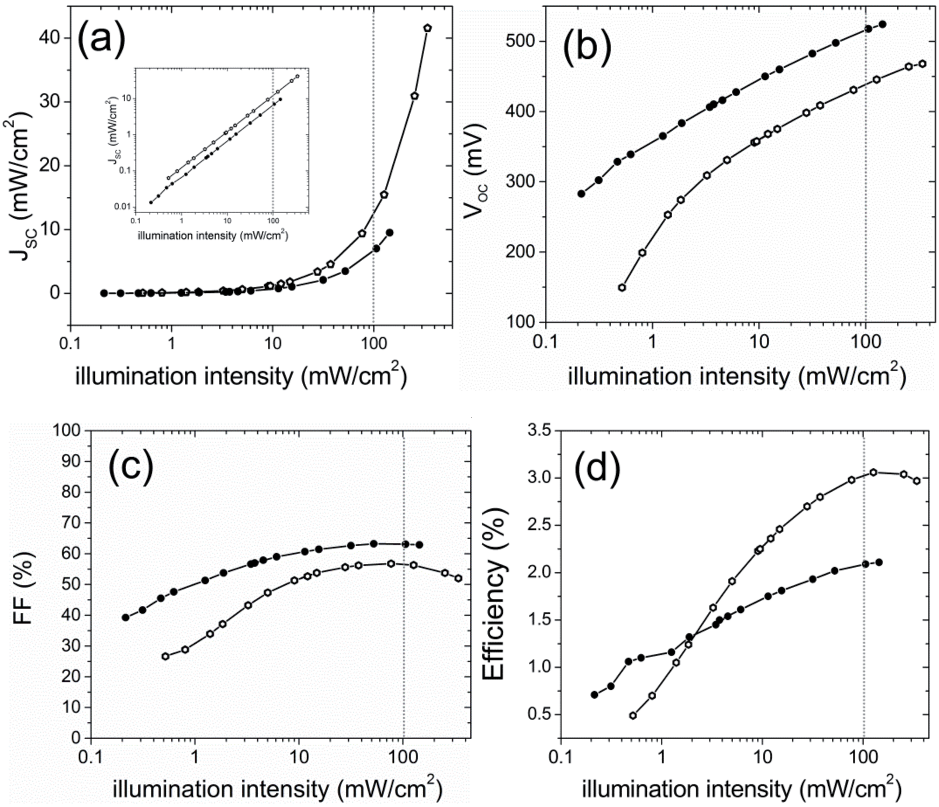

Figure 9. Output of the *structured* cell (empty symbols) and that of the *flat* (filled symbols) solar cell at varied irradiance: short circuit current J_{SC} **(a)**, open-circuit voltage V_{OC} **(b)**, fill factor FF **(c)** and conversion efficiency η **(d)** [II].

A significant buffer photodoping has an influence on the band-bending and on the built-in field and by that affects the collection efficiency differently at varied irradiance [5, 51, 164, 179]. However, it is yet not sure, whether the illumination dependent G'_{SH} is the only factor to affect the ideality factor in such a manner that n also deteriorates with increasing the light intensity (Figure 5b); or if the G'_{SH} illumination dependency plays any role in the shift of the dominant recombination type when changing from dark to illuminated conditions (Figure 5a). Nevertheless, when considering the illumination dependent G'_{SH} two effects present in the sprayed cell could have an explanation: the cross-over of the *dark* and *light* I-V curves (a), and the violation of the shifting approximation (b).

(a) The I-V *crossover* is a non-ideality that is commonly present for CIS devices as an intersection of the dark and light I-V characteristics evident at higher bias voltages $V>V_{OC}$ (Figure 10). Based on reference [5] the photodoping of the buffer layer decreases the potential drop over the buffer layer, thus reducing an existing electron barrier in the conduction band, and by that increases the diode current under illumination.

(b) The *violation of the shifting approximation* means that the *light* I-V cannot be obtained from the *dark* I-V by simply shifting the curve downwards by J_{SC} in the vertical direction. The violation is visually evident at bias voltages $V<V_{mpp}$ (Figure 10). This phenomenon could be explained by the illumination dependent In_2S_3:Cu shunt path (G'_{SH}) that would drain a higher current when the cell is illuminated, based on [5].

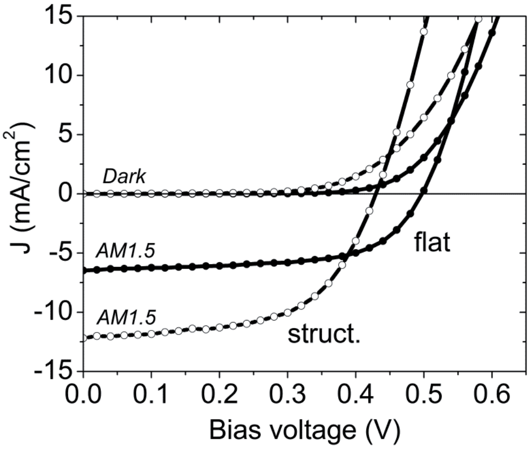

Figure 10. J-V of the *structured* cell (open symbols) and *flat* cell (filled symbols) in dark and at illumination under solar simulator at T=300K. Violation of the shifting-approximation, and the cross-over effect of the dark and light J-V are present for both cells [II].

3.1.7. Summary

Analysis of the sprayed ETA solar cell structure ($ZnO_{NR}/In_2S_3/CuInS_2$) was based on I-V, EQE and admittance analysis. The use of a structured ZnO_{NR} layer allows to roughly *double* the light absorption ability and the resulting short-circuit current density in the cell at one sun, when compared to a planar reference cell. External quantum efficiency is as high as 70% in the structured versus 35% in the reference cell. The respective gain in efficiency from 2% up to 3% is less than a factor of two due to a small decrease in the open-circuit voltage and fill factor in the structured cell.

The cell suffers from a somewhat high series resistance, while the shunt-conductance values are tolerable. Nevertheless, the shunt values are photosensitive and increase several orders in magnitude when increasing the irradiance. The photosensitivity can be explained based on unintentional doping of the buffer layer with copper that originate from unreacted Cu_XS binaries in the absorber. In addition, the cell shows lower than the expected absorption edge at 1.3 eV. We offered a speculation that during the copper diffusion into the buffer, an indium rich ternary

($CuIn_5S_8$) is formed at the expense of buffer material. When compared to a reference cell based on flat ZnO layer, the results on ZnO_{NR}-based cell suggest lower growth temperature of the absorber, higher defect densities, and higher contribution of tunneling to the recombination – factors that hint the possibility of a higher concentration of Cu_XS in the absorber material of the structured cell.

3.2. Solar cells´ materials studies

3.2.1. Structural properties of $CuInS_2$ thin films

The films discussed here are deposited onto a borosilicate substrate at 250°C, close to the lowest applicable temperature that is determined by the decomposition of the precursor complexes of the CIS [150]. The use of solutions with $[Cu^{2+}]/[In^{3+}]=1.0$ results in as-deposited films that, in addition to CIS, contain another phase (marked with ′X′ in Figure 11), while the use of solutions with $[Cu^{2+}]/[In^{3+}]=1.1$ results in CIS phase only as determined by XRD (Figure 11). Oxygen was not detected in the films when evaluated by XPS; 3–4% chlorine residues were present according to EDX [IV].

The main secondary phases in CIS are $CuIn_5S_8$ for Cu-poor samples and Cu_XS for Cu-rich samples [111, 148]. The XRD ′shoulder′ at 27° (marked with ′X′ in Figure 11) has been reported to be absent in Cu-rich films [105, 110, 123]. The ′In-rich′ ternary compound ($CuIn_5S_8$) is more likely to be present as opposed to β-In_2S_3 because the latter is not expected to coexist (in equilibrium) with the $CuInS_2$ [108]. A separate In-rich ternary phase is likely to be present, as discussed for CISe by co-evaporation [16]. We note that optical measurements (not shown) did not show significant differences in the transmittance data of the CIS-1.0 and CIS-1.1 films.

When annealed, the films are highly (112) orientated and consist of $CuInS_2$ (JCPDS 00-027-0159), independent of the molar ratios used in the spray solution (Figure 11). The H_2S treatment removes chlorine residues and increases sulfur content, as determined by EDX [IV]. For the CIS-1.0 films, annealing for 10 minutes resulted in an increase of the crystallite size up to 70 nm, with little gain for longer treatments (Figure 12a). As for the CIS-1.1 films, no more than 5 minutes of annealing time was needed to reach crystallite sizes of 80 nm (Figure 12a).

Ideally, the diffraction analysis rely on homogeneous distribution of phases with random orientation, having a detection limit of a trace phase in a majority matrix of 0.5% by weight [1]. For example, the nanocrystalline or amorphous Cu_XS (or In-rich secondaries) may not be detectable by XRD [107, 119]. Likewise, the CA ordering is not always distinguishable by the (001) reflection at a low angle of 16° [103, 104, 107, 114, 119, 180]. Also, it has been reported that an increase of the CA phase content relates with a decrease of (200) intensity of the XRD reflection

[103]. However, the Raman spectroscopy detects disorder with a higher sensitivity than XRD does [107]. That is, in case the vibrational modes of the material are Raman-active and the Raman setup is sensitive enough to detect scattered light with respect to the wavelength of the excitation. A higher content of chalcopyrite ordering (CH) in the CIS films has been well correlated with a higher conversion efficiency of the respective solar cells. The quality factor of the CIS films is determined from the respective intensities of the fitted Raman peaks as follows $QF = I_{CH} / (I_{CH} + I_{CA})$, where I_{CA} is the intensity of the Raman peak due to the presence of domains with Cu-Au ordering (CA) which coexist with the phase with CH ordering [103, 106, 107, 109, 180, 181]. The disordered CA phase is correlated with the presence of sulfur vacancies V_S and antisite defects Cu_{In} and In_{Cu} [107, 114, 182].

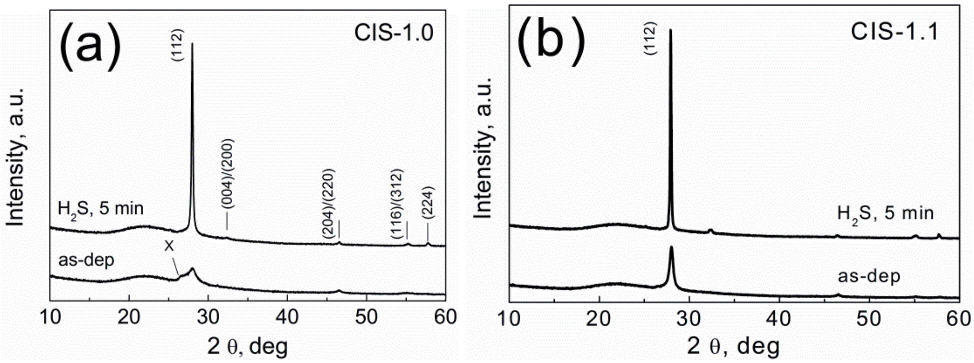

Figure 11. XRD diffractograms of the as-deposited at 250°C films (lower curves) and that of the annealed for 5 min at 530°C in N_2+H_2S (95%+5%) atmosphere films (upper curves). The CIS-1.0 **(a)** and CIS-1.1 **(b)** stand for films deposited with $[Cu^{2+}]/[In^{3+}]=1$ and 1.1 in the precursor solution. The unknown phase is marked with ´X´ [IV].

The CIS films, when grown onto borosilicate glass, consist of crystallites with sizes less than 20 nm (Figure 12a) and a low chalcopyrite content of ~30% (Figure 12b). Despite the high gain of crystallinity when CIS-1.1 are annealed, the quality factor, that is related to the chalcopyrite content, saturates at ca 50% (Figure 12b) at 10 minutes, whereas for the CIS-1.0 films the content reach as high as 76% at 60 minutes of annealing. Most likely, the Cu_XS phase is the agent that affects such behavior. Namely, the sprayed CIS films, especially when grown below 300°C may contain residues of non-reacted binary sulfides and residues originated from starting chemicals. The Cu_XS phase, when present in the as-deposited films, segregates onto the film surface [109, 119, 148, 182-184], where it can be detected by Raman spectroscopy. The CIS-1.0 films reveal Raman peak characteristic of Cu_XS after 60 minutes of annealing (Figure 13a), whereas the CIS-1.1 films the peak appear already at 10 minutes of annealing (Figure 13a). The as-deposited CIS-1.1 films do not show presence of Cu_XS due to etching in KCN. For the co-evaporated CIS, the CA phase was reported to disappear during sulfurization at 550°C [180], at a somewhat higher temperature when compared to 530°C that was used here.

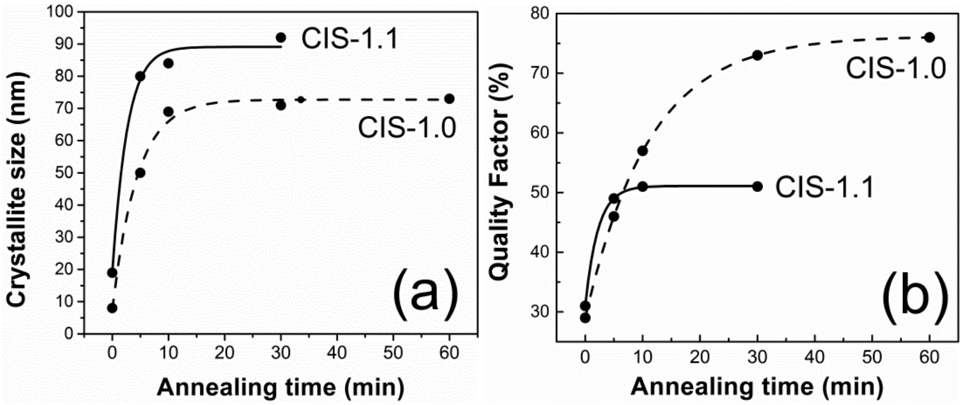

Figure 12. **(a)** Crystallite size by XRD of CIS-1.0 and CIS-1.1 films at varied duration of annealing in H_2S. **(b)** Quality factor by Raman, a characteristic of the percentage of chalcopyrite (CH) phase, in CIS-1.0 and CIS-1.1 films. Raman spectra are presented in Figure 13 [IV].

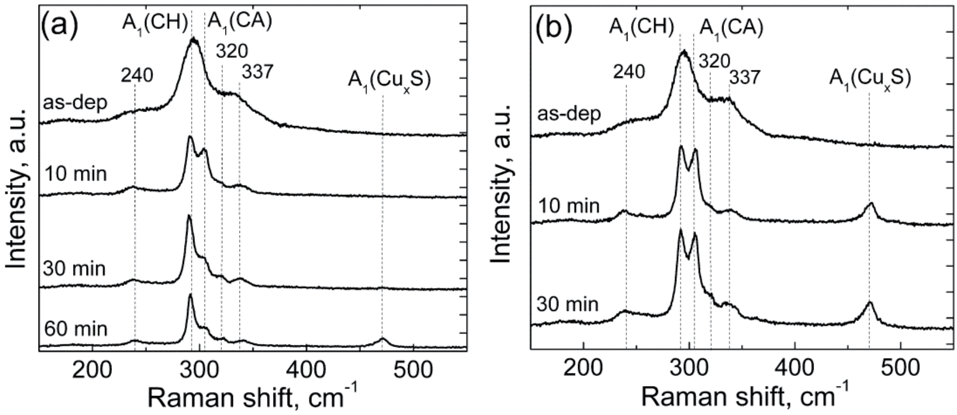

Figure 13. Raman spectra of the as-deposited and that of the annealed CIS-1.0 films **(a)** and CIS-1.1 films **(b)** at varied durations of annealing at 530°C in H_2S [IV]. Raman peaks at 240, 292, 320, and 337 cm^{-1} are attributed to CH ordered CIS phase; the A_1 (CH) mode at 292 cm^{-1} is the vibration of sulfur sublattice, the Raman peak centered at 303 cm^{-1} is the A_1 mode of the Cu-Au ordered (CA) phase [100, 104, 180, 185].

It has been reported that the presence of Cu_XS act as flux and support the growth of crystallites in CIS by the two-step method [50] and in CIS by spray [122, 123]. The higher content of Cu_XS in CIS-1.1 films promotes growth of the crystallite size when compared to growth from the ′stoichiometric solutions′ (Figure 12a) but, seemingly, retards the formation of CH phase (Figure 12b) during the high-temperature treatment of the sprayed films. In contrast, an *excess* of Cu_XS binary has been noted to *support* CA to CH transformation in the case of co-evaporated CIS films [181]. A Cu-rich composition is, in fact, generally associated with a higher CH content and thus, a higher CIS quality; while the In-rich secondary ternary phase ($CuIn_5S_8$) is directly related to the disorder in CIS [103, 149]. Also, it has been reported that the removal of Cu_XS prior to annealing will *inhibit* the

$CuIn_5S_8$ to $CuInS_2$ transformation [109]. However, we did not observe the ′X′ peak (tentatively ascribed to $CuIn_5S_8$) by XRD (Figure 11) and the CIS-1.1 films do contain Cu_XS as determined by Raman (Figure 13). We cannot entirely exclude that traces of $CuIn_5S_8$ are present in the as-deposited CIS-1.1 films. Also, the peak near 337 cm^{-1} that remains pronounced in the CIS-1.1 films (Figure 13b) have been associated with the presence $CuIn_5S_8$ [84, 110, 148, 181].

The FWHM of the A_1 (CH) Raman peak is as low as 6.2 cm^{-1} in the case of CIS-1.0 films when annealed. However, linewidths larger than 3.8 cm^{-1} are reported to result in a deterioration of the output of the respective solar cells (V_{OC}<700meV, neglible effect on the J_{SC}) that use co-evaporated CIS thin film in a conventional substrate configuration [50, 100], and correlated with the increased share of the disordered, metastable CA phase [180]. In case of Raman linewidths larger than 3.8 cm^{-1} a sharp increase of the ideality to values larger than 2 and an immediate drop of the V_{OC} below 700 meV is present in the conventional thin film cells [50]. The rapid decrease of the V_{OC} has also been related to the change of the dominating recombination mechanism from bulk to interface when decreasing the absorber quality [11]. An ETA cell with a conversion efficiency of 5% based on TiO_2 and sprayed CIS has reported CA content as low as 5–10% by weight, where the CA content was evaluated from XRD pattern [114].

In this work, it is difficult to assign the high ideality factors of the sprayed cells to the existence of poor absorber quality alone (FWHM>6.2 cm^{-1}). An ETA cell should conceptually be able to accommodate a very poor quality absorber. Nevertheless, absorber quality cannot be excluded as a factor that lowers the output of the sprayed cell herein. A single phase is always desirable, whereas Cu_XS binaries are not welcome in the CIS as detected even in the films grown from ′stoichiometric solutions′ (Figure 13a, at 60 min). The Cu_XS, when present, is likely to cause higher absorber defect densities and higher tunneling contribution to the recombination when applied in solar cells as absorber material, and to release copper as an unintentional dopant (§3.1.7 Summary).

3.2.2. Structural properties of In_2S_3 thin films

The structure of undoped In_2S_3 films by CSP is analyzed based on Raman spectroscopy. The phase composition of the as-deposited films is of interest for the sprayed solar cell application. Additionally, we keep in mind the possible application of In_2S_3 as a host material for doping with a transition metal element [I]. It had been shown that the preferred location of the dopant atom is the octahedrally to sulfur coordinated indium location in the In_2S_3 lattice, when aiming to create a truly delocalized band of electron states called the intermediate band (IB) [63]. In other words, a spatially continuous band similar to conduction or valence band must be ensured to exclude non-radiative recombination through IB as would be in the case of localized electron states [14].

In the Raman spectra of the sprayed In_2S_3 films (Figure 14a, b) peaks other than β-In_2S_3 were not detected. The peak that corresponds to the tetrahedral sites is near 244 cm^{-1} and that of the octahedral site near 306 cm^{-1} [186, 187]. Clearly, the use of higher substrate temperatures T_S of 320°C are advantageous for obtaining higher quality as-deposited films, more precisely seen by comparing the respective widths of Raman peaks of either lattice location (Table 5).

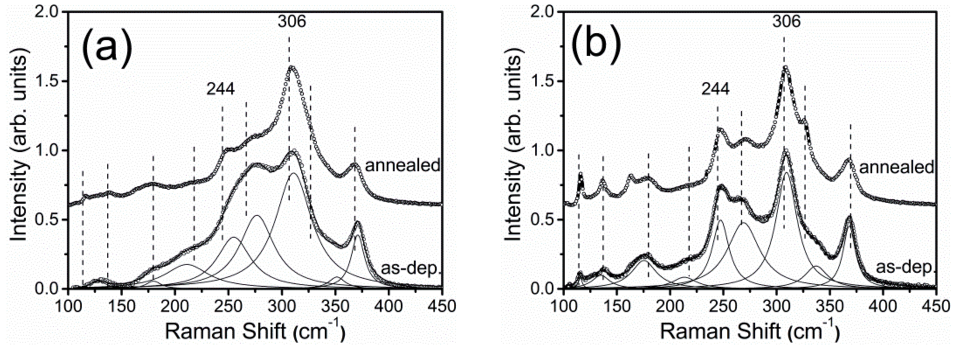

Figure 14. Raman spectra of the as-deposited and annealed In_2S_3 films deposited by CSP at substrate surface temperatures T_S of 205°C **(a)** and 320°C **(b)**. Dashed lines indicate the expected Raman reflections of β-In_2S_3 [69, 188], also listed in [I]. Fitting of data is shown for as-deposited films. Corresponding XRD patterns are presented in Figure 15. The spectra are shifted vertically.

Table 5. Result of fitting the position and width of the Raman peaks of interest of the as-deposited at substrate temperatures T_S of 205 and 320°C, and annealed In_2S_3 films [I].

Indium site		Octahedral		Tetrahedral	
		Peak, cm^{-1}	FWHM, cm^{-1}	Peak, cm^{-1}	FWHM, cm^{-1}
As-deposited	T_S=205°C	259	47	312	33
H_2S treated		249	24	310	34
As-deposited	T_S=320°C	247	19	309	24
H_2S treated		247	14	308	19

When annealed in H_2S, a significant increase of the quality of the crystal ordering with octahedrally coordinated sites is evident; intuitively, the peak width decreases much less from 19 to 14 cm^{-1} when starting from a film with a higher quality deposited at 320°C; whereas for films deposited at a lower T_S=205°C a more substantial decrease from 47 to 24 cm^{-1} is present; and yet, the peak width remain smaller for films deposited at 320°C (Table 5).

The illustrated tendencies are also present when looking at the positions of the Raman peaks, whether comparing the effect of temperature or annealing on the film quality. That is, the peaks red-shift toward expected values at 244 and 306 cm^{-1} for octahedral and tetrahedral coordination, respectively (Table 5); whereas the relative shift remain larger for the films grown at lower temperature of 205°C; and yet the peak values still remain closer to that expected when films were grown at 320°C (with or without annealing). A red shift of Raman peaks toward expected positions is expected in case compressive stress is relieved in the films [189].

The lattice parameters improve accordingly. For example, the length *a* of the square base of the tetrahedral unit cell of the In_2S_3 undergo 1% and 0.5% relative increase when the films are grown at 205°C and 320°C, respectively (Figure 15).

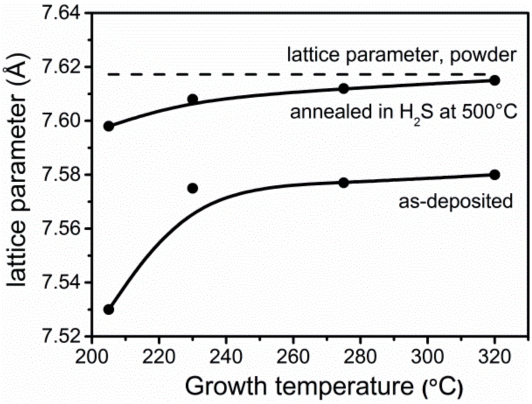

Figure 15. Lattice parameter *a* of the as-deposited and of the annealed In_2S_3 films that were grown at varied substrate temperatures of 205–320 °C. The dashed line indicate the expected value of *a* of the β-In_2S_3 powder reference [I].

And finally, the stoichiometry of the films also increases when observing the S/In atomic ratios before and after annealing (Table 6). The tendencies discussed remain except that the 205°C film tend to show a closer to expected [S]/[In] ratio of 1.38 when compared to that obtained at 320°C, after annealing. Although the relative changes of the [S]/[In] ratios are reliable, it could very well be that the absolute [S]/[In] values are not a suitable matter for discussion, since the EDX results were not calibrated with a stoichiometrical material (In_2S_3 monocrystal). The relevance of the Cl content is discussed further below.

Thus, growth temperatures as high as 320°C and post-deposition annealing at 500°C in H_2S would be a preferable route to obtain a higher quality In_2S_3 especially when preferring to achieve the octahedral coordination of cations.

Table 6. Element composition in units of at.% as measured by EDX of the as-deposited and the annealed In_2S_3 films grown at substrate temperatures of 205°C and 320°C. Atomic ratio of [S]/[In]=3/2 is expected from a stoichiometrical In_2S_3.

		In	S	Cl	S / In
As-deposited	T_S=205°C	40.9	52.1	7.0	1.27
H_2S treated		40.2	55.5	4.3	1.38
As-deposited	T_S=320°C	41.7	55.3	3.0	1.33
H_2S treated		41.6	56.3	2.1	1.35

The discussed films were based on aqueous solvent. An interesting conclusion can be drawn when comparing the Raman spectra of In_2S_3 when deposited using either aqueous or alcoholic solvent in the precursor solutions (Figure 16). The films grown at 320°C when using aqueous solvent, and films grown at a lower temperature of 285°C when using alcoholic solvent, are with a similar quality. That is, the resolved details and peak widths of the Raman profile are comparable (Figure 16). It seems that, in case of alcoholic solution sprayed, the growth temperature in the reaction zone of pyrolysis is relatively higher. A similar phenomenon was proposed, based on the photoluminescence spectra, when growing ZnO nanorods by CSP, and was explained based on the higher volatility of the alcoholic solvent [III], that causes less heat loss and a lower cooling rate when compared to the use of aqueous solutions. The use of lower substrate temperatures is crucial when the substrate is heat sensitive. In particular, such is the case for solar cells that are deposited in a sequence of different semiconducting layers. Therefore, the use of alcoholic solutions provides a way to decrease the substrate temperature without affecting the film quality as evaluated by Raman.

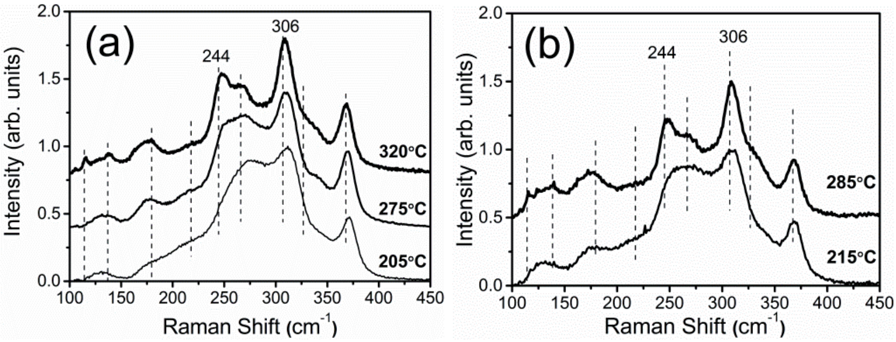

Figure 16. Raman spectra of as-deposited In_2S_3 films grown at varied substrate temperatures (indicated in the figure) using either aqueous **(a)** or alcoholic **(b)** spray solutions [I]. The spectra have been shifted vertically.

The chlorine is an n-type dopant in the chalcopyrites [68, 90]. A reduction of the chlorine content as a residue, and the related secondary phases, is highly favorable when the indium sulfide will be used as the buffer layer in a thin film chalcopyrite cell, as shown for the ILGAR deposited In_2S_3 [24].

The Cl content in the films decreases in a manner discussed earlier: 7.0 to 4.3 at.% when deposited at 205°C and subjected to annealing, and from 3 to 2.1 at.% when the deposition temperature was 320°C (Table 6). Thus, a somewhat larger relative decrease of chlorine is provoked by the annealing procedure when the as-deposited films were grown at a lower temperature. Hence, for the sprayed solar cell application, the use higher growth temperatures (300°C) are justified whereas further annealing of the ZnO/In_2S_3 substrate structure might be profitable.

A chlorine content of 12–14% versus 0% increases the E_g of the ILGAR deposited In_2S_3 from 2.0 to 2.4 eV leading to higher EQE of the respective cells

[24]. The small amount of Cl residues in the In_2S_3 buffer was speculated to inhibit Cu diffusion into buffer [24] which may seem advantageous for technologies that use Cl-containing precursors. However, the cells that contained Cl in the buffer had lower FF and V_{OC} [24]. Thus, the cited authors stand firm that a Cl-free buffer, which leads to higher cell efficiencies, is preferred. Another significant source of E_g variance in between 2.0 up to 2.9 eV is the oxygen content in the In_2S_3 [82]. The contamination via Cu diffusion was discussed (3.1.4. Copper diffusion into buffer layer).

In case of the sprayed cell, the drastic effect of increased buffer layer thickness to the EQE has already been discussed (Figure 3c). However, the speculated cause of V_{OC} and FF decrease this far was primarily the presence of photosensitive shunts rather than issues due to low buffer layer thickness. The buffer when sprayed as a flat layer is a compact, pin-hole free layer. Although any discontinuities cannot be excluded when grown onto the ZnO_{NR} layer, the CSP seem to allow a uniform coverage of the highly structured ZnO_{NR} substrate (Figure 17). Nevertheless, similar thicknesses of In_2S_3 at the top and bottom part of the nanorods is difficult to guarantee without adapting ALD, as also stated for spray-ILGAR covered ZnO nanorods [29].

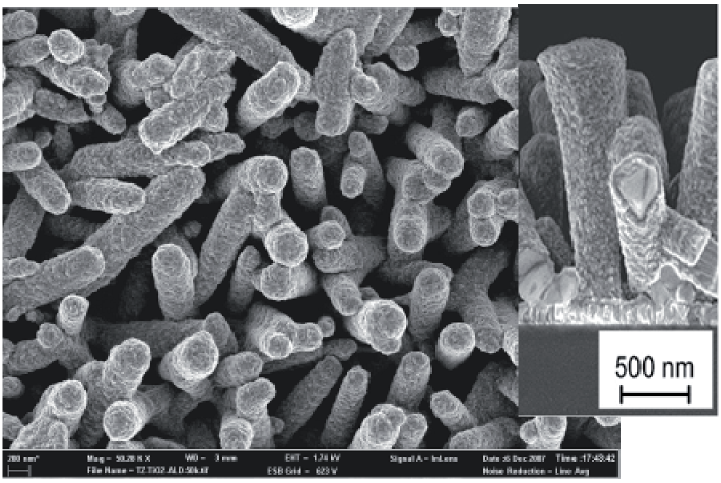

Figure 17. SEM image of ZnO_{NR} layer, with nanorods up to a micrometer in length that have been covered uniformly by a thin In_2S_3 buffer layer. Both layers have been deposited by CSP.

3.2.3. Properties of ZnO_{NR} layers

The ZnO window layer in the sprayed ZnO_{NR}/In_2S_3/CIS cell is the n type component of the pn junction that has to transmit visible light and serve as a light-trap.

Photoluminescence of ZnO_{NR} layers

The analysis of photoluminescence of the ZnO_{NR} revealed higher quality layers when grown onto ITO/SLG when compared to layers grown onto a bare SLG (soda lime glass) substrate (Figure 18). The conclusion was drawn from the observation that the ratio of lower energy emission (′red′ band) to near band emission (NBE) has been significantly reduced in case of the ZnO_{NR} grown onto ITO. Possible causes of the higher quality ZnO_{NR} when grown onto ITO may be: favorable seeding properties; diffusion blocking during high temperature growth at 550°C (near the limit of SLG use); or better heat distribution due to the high-conductivity ITO. Further experiments on various or modified substrates are necessary for confirmation.

Although the red band (Figure 18) could be attributed to interstitial oxygen [190, 191] the possible origin of this emission in the sprayed layers remains speculative without exhaustive experiments. The increase of the emission below 2 eV (the red band) was in anticorrelation with the green emission centered at 2.5 eV (Figure 19), that is, the bands do not tend to co-exist. The phenomena has been observed by others, whereas the green and orange luminescence were attributed to oxygen-poor and oxygen-rich sample conditions, respectively [192].

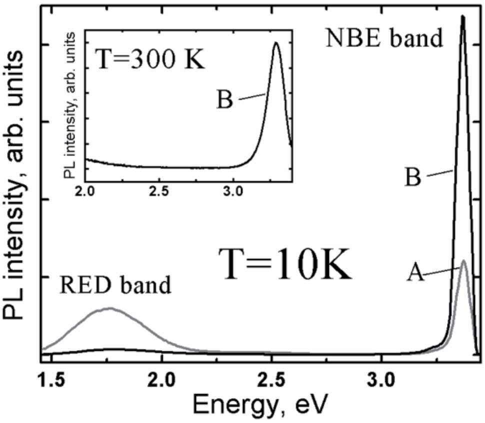

Figure 18. Photoluminescence of ZnO_{NR} grown on soda-lime glass **(A)** and on ITO/SLG **(B)**, both at 550°C by CSP, at otherwise similar growth conditions [III].

At the same time the green band in the sprayed ZnO_{NR} increased along with the carrier concentration in the samples [VI]. Thus very likely, the less resistive samples that simultaneously showed the green band could have a larger concentration of oxygen vacancies (V_O) as a deep donor or conversely, a higher concentration of interstitial zinc (Zn_i) as a shallow donor, or related complex, despite the higher formation energy of Zn_i [193]. However, since the deposition of ZnO_{NR} was in air, the higher growth temperatures of 550°C should lead to the thermodynamically more favored decrease of V_O rather than an increase of Zn_i.

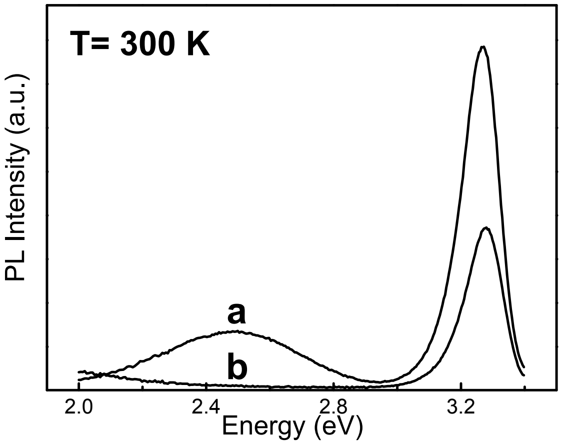

Figure 19. Photoluminescence spectra at 300K of ZnO_{NR} deposited at substrate temperatures of 480°C **(a)** and 550°C **(b)** [VI]. The ´red´ band of (b) extends to the left, only a ´shoulder´ is seen in this figure.

The prevalence of the NBE transitions and the FWHM of the band as low as 4.5 meV at 10K suggest a low defect density in the ZnO_{NR} layer when grown onto ITO substrates at higher temperatures of 550°C, thus a low carrier density is likely. In contrast, higher carrier concentrations could be expected at lower film qualities due to a higher number of defects. Indeed, carrier concentration in ZnO_{NR} can be increased orders of magnitude from 10^{15} cm^{-3} when grown at 550°C up to 10^{17} cm^{-3} when grown at 480°C [VI].

When decreasing the ZnO_{NR} growth temperature from 550°C to 480°C (Figure 20a, b), alcoholic solutions instead of aqueous precursor solutions have to be used, otherwise long nanorods are not formed (Figure 20b, c). When adapting alcoholic solvent at a lower growth temperature, the density and the sizes of the rods resembles those when aqueous solutions are used sprayed onto the substrate at 550°C (Figure 20a, c). This leads to an assumption that the loss of the substrate heating (from 550°C to 480°C) is simply compensated due to the higher volatility of the alcoholic solvent; similar to what was observed in the case of In_2S_3 films when deposited using either aqueous or alcoholic precursor solutions (Figure 16). Indeed, there are indications to support this presumption as was illustrated in [III]; however, the simultaneously observed higher defect density in the films grown at 480°C

(Figure 19) does not strictly allow such a simple deduction. Therefore, although the temperature effects cannot be overlooked when using alcoholic instead of aqueous solutions, the dominant factor to induce growth of ′decent′ nanorods at lowered growth temperatures (Figure 20b, c) is most likely the significantly smaller droplet sizes when using spray of alcoholic solutions. This conclusion coincides with that of Dedova et. al. [194] who stated that a denser surface coverage by nanorods and thinner nanorods are present when alcoholic solutions are used, explained by the smaller droplet sizes induced by low surface tension and lower viscosity of the alcoholic solvent.

In addition, the observation that In_2S_3 films retain their quality at a lower growth temperature when deposited using alcoholic instead aqueous precursor solution (Figure 16) cannot simply be extended to the nanostructured ZnO case here. We remind the speculation proposed during the ETA cell analysis; the absorber growth onto ZnO_{NR} seemed to be with a lower temperature from that when grown onto the flat ZnO (§3.1.2 Shunt-conductance, and §3.1.4 Copper diffusion into buffer layer). It is likely, that the temperature gradient from the substrate to the zone of pyrolysis is different, and more complicated, during the growth of thin films from that of nanostructured layers. Thermal simulations may provide further insight here.

Here, the use of alcoholic solvent induced changes in the ZnO_{NR} morphology. The ability to use lowered substrate surface temperatures, by the use of alcoholic solutions, has other practical implications. For one, the SGL is likely to deform at temperatures 550°C and above, while temperatures less than 480°C may be required to stay below the strain point of SGL. [146]. Furthermore, lower substrate temperatures allow less thermal stress and faster heat-up and cool-down periods during e.g. absorber growth [146].

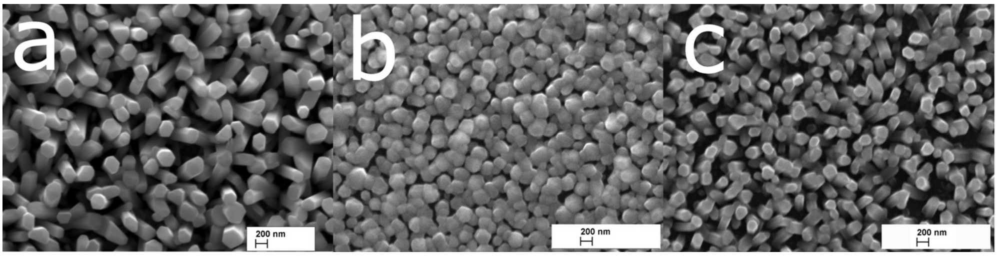

Figure 20. SEM images of ZnO nanorod layers deposited by CSP. The layers **(a, b, c)** were deposited onto ITO/SGL substrate at growth temperature of 550°C **(a)** or 480°C **(b, c)** using aqueous **(a, b)** or alcoholic solutions **(c)** [III].

Electrical properties of ZnO$_{NR}$ layers for ETA cell application

Carrier concentrations 10^{15} to 10^{17} were determined in the ZnO$_{NR}$ when as-grown by spray [VI]. This section provides discussion on whether the electronic properties of the sprayed ZnO$_{NR}$ are acceptable for the sprayed solar cell window application.

The main loss in the optical window layer is the reflection as high as 9% in the case of flat ZnO window, one of the largest losses in the cell [58]. Another cause of reflection and absorption losses in a solar cell is the intraband transitions in the near-infrared region due to free-carrier absorption [16, 30, 51]. The photocurrent loss due to free-carrier absorption in a flat highly-doped ZnO are estimated to be around 4% [58]. In addition to affecting the absorption of incident light in a completed device, the higher density of free carriers will reduce the infrared transmission during the deposition process, and hence, result in a reduction of the growth temperature of the absorber when grown on a highly conductive versus nominally undoped window layers. A lower emissivity of a substrate, on the other hand, causes the temperature of the TCO itself or other similar window layer, to be somewhat higher [68]. These small changes may have a drastic effect on the final absorber quality and device performance: for example simply by changing from flat ZnO to nanorod layer substrate, we observe signs of lowered growth temperature of the absorber, as speculated earlier (§3.1.2 Shunt-conductance, and §3.1.4 Copper diffusion into buffer layer). The deposition temperature of the absorber is crucial to the cell quality, especially when copper diffusion from chalcopyrite absorber to indium sulfide is involved, as also stressed by other authors [170].

In the sprayed superstrate cell herein, the ITO is the highly-doped TCO layer and the front contact. Although ITO should in the long term be replaced, the drive is mainly due to the cost rather than issues with absorption. By CSP we have successfully deposited ZnO:In layers with resistivities 10^{-3}–10^{-1} Ωcm, carrier densities 10^{18}–10^{20} cm^{-3} and mobilities up to 5–15 cm^{2}/Vs [195].

Cells that use wide-bandgap absorbers, such as the CIS, are much less sensitive to infrared losses. When aiming to decrease free-carrier absorption in window layers, other than the TCO, one should increase the carrier mobility at the expense of carrier density to decrease the free-carrier absorption [14, 58]. Therefore, highly conductive ZnO nanostructures may not be important for an efficient ETA device. There are other considerations supporting this conclusion as follows.

An intrinsic ZnO is routinely deposited in between the ZnO:Al contact and the buffer layer in the high-efficient thin film chalcopyrite cells [14, 17], for reasons discussed (§3.1.1 Series resistance). The likely advantage is that a ZnO with a low conductivity ′protect′ the V_{OC}, due to lateral inhomogeneities present in the cell, at the expense of introducing tolerable R_S or even to protect from direct shunting between the TCO and the back contact. Thus, it may not be reasonable to pursue a highly conductive ZnO_{NR} as a priority when further developing the ETA cell. Instead, it could be that efforts should be made to ′connect′ the ZnO_{NR} at the bottom, e.g. with an intrinsic ZnO, to decrease possible inhomogeneities and the likely shunting due to gaps in between the ZnO nanorods. It could be reasonable to cover the ZnO_{NR} uniformly with a ′superstrate′ layer e.g. by sol-gel dipping.

One would expect a lower absorber p-doping, or conversely, a higher window n-doping to result in a higher V_{OC} of the cell due to asymmetric expansion of the depletion layer into the absorber, an inherent advantage of the heterojunction design [9, 58, 177]. Since in an ETA cell, the absorber is assumed to be fully or near-depleted, a further increase of the n-doping would result in a higher electric field. In turn, higher field strength may set-off or enhance tunneling recombination (3.1.3. Ideality factor). Therefore, a relatively low n-doping of the window may better accommodate the ETA cell performance; and a highly doped ZnO_{NR} layer should not be considered a priority when aiming to decrease series resistance and developing the all-layers-sprayed ETA cell.

These considerations are not to be taken universally. Further experiments are needed to confirm statements above. Extensive simulations may not lead to a valid result due to enormous amount of unknown parameters required; therefore, an empirical route is preferred. Again, at this stage of studies, it would be inept to start optimizing ZnO_{NR} electrical properties since there are other, more obvious and dominant, causes of poor performance.

For comparison, as determined by infrared reflectance, carrier concentrations of 10^{20} and 10^{21} cm^{-3} and a mobility of 23 and 12 cm^2/Vs, respectively, are reported for ZnO nanowires when undoped and doped by aluminium, as deposited by electrodeposition [44, 76]. For potential dye cell application, ZnO nanowires grown on FTO were reported with carrier density of 10^{18} cm^{-3} and a mobility of 1–5 cm^2/Vs. The wires were considered good electrical conductors well suited for potential dye cell application [71]. This is due to larger mobility of carriers in the highly-crystalline channels, when compared to the slow diffusive transport in a conventional TiO_2 nanoparticle/dye suspension, despite the lower surface areas provided by nanowires. Another study confirms that the use of ZnO nanorods with no grain boundaries, instead of TiO_2 particles, is preferable and that relatively low carrier densities in the range of 10^{17} to 10^{18} cm^{-3} would especially be suitable for ETA application to decrease tunneling probability [74]. Such values are accessible by spray and close to those determined in the sprayed ZnO nanorods showing carrier densities 10^{15}–10^{17} cm^{-3} as was shown in [VI].

Morphological properties of ZnO_{NR} layers for ETA cell application

The internal surface area of TiO_2 particles is several hundred times higher when compared to a planar layer [36]. For the ZnO nanorods, the ratio is at least an order of magnitude lower [38, 71, 93]. The use of nanostructures, such as ZnO_{NR}, are nevertheless being also studied as a possible alternative for dye cell application due to favorable electron transport that is expected to be orders of magnitude higher from that in a random nanocrystalline particle network [71]. For an ETA cell, the absorption coefficient is much higher compared to dyes, thus, a very high internal surface is not required, and the ZnO nanowires, -rods, -pillars offer an excellent solution for increasing the effective area of absorbers [26, 74]. Another distinguished feature is that the solid-state conductors used in an ETA cell support collection by drift, whereas in dye cells this mechanism is obstructed by the electrolyte that screens macroscopic electric fields [2, 27, 71, 74].

Following the last arguments, one may wonder what the optimum nanorod length is for ETA solar cell use, and what the criteria are for choosing a specific morphology, that is length and aspect ratio, of the nanorods. In this work, the optimum ZnO nanorod length was ca 500–600 nm (Figure 21) whereas it is not yet precisely clear why cells with longer rods show inferior efficiency (Table 4). The smaller V_{OC}, when longer rod are used, have been mostly attributed to increased interface recombination; whereas the opposite tendency of V_{OC} and J_{SC} while increasing the surface area is considered a general limiting factor of the ETA cells [33, 77]. Another reason could be that a conformal coating of the ZnO_{NR} with an absorber is more difficult when longer rods have been used. Other possible causes were presented (§3.1.5. Open-circuit voltage).

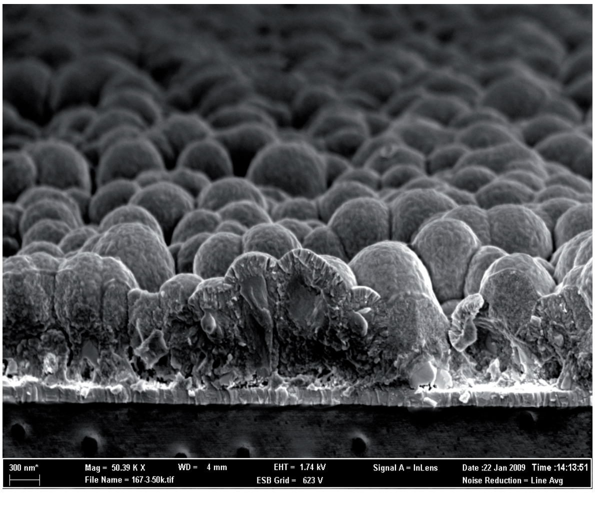

Figure 21. SEM image of sprayed ETA cell that use ZnO_{NR} layer with height of ca 600 nm, and has V_{OC}=420 mV, J_{SC}= 16.7 mA/cm^2, FF = 58.0 % and η = 4.0 % [V].

An efficiency of 6.1% has been reported for a cell based on ZnO nanorod layer covered with a-Si:H, whereas the use of nanorods with the length of 1800 nm instead of 600 nm gave only a marginal improvement in the current, a drop in the FF and efficiency; ultimately yielding highest cell efficiencies by using nanorods with lengths 600 nm and an absorber thickness of 200 nm. These results resemble that in Table 4. At the same time, significant absorption enhancement has been reported at the red side of the absorption spectra when increasing the surface roughness [54, 77] which agrees with that observed in Figure 6. As a counter example, Li et al. reported an *increase* of efficiency from 4.3% to 4.7% when ZnO nanorod length was increased from 1 to 2 µm in a cell that uses a 150 nm thick a-Si:H absorber layer deposited by plasma enhanced chemical vapor deposition [127].

Another factor that influences the scattering efficiency is the particle size when compared to the wavelength of the incident light [129]. If the characteristic size of the scattering particles is much smaller, e.g. 50 nm, the scattering effect is neglible; whereas for sizes comparable to wavelength the scattering is expected to be highest [44, 129, 196]. Thus, sub-micron sized, and a wide dispersion of particle sizes would seem the best solution to attack a broad region of visible wavelengths as shown for the dye cells that use aggregates of hierarchical nanostructures [129, 196]. However, for the dye cells, larger particles significantly reduce cell output due to reduced internal surface area. Ultimately, whether a DSSC or a SSSC, a trade-off would be expected between large internal surface area via the use of smaller particles versus the carrier transport via larger continuous conductive paths as well as better scattering properties [18, 33, 49].

In case of the sprayed ETA cell herein, a length of 500–600 nm could therefore be considered optimum in sense of the solar spectrum. However, a possible size distribution of the vertically standing nanorods could lead to inhomogeneous coverage of the rods by buffer/absorber, and thus, conflict the requirement of locally homogeneous cell output. And finally, although the CSP is an efficient method to cover nanorods that have moderate length and aspect ratio, a uniform coverage of densely packed long rods with an absorber is doubtful, unless adapting for the time-consuming ALD. Thus, various factors affect the choice of ZnO morphology for solar cell use. In case of the sprayed ETA cell herein, development has mostly followed the empirical route.

Another consideration for using a nanorod instead of a nanoparticle window layer is the need for the impregnation of the electron conductor and the absorber with a counter-electrode. For example, polymers are reported to suffer from insufficient penetration into the mesoporous oxide of the dye or hybrid cells [4, 18, 197, 198]. In case of the ETA cells, penetration of the solid hole conductor is higher when larger TiO_2 particles are used, yielding a better performance of the respective cell [27], or when thinner TiO_2 layers are used [32]. Likewise, we expect the infiltration of a future-candidate hole-conductor into the sprayed ETA cell to be acceptable, due to much larger spacings available between the ZnO nanorods. However, it seems that recombination through the substrate is an issue for majority of solid state cells that use hole transport media [28]. Therefore, the use of a shunt-blocking compact layer between, below, or, on top of the nanorods should precede any attempts to achieve a high gap-filling ability.

3.2.4. Summary of materials studies

The CIS absorber layers were grown at lowest applicable temperature of 250°C for the spray method. Two solutions were used: ′stoichiometrical′ with Cu/In molar ratio 1:1 and slightly Cu-rich solutions with Cu/In molar ratio 1.1:1. The as-deposited films from ′stoichiometrical′ solutions had an extra phase, presumably $CuIn_5S_8$ based on XRD and Raman results. No oxygen was present as evaluated by XPS; however, 3–4% of chlorine residue was present according to EDX. Raman spectra reveal peak that belong to Cu_XS phase after 10 minutes of annealing of CIS films deposited using Cu/In ratio of 1.1/1, and after 60 minutes of annealing of films that used Cu/In ratio of 1/1. Thus, we presume that the concentration of Cu_XS is higher in the films deposited using 1.1/1 solutions. Throughout the 5–60 minutes of annealing time percentage of ordered CIS phase remains higher in the films deposited from ′stoichiometrical′ solutions (up to 76%), whereas the crystallite sizes remained higher (up to 90 nm) in films deposited from the Cu-rich solutions. The latter could be explained based on a larger concentration of Cu_XS in these films. The presence of the Cu_XS phase is clearly a disadvantage for solar cell application.

The indium sulfide films deposited by spray consist of single phase β-In_2S_3 with chlorine residues. The chlorine residues are 7 and 3% at growth temperatures of 205 to 320°C and further decrease to 4.3 or 2.1%, respectively, when annealed. Structural improvements are present when the films are annealed in H_2S. We observe a significant increase of the quality (ordering, relieved stress) of the lattice with octahedrally coordinated indium, increase of the lattice parameter of β-In_2S_3 toward the expected value, and an increase of stoichiometry. The relative changes of the crystal quality remain larger when annealing films with the lower growth temperature of 205°C. Still, the films grown at 320°C remain superior in sense of crystal quality as determined by Raman and XRD. The use of alcoholic instead of aqueous solutions allow to use somewhat lower substrate temperatures while retaining film quality similar as evaluated by Raman results. Although no secondary crystalline phases are present beside the β-In_2S_3, the chlorine residues are likely to be a disadvantage for solar cell application.

The quality of ZnO_{NR} layers when grown by spray were evaluated by photoluminescence. The use of ITO as substrate results in a significantly improved the crystal quality of ZnO_{NR} layers when compared to the use of soda-lime glass. The defect density in ZnO_{NR} decreases when the growth temperature is increased from 480°C to 550°C. At 480°C, alcoholic solutions have to be used to retain the surface morphology similar to that in films grown from aqueous solution at 550°C. Carrier concentration in ZnO_{NR} can be increased from 10^{15} cm^{-3} when grown at 550°C up to 10^{17} cm^{-3} when grown at 480°C, in correlation with defect studies from photoluminescence. The optical and electrical properties are sufficient, and are not likely to restrict the sprayed ETA cell performance.

4. CONCLUSIONS and OUTLOOK

A low-cost $ZnO_{NR}/In_2S_3/CuInS_2$ solar cell by chemical spray that uses extremely thin In_2S_3 buffer and $CuInS_2$ absorber layers infiltrated in between ZnO nanorods, was characterized:

1. The use of a structured ZnO_{NR} layer allowed to roughly double the light absorption ability and resulting current densities in the cell, and to increase the conversion efficiency of the cell by a factor of 1.5 when compared to a planar reference cell. External quantum efficiency is as high as 70% in the structured versus 35% in the reference cell. The length of nanorods in the ZnO_{NR} layer has been optimized to ca 600 nm in the present configuration. The series resistance of the cell decreases from 4 Ωcm^2 at 0.5 mW/cm^2 irradiance down to 2 Ωcm^2 at 100 mW/cm^2 irradiance.

2. Shunt conductance, indicative of leakage in the cell, is photosensitive and increases several orders in magnitude when increasing the irradiance. The photosensitivity could be explained with the presence of In_2S_3:Cu layer at the absorber/buffer interface. The copper, as an unintentional dopant in the buffer, is likely to originate from unreacted Cu_XS in the absorber.

3. In the structured cell, the absorber quality as well as the shunt photosensitivity was lower when compared to the reference cell with planar ZnO. These observations led to the assumption that the absorber growth temperature, and thus outdiffusion of copper is lower in case of using the ZnO_{NR} window, which lead to a higher concentration of Cu_XS residues in the absorber of the structured cell.

4. The absorption edge of the nanostructured cell is 1.3 eV, lower from that in the planar reference cell with 1.5 eV. A speculative explanation was provided based on $CuIn_5S_8$ formation at the expense of the buffer layer, owing to the copper diffusion.

5. Carrier tunneling is a significant contributor to carrier recombination of the cell in dark conditions, in particular for the cell based on the ZnO_{NR} layer that has a thinner absorber. A higher concentration of Cu_XS is a likely factor that could contribute to tunneling in the lower quality absorber of the structured cell. As the irradiance increases, cell output deteriorates, indicated by higher ideality factors. At illuminated conditions, the recombination is thermally activated. Thus, at illuminated conditions the whole cell behavior is different from that in the dark.

Based on materials studies, following conclusions can be drawn:

6. The CIS studies confirm that Cu_XS residues, which can be removed by etching in KCN, are present on the surface of the as-deposited at 250°C films. The use of Cu/In molar ratio 1/1 in the spray solution results in an additional phase, presumably $CuIn_5S_8$ in the as-deposited films that is removed during annealing H_2S. The films as-deposited using slightly copper rich solutions with Cu/In molar ratio of 1.1/1 consist of CIS only as determined by XRD. After annealing in H_2S, films from either solution had residues of Cu_XS as determined by Raman.

7. The indium sulfide films grown at 205 to 320°C by spray consist of single phase β-In_2S_3 with chlorine residues. Films deposited at 320°C are with higher quality. When annealing in H_2S, we observe a significant increase of the quality (ordering, relieved stress) of the lattice with octahedrally coordinated indium, increase of the lattice parameter of β-In_2S_3 toward the expected value, an increase of stoichiometry and decrease of chlorine residues down to 2.1%. The use of alcoholic instead of aqueous solution allows to lower substrate temperatures while retaining film quality.

8. The ZnO_{NR} layers consist of high quality hexagonal nanorod crystals, with (002) plane oriented parallel to substrate, when deposited onto ITO at 550°C; the use of glass substrate result in layers with a lower quality. The use of alcoholic spray solution is needed to sustain the morphology of the layers when growth temperature is lowered to 480°C. The carrier density in the nanorods increase from 10^{15} to 10^{17} cm^{-3} when growth temperature is lowered from 550°C to 480°C, in correlation with increased defect density in the layers.

Further ambitions for developing the sprayed cell

Some possible development routes of the sprayed cell have already been hinted: the use of another, preferably Cu-free absorber; the search for a possibility to either ′connect′ the ZnO nanorod gaps with a filler material, or to use a dense compact ZnO layer as the substrate for ZnO_{NR}; to introduce a hole-conductor; and to use a metallic back-contact. In sense of the cost, a significant drawback of the cell is the use of ITO as the front contact. This is the most expensive part of the cell and should, in long term, be replaced with a low cost alternative, ideally ZnO:In by spray to realize the truly all-layers-sprayed, all-solid-state inorganic cell with the extremely-thin-absorber at a very-low-cost.

Operational stability is usually not a concern for all-inorganic cells. In laboratory conditions in air, no deterioration was present in the studied cell output for several years. However, light soaking for several hundred hours has not been studied in the sprayed cells. A significant problem though is the weary graphite-based back contact which was applied by hand at room temperature, usually with no treatment. Although robust for measurements, we suspect poor wetting and long-term adhesion problems; some results also indicate poor suitability for low-temperature electrical measurements. The area-normalized series resistance, that nevertheless shows some variance with area, is an indicator that the back-contact is not suitable. Metallic back contact should be used in a longer term.

The physical characterization methods and models used were well-established standard methods or, some, considered as ′advanced′ at most. In future, the use of additional methods could be advised such as time-resolved photoluminescence for carrier lifetime measurements, drive level capacitance profiling for carrier profiling of the absorber; determination of band-diagram and the possible discontinuities of the bands by photoelectron spectroscopy; and electron-beam induced current for detailed visualization of the junction behavior, or light-beam induced current for visualization of the spatial homogeneity of the cell output. Also, we have not yet published any results based on the cell output at varied angles of the incident light.

ACKNOWLEDGEMENTS

My gratitude to Dr. Malle Krunks, Leading Research Scientist and Laboratory Manager, for her guidance during my doctoral studies. I am thankful to Dr. Arvo Mere for technical supervision, to Dr. Atanas Katerski for solar cell and CIS preparation, to Dr. Tatjana Dedova for deposition of ZnO layers, to Dr. Kairi Otto for deposition of In_2S_3, to Prof. Jüri Krustok for discussions, to Mati Danilson and Taavi Raadik for support with Raman and photoluminescence measurements, to Dr. Valdek Mikli for SEM and EDX analysis and to Dr. Olga Volobujeva for SEM analysis.

I am grateful to Prof. Marc Burgelman for the invitation to ELIS and for the availability of the measurement setups. With Aimi Abass I had helpful discussions and he made me feel welcome in the ELIS Institute in the Ghent University. I want to thank Dr. Koen Decock and Dr. Samira Khelifi for sharing their knowledge on solar cell characterization.

I wish to thank Prof. Andres Öpik, the Dean of the Faculty of Chemical and Materials Technology and the Director of the doctoral school "Functional materials and technologies" in Tallinn University of Technology for providing the opportunity to participate in the PhD studies of the faculty and in the graduate school; and Prof. Enn Mellikov, Head of the Department of Materials Science, for the opportunity to use high-end research equipment within the Department.

The work is financially supported by Estonian Ministry of Education and Research (IUT19-4 and SF0140092s08); Estonian Science Foundation (ETF9081, ETF6954); European Union through the European Regional Development Fund: Project TK114 (Centre of Excellence “Mesosystems: Theory and Applications”, TK114, 3.2.0101.11-0029) and AR12118 (“Efficient plasmonic absorbers for solar cells”, 3.2.1101.12-0023); graduate school “Functional materials and technologies” receiving funding from the European Social Fund under Project 1.2.0401.09-0079 in Estonia; and European Social Fund’s Doctoral Studies and Internationalisation Programme DoRa.

ABSTRACT

The conventional electrical power sources, although cheaper per unit power, have a huge environmental impact. Solar cells do not pollute when converting energy, a factor not usually accounted for price calculations. The use of low-cost technology, such as the chemical spray pyrolysis, is of very high importance when an electronic device and related technology should be scaled up to sustain the growing populations, households and industry for power conversion.

The doctoral thesis is based on 6 publications. In the thesis, an inorganic $ZnO_{NR}/In_2S_3/CuInS_2$ solar cell by spray with an extremely thin absorber (ETA) is thoroughly investigated, where ZnO_{NR} stands for ZnO nanorods. This experimental work aims to characterize the cell and the relevant materials deposited and treated at various conditions. For cell characterization, we used current-voltage characteristics, external quantum efficiency and admittance spectroscopy. We used XRD, EDX, SEM, photoluminescence and Raman spectroscopy for materials′ studies. The thin films and solar cells were prepared in the Laboratory of Thin Film Chemical Technologies at the Department of Materials Science, Tallinn University of Technology (TUT). The author did most of the measurements in the Department of Materials Science of TUT, while an irreplaceable part of the data was obtained by the author in the Electronics and Information Systems department (ELIS), Ghent University.

The optimized cell with 600 nm thick ZnO_{NR} layer has a higher absorption ability, up to twice larger current density and a higher light-to-electricity conversion efficiency when compared to a flat reference cell. High series resistance is present in both cells, and current losses due to shunts increase with irradiance. The use of ZnO nanorod layer, when compared to use of planar ZnO, results in a cell with: (1) notably higher current densities, yet lowered voltages; (2) somewhat higher series resistance but notably higher shunt-conductivity; (3) significantly lower photosensitivity of shunts, yet higher photosensitivity of carrier recombination; (4) significantly higher recombination losses due to carrier tunneling; (5) higher defect densities in $CuInS_2$ absorber material; (6) lower than expected (1.5 eV) absorption edge at 1.3 eV. Studies of $CuInS_2$ absorber films, when grown ex-situ as separate layers, confirm that Cu_XS is present in the surface and in the bulk of the $CuInS_2$ films grown at 250°C onto glass. Cells that use planar ZnO deteriorate when $CuInS_2$ growth temperature is elevated from 250°C to 320°C. Based on the results, we propose hypotheses regarding the cell with ZnO nanorods: (i) the higher current densities can be attributed to the ability of ZnO_{NR} to scatter light and to assist light absorption; (ii) growth temperature of $CuInS_2$ is supposedly lower in the cell based on ZnO nanorods; (iii) copper is released from Cu_XS residues in absorber and diffuses towards the pre-grown In_2S_3 layer; (iv) the unintentional doping causes photoconductivity of the buffer, and deterioration of the cell output when increasing irradiation on the cells; (v) rate of Cu diffusion is supposedly lower in cells with ZnO nanorods layer; (vi) concentration of Cu_XS residues is likely to be higher in the absorber material of the structured cell (vii) formation of $CuIn_5S_8$ at the expense of

In_2S_3 is probable in the structured cell. Nevertheless, the outlook is very promising. To eliminate problems associated with Cu diffusion, binary compounds like Sb_2S_3 or SnS for use as absorber material are considered to further develop the low-cost solar cell by the CSP.

The indium sulfide layers when grown in the ranges of 205 to 320°C consist of β-In_2S_3 phase and have chlorine residues due to the precursor used. Although no secondary crystalline phases are present beside the β-In_2S_3, the chlorine residues are likely to be a disadvantage for solar cell application. The use of higher growth temperatures and post-deposition annealing in for 30 min at 500°C allows to reduce the chlorine content to 2.1 at.%. Also, we observe a significant increase of the β-In_2S_3 quality (ordering, relieved stress) of the lattice with octahedrally coordinated indium, increase of the lattice parameters of β-In_2S_3 toward the expected values, and an increase of stoichiometry. The relative change in the structural quality is larger when annealing films with the lower growth temperature of 205°C. Still, the films grown at 320°C remain superior in sense of crystal quality. The use of alcohol, added in the aqueous solutions, allows to use lower substrate temperatures while retaining crystal ordering of the film, and thus the structural quality.

The ZnO_{NR} layers consist of high quality c-axis oriented hexagonal nanorod crystals when deposited onto ITO at 550°C. The use of soda-lime glass substrate results in ZnO_{NR} layers with a lower quality. The addition of alcohol in the aqueous spray solution is needed to sustain the morphology of the layers when growth temperature is lowered to 480°C. The carrier density in the nanorods increases from 10^{15} to 10^{17} cm^{-3} when growth temperature is lowered from 550°C to 480°C, in correlation with increased defect density in the layers. The optical and electrical properties of the ZnO_{NR} layers are adequate, and not likely to restrict the performance of the sprayed cell.

KOKKUVÕTE

Päikesepatareide kasutamine on üks säästlikumaid viise rohelise elektrienergia tootmiseks. Konventsionaalsed elektrienergia pakkujad ei arvesta oma hinnas kaudseid ja tihti pöördumatuid keskkonna mõjutusi. Sellise “odava” energia tarbimine on pelgalt illusioon ja osutub inimkonnale pikas plaanis väga kalliks. Kuid hoolimata sellest kriitikast, nõuab ka päikesepatareide laialdasem kasutuselevõtt nende hinna alandamist. Lihtsad ja odavad tehnoloogiad on võtmesõna, et päikesepatareid jõuaksid tavakasutusse kodudes ning tööstuses. Pihustuspürolüüs on üks nendest meetoditest, mille abil päikesepatarei tootmise hinda oluliselt alandada.

Doktoritöö põhineb kuuel publikatsioonil. Uurisin põhjalikult lihtsal ja odaval keemilise pihustuspürolüüsi meetodil valmistatud $ZnO_{NR}/In_2S_3/CuInS_2$ päikesepatarei omadusi, kus ZnO_{NR} tähistab nanovardaid. Kasutatud absorbermaterjal ($CuInS_2$) on oluliselt õhem ning madalama kvaliteediga, seega odavam kui tootmises olevatel päikesepatareidel. Antud meetod päikesepatarei sadestamiseks on uudne ning päikesepatarei sellises konfiguratsioonis väga vähe uuritud. Töö eesmärk oli iseloomustada pihustuspürolüüsi meetodil valmistatud päikesepatareid ning erinevatel sadestus- ja töötlustingimustel valmistatud koostismaterjalide omadusi. Päikesepatarei iseloomustamiseks kasutasin volt-amper karakteristikuid, kvantefektiivsust ning näivjuhtivuse spektroskoopiat. Materjalide iseloomustamiseks kasutati XRD, EDX, SEM meetodeid, fotoluminestsents ning Raman spektroskoopiat. Õhukesed kiled ja päikesepatareid valmistati Keemiliste Kiletehnoloogiate Teaduslaboratooriumis (Materjaliteaduse Instituut, Tallinna Tehnikaülikool). Samuti viidi TTÜ-s läbi enamik mõõtmisi, ühed olulisemad katseandmed mõõtis autor välislaboris (Electronics and Information Systems department (ELIS), Ghent University).

Struktureeritud ZnO_{NR} nanovarrastel põhineva kihi kasutamisega õhukese pideva ZnO kile asemel suureneb päikesepatarei neeldumisvõime, voolutihedus tõuseb kuni kahekordseks ning suureneb valguse elektriks muundamise efektiivsus. Uuritud päikesepatarei konfiguratsiooni jaoks oli ZnO_{NR} kihi optimaalne paksus 600 nm. Mõlemas päikesepatareis on olulised voolukaod järjestiktakistuse ning lekkevoolu tõttu, viimane suureneb oluliselt valgustus-intensiivsuse kasvades. Struktuurse päikesepatarei omadused, võrreldes tasapinnalise päikesepatareiga, on järgmised: (1) oluliselt kõrgem lühisvool, kuid alanenud avatud ahela pinge; (2) suurem järjestiktakistus ja oluliselt suurem lekkevool; (3) oluliselt madalam lekkevoolu fototundlikkus, kuid kõrgem fototundlikkus laengukandjate rekombinatsiooni mõttes; (4) oluliselt suuremad rekombinatsioonilised kaod laengukandjate tunnelleerumise tõttu; (5) suurem absorbermaterjali defektsus; (6) oodatavast (1.5 eV) väiksem neeldumispiir 1.3 eV. Lisaks näitab *ex-situ* absorbermaterjali uuring, et 250 °C sadestatud $CuInS_2$ sisaldab Cu_XS faasi nii pinnas kui kile sees. Päikesepatarei omadused tasapinnalise ZnO aknamaterjali korral halvenevad juhul, kui absorbermaterjali kasvutemperatuuri tõsta (250 °C kuni

320 °C). Sellised tähelepanekud võimaldavad meil püstitada järgmised hüpoteesid struktuurse päikesepatarei kohta: (i) suurenenud voolutihedus on põhjustatud suurenenud valguse hajutamisest ning neeldumisest absorberis ZnO_{NR} kihi tõttu; (ii) absorbermaterjali kasvutemperatuur on oletatavalt madalam ZnO nanovarrastel põhinevas päikesepatareis; (iii) vask, mis pärineb Cu_XS lisafaasist absorberis, difundeerub In_2S_3 kihti; (iv) legeerimise tulemusel muutub In_2S_3 elektriline juhtivus fototundlikuks ning põhjustab päikesepatarei omaduste halvenemist valgustus-intensiivsuse kasvamisel; (v) vase difundeerumise kiirus on oletatavalt madalam ZnO_{NR} põhinevas päikesepatareis; (vi) lisafaaside (Cu_XS) kontsentratsioon struktuurse päikesepatarei absorbermaterjalis on tõenäoliselt kõrgem; (vii) $CuIn_5S_8$ moodustumine absorberi ja In_2S_3 piirpinnal In_2S_3 arvelt on tõenäoline. Need järeldused ja oletused võimaldavad meil pihustuspürolüüsi meetodil valmistatud odavat päikesepatareid edasi arendada. Vase difusiooni võimaldab vältida Sb_2S_3 või SnS kasutamine absorberina.

Indiumsulfiidkile, mis sadestati temperatuuridel 205 kuni 320 °C, koosneb β-In_2S_3 faasist, mis sisaldab lähteainest pärinevat kloori. Hoolimata suhteliselt puhtast materjalist, on kloori sisaldus pigem mittesoovitav nähtus kile rakendamiseks päikesepatareis. Kõrgem kasvutemperatuur või järelkuumutamine (30 min, 500 °C) viib kloori sisalduse madalamaks (2.1 at.%); samuti suureneb oluliselt β-In_2S_3 kristallis indiumi oktaeedriline korrastatus ning vähenevad pinged kiles, β-In_2S_3 kristalli võreparameetrid suurenevad sobivalt ning paraneb stohhiömeetria. Kuigi nimetatud muutused kile struktuurses kvaliteedis on suuremad 205 °C juures kasvatatud kilede järelkuumutamisel, on 320 °C juures kasvatatud kiled paremate omadustega ka peale järeltöötlust. Lähteaine vesilahus, millele on lisatud alkoholi, võimaldab kasutada madalamat substraadi temperatuuri β-In_2S_3 kasvatamiseks ja säilitada materjali korrastatust ning seega kile kvaliteeti struktuurses mõttes.

Nanovarrastest koosnevad ZnO_{NR} kihid, mis on kasvatatud ITO elektroodile 550 °C temperatuuril, koosnevad c-teljeliselt orienteeritud ning optiliselt kõrge kvaliteediga heksagonaalsetest kristallidest. Oluliselt madalama kvaliteediga on klaasile kasvatatud kihid. Lähteaine lahus, mis sisaldab alkoholi vesilahuses, võimaldab kasutada madalamat sadestustemperatuuri (480 °C) nanovarraste kasvatamiseks. Laengukandjate kontsentratsioon nanovarrastes on vahemikus 10^{15} kuni 10^{17} cm^{-3}, mis vastab suurenenud defektsusele kui sadestustemperatuuri alandada 550 °C kuni 480 °C. Nanovarraste optilised ning elektrilised omadused on sobilikud antud tüüpi päikesepatareis rakendamiseks.

REFERENCES

[1] K. Durose, S.E. Asher, W. Jaegermann, D. Levi, B.E. McCandless, W. Metzger, H. Moutinho, P.D. Paulson, C.L. Perkins, J.R. Sites, G. Teeter, M. Terheggen, Physical characterization of thin-film solar cells, Prog. Photovolt: Res. Appl., 12 (2004) 177-217.

[2] B.A. Gregg, Excitonic Solar Cells, J. Phys. Chem. B, 107 (2003) 4688-4698.

[3] K. Ernst, A. Belaidi, R. Könenkamp, Solar cell with extremely thin absorber on highly structured substrate, Semicond. Sci. Technol., 18 (2003) 475-479.

[4] J.A. Chang, J.H. Rhee, S.H. Im, Y.H. Lee, H.-j. Kim, S.I. Seok, M.K. Nazeeruddin, M. Gratzel, High-Performance Nanostructured Inorganic−Organic Heterojunction Solar Cells, Nano Lett., 10 (2010) 2609-2612.

[5] R. Scheer, H.W. Schock, Chalcogenide Photovoltaics: Physics Technologies, and Thin Film Devices, Wiley-VCH, Weinheim, 2011.

[6] R. Scheer, T. Walter, H.W. Schock, M.L. Fearheiley, H.J. Lewerenz, $CuInS_2$ based thin film solar cell with 10.2% efficiency, Appl. Phys. Lett., 63 (1993) 3294-3296.

[7] R. Klenk, Characterisation and modelling of chalcopyrite solar cells, Thin Solid Films, 387 (2001) 135-140.

[8] V. Nadenau, D. Hariskos, H.-W. Schock, M. Krejci, F.-J. Haug, A.N. Tiwari, H. Zogg, G. Kostorz, Microstructural study of the $CdS/CuGaSe_2$ interfacial region in $CuGaSe_2$ thin film solar cells, J. Appl. Phys., 85 (1999) 534-542.

[9] I. Hengel, A. Neisser, R. Klenk, M.C. Lux-Steiner, Current transport in $CuInS_2$:Ga/Cds/ZnO – solar cells, Thin Solid Films, 361–362 (2000) 458-462.

[10] C. Grasso, M. Burgelman, Theoretical study on the effect of an intermediate layer in CIS-based ETA-solar cells, Thin Solid Films, 451–452 (2004) 156-159.

[11] R. Scheer, Open questions after 20 years of $CuInS_2$ research, Prog. Photovolt: Res. Appl., 20 (2012) 507-511.

[12] G.F. Brown, J. Wu, Third generation photovoltaics, Laser Photonics Rev., 3 (2009) 394-405.

[13] G. Conibeer, Third-generation photovoltaics, Mater. Today, 10 (2007) 42-50.

[14] T.M. Razykov, C.S. Ferekides, D. Morel, E. Stefanakos, H.S. Ullal, H.M. Upadhyaya, Solar photovoltaic electricity: Current status and future prospects, Sol. Energy, 85 (2011) 1580-1608.

[15] C. Adrian, B. Stephan, P. Fabian, B. Patrick, G. Christina, R.U. Alexander, F. Carolin, K. Lukas, P. Julian, S. Sieghard, V. Rajneesh, N. Shiro, E.R. Yaroslav, B. Gerhard, N.T. Ayodhya, Highly efficient Cu(In,Ga)Se_2 solar cells grown on flexible polymer films, Nat. Mater., 10 (2011) 857-861.

[16] U. Rau, H.W. Schock, Electronic properties of Cu(In,Ga)Se_2 heterojunction solar cells–recent achievements, current understanding, and future challenges, Appl Phys A, 69 (1999) 131-147.

[17] P. Jackson, D. Hariskos, E. Lotter, S. Paetel, R. Wuerz, R. Menner, W. Wischmann, M. Powalla, New world record efficiency for Cu(In,Ga)Se_2 thin-film solar cells beyond 20%, Prog. Photovolt: Res. Appl., 19 (2011) 894-897.

[18] M. Wright, A. Uddin, Organic—inorganic hybrid solar cells: A comparative review, Sol. Energy Mater. Sol. Cells, 107 (2012) 87-111.

[19] K. Taretto, U. Rau, Modeling extremely thin absorber solar cells for optimized design, Prog. Photovolt: Res. Appl., 12 (2004) 573-591.

[20] M.A. Green, K. Emery, Y. Hishikawa, W. Warta, E.D. Dunlop, Solar cell efficiency tables (version 43), Prog. Photovolt: Res. Appl., 22 (2014) 1-9.

[21] T.K. Todorov, J. Tang, S. Bag, O. Gunawan, T. Gokmen, Y. Zhu, D.B. Mitzi, Beyond 11% Efficiency: Characteristics of State-of-the-Art $Cu_2ZnSn(S,Se)_4$ Solar Cells, Adv. Energy Mater., 3 (2013) 34-38.

[22] M.A. Green, The path to 25% silicon solar cell efficiency: History of silicon cell evolution, Prog. Photovolt: Res. Appl., 17 (2009) 183-189.

[23] J. Krustok, R. Josepson, M. Danilson, D. Meissner, Temperature dependence of $Cu_2ZnSn(Se_xS_{1-x})4$ monograin solar cells, Solar Energy, 84 (2010) 379-383.

[24] R. Sáez-Araoz, J. Krammer, S. Harndt, T. Koehler, M. Krueger, P. Pistor, A. Jasenek, F. Hergert, M.C. Lux-Steiner, C.-H. Fischer, ILGAR In_2S_3 buffer layers for Cd-free $Cu(In,Ga)(S,Se)_2$ solar cells with certified efficiencies above 16%, Prog. Photovolt: Res. Appl., 20 (2012) 855-861.

[25] G. Brown, P. Stone, J. Woodruff, B. Cardozo, D. Jackrel, Device characteristics of a 17.1% efficient solar cell deposited by a non-vacuum printing method on flexible foil, in: Photovoltaic Spec. Conf. (PVSC), 2012 38th IEEE, 2012, pp. 003230-003233.

[26] I. Mora-Sero, S. Gimenez, F. Fabregat-Santiago, E. Azaceta, R. Tena-Zaera, J. Bisquert, Modeling and characterization of extremely thin absorber (eta) solar cells based on ZnO nanowires, Phys. Chem. Chem. Phys., 13 (2011) 7162-7169.

[27] G. Hodes, D. Cahen, All-Solid-State, Semiconductor-Sensitized Nanoporous Solar Cells, Acc. Chem. Res., 45 (2012) 705-713.

[28] G. Hodes, Comparison of Dye- and Semiconductor-Sensitized Porous Nanocrystalline Liquid Junction Solar Cells, J. Phys. Chem. C, 112 (2008) 17778-17787.

[29] A. Goossens, J. Hofhuis, Spray-deposited $CuInS_2$ solar cells, Nanotechnol., 19 (2008) 424018.

[30] P. Liska, K.R. Thampi, M. Grätzel, D. Brémaud, D. Rudmann, H.M. Upadhyaya, A.N. Tiwari, Nanocrystalline dye-sensitized solar cell/copper indium gallium selenide thin-film tandem showing greater than 15% conversion efficiency, Appl. Phys. Lett., 88 (2006) 203103.

[31] I. Gur, N.A. Fromer, M.L. Geier, A.P. Alivisatos, Air stable all-inorganic nanocrystal solar cells processed from solution, Science, 310 (2005) 462-465.

[32] I. Mora-Seró, J. Bisquert, Breakthroughs in the Development of Semiconductor-Sensitized Solar Cells, J. Phys. Chem. Lett., 1 (2010) 3046-3052.

[33] T. Dittrich, A. Belaidi, A. Ennaoui, Concepts of inorganic solid-state nanostructured solar cells, Sol. Energy Mater. Sol. Cells, 95 (2011) 1527-1536.

[34] W. Cai, X. Gong, Y. Cao, Polymer solar cells: Recent development and possible routes for improvement in the performance, Sol. Energy Mater. Sol. Cells, 94 (2010) 114-127.

[35] S. Esiner, H. van Eersel, M.M. Wienk, R.A.J. Janssen, Triple Junction Polymer Solar Cells for Photoelectrochemical Water Splitting, Advanced Materials, 25 (2013) 2932-2936.

[36] I. Kaiser, K. Ernst, C.H. Fischer, R. Könenkamp, C. Rost, I. Sieber, M.C. Lux-Steiner, The eta-solar cell with $CuInS_2$: A photovoltaic cell concept using an extremely thin absorber (eta), Sol. Energy Mater. Sol. Cells, 67 (2001) 89-96.

[37] K. Ernst, R. Engelhardt, K. Ellmer, C. Kelch, H.J. Muffler, M.C. Lux-Steiner, R. Könenkamp, Contacts to a solar cell with extremely thin CdTe absorber, Thin Solid Films, 387 (2001) 26-28.

[38] C. Lévy-Clément, R. Tena-Zaera, M.A. Ryan, A. Katty, G. Hodes, CdSe-Sensitized p-CuSCN/Nanowire n-ZnO Heterojunctions, Adv. Mater., 17 (2005) 1512-1515.

[39] B. Julian, P. Norman, M. Soo-Jin, H.-B. Robin, G. Peng, K.N. Mohammad, G. Michael, Sequential deposition as a route to high-performance perovskite-sensitized solar cells, Nature, 499 (2013) 316-319.

[40] M.P. Genovese, I.V. Lightcap, P.V. Kamat, Sun-Believable Solar Paint. A Transformative One-Step Approach for Designing Nanocrystalline Solar Cells, ACS Nano, 6 (2011) 865-872.

[41] S.-J. Moon, Y. Itzhaik, J.-H. Yum, S.M. Zakeeruddin, G. Hodes, M. Grätzel, Sb_2S_3-Based Mesoscopic Solar Cell using an Organic Hole Conductor, J. Phys. Chem. Lett., 1 (2010) 1524-1527.

[42] Y. Itzhaik, O. Niitsoo, M. Page, G. Hodes, Sb_2S_3-Sensitized Nanoporous TiO_2 Solar Cells, J. Phys. Chem. C, 113 (2009) 4254-4256.

[43] O. Niitsoo, S.K. Sarkar, C. Pejoux, S. Rühle, D. Cahen, G. Hodes, Chemical bath deposited CdS/CdSe-sensitized porous TiO_2 solar cells, J. Photochem. Photobiol., A, 181 (2006) 306-313.

[44] R. Tena-Zaera, M.A. Ryan, A. Katty, G. Hodes, S. Bastide, C. Lévy-Clément, Fabrication and characterization of ZnO nanowires/CdSe/CuSCN eta-solar cell, Comptes Rendus Chimie, 9 (2006) 717-729.

[45] J.A. Chang, S.H. Im, Y.H. Lee, H.-j. Kim, C.-S. Lim, J.H. Heo, S.I. Seok, Panchromatic Photon-Harvesting by Hole-Conducting Materials in Inorganic–Organic Heterojunction Sensitized-Solar Cell through the Formation of Nanostructured Electron Channels, Nano Lett., 12 (2012) 1863-1867.

[46] A. Belaidi, T. Dittrich, D. Kieven, J. Tornow, K. Schwarzburg, M. Lux-Steiner, Influence of the local absorber layer thickness on the performance of ZnO nanorod solar cells, Phys. Status Solidi RRL, 2 (2008) 172-174.

[47] S. Nezu, G. Larramona, C. Choné, A. Jacob, B. Delatouche, D. Péré, C. Moisan, Light Soaking and Gas Effect on Nanocrystalline TiO_2/Sb_2S_3/CuSCN Photovoltaic Cells following Extremely Thin Absorber Concept, J. Phys. Chem. C, 114 (2010) 6854-6859.

[48] M. Krunks, E. Kärber, A. Katerski, K. Otto, I. Oja Acik, T. Dedova, A. Mere, Extremely thin absorber layer solar cells on zinc oxide nanorods by chemical spray, Sol. Energy Mater. Sol. Cells, 94 (2010) 1191-1195.

[49] S. Rühle, M. Shalom, A. Zaban, Quantum-Dot-Sensitized Solar Cells, Chem. Phys. Chem., 11 (2010) 2290-2304.

[50] R. Scheer, R. Klenk, J. Klaer, I. Luck, $CuInS_2$ based thin film photovoltaics, Sol. Energy, 77 (2004) 777-784.

[51] S.S. Hegedus, W.N. Shafarman, Thin-film solar cells: device measurements and analysis, Prog. Photovolt: Res. Appl., 12 (2004) 155-176.

[52] W.K. Metzger, I.L. Repins, M. Romero, P. Dippo, M. Contreras, R. Noufi, D. Levi, Recombination kinetics and stability in polycrystalline $Cu(In,Ga)Se_2$ solar cells, Thin Solid Films, 517 (2009) 2360-2364.

[53] K. Taretto, U. Rau, Influence of built-in voltage in optimized extremely thin absorber solar cells, Thin Solid Films, 480–481 (2005) 447-451.

[54] D. Kieven, T. Dittrich, A. Belaidi, J. Tornow, K. Schwarzburg, N. Allsop, M. Lux-Steiner, Effect of internal surface area on the performance of $ZnO/In_2S_3/CuSCN$ solar cells with extremely thin absorber, Appl. Phys. Lett., 92 (2008) 153107.

[55] T. Dittrich, D. Kieven, A. Belaidi, M. Rusu, J. Tornow, K. Schwarzburg, M.C. Lux-Steiner, Formation of the charge selective contact in solar cells with extremely thin absorber based on ZnO-nanorod/In_2S_3/CuSCN, J. Appl. Phys., 105 (2009) 034509.

[56] T. Dittrich, D. Kieven, M. Rusu, A. Belaidi, J. Tornow, K. Schwarzburg, M. Lux-Steiner, Current-voltage characteristics and transport mechanism of solar cells based on ZnO nanorods/In_2S_3/CuSCN, Appl. Phys. Lett., 93 (2008) 053113.

[57] H. Diepers, Solar cell comprising semiconductive whiskers, US 4099986 A, in: M. Siemens Aktiengesellschaft, Fed. Rep. of Germany (Ed.), 1978.

[58] S. Siebentritt, What limits the efficiency of chalcopyrite solar cells?, Sol. Energy Mater. Sol. Cells, 95 (2011) 1471-1476.

[59] R. Klenk, S. Bakehe, R. Kaigawa, A. Neisser, J. Reiß, M.C. Lux-Steiner, Optimising the open-circuit voltage of $Cu(In,Ga)S_2$ solar cells—design and analysis, Thin Solid Films, 451–452 (2004) 424-429.

[60] A. Polman, H.A. Atwater, Photonic design principles for ultrahigh-efficiency photovoltaics, Nat. Mater., 11 (2012) 174–177.

[61] G.P. Smestad, F.C. Krebs, C.M. Lampert, C.G. Granqvist, K.L. Chopra, X. Mathew, H. Takakura, Reporting solar cell efficiencies in Solar Energy Materials and Solar Cells, Sol. Energy Mater. Sol. Cells, 92 (2008) 371-373.

[62] A. Luque, A. Martí, E. Antolín, C. Tablero, Intermediate bands versus levels in non-radiative recombination, Phys. B, 382 (2006) 320-327.

[63] R. Lucena, I. Aguilera, P. Palacios, P. Wahnon, J.C. Conesa, Synthesis and Spectral Properties of Nanocrystalline V-Substituted In_2S_3, a Novel Material for More Efficient Use of Solar Radiation, Chem. Mater., 20 (2008) 5125-5127.

[64] P. Wahnon, J.C. Conesa, P. Palacios, R. Lucena, I. Aguilera, Y. Seminovski, F. Fresno, V-doped SnS_2: a new intermediate band material for a better use of the solar spectrum, Phys. Chem. Chem. Phys., 13 (2011) 20401-20407.

[65] S. Khelifi, J. Verschraegen, M. Burgelman, A. Belghachi, Numerical simulation of the impurity photovoltaic effect in silicon solar cells, Renewable Energy, 33 (2008) 293-298.

[66] R.R. Chamberlin, J.S. Skarman, Chemical Spray Deposition Process for Inorganic Films, J. Electrochem. Soc., 113 (1966) 86-89.

[67] P.S. Patil, Versatility of chemical spray pyrolysis technique, Mater. Chem. Phys., 59 (1999) 185-198.

[68] J.B. Mooney, S.B. Radding, Spray Pyrolysis Processing, Annu. Rev. Mater. Sci., 12 (1982) 81-101.

[69] P. Pistor, R. Caballero, D. Hariskos, V. Izquierdo-Roca, R. Wächter, S. Schorr, R. Klenk, Quality and stability of compound indium sulphide as source material for buffer layers in Cu(In,Ga)Se solar cells, Sol. Energy Mater. Sol. Cells, 93 (2009) 148-152.

[70] J.C. Fan, K.M. Sreekanth, Z. Xie, S.L. Chang, K.V. Rao, p-Type ZnO materials: Theory, growth, properties and devices, Prog. Mater. Sci., 58 (2013) 874-985.

[71] M. Law, L.E. Greene, J.C. Johnson, R. Saykally, P. Yang, Nanowire dye-sensitized solar cells, Nat. Mater., 4 (2005) 455-459.

[72] U. Rau, M. Schmidt, Electronic properties of ZnO/CdS/Cu(In,Ga)Se_2 solar cells — aspects of heterojunction formation, Thin Solid Films, 387 (2001) 141-146.

[73] W.K. Metzger, I.L. Repins, M.A. Contreras, Long lifetimes in high-efficiency Cu(In,Ga)Se_2 solar cells, Appl. Phys. Lett., 93 (2008) 022110.

[74] J. Tornow, K. Schwarzburg, Transient Electrical Response of Dye-Sensitized ZnO Nanorod Solar Cells, J. Phys. Chem. C, 111 (2007) 8692-8698.

[75] R. Herberholz, M. Igalson, H.W. Schock, Distinction between bulk and interface states in $CuInSe_2$/Cd/ZnO by space charge spectroscopy, J. Appl. Phys., 83 (1998) 318-325.

[76] R. Konenkamp, K. Boedecker, M.C. Lux-Steiner, M. Poschenrieder, F. Zenia, C. Levy-Clement, S. Wagner, Thin film semiconductor deposition on free-standing ZnO columns, Appl. Phys. Lett., 77 (2000) 2575-2577.

[77] C.-I. Ho, W.-C. Liang, D.-J. Yeh, V.-C. Su, P.-C. Yang, S.-Y. Chen, T.-T. Yang, J.-H. Lee, C.-H. Kuan, I.-C. Cheng, S.-C. Lee, Influence of the absorber layer thickness and rod length on the performance of three-dimensional nanorods thin film hydrogenated amorphous silicon solar cells, J. Appl. Phys., 113 (2013) 163106.

[78] T. Dedova, J. Klauson, C. Badre, T. Pauporté, R. Nisumaa, A. Mere, O. Volobujeva, M. Krunks, Chemical spray deposition of zinc oxide nanostructured layers from zinc acetate solutions, phys. status solidi (a), 205 (2008) 2355-2359.

[79] T. Dedova, M. Krunks, M. Grossberg, O. Volobujeva, I. Acik, A novel deposition method to grow ZnO nanorods: Spray pyrolysis, Superlattices Microstruct., 42 (2007) 444 - 450.

[80] T. Dedova, O. Volobujeva, J. Klauson, A. Mere, M. Krunks, ZnO nanorods via spray deposition of solutions containing zinc chloride and thiocarbamide, Nanoscale Res. Lett., 2 (2007) 391 - 396.

[81] M. Krunks, T. Dedova, I. Oja Acik, Spray pyrolysis deposition of zinc oxide nanostructured layers, Thin Solid Films, 515 (2006) 1157 - 1160.

[82] N. Barreau, Indium sulfide and relatives in the world of photovoltaics, Sol. Energy, 83 (2009) 363-371.

[83] S. Marsillac, N.S. Mangale, V. Gade, S.V. Khare, Structural and electronic properties of β-In_2X_3 (X=O, S, Se, Te) using ab initio calculations, Thin Solid Films, 519 (2011) 5679-5683.

[84] I.V. Bodnar, A.G. Karoza, E.A. Kudritskaya, A.G. Smirnova, Vibrational spectra of In_2S_3, $CuIn_5S_8$ and $AgIn_5S_8$ compounds with a spinel structure, J. Appl. Spectrosc., 64 (1997) 279-282.

[85] T. Gödecke, K. Schubert, On the Phase Diagram InS_M, Zeitschrift für Metallkunde, 76 (1985) 358-364.

[86] A.Y. Zavrazhnov, A.V. Naumov, P.V. Anorov, E.G. Goncharov, V.I. Sidei, V.S. Pervov, T-x phase diagram of the In-S system, Inorg. Mater., 42 (2006) 1294-1298.

[87] N. Barreau, A. Mokrani, F. Couzinié-Devy, J. Kessler, Bandgap properties of the indium sulfide thin-films grown by co-evaporation, Thin Solid Films, 517 (2009) 2316-2319.

[88] D. Hariskos, S. Spiering, M. Powalla, Buffer layers in $Cu(In,Ga)Se_2$ solar cells and modules, Thin Solid Films, 480–481 (2005) 99-109.

[89] M. Mathew, M. Gopinath, C.S. Kartha, K. P.Vijayakumar, Y. Kashiwaba, T. Abe, Tin doping in spray pyrolysed indium sulfide thin films for solar cell applications, Sol. Energy, 84 (2010) 888-897.

[90] N.A. Allsop, A. Schönmann, H.J. Muffler, M. Bär, M.C. Lux-Steiner, C.H. Fischer, Spray-ILGAR indium sulfide buffers for $Cu(In,Ga)(S,Se)_2$ solar cells, Prog. Photovolt: Res. Appl., 13 (2005) 607-616.

[91] S. Siebentritt, Alternative buffers for chalcopyrite solar cells, Sol. Energy, 77 (2004) 767-775.

[92] J. Verschraegen, M. Burgelman, J. Penndorf, Temperature dependence of the diode ideality factor in $CuInS_2$-on-Cu-tape solar cells, Thin Solid Films, 480–481 (2005) 307-311.

[93] A. Belaidi, T. Dittrich, D. Kieven, J. Tornow, K. Schwarzburg, M. Kunst, N. Allsop, M.C. Lux-Steiner, S. Gavrilov, ZnO-nanorod arrays for solar cells with extremely thin sulfidic absorber, Sol. Energy Mater. Sol. Cells, 93 (2009) 1033-1036.

[94] K. Decock, S. Khelifi, S. Buecheler, F. Pianezzi, A.N. Tiwari, M. Burgelman, Defect distributions in thin film solar cells deduced from admittance measurements under different bias voltages, J. Appl. Phys., 110 (2011) 063722.

[95] S. Buecheler, F. Pianezzi, C. Fella, A. Chirila, K. Decock, M. Burgelman, A.N. Tiwari, Interface formation between $CuIn_{1-x}Ga_xSe_2$ absorber and In_2S_3 buffer layer deposited by ultrasonic spray pyrolysis, Thin Solid Films, 519 (2011) 7560-7563.

[96] K. Otto, P. Bombicz, J. Madarász, I. Oja Acik, M. Krunks, G. Pokol, Structure and evolved gas analyses (TG/DTA-MS and TG-FTIR) of mer-trichlorotris(thiourea)-indium(III), a precursor for indium sulfide thin films, J. Therm. Anal. Calorim., 105 (2011) 83-91.

[97] K. Otto, I. Oja Acik, K. Tõnsuaadu, A. Mere, M. Krunks, Thermoanalytical study of precursors for In_2S_3 thin films deposited by spray pyrolysis, J. Therm. Anal. Calorim., 105 (2011) 615-623.

[98] K. Otto, A. Katerski, A. Mere, O. Volobujeva, M. Krunks, Spray pyrolysis deposition of indium sulphide thin films, Thin Solid Films, 519 (2011) 3055-3060.

[99] K. Otto, A. Katerski, O. Volobujeva, A. Mere, M. Krunks, Indium sulfide thin films deposited by chemical spray of aqueous and alcoholic solutions, Energy Procedia, 3 (2011) 63-69.

[100] E. Rudigier, T. Enzenhofer, R. Scheer, Determination of the quality of $CuInS_2$-based solar cells combining Raman and photoluminescence spectroscopy, Thin Solid Films, 480–481 (2005) 327-331.

[101] S. Marsillac, M.C. Zouaghi, J.C. Bernède, T. Ben Nasrallah, S. Belgacem, Evolution of the properties of spray-deposited $CuInS_2$ thin films with post-annealing treatment, Sol. Energy Mater. Sol. Cells, 76 (2003) 125-134.

[102] T.T. Thai, P.P. Hung, V.T. Son, V.T. Bich, Optical Properties of $CuInS_2$ Thin Films Prepared by Spray Pyrolysis, Commun. Phys., 22 (2012).

[103] J. Alvarez-García, A. Pérez-Rodríguez, B. Barcones, A. Romano-Rodríguez, J.R. Morante, A. Janotti, S.-H. Wei, R. Scheer, Polymorphism in $CuInS_2$ epilayers: Origin of additional Raman modes, Appl. Phys. Lett., 80 (2002) 562-564.

[104] J. Álvarez-García, B. Barcones, A. Pérez-Rodríguez, A. Romano-Rodríguez, J.R. Morante, A. Janotti, S.-H. Wei, R. Scheer, Vibrational and crystalline properties of polymorphic $CuInC_2$ (C=Se,S) chalcogenides, Phys. Rev. B, 71 (2005) 054303.

[105] J.S.M. Aloysius F. Hepp, John E. Dickman, Michael H.-C. Jin, Kulbinder K. Banger, Christopher V. Kelly, Angel R. Aquino González, Angus A. Rockett, Aerosol-assisted chemical vapor deposited thin films for space photovoltaics, NASA technical memorandum, Cleveland, Ohio, 2006.

[106] S.-H. Wei, S.B. Zhang, A. Zunger, Band structure and stability of zinc-blende-based semiconductor polytypes, Phys. Rev. B, 59 (1999) R2478-R2481.

[107] D.-Y. Lee, J. Kim, Characterization of sprayed $CuInS_2$ films by XRD and Raman spectroscopy measurements, Thin Solid Films, 518 (2010) 6537-6541.

[108] H. Metzner, M. Brüssler, K.D. Husemann, H.J. Lewerenz, Characterization of phases and determination of phase relations in the Cu-In-S system by γ-γ perturbed angular correlations, Phys. Rev. B, 44 (1991) 11614-11623.

[109] B. Barcones, A. Pérez-Rodríguez, L. Calvo-Barrio, A. Romano-Rodríguez, J.R. Morante, E. Rudigier, I. Luck, J. Djordjevic, R. Scheer, In situ and ex situ characterisation of thermally induced crystallisation of $CuInS_2$ thin films for solar cell, Thin Solid Films, 480–481 (2005) 362-366.

[110] I. Oja, M. Nanu, A. Katerski, M. Krunks, A. Mere, J. Raudoja, A. Goossens, Crystal quality studies of $CuInS_2$ films prepared by spray pyrolysis, Thin Solid Films, 480–481 (2005) 82-86.

[111] M. Nanu, L. Reijnen, B. Meester, A. Goossens, J. Schoonman, $CuInS_2$–TiO_2 heterojunctions solar cells obtained by atomic layer deposition, Thin Solid Films, 431–432 (2003) 492-496.

[112] S.B. Zhang, S.-H. Wei, A. Zunger, H. Katayama-Yoshida, Defect physics of the $CuInSe_2$ chalcopyrite semiconductor, Phys. Rev. B, 57 (1998) 9642-9656.

[113] J.D. Harris, K.K. Banger, D.A. Scheiman, M.A. Smith, M.H.C. Jin, A.F. Hepp, Characterization of $CuInS_2$ films prepared by atmospheric pressure spray chemical vapor deposition, Mater. Sci. Eng., B, 98 (2003) 150-155.

[114] M. Nanu, J. Schoonman, A. Goossens, Nanocomposite Three-Dimensional Solar Cells Obtained by Chemical Spray Deposition, Nano Lett., 5 (2005) 1716-1719.

[115] T.K. Todorov, O. Gunawan, T. Gokmen, D.B. Mitzi, Solution-processed Cu(In,Ga)(S,Se)$_2$ absorber yielding a 15.2% efficient solar cell, Prog. Photovolt: Res. Appl., 21 (2013) 82-87.

[116] K. Siemer, J. Klaer, I. Luck, J. Bruns, R. Klenk, D. Bräunig, Efficient CuInS$_2$ solar cells from a rapid thermal process (RTP), Sol. Energy Mater. Sol. Cells, 67 (2001) 159-166.

[117] J. Klaer, I. Luck, A. Boden, R. Klenk, I.G. Perez, R. Scheer, Mini-modules from a CuInS$_2$ baseline process, Thin Solid Films, 431–432 (2003) 534-537.

[118] J. Klaer, J. Bruns, R. Henninger, K. Siemer, R. Klenk, K. Ellmer, D. Bräunig, Efficient CuInS$_2$ thin-film solar cells prepared by a sequential process, Semicond. Sci. Technol., 13 (1998) 1456.

[119] C. Camus, N.A. Allsop, S.E. Gledhill, W. Bohne, J. Röhrich, I. Lauermann, M.C. Lux-Steiner, C.H. Fischer, Properties of Spray ILGAR CuInS$_2$ thin films, Thin Solid Films, 516 (2008) 7026-7030.

[120] D. Braunger, T. Durr, D. Hariskos, C. Koble, T. Walter, N. Wieser, H.W. Schock, Improved open circuit voltage in CuInS$_2$-based solar cells, in: Conf. Rec. IEEE Photovoltaic Spec. Conf., 1996, pp. 1001-1004.

[121] A. Fischereder, T. Rath, W. Haas, H. Amenitsch, D. Schenk, A. Zankel, R. Saf, F. Hofer, G. Trimmel, Investigation of CuInS$_2$ Thin Film Formation by a Low-Temperature Chemical Deposition Method, ACS Appl. Mater. Interfaces, 4 (2011) 382-390.

[122] M. Krunks, O. Bijakina, V. Mikli, H. Rebane, T. Varema, M. Altosaar, E. Mellikov, Sprayed CuInS$_2$ thin films for solar cells: The effect of solution composition and post-deposition treatments, Sol. Energy Mater. Sol. Cells, 69 (2001) 93-98.

[123] M. Krunks, O. Kijatkina, A. Mere, T. Varema, I. Oja, V. Mikli, Sprayed CuInS$_2$ films grown under Cu-rich conditions as absorbers for solar cells, Sol. Energy Mater. Sol. Cells, 87 (2005) 207-214.

[124] M. Krunks, A. Mere, A. Katerski, V. Mikli, J. Krustok, Characterization of sprayed CuInS$_2$ films annealed in hydrogen sulfide atmosphere, Thin Solid Films, 511–512 (2006) 434-438.

[125] A. Katerski, M. Danilson, A. Mere, M. Krunks, Effect of the growth temperature on chemical composition of spray-deposited CuInS$_2$ thin films, Energy Procedia, 2 (2010) 103-107.

[126] M. Burgelman, P. Nollet, Admittance spectroscopy of thin film solar cells, Solid State Ionics, 176 (2005) 2171-2175.

[127] L. Hung-Hsien, P.-Y. Yang, C. Si-Ming, L. Han-Wen, C. Huang-Chung, A Novel Coaxial-Structured Amorphous-Silicon p-i-n Solar Cell With Al-Doped ZnO Nanowires, IEEE Electron Device Lett., 32 (2011) 928-930.

[128] Y.-J. Lee, D.S. Ruby, D.W. Peters, B.B. McKenzie, J.W.P. Hsu, ZnO Nanostructures as Efficient Antireflection Layers in Solar Cells, Nano Lett., 8 (2008) 1501-1505.

[129] Q. Zhang, T.P. Chou, B. Russo, S.A. Jenekhe, G. Cao, Polydisperse Aggregates of ZnO Nanocrystallites: A Method for Energy-Conversion-Efficiency Enhancement in Dye-Sensitized Solar Cells, Adv. Funct. Mater., 18 (2008) 1654-1660.

[130] M. Krunks, A. Katerski, T. Dedova, I. Oja Acik, A. Mere, Nanostructured solar cell based on spray pyrolysis deposited ZnO nanorod array, Sol. Energy Mater. Sol. Cells, 92 (2008) 1016-1019.

[131] I. Oja Acik, A. Katerski, A. Mere, J. Aarik, A. Aidla, T. Dedova, M. Krunks, Nanostructured solar cell by spray pyrolysis: Effect of titania barrier layer on the cell performance, Thin Solid Films, 517 (2009) 2443-2447.

[132] J. Bisquert, I. Mora-Seró, Simulation of Steady-State Characteristics of Dye-Sensitized Solar Cells and the Interpretation of the Diffusion Length, J. Phys. Chem. Lett., 1 (2009) 450-456.

[133] M. Sakhaf, M. Schmeits, Capacitance and conductance of semiconductor heterojunctions with continuous energy distribution of interface states, J. Appl. Phys., 80 (1996) 6839-6848.

[134] L.C. Kimerling, Influence of deep traps on the measurement of free-carrier distributions in semiconductors by junction capacitance techniques, J. Appl. Phys., 45 (1974) 1839-1845.

[135] T. Eisenbarth, T. Unold, R. Caballero, C.A. Kaufmann, H.-W. Schock, Interpretation of admittance, capacitance-voltage, and current-voltage signatures in Cu(In,Ga)Se_2 thin film solar cells, J. Appl. Phys., 107 (2010) 034509.

[136] J.T. Heath, J.D. Cohen, W.N. Shafarman, Bulk and metastable defects in $CuIn_{1-x}Ga_xSe_2$ thin films using drive-level capacitance profiling, J. Appl. Phys., 95 (2004) 1000-1010.

[137] M. Ćwil, M. Igalson, P. Zabierowski, C.A. Kaufmann, A. Neisser, Capacitance profiling in the CIGS solar cells, Thin Solid Films, 515 (2007) 6229-6232.

[138] M. Wolf, H. Rauschenbach, Series resistance effects on solar cell measurements, Adv. Energy Convers., 3 (1963) 455-479.

[139] J. Lauwaert, K. Decock, S. Khelifi, M. Burgelman, A simple correction method for series resistance and inductance on solar cell admittance spectroscopy, Sol. Energy Mater. Sol. Cells, 94 (2010) 966-970.

[140] J.H. Scofield, Effects of series resistance and inductance on solar cell admittance measurements, Sol. Energy Mater. Sol. Cells, 37 (1995) 217-233.

[141] S. Kolodinski, J.H. Werner, T. Wittchen, H.J. Queisser, Quantum efficiencies exceeding unity due to impact ionization in silicon solar cells, Appl. Phys. Lett., 63 (1993) 2405.

[142] R.D. Schaller, M. Sykora, J.M. Pietryga, V.I. Klimov, Seven Excitons at a Cost of One: Redefining the Limits for Conversion Efficiency of Photons into Charge Carriers, Nano Lett., 6 (2006) 424-429.

[143] Z. Djebbour, A. Darga, A. Migan Dubois, D. Mencaraglia, N. Naghavi, J.F. Guillemoles, D. Lincot, Admittance spectroscopy of cadmium free CIGS solar cells heterointerfaces, Thin Solid Films, 511–512 (2006) 320-324.

[144] T. Walter, R. Herberholz, C. Muller, H.W. Schock, Determination of defect distributions from admittance measurements and application to Cu(In,Ga)Se_2 based heterojunctions, J. Appl. Phys., 80 (1996) 4411-4420.

[145] J.R. Sites, J.E. Granata, J.F. Hiltner, Losses due to polycrystallinity in thin-film solar cells, Sol. Energy Mater. Sol. Cells, 55 (1998) 43-50.

[146] W.N. Shafarman, J. Zhu, Effect of substrate temperature and deposition profile on evaporated Cu(InGa)Se_2 films and devices, Thin Solid Films, 361–362 (2000) 473-477.

[147] M. Gloeckler, J.R. Sites, W.K. Metzger, Grain-boundary recombination in Cu(In,Ga)Se_2 solar cells, J. Appl. Phys., 98 (2005) 113704.

[148] Alvarez-Garcia, R. J. Perez, A., R. Romano, J.R. Morante, L. Calvo-Barrio, R. Scheer, R. Klenk, Microstructure and secondary phases in coevaporated $CuInS_2$ films: Dependence on growth temperature and chemical composition, J. Vac. Sci. Technol., A, 19 (2001) 232-239.

[149] J. Álvarez-García, J. Marcos-Ruzafa, A. Pérez-Rodríguez, A. Romano-Rodríguez, J.R. Morante, R. Scheer, MicroRaman scattering from polycrystalline $CuInS_2$ films: structural analysis, Thin Solid Films, 361–362 (2000) 208-212.

[150] I. Oja Acik, K. Otto, M. Krunks, K. Tõnsuaadu, A. Mere, Thermal behaviour of precursors for $CuInS_2$ thin films deposited by spray pyrolysis, J. Therm. Anal. Calorim., 113 (2013) 1455-1465.

[151] P.O. Grabitz, U. Rau, J.H. Werner, A multi-diode model for spatially inhomogeneous solar cells, Thin Solid Films, 487 (2005) 14-18.

[152] J. Reiβ, J. Malmström, A. Werner, I. Henge, R. Klenk, M.C. Lux-Steiner, Current Transport in $CuInS_2$ Solar Cells Depending on Absorber Preparation., Mater. Res. Soc. Symp. Proc. 668, H9.4 (2001).

[153] J. Krustok, R. Josepson, T. Raadik, M. Danilson, Potential fluctuations in $Cu_2ZnSnSe_4$ solar cells studied by temperature dependence of quantum efficiency curves, Phys. B, 405 (2010) 3186-3189.

[154] R. O'Hayre, M. Nanu, J. Schoonman, A. Goossens, Q. Wang, M. Grätzel, The Influence of TiO_2 Particle Size in TiO_2/$CuInS_2$ Nanocomposite Solar Cells, Adv. Funct. Mater., 16 (2006) 1566-1576.

[155] R. O'Hayre, M. Nanu, J. Schoonman, A. Goossens, A parametric study of TiO_2/$CuInS_2$ nanocomposite solar cells: how cell thickness, buffer layer thickness, and TiO_2 particle size affect performance, Nanotechnol., 18 (2007) 055702.

[156] J. Briscoe, S. Dunn, Extremely thin absorber solar cells based on nanostructured semiconductors, Mater. Sci. Technol., 27 (2011) 1741-1756.

[157] A. Katerski, A. Mere, V. Kazlauskiene, J. Miskinis, A. Saar, L. Matisen, A. Kikas, M. Krunks, Surface analysis of spray deposited copper indium disulfide films, Thin Solid Films, 516 (2008) 7110 - 7115.

[158] M. Krunks, E. Mellikov, O. Bijakina, Copper sulfides by chemical spray pyrolysis process, Phys. Scr., T69 (1997) 189-192.

[159] M. Krunks, O. Kijatkina, H. Rebane, I. Oja, V. Mikli, A. Mere, Composition of $CuInS_2$ thin films prepared by spray pyrolysis, Thin Solid Films, 403–404 (2002) 71-75.

[160] A. Katerski, E. Kärber, M. Krunks, V. Mikli, A. Mere, Development of sprayed $CuInS_2$ thin film absorber for nanostructured solar cell, Mater. Res. Soc. Symp. Proc. 1447: mrss12-1447-w10-47, 1447 (2012).

[161] J. Marlein, M. Burgelman, Empirical J-V modelling of CIGS solar cells, in: International workshop on numerical modelling of thin film solar cells, 28-30 March, Gent (Belgium), 2007, pp. 227–233.

[162] E. Kärber, I. Oja Acik, A. Katerski, A. Mere, M. Krunks, Nanostructured solar cell prepared by chemical spray pyrolysis method, in: European Society for Quantum Solar Energy Conversion 2010 Winter workshop, March 7-13, Brigels (Breil), Graubünden (Switzerland), 2010.
[163] G. Hodes, Some problematic practical aspects of semiconductor-sensitized, nanoporous solar cells, in: European Society for Quantum Solar Energy Conversion 2010 Winter workshop, March 7-13, Brigels (Breil), Graubünden (Switzerland), 2010.
[164] M. Gloeckler, J.R. Sites, Apparent quantum efficiency effects in CdTe solar cells, J. Appl. Phys., 95 (2004) 4438-4445.
[165] J.M. Gilles, H. Hatwell, G. Offergeld, J. van Cakenberghe, Photoconductivity in Indium Sulfide, Phys. Status Solidi B, 2 (1962) K73-K77.
[166] J. Marlein, K. Decock, M. Burgelman, Analysis of electrical properties of CIGSSe and Cd-free buffer CIGSSe solar cells, Thin Solid Films, 517 (2009) 2353-2356.
[167] V. Nadenau, U. Rau, A. Jasenek, H.W. Schock, Electronic properties of $CuGaSe_2$-based heterojunction solar cells. Part I. Transport analysis, J. Appl. Phys., 87 (2000) 584-593.
[168] U. Rau, Tunneling-enhanced recombination in $Cu(In,Ga)Se_2$ heterojunction solar cells, Appl. Phys. Lett., 74 (1999) 111-113.
[169] U. Rau, A. Jasenek, H.W. Schock, F. Engelhardt, T. Meyer, Electronic loss mechanisms in chalcopyrite based heterojunction solar cells, Thin Solid Films, 361–362 (2000) 298-302.
[170] S. Gall, N. Barreau, S. Harel, J.C. Bernède, J. Kessler, Material analysis of PVD-grown indium sulphide buffer layers for $Cu(In,Ga)Se_2$-based solar cells, Thin Solid Films, 480–481 (2005) 138-141.
[171] D. Abou-Ras, G. Kostorz, A. Strohm, H.-W. Schock, A.N. Tiwari, Interfacial layer formations between $Cu(In,Ga)Se_2$ and In_xS_y layers, J. Appl. Phys., 98 (2005) 123512.
[172] A.F. Qasrawi, N.M. Gasanly, Photoelectronic and electrical properties of $CuIn_5S_8$ single crystals, Cryst. Res. Technol., 38 (2003) 1063-1070.
[173] G. Marin, S.M. Wasim, C. Rincón, G. Sánchez Pérez, C. Power, A.E. Mora, Temperature dependence of the fundamental absorption edge in $CuIn_3Se_5$, J. Appl. Phys., 83 (1998) 3364-3366.
[174] A. Jasenek, U. Rau, V. Nadenau, H.W. Schock, Electronic properties of $CuGaSe_2$-based heterojunction solar cells. Part II. Defect spectroscopy, J. Appl. Phys., 87 (2000) 594-602.
[175] M. Turcu, U. Rau, Compositional trends of defect energies, band alignments, and recombination mechanisms in the $Cu(In,Ga)(Se,S)_2$ alloy system, Thin Solid Films, 431–432 (2003) 158-162.
[176] M. Turcu, U. Rau, Fermi level pinning at $CdS/Cu(In,Ga)(Se,S)_2$ interfaces: effect of chalcopyrite alloy composition, J. Phys. Chem. Solids, 64 (2003) 1591-1595.
[177] H. Wilhelm, H.-W. Schock, R. Scheer, Interface recombination in heterojunction solar cells: Influence of buffer layer thickness, J. Appl. Phys, 109 (2011) 084514.

[178] S. Siebentritt, Wide gap chalcopyrites: material properties and solar cells, Thin Solid Films, 403–404 (2002) 1-8.

[179] H. Bayhan, M. Bayhan, A simple approach to determine the solar cell diode ideality factor under illumination, Sol. Energy, 85 (2011) 769-775.

[180] J. Alvarez-García, E. Rudigier, N. Rega, B. Barcones, R. Scheer, A. Pérez-Rodríguez, A. Romano-Rodríguez, J.R. Morante, Growth process monitoring and crystalline quality assessment of $CuInS(Se)_2$ based solar cells by Raman spectroscopy, Thin Solid Films, 431–432 (2003) 122-125.

[181] E. Rudigier, B. Barcones, I. Luck, T. Jawhari-Colin, A. Pérez-Rodríguez, R. Scheer, Quasi real-time Raman studies on the growth of Cu–In–S thin films, J. Appl. Phys., 95 (2004) 5153-5158.

[182] M. Nanu, J. Schoonman, A. Goossens, Raman and PL study of defect-ordering in $CuInS_2$ thin films, Thin Solid Films, 451–452 (2004) 193-197.

[183] T. Schmid, C. Camus, S. Lehmann, D. Abou-Ras, C.-H. Fischer, M.C. Lux-Steiner, R. Zenobi, Spatially resolved characterization of chemical species and crystal structures in $CuInS_2$ and $CuGa_xSe_y$ thin films using Raman microscopy, Phys. Status Solidi A, 206 (2009) 1013-1016.

[184] R. Klenk, J. Klaer, R. Scheer, M.C. Lux-Steiner, I. Luck, N. Meyer, U. Rühle, Solar cells based on $CuInS_2$—an overview, Thin Solid Films, 480–481 (2005) 509-514.

[185] J. Alvarez-García, A. Pérez-Rodríguez, A. Romano-Rodríguez, L. Calvo-Barrio, B. Barcones, J.R. Morante, K. Siemer, I. Luck, R. Klenk, Microstructural characterisation of $CuInS_2$ polycrystalline films sulfurised by rapid thermal processing, Thin Solid Films, 387 (2001) 219-221.

[186] H. Tao, S. Mao, G. Dong, H. Xiao, X. Zhao, Raman scattering studies of the Ge–In sulfide glasses, Solid State Commun., 137 (2006) 408-412.

[187] H. Tao, H. Zang, G. Dong, J. Zeng, X. Zhao, Raman and infrared spectroscopic study of the defect spinel $In_{21.333}S_{32}$, Optoelectron. Adv. Mater., Rapid Commun., 2 (2008) 356-359.

[188] K. Kambas, J. Spyridelis, M. Balkanski, Far Infrared and Raman Optical Study of α- and β-In_2S_3 Compounds, Phys. Status Solidi B, 105 (1981) 291-296.

[189] M. Winkler, O. Tober, J. Penndorf, K. Szulzewsky, D. Röser, G. Lippold, K. Otte, Phase constitution and element distribution in Cu-In-S based absorber layers grown by the CISCuT-process, Thin Solid Films, 361–362 (2000) 273-277.

[190] R. Cross, M. De Souza, E. Narayanan, A low temperature combination method for the production of ZnO nanowires, Nanotechnol., 16 (2005) 2188 - 2192.

[191] K. Tam, C. Cheung, Y. Leung, A. Djurisic, C. Ling, C. Beling, S. Fung, W. Kwok, W. Chan, D. Phillips, L. Ding, W. Ge, Defects in ZnO nanorods prepared by a hydrothermal method, J. Phys. Chem. B, 110 (2006) 20865 - 20871.

[192] S. Studenikin, N. Golego, M. Cocivera, Fabrication of green and orange photoluminescent, undoped ZnO films using spray pyrolysis, J. Appl. Phys., 84 (1998) 2287 - 2294.

[193] D. Look, C. Coskun, B. Claflin, G. Farlow, Electrical and optical properties of defects and impurities in ZnO, Phys. B, 340-342 (2003) 32 - 38.

[194] T. Dedova, M. Krunks, A. Mere, J. Klauson, O. Volobujeva, Preparation of shape and size-controlled zinc oxide nanostructures by chemical spray pyrolysis

technique, Mater. Res. Soc. Symp. Proc. 957: Warrendale, PA, 2007, p. 0957-K10-26., (2007) 359 - 365.

[195] M. Kriisa, M. Krunks, E. Kärber, M. Kukk, V. Mikli, A. Mere, Effect of Solution Spray Rate on the Properties of Chemically Sprayed ZnO:In Thin Films, J. Nanomater., (2013) 423632.

[196] Q. Zhang, T.P. Chou, B. Russo, S.A. Jenekhe, G. Cao, Aggregation of ZnO Nanocrystallites for High Conversion Efficiency in Dye-Sensitized Solar Cells, Angew. Chem., Int. Ed., 47 (2008) 2402-2406.

[197] L. Yang, U.B. Cappel, E.L. Unger, M. Karlsson, K.M. Karlsson, E. Gabrielsson, L. Sun, G. Boschloo, A. Hagfeldt, E.M.J. Johansson, Comparing spiro-OMeTAD and P3HT hole conductors in efficient solid state dye-sensitized solar cells, Phys. Chem. Chem. Phys., 14 (2012) 779-789.

[198] C.-Y. Hsu, Y.-C. Chen, R.Y.-Y. Lin, K.-C. Ho, J.T. Lin, Solid-state dye-sensitized solar cells based on spirofluorene (spiro-OMeTAD) and arylamines as hole transporting materials, Phys. Chem. Chem. Phys., 14 (2012) 14099-14109.

Appendix A

Article I

E. Kärber, K. Otto, A. Katerski, A. Mere, M. Krunks. (2013). “Raman spectroscopic study of In_2S_3 films prepared by spray pyrolysis”, Materials Science in Semiconductor Processing, *in press.*

Contents lists available at ScienceDirect

Materials Science in Semiconductor Processing

journal homepage: www.elsevier.com/locate/mssp

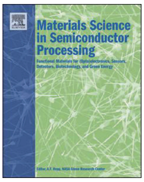

Raman spectroscopic study of In_2S_3 films prepared by spray pyrolysis

E. Kärber*, K. Otto, A. Katerski, A. Mere, M. Krunks

Department of Materials Science, Tallinn University of Technology, Ehitajate tee 5, 19086 Tallinn, Estonia

ARTICLE INFO

Keywords:
In_2S_3
Chemical spray pyrolysis
Raman spectroscopy
XRD
EDX

ABSTRACT

Indium sulfide (In_2S_3) thin films are of interest as buffer layers in chalcopyrite absorber based solar cells; and as media providing two-photon absorption for intermediate-band solar cells. We investigated the suitability of chemical spray pyrolysis (CSP) for growing In_2S_3 thin films in a structural order where indium atoms are preferentially in the octahedral sites. We sprayed aqueous or alcoholic solutions of indium chloride ($InCl_3$) and thiourea ($SC(NH_2)_2$) precursors onto a substrate with surface temperatures (T_S) of 205, 230, 275 and 320 °C. The as-deposited films grown from aqueous solutions were annealed in 5% H_2S containing atmosphere at 500 °C. We used Raman spectroscopy, X-ray diffraction and Energy Dispersive X-ray spectroscopy to evaluate the effect of growth temperature and the effect of annealing on the film structure and stoichiometry. The use of alcoholic solvent instead of aqueous allows us to use much lower T_S while preserving the quality of the β-In_2S_3 films obtained. Similarly, films with increased stoichiometry and quality are present at a higher T_S; and when annealed. The annealing of the films grown at T_S of 205 °C results in a much higher gain of the crystal quality compared to the gain when annealing the films grown at T_S of 320 °C, although the quality remain higher when deposited at T_S of 320 °C. Simultaneously with the increase of the film quality, there is a sign of increased quality of the crystal ordering with indium in the octahedral sites. Such a crystal ordering favor the use of CSP deposited In_2S_3 films in the intermediate band solar cells.

1. Introduction

Indium sulfide (In_2S_3) thin films are used as a substitute for cadmium sulfide (CdS) in solar cells that use chalcopyrite as an absorber material [1,2]. Additionally, In_2S_3 itself can provide the active absorption medium in a new type of solar cells called intermediate band solar cells [3]. In such cells, when doped by a transition metal, In_2S_3 allows an electron band-to-band excitation by absorbing two sub-bandgap photons. In the present work, we study if the chemical spray pyrolysis (CSP) deposition method in conjunction with thermal treatment in H_2S allows to prepare In_2S_3 thin films that fulfill expectations for an intermediate band solar cell.

It has been shown that the preparation method dictates the crystalline, electrical and optical properties of In_2S_3 thin films [4]. The CSP grown In_2S_3 has been used as a buffer layer in thin film solar cells and in extremely thin inorganic absorber (eta) layer solar cells [2,5]; a study on the feasibility of In_2S_3 as an electron selective layer in a polymer solar cell has been published [6]. The CSP is an economical, simple and a non-vacuum method available in pneumatic and ultrasonic spray modes [2,7,8].

The crystal structure and the optical properties of the CSP-deposited In_2S_3 films at different deposition temperatures and molar ratios of indium and sulfur sources (In:S) in either aqueous or alcoholic spray solutions have been published [2,7–11].

XPS study of In_2S_3 films shows that oxygen bounded to indium is present in all sprayed films grown in the temperature range of 205–365 °C, however oxygen

---

* Corresponding author. Tel.: +372 6203369; fax: +372 6203367.
E-mail address: erki.karber@ttu.ee (E. Kärber).

1369-8001/$ - see front matter © 2013 Elsevier Ltd. All rights reserved.
http://dx.doi.org/10.1016/j.mssp.2013.10.007

concentration is always higher in the films prepared from the $InCl_3$:$SC(NH_2)_2$=1:3 solution compared to those obtained by spray of the $InCl_3$:$SC(NH_2)_2$=1:6 solution [8]. In addition, the use of the $InCl_3$:$SC(NH_2)_2$=1:6 solution leads to a slightly larger crystallite size [8]. To understand the relevance of the sulfur source content in the spray solution and the origin of the oxygen content in the films, the formation chemistry of In_2S_3 in spray pyrolysis process has been studied. As a result of thermal analysis, we found that the formation of In_2S_3 films in the CSP process passes through an intermediate complex compound, $In(tu)_3Cl_3$ that formed in aqueous solutions containing $InCl_3$ and $SC(NH_2)_2$ as starting chemicals. The excess of thiourea compared to solution containing $InCl_3$: $SC(NH_2)_2$ at a molar ratio of 1:3 (which is needed for formation of $In(tu)_3Cl_3$ complex), minimizes the formation of In_2O_3 phase [12,13]. Therefore, in this study, the $InCl_3$:$SC(NH_2)_2$ molar ratio of 1:6 instead of 1:3 in the spray solution is used to deposit In_2S_3 films.

Raman spectroscopy has been used to characterize In_2S_3 films prepared by different methods such as co-evaporation of In and S [14], flash evaporation technique [15], electrochemical deposition [16], chemical spray pyrolysis [11,17], chemical bath deposition [18], atomic layer deposition [19] and photochemical deposition technique [20].

The literature on Raman spectroscopy of the CSP-deposited In_2S_3 is yet insufficient. Valdés et. al. presented a Raman spectrum of the sprayed TiO_2/In_2S_3 layers [17]. Spasevska et. al. studied the effect of growth temperature and post-deposition annealing at varied temperatures in air on the properties of In_2S_3 films using ultrasonic spray of $InCl_3$ and $SC(NH_2)_2$ aqueous solution at a molar ratio of 1:7 [11]. An improvement of In_2S_3 film quality was reported when increasing the deposition temperature from 220 to 340 °C or when applying post-deposition annealing in air [11]. The use of alternative solvents in spray solution and the effect of post-deposition annealing in H_2S have not been reported on the Raman spectra of In_2S_3 films deposited by CSP.

We focus on Raman study of In_2S_3 thin films deposited at different growth temperatures using pneumatically sprayed aqueous or alcoholic solutions; and the effect of post-deposition heat treatment on In_2S_3 in H_2S atmosphere. We aim to improve the In_2S_3 film grown by spray so that it would be considered attractive as a host material suitable for doping and thus usable as an absorber in the intermediate band solar cell [3].

2. Experimental

Aqueous or alcoholic solutions, containing indium chloride ($InCl_3$) and thiourea ($SC(NH_2)_2$) as precursors, have been used to deposit In_2S_3 thin films by CSP; respective CSP procedure in more detail can be found in [8,10]. Here we use $InCl_3$ to $SC(NH_2)_2$ molar ratio of 1:6 (with the $[In^{3+}]$ concentration of 2×10^{-3} mol/L), and deionized water or alcoholic mixture (H_2O:C_2H_5OH=1:1, by volume) as solvent in the precursor solution. The solutions were pneumatically sprayed onto a preheated soda-lime or borosilicate glass substrate placed on a tin bath at a temperature of 250, 280, 330 and 380 °C, corresponding to a surface temperature of the substrate T_S of 205, 230, 275 and 320 °C in case of the aqueous solutions sprayed. The temperature differences are due to an inevitable temperature gradient in the substrate; while the main factor is the cooling effect of the carrier gas. In addition, the use of aqueous solutions resulted in a 10 °C lower T_S compared to that when alcoholic solutions were deposited at similar tin bath temperatures. After deposition, the films grown from aqueous solutions onto borosilicate glass were heat-treated for 30 min at 500 °C; subjected to flowing gas in proportion of 5% H_2S (99.99% purity) and 95% N_2 (99.999% purity); followed by cooling to room-temperature at a rate of 25 °C/min.

X-ray diffraction (XRD) patterns were recorded by a Rigaku Ultima IV diffractometer with Cu Kα radiation (λ=1.5406 Å, 40 kV at 40 mA) using the silicon strip detector D/teX Ultra. Crystallite size and lattice constants were calculated using Rigaku PDXL Version 1.4.0.3 software; NIST external standard (LaB_6) was used to determine the instrumental peak broadening. The crystallite size was calculated using the Debye-Scherrer method and a Scherrer constant of 0.94, using the full width at half maximum (FWHM) of the XRD peak with highest intensity. The Raman spectra were measured in a backscattering configuration at room temperature using a confocal micro-Raman spectrometer HORIBA Jobin Yvon Model HR 800. The excitation radiation wavelength was 532 nm while the power density was sufficiently low without excessive heating the sample area of ca 100 μm^2, during 100 s of data acquisition. The Raman peak analysis is based on Lorenzian-fitting performed in the range of 100–450 cm^{-1}. The elemental composition of the films was evaluated by Energy Dispersive X-ray (EDX) analysis using an Oxford Instruments spectrometer with INCA Energy system, at a Zeiss EVO-MA15 scanning electron microscope operating at an accelerating voltage of 7 kV.

3. Results and discussion

3.1. Effect of film growth temperature and solvent type on the Raman spectra of the sprayed In_2S_3

Raman scattering spectroscopy gives knowledge about the vibration modes characteristic of a crystal phase. The modes are affected by local atomic arrangement, including factors like stress, defects and structural disorder. According to Raman spectra, see Fig. 1, the as-deposited films consist of β-In_2S_3 [21]. In this study, the peaks expected near 244 and 306 cm^{-1} are of interest. These peaks have been attributed to the vibrations of InS_6 octahedra and InS_4 tetrahedra, respectively [22,23]. In the β-In_2S_3 the cation vacancies are ordered in the tetrahedral sites while most of the indium (75%) is expected to be in the octahedral sites [3]. In particular, the existence of the octahedral sites has been proven to support two-photon absorption process in vanadium-doped In_2S_3 for the intermediate solar cell application [3].

An increase of T_S up to 320 °C resulted in a pronounced 'octahedral peak' at 244 cm^{-1} for films deposited using aqueous solutions, see Fig. 1a. Yet, the use of alcoholic solutions allows to reach a similar Raman profile already at a lower T_S of 285 °C (Fig. 1b). It seems that, in case of

Please cite this article as: E. Kärber, et al., Materials Science in Semiconductor Processing (2013), http://dx.doi.org/10.1016/j.mssp.2013.10.007

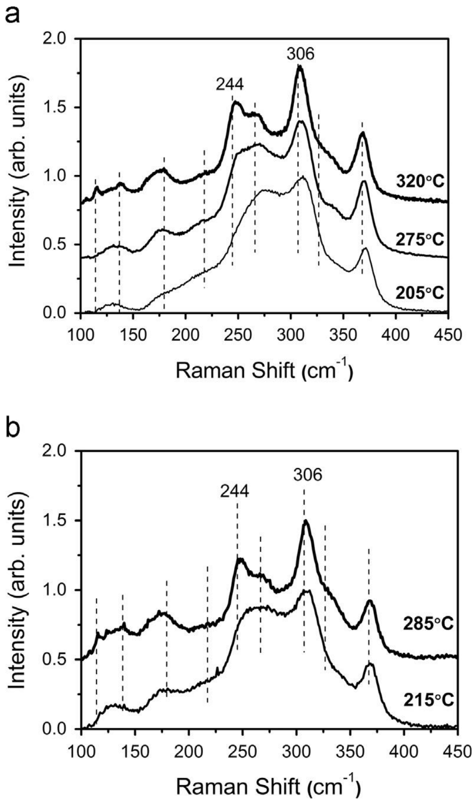

Fig. 1. Raman spectra of the as-deposited In_2S_3 films grown at varied substrate temperatures T_S from aqueous (a) or alcoholic (b) solutions by spray pyrolysis. The dashed lines indicate the positions of the 113, 137, 180, 217, 244, 266, 306, 326 and 367 cm^{-1} Raman reflections of β-In_2S_3 [21]. The reflections near 244 and 306 cm^{-1} were attributed to the vibration of InS_6 and InS_4, respectively [22].

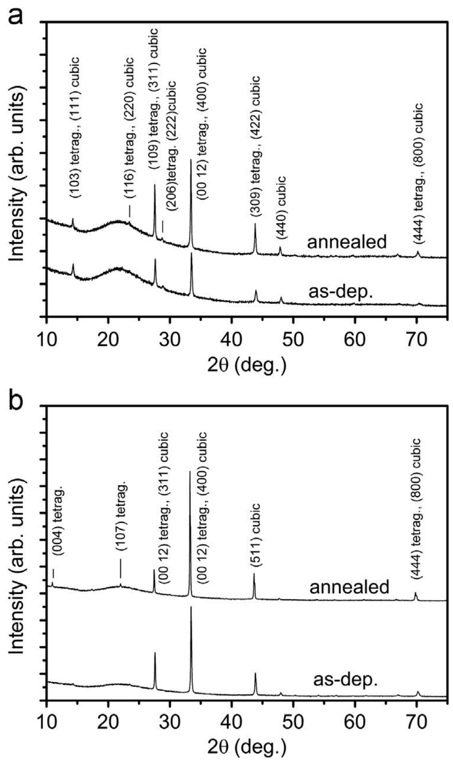

Fig. 2. XRD patterns of the as-deposited In_2S_3 films, and those of films annealed in H_2S, deposited by spray pyrolysis from aqueous solutions at substrate surface temperatures T_S of 205 °C (a) and 320 °C (b). Independent of T_S the as-deposited and the annealed films show similar preferred orientation; that is (0 0 12) tetragonal or (400) cubic crystallite faces parallel to substrate. The respective XRD reflection is seen at 2θ of 33.3–33.5°.

alcoholic solutions sprayed, the real growth temperature in the reaction zone of pyrolysis is significantly elevated from that measured on the substrate surface (T_S); thereby allowing to reach similar film quality at a lower T_S, when compared to the spray of aqueous solutions. While using alcoholic solutions, elevated growth temperatures were also likely when growing ZnO nanorods by CSP [24] and were explained based on the higher volatility of the alcoholic solvent that causes less heat loss and a lower cooling rate, when compared to the use of aqueous solutions. In this view, and for conciseness, we continue in-depth analysis on the annealing effects on films deposited from aqueous solutions only.

3.2. Effect of post-deposition annealing in H_2S on the structure of In_2S_3 deposited at varied growth temperatures by spray

High temperature annealing is known to affect film stoichiometry and crystallinity [25]. The XRD patterns of the In_2S_3 films grown from aqueous solutions using T_S of 205 °C and 320 °C are presented in Fig. 2a and b, respectively. The XRD analysis proposed that the films consist of (0 0 12) orientated β-In_2S_3 crystallites (JCPDS 01-074-7284) or the (400) orientated α-In_2S_3 crystallites (JCPDS 01-084-1385) [26], whereas the crystallite orientation remains similar in various samples. The mean crystallite size (CS) in films deposited at T_S of 205 °C increased from 50 nm to 79 nm when annealed, while the CS in films deposited at T_S of 320 °C increased from 79 nm to 97 nm. We omit distinguishing between the α and β phase of the In_2S_3, since most XRD reflections coincide. The phase diagram of In_2S_3 [27] suggests that for stoichiometric films the β-In_2S_3 is most likely when considering the T_S used. However, an excess of indium (content above 40.5 at% [27]) allows the formation of α-In_2S_3 at film growth temperatures used. Indeed, the In_2S_3 films here show atomic ratio $[S]/[In] < 3/2$ (discussed further below, see Table 2), however the excess of indium can be more likely be attributed to secondary phases (such a $InCl_3$) as chlorine is detected in films by EDX. Likewise, the Raman spectra (Fig. 1) seem to suggest the prevalence of β-In_2S_3 films. Therefore, although a mixture of α-In_2S_3 (cubic) and β-In_2S_3 (tetragonal) phases is also possible, we tend to assume β-In_2S_3 throughout this paper which is a commonly reported phase for films deposited by spray of aqueous or alcoholic solutions containing $InCl_3$ and SC$(NH_2)_2$ using pneumatic or ultrasonic CSP [2,8,9].

Please cite this article as: E. Kärber, et al., Materials Science in Semiconductor Processing (2013), http://dx.doi.org/10.1016/j.mssp.2013.10.007

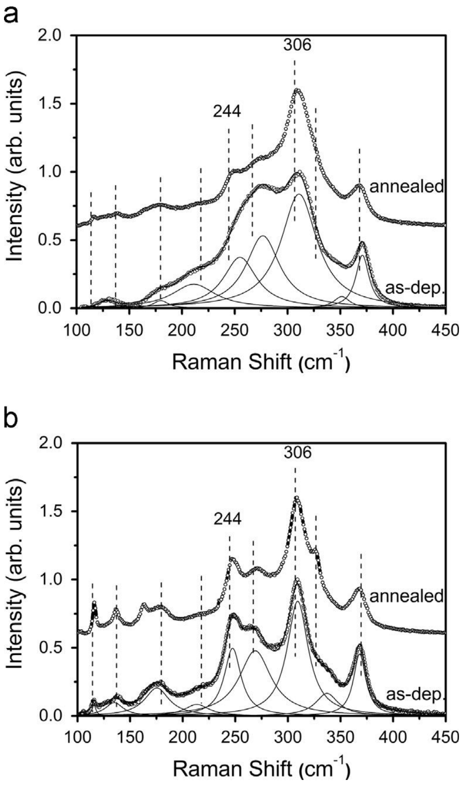

Fig. 3. Raman spectra of the as-deposited In_2S_3 films, and those of films annealed in H_2S, deposited by spray pyrolysis from aqueous solutions at substrate surface temperatures T_S of 205 °C (a) and 320 °C (b). The expected Raman peak positions are listed in Fig. 1. For the as-deposited films, Raman spectra are shown with fitting which follows closely the raw data points. Corresponding XRD patterns are presented in Fig. 2.

Table 1
Result of fitting the position and the full width at half maximum (FWHM) of the Raman peaks of interest of the as-deposited from aqueous solutions, and that of the annealed In_2S_3 films grown at substrate surface temperatures T_S of 205 and 320 °C. The Raman peaks near 244 and 306 cm^{-1} are characteristic of the octahedral and tetrahedral indium sites, respectively [22].

Indium site		Octahedral		Tetrahedral	
		Peak (cm^{-1})	FWHM, (cm^{-1})	Peak (cm^{-1})	FWHM (cm^{-1})
As-deposited	**T_S=205 °C**	259	47	312	33
H_2S treated		249	24	310	34
As-deposited	**T_S=320 °C**	247	19	309	24
H_2S treated		247	14	308	19

Ultimately, when taking into account the aim of this paper, we are not restricted in further Raman analysis, since the octahedral and tetrahedral sites of indium occur in either the α-In_2S_3, β-In_2S_3 or the γ-In_2S_3 polymorph [3].

The Raman spectra corresponding to films with XRD patterns shown in Fig. 2a and b are presented in Fig. 3a and b, respectively. Mathematical fitting of the Raman profile allows to obtain knowledge about the position and the full width at half maximum (FWHM) of the Raman peaks of interest. The FWHM of the 'octahedral peak' decreases significantly, from 47 to 19 cm^{-1}, as the substrate temperature T_S is increased from 205 to 320 °C, see Table 1. The FWHM decrease is a sign of an increase of the quality of the In_2S_3 crystal phase with octahedral indium sites. However, the width of the peak corresponding to tetrahedral sites decreases modestly, from 33 to 24 cm^{-1}.

Similarly, the effect of annealing on the films deposited at a lower T_S of 205 °C has a strong effect on the 'octahedral peak' width that changes from 47 to 24 cm^{-1}; while there is no decrease within fitting uncertainty in the width of the 'tetrahedral peak' changing from 33 to 34 cm^{-1}, hence no further improvement of the corresponding crystalline arrangement. When deposited at a higher T_S of 320 °C, the decrease of the 'octahedral peak' width upon annealing is already much smaller, from 19 to 14 cm^{-1}, when compared to that at lower T_S of 205 °C. However, the width of the 'tetrahedral peak' does show a minor improvement from 24 to 19 cm^{-1}, unlike at T_S of 205 °C.

For comparison, the electrochemically grown indium sulfide thin films are close to amorphous when deposited at room temperature and show Raman peaks characteristic of β-In_2S_3 after annealing at 400 °C in N_2 atmosphere for 1 h [16]. The nanocrystalline indium sulfide grown by CBD remain with wide Raman bands, representing low crystallinity, when annealed at 200 °C in N_2 [18]. Only broad features in Raman spectra are present with films as-deposited by flash evaporation of indium sulfide source, and when air-annealed at 200 °C for 10 min [15]. However, indium sulfide dendrites grown by ultrasonic-element-reaction route at 180 °C show fifteen Raman peaks characteristic of the β-In_2S_3 [28].

An increase in the quality of a crystal ordering is expected to reflect in the narrowing of FWHM as well as in the red-shift of the associated peaks, as it is well-established for $CuInS_2$ [29]. In addition, a larger crystallite size is shown to reflect in narrower Raman peaks [30]. In our case, the changes in the width of the 'octahedral' Raman peak correlate well with changes observed in the mean crystallite size determined by XRD. When films deposited at T_S=205 °C are subjected to annealing, we observed a significant decrease of the FWHM of the Raman peak from 47 to 24 cm^{-1} and, simultaneously, an increase of the crystallite size from 50 to 79 nm. For films deposited at a higher T_S of 320 °C respective changes are present, FWHM decrease from 19 to 14 cm^{-1} while the crystallite size increases from 79 to 97 nm. An increase in the quality of the octahedral ordering is likely, taken into account that most of the indium in the defect spinel structure (β-In_2S_3) is expected to be in the octahedral position [3,28].

Simultaneously with significant narrowing of the Raman peaks, when changing T_S from 205 °C to 320 °C, we observe a shift of the particular fitted Raman peaks towards that reported by Tao [22] (a red-shift towards 244 and 306 cm^{-1}) indicating decreased disorder in the films deposited at higher temperatures. The shift of the 'octahedral peak' upon annealing is noticeable, from 259 to 249 cm^{-1}, for films deposited at 205 °C; the peak remains at 247 cm^{-1} for films deposited at a higher temperature of

Please cite this article as: E. Kärber, et al., Materials Science in Semiconductor Processing (2013), http://dx.doi.org/10.1016/j.mssp.2013.10.007

320 °C. Only small shifts in the positions of the 'tetrahedral peak' are present. The results indicate that the use of annealing seems to be of more benefit to crystal quality (with octahedral ordering) when applied to films deposited at the lower T_S of 205 °C. This claim can be further supported by the following.

While increasing T_S from 205 to 320 °C, the values of lattice parameter a (assuming β-In_2S_3) increase from 7.53 to 7.58 Å in the as-deposited films; while after annealing the values of a tend to converge towards that of β-In_2S_3 powder reference at 7.62 Å, see Fig. 4. The use of annealing of the In_2S_3 thin films seems to be especially beneficial when using T_S lower than 230 °C. For example, at 205 °C the annealing results in an increase of a from 7.53 to 7.60 Å (~1%) while for T_S of 320 °C the improvement of a is only about 0.5%. The higher benefit of the use of annealing on the films grown at lower temperatures is also deduced from the following EDX analysis.

Table 2 presents the elemental composition by EDX of the In_2S_3 films by CSP. The chlorine content in the films decreases from 7.0 to 4.3 at% when deposited at 205 °C and subjected to annealing, respectively. A significantly lower chlorine content of 3% in the as-deposited at T_S of 320 °C films further lowered to 2.1 at% when annealed. Thus, a somewhat larger relative decrease of chlorine, 39% versus 30%, upon annealing is present when the as-deposited films were grown at a T_S of 205 and 320 °C, respectively.

The decrease of chlorine is in correlation with the decrease of the widths of the studied Raman bands, with the shift of the fitted Raman peaks towards expected values (Table 1) and with the increase of the crystallite size – all signs of reduced disorder when the films are annealed. A reduction of the chlorine content and related secondary phases is highly favorable when the indium sulfide will be used as the buffer layer in a thin film chalcopyrite cell [1].

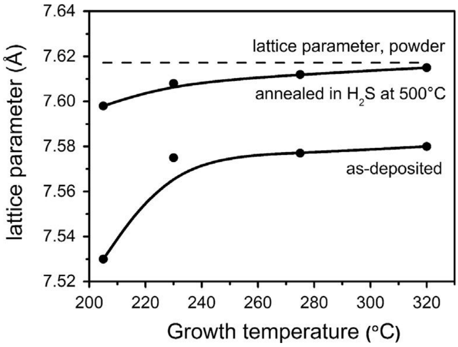

Fig. 4. The lattice parameter a by XRD of In_2S_3 films as-deposited by spray of aqueous solutions, and that of the annealed films, versus substrate temperatures of 205–320 °C. The dashed line shows the expected value of a of the β-In_2S_3 powder reference (JCPDS card no. 01-074-7284) [26].

Table 2
Elemental composition in atomic percent (at%) by EDX of the as-deposited and the annealed In_2S_3 films grown from aqueous solutions at substrate surface temperatures T_S of 205 °C and 320 °C. An atomic ratio [S]/[In]=3/2 is expected from a stoichiometrical In_2S_3.

		In	S	Cl	S/In
As-deposited	**T_S=205 °C**	40.9	52.1	7.0	1.27
H_2S treated		40.2	55.5	4.3	1.38
As-deposited	**T_S=320 °C**	41.7	55.3	3.0	1.33
H_2S treated		41.6	56.3	2.1	1.35

Similarly, based on Table 2, annealing results in an increase of S/In atomic ratio by 8.7% and 1.5% when applied to In_2S_3 films grown at T_S of 205 and 320 °C, respectively. Thus, the benefit of annealing is more profitable for films deposited at lower temperatures, as also indicated by Raman and XRD study.

4. Conclusions

In_2S_3 films were grown in air by chemical spray pyrolysis (CSP) at substrate surface temperatures of 205–320 °C using indium chloride and thiourea as precursors. The use of an alcoholic instead of an aqueous solvent allows us to use lower substrate temperatures while retaining the film growth temperature and film quality. An increase of the substrate temperature from 205 to 320 °C results in: an increase of the crystallite size; a shift of the studied Raman peaks toward expected positions; a decrease of the widths of the studied Raman peaks; a decrease of the chlorine content; an improvement of stoichiometry and an increase of the lattice parameter. These signs indicated that the crystal quality of In_2S_3 increases up to the highest temperatures used: 320 and 285 °C for aqueous and alcoholic solvent, respectively; these temperatures are supposed as optimum for growth of In_2S_3 thin films with highest crystal quality by CSP in air.

Post-deposition annealing in H_2S at 500 °C leads to increased crystallite size; results in a further decrease of the chlorine content; improvement of the stoichiometry and an increase of the lattice parameters close to that of the β-In_2S_3 powder reference. The quality of the crystal ordering with indium in the octahedral sites increase when elevating the film's growth temperature from 205 to 320 °C or when the as-deposited films are subjected to annealing at 500 °C in H_2S. The annealing of the films grown at T_S of 205 °C results in a much higher gain of the crystal quality compared to the gain when annealing films grown at T_S of 320 °C, although the film quality remain higher when deposited at T_S of 320 °C.

We conclude that the In_2S_3 thin films could most likely be considered a host material suitable for doping with a transition metal, and thus usable as an absorber in the intermediate band solar cell, when grown at T_S of 320 °C by CSP and followed by thermal treatment at 500 °C in H_2S.

Acknowledgment

Financial support by the Estonian Ministry of Education and Research (SF0140092s08); the Estonian Science Foundation (ETF9081); and the European Union through the European Regional Development Fund: Project TK114 (Centre of Excellence "Mesosystems: Theory and Applications", TK114, 3.2.0101.11-0029) and AR12118 ("Efficient plasmonic absorbers for solar cells", 3.2.1101.12-0023) are

Please cite this article as: E. Kärber, et al., Materials Science in Semiconductor Processing (2013), http://dx.doi.org/10.1016/j.mssp.2013.10.007

gratefully acknowledged; E.K. acknowledges graduate school “Functional materials and technologies” receiving funding from the European Social Fund under Project 1.2.0401.09-0079 in Estonia. Dr. Valdek Mikli from the Centre for Materials Research at Tallinn University of Technology is thanked for the EDX study.

References

[1] R. Sáez-Araoz, J. Krammer, S. Harndt, T. Koehler, M. Krueger, P. Pistor, A. Jasenek, F. Hergert, M.C. Lux-Steiner, C.-H. Fischer, Prog. Photovolt.: Res. Appl. 20 (2012) 855–861.
[2] S. Buecheler, D. Corica, D. Guettler, A. Chirila, R. Verma, U. Müller, T.P. Niesen, J. Palm, A.N. Tiwari, Thin Solid Films 517 (2009) 2312–2315.
[3] R. Lucena, I. Aguilera, P. Palacios, P. Wahnon, J.C. Conesa, Chem. Mater. 20 (2008) 5125–5127.
[4] N. Barreau, Sol. Energy 83 (2009) 363–371.
[5] M. Krunks, E. Kärber, A. Katerski, K. Otto, I. Oja Acik, T. Dedova, A. Mere, Sol. Energy Mater. Sol. Cells 94 (2010) 1191–1195.
[6] M.R. Rajesh Menon, M.V. Maheshkumar, K. Sreekumar, C. Sudha Kartha, K.P. Vijayakumar, Sol. Energy Mater. Sol. Cells 94 (2010) 2212–2217.
[7] M. Calixto-Rodriguez, A. Tiburcio-Silver, A. Ortiz, A. Sanchez-Juarez, Thin Solid Films 480–481 (2005) 133–137.
[8] K. Otto, A. Katerski, A. Mere, O. Volobujeva, M. Krunks, Thin Solid Films 519 (2011) 3055–3060.
[9] T.T. John, S. Bini, Y. Kashiwaba, T. Abe, Y. Yasuhiro, C.S. Kartha, K.P. Vijayakumar, Semicond. Sci. Technol. 18 (2003) 491.
[10] K. Otto, A. Katerski, O. Volobujeva, A. Mere, M. Krunks, Energy Procedia 3 (2011) 63–69.
[11] H. Spasevska, C.C. Kitts, C. Ancora, G. Ruani, Int. J. Photoenergy 2012 (2012).
[12] K. Otto, P. Bombicz, J. Madarász, I. Oja Acik, M. Krunks, G. Pokol, J. Therm. Anal. Calorim. 105 (2011) 83–91.
[13] K. Otto, I. Oja Acik, K. Tõnsuaadu, A. Mere, M. Krunks, J. Therm. Anal. Calorim. 105 (2011) 615–623.
[14] C. Laurencic, L. Arzel, F.C. Devy, N. Barreau, Thin Solid Films 519 (2011) 7553–7555.
[15] R. Verma, D. Datta, A. Chirila, D. Güttler, J. Perrenoud, F. Pianezzi, U. Müller, S. Kumar, A.N. Tiwari, J. Appl. Phys. 108 (2010).
[16] A.M.A. Haleem, M. Ichimura, Thin Solid Films 516 (2008) 7783–7789.
[17] M. Valdés, A. Goossens, M. Vázquez, Mater. Chem. Phys. 125 (2011) 860–865.
[18] B. Asenjo, C. Guillén, A.M. Chaparro, E. Saucedo, V. Bermudez, D. Lincot, J. Herrero, M.T. Gutiérrez, J. Phys. Chem. Solids 71 (2010) 1629–1633.
[19] J. Rousset, F. Donsanti, P. Genevée, G. Renou, D. Lincot, Sol. Energy Mater. Sol. Cells 95 (2011) 1544–1549.
[20] R. Kumaresan, M. Ichimura, N. Sato, P. Ramasamy, Mater. Sci. Eng. B 96 (2002) 37–42.
[21] K. Kambas, J. Spyridelis, M. Balkanski, Phys. Status Solidi B 105 (1981) 291–296.
[22] H. Tao, S. Mao, G. Dong, H. Xiao, X. Zhao, Solid State Commun. 137 (2006) 408–412.
[23] H. Tao, H. Zang, G. Dong, J. Zeng, X. Zhao, Optoelectron. Adv. Mater.: Rapid Commun. 2 (2008) 356–359.
[24] E. Kärber, T. Raadik, T. Dedova, J. Krustok, A. Mere, V. Mikli, M. Krunks, Nanoscale Res. Lett. 6 (2011) 1–7.
[25] R. Ranjith, T.T. John, C. Sudha Kartha, K.P. Vijayakumar, T. Abe, Y. Kashiwaba, Mater. Sci. Semicond. Process. 10 (2007) 49–55.
[26] International Centre for Diffraction Data (ICDD), Powder Diffraction, File (PDF), PDF-2 Release 2008.
[27] T. Gödecke, K. Schubert, Z. Metallkd. 76 (1985) 358–364.
[28] Y. Xiong, Y. Xie, G. Du, X. Tian, Y. Qian, J. Solid State Chem. 166 (2002) 336–340.
[29] J. Alvarez-Garcia, E. Rudigier, N. Rega, B. Barcones, R. Scheer, A. Perez-Rodriguez, A. Romano-Rodriguez, J.R. Morante, Thin Solid Films 431–432 (2003) 122–125.
[30] G. Gouadec, P. Colomban, Prog. Cryst. Growth Charact. Mater. 53 (2007) 1–56.

Appendix A

Article II

E. Kärber, A. Abass, S. Khelifi, M. Burgelman, A. Katerski, M. Krunks. (2013). “Electrical characterization of all-layers-sprayed solar cell based on ZnO nanorods and extremely thin CIS absorber” Solar Energy, 91, 48–58.

ELSEVIER

Available online at www.sciencedirect.com

SciVerse ScienceDirect

Solar Energy 91 (2013) 48–58

SOLAR ENERGY

www.elsevier.com/locate/solener

Electrical characterization of all-layers-sprayed solar cell based on ZnO nanorods and extremely thin CIS absorber

Erki Kärber [a,*], Aimi Abass [b], Samira Khelifi [b], Marc Burgelman [b], Atanas Katerski [a], Malle Krunks [a]

[a] Department of Materials Science, Tallinn University of Technology, Ehitajate tee 5, 19086 Tallinn, Estonia
[b] Gent University, Department of Electronics and Information Systems (ELIS), Pietersnieuwstraat 41, B-9000 Gent (B), Belgium

Received 26 October 2012; received in revised form 3 January 2013; accepted 15 January 2013
Available online 27 February 2013

Communicated by: Associate Editor Takhir Razykov

Abstract

Nanostructured $ZnO/In_2S_3/CuInS_2$ superstrate solar cell with all component layers deposited by a low cost chemical spray pyrolysis (CSP) method is characterized. The characteristics of a cell based on a nano-columnar ZnO window layer and a thin film reference prepared by spray are compared. The aim is to determine the dominating non-ideality and the recombination mechanism of these cells in both dark and illuminated conditions and relate the findings to the imperfections in the cell materials. We performed J–V–T (current–voltage–temperature) measurements in dark and under 0.5–100 mW/cm^2 illumination intensities, and admittance spectroscopy, in the temperature range of 100–360 K. We further measured EQE (external quantum efficiency) at room temperature. The solar cell outputs at AM1.5 of the flat reference cell are: $V_{oc} = 497$ mV, $J_{sc} = 6.4$ mA/cm^2, $FF = 62\%$, $\eta = 2\%$. The use of a nanostructured instead of a flat window layer resulted in short-circuit current density $J_{sc} = 12.2$ mA/cm^2 and efficiency of $\eta = 3\%$ at the expense of slightly reduced open-circuit voltage $V_{oc} = 430$ mV and fill factor $FF = 58\%$. Interestingly, the nanostructured cell performs worse than the flat reference at low illumination intensity, as also indicated by illumination dependent shunt conductance. The diode ideality factor of both cells has a significant temperature and illumination dependence. The absorber bandgaps deduced from EQE are 1.5 eV for the flat cell and 1.3 eV for the structured cell. The nanostructured cell shows an increase of light scattering ability accompanied by a less effective charge carrier separation, compared to those of the flat reference cell. The extrapolation of $V_{oc}(T)$ to 0 K yields 740–830 meV and 950–990 meV at varied illumination intensity, for the structured and the flat reference cell respectively, pointing to a non-midgap defect recombination. C–f–T (capacitance – ac frequency – temperature) analysis indicates that the structured cell has a higher concentration of defects and an additional band of defects. This further explains the limited performance enhancement of the structured cell over the flat cell. The illumination dependent cell parameters reveal that copper diffusion from absorber to buffer layer is likely. To eliminate problems associated with Cu diffusion, binary compounds like Sb_2S_3 or SnS for use as absorber material are considered to further develop the low-cost superstrate type solar cell deposited by the CSP method.

Keywords: Inorganic nanostructured solar cell; Superstrate cell; Extremely thin absorber (ETA); Chemical spray pyrolysis; Copper indium disulfide

---

1. Introduction

Recent publications have reviewed inorganic solid-state nanostructured solar cell concepts, limitations (Dittrich et al., 2011) and the rationale of an extremely thin absorber (ETA) (Hodes and Cahen, 2012). Despite the common understanding that the ETA cell is still a challenge (Dittrich et al., 2011; Hodes and Cahen, 2012), prospect for lowering the production costs is promising (Dittrich et al., 2011; Hodes and Cahen, 2012). A solar cell where the absorber layer is deposited as the first layer is referred

---

* Corresponding author. Tel.: +372 6203369; fax: +372 6203367.
E-mail address: erki.krbr@gmail.com (E. Kärber).

0038-092X/$ - see front matter © 2013 Elsevier Ltd. All rights reserved.
http://dx.doi.org/10.1016/j.solener.2013.01.020

to as a substrate type solar cell (Cherian et al., 2012). In this work, the solar cell is made in a superstrate configuration where the absorber layer is deposited last. The ETA solar cell was fabricated on top of a structured window layer comprised of ZnO nanorods. Starting from the ZnO nanorod window layer, the *n*-type In_2S_3 buffer is deposited, followed by the *p*-type $CuInS_2$ (CIS) absorber film which is used as the sensitizer. All layers of the solar cell have been deposited by the chemical spray pyrolysis (CSP) method, for a cost-effective approach. For a characteristic SEM (scanning electronic microscope) image see Fig. 6 in Krunks et al. (2010).

ETA cells have been made using mainly nanoporous ZnO (Dittrich et al., 2011; Hodes and Cahen, 2012; Lévy-Clément et al., 2005) or TiO_2 (Hodes and Cahen, 2012; Ernst et al., 2003; Herzog et al., 2009) as the window layer. These studies used various absorbers like Se, PbS, CdSe, CdS, In_2S_3, Cu_XS, Sb_2S_3 grown by chemical bath deposition (Hodes and Cahen, 2012), CdSe grown by electrochemical deposition (Hodes and Cahen, 2012; Lévy-Clément et al., 2005), CdTe grown by electrochemical deposition (Ernst et al., 2003) and In_2S_3 by SILAR (successive ionic-layer adsorption and reaction) (Dittrich et al., 2011; Herzog et al., 2009). Similarly, CIS has been deposited by chemical spray (Krunks et al., 2010; Goossens and Hofhuis, 2008), ALD (atomic layer deposition) (Goossens and Hofhuis, 2008) and ILGAR (Ion Layer Gas Reaction) (Kaiser et al., 2001) to be used as an absorber on a nanoporous TiO_2 (Herzog et al., 2009; Goossens and Hofhuis, 2008; Kaiser et al., 2001; Kieven et al., 2008) or a nanocolumnar ZnO window layer (Dittrich et al., 2011; Krunks et al., 2010; Kieven et al., 2008), respectively.

CIS is a semiconductor with chalcopyrite structure that has a high optical absorption coefficient and optimal direct bandgap of 1.5 eV for photovoltaic (PV) application. Thin film solar cells with efficiencies >10% have been reported with CIS absorber grown by two-step processes – vacuum deposition of Cu–In precursor films, followed by sulfurization (Siemer et al., 2001a; Antony et al., 2004; Klaer et al., 1998). Sulfurcell (the first company to manufacture solar modules based on CIS) uses the two step process technique (Scheer et al., 2004). Solar cells based on CISCuT ($CuInS_2$ on Cu-tape) grown absorber layers are reported to reach efficiencies of 5–9% (Winkler et al., 2000, 2004; Verschraegen et al., 2005). Although extensively studied, there are still fundamental questions to be answered after 20 years of CIS research (Scheer, 2012).

Due to their low production costs, chemical methods like ILGAR (Kaiser et al., 2001; Muffler et al., 2001; Camus et al., 2008) and chemical spray (Krunks et al., 2010; Goossens and Hofhuis, 2008) have been used for CIS absorber deposition for thin film solar cells with efficiencies of up to 7% (Goossens and Hofhuis, 2008). The sprayed CIS has been used in $CuInS_2/In_2S_3$ solar cells in which the constituent layers are planar when viewed from the cross-section (Theresa John et al., 2005) or in a $CuInS_2/TiO_2$ solar cell where so-called interpenetrating network of the *p* and *n* type semiconductors occur to form a nanocomposite (Goossens and Hofhuis, 2008).

The superstrate $ZnO_{rod}/In_2S_3/CuInS_2$ type cell prepared in our lab by spray shows a conversion efficiency of up to 4.2% (Krunks et al., 2010). However, the open circuit voltage V_{oc} of the cell is restricted to around 0.5 V which is much lower than that ideally expected of a cell with a 1.5 eV bandgap. Thus, an evaluation of the recombination mechanism is necessary to understand the loss in the V_{oc}.

The aim of this study is to determine the reasons that hinder the cell performance, i.e. the dominating non-ideality and the recombination mechanisms, in order to improve the conversion efficiency of the nanostructured cell (further referred to as a *structured* cell) deposited by CSP. For comparison, a reference cell with planar layers deposited by spray, and referred to as a *flat* cell is included in the analysis. We made an effort to relate the solar cell imperfections to material properties. Interestingly the advantage which the *structured* cell has over the *flat* cell at higher illumination intensities is lost at low illumination intensities.

The desired attributes of an ETA solar cell in general are effective charge carrier separation within the absorber and high light absorption due to scattering abilities of the cell (Kaiser et al., 2001). However, in this work we show that an increase in the light absorption ability is accompanied by a less effective charge carrier separation when using a solar cell with a nanostructured window layer instead of an all-*flat*-layers $ZnO/In_2S_3/CuInS_2$ solar cell made by CSP. No similar studies on superstrate type $ZnO_{rod}/In_2S_3/CuInS_2$ inorganic ETA-cell deposited by the low-cost CSP technology have been published.

2. Experimental

2.1. Sample preparation

The superstrate type $ZnO/In_2S_3/CuInS_2$ solar cells are prepared by the CSP method in air. The *structured* $ZnO_{rod}/In_2S_3/CuInS_2$ cell is prepared in the following order. The conductive front electrode – a commercial ITO/glass substrate is cleaned in an ultrasonic bath and etched chemically. On top of the ITO, a window layer consisting of ZnO nanorods is grown in the first stage, followed by a two-stage In_2S_3 buffer deposition and covered by the CIS absorber layer in the last stage. The CIS absorber is deposited from a precursor solution containing $CuCl_2$, $InCl_3$ and $CS(NH_2)_2$ at the molar ratio of 1:1:3, the film growth temperature was ca 270 °C. Finally, carbon paste was applied to make back-contacts (in the area of 2 mm^2) on top of the CIS absorber. The *flat* reference cell is deposited in similar conditions, except the ZnO window layer which is grown as a compact (*flat*) layer. The whole in-line procedure for deposition of the cells by CSP takes approximately 1.5 h to complete. Detailed sample preparation can be found elsewhere (Krunks et al., 2010, 2008).

2.2. Sample characterization

We measured *J–V* (current–voltage) temperature dependence in dark and under 0.5–100 mW/cm^2 illumination intensities, external quantum efficiency *EQE*(λ) measured and temperature dependent admittance *C–f* (capacitance – ac frequency). For the *J–V*(*T*) and *C–f*(*T*), the solar cells were mounted on a cold-finger in a N$_2$-cooled cryostat. The temperature of the cold-finger was increased from 100 K up to 360 K in steps of 20 K. A four point probe technique was used for *J–V*(*T*) and *C–f*(*T*) measurements, using a computer controlled KEITHLEY 236 Source Measure Unit and HP 4192A LF Impedance Analyzer, respectively. For *J–V*(*T*) under different light intensities, we used an Oriel 6143 white light lamp together with neutral density filters. Admittance spectroscopy was carried out in dark by varying the frequency from 100 Hz to 10 MHz and using an ac test voltage of 30 mV. The solar cell outputs were measured at standard test conditions (AM1.5, 100 mW/cm^2, 25 °C). The *EQE* was measured at room temperature in a wavelength range of 370–1240 nm (1.0–3.4 eV) with no dc-bias.

3. Results and discussion

3.1. Analysis of the EQE spectra

The *EQE* spectra for the *structured* and the *flat* cell are presented in Fig. 1a. It is desirable to have a high *EQE* at wavelengths where the solar irradiance is high. This requirement is better fulfilled for the *flat* cell showing maximum *EQE* of 35% near 2.3 eV unlike the *structured* cell where a maximum *EQE* of 70% is found around 1.9 eV. Still, the *EQE* of the *structured* cell is as much as twice larger from that of the reference cell. This could be either from absorption enhancement, decreased recombination, or both. We will later show that the second possibility – decreased recombination – is not likely. Thus, it could be concluded that an increase of the optical path due to multiple reflections (scattering) in the rough ZnO layer yields a higher absorption ability in the *structured* cell. A similar report on a ZnO$_{rod}$/In$_2$S$_3$/CuSCN solar cell which uses an ILGAR-deposited In$_2$S$_3$ as extremely thin absorber layer can be found in Kieven et al., (2008).

Unexpectedly, the *structured* cell shows a red-shift of the absorption edge when compared to that of the *flat* cell, indicating that the absorber of the *structured* cell has a lower bandgap (E_g). The E_g is obtained using the relation $EQE \approx A(E - E_g^*)^{1/2}/E$, valid for direct transition near the bandgap energy $E \approx E_g$, where E is the photon energy (Krustok et al., 2010). Here, the constant A includes all parameters that do not depend on E. The evaluated bandgaps are 1.3 eV and 1.5 eV for the absorber of the *structured* and the *flat* cell, respectively, see Fig. 1b. The cause of a smaller bandgap of the absorber of the *structured* cell is unclear. A possible explanation could be the presence of an additional phase like CuIn$_5$S$_8$, which shows a bandgap value of 1.31 eV (Qasrawi and Gasanly, 2003) or Cu$_2$S with an indirect bandgap of 1.21 eV (Wu et al., 2008; Page et al., 2009). The existence of secondary phases is expected as in the CSP process the CIS forms from binary sulfides (Cu$_X$S, In$_2$S$_3$) Krunks et al., 1997, while binary sulfides form upon thermal degradation of corresponding metal chloride thiourea complexes at temperatures above 200 °C (Otto et al., 2011). Thus, sprayed CIS films, especially those grown at temperatures below 300 °C may contain residues of non-reacted binary sulfides and residues originated from starting chemicals (Krunks et al., 2002). Presently, there are no significant differences detected in the Raman spectra (not shown) of the absorbers of the *flat* and the *structured* cell. Nevertheless, we have shown previously that an extra copper containing phase exists in the sprayed CIS films prepared at similar conditions, as the relevant peaks characteristic of Cu$_X$S are resolved in the Raman spectra of CIS films after annealing in H$_2$S atmosphere (Kärber et al., 2011). Therefore, we might expect a higher content of copper containing phase (likely Cu$_X$S) in the absorber of the *structured* cell. A possible explanation for a higher content of Cu$_X$S (and likely, of unreacted In$_2$S$_3$) could be unintentionally lowered growth temperature for the absorber when

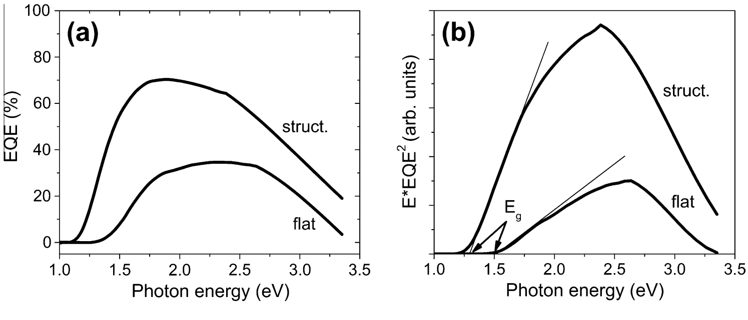

Fig. 1. (a) External quantum efficiency (*EQE*) measured at $T = 300$ K of the *structured* and the *flat* ZnO/In$_2$S$_3$/CuInS$_2$ solar cells grown by the CSP method. An improvement of the *EQE* is assigned to an improved photon absorption in the *structured* cell. (b) A modified *EQE* plot yields values of 1.3 eV and 1.5 eV as a bandgap E_g estimation of the absorber material in the *structured* and *flat* solar cells, respectively.

deposited on the *structured* ZnO/In_2S_3 layer as compared to the growth temperature when a *flat* window/buffer substrate is used. This speculation is supported by the fact that a lower photosensitivity of the shunt conductance occurs in the *structured* cell, discussed in Section 3.2. A small content of secondary phase is, however, not the only cause of a lowered open circuit voltage V_{oc}, as shown by the *J–V–T* (current–voltage–temperature) analysis. In fact, the impact of a higher interface recombination might be just as disadvantageous for the V_{oc}, when using the *structured* cell, as discussed in Section 3.2.

3.2. Analysis of the J–V characteristics

The *J–V* characteristics of the *structured* and the *flat* cell are presented in Fig. 2. For both cells, the characteristic at illumination cannot simply be obtained from the dark current by shifting the *J–V* curve downwards in vertical direction, which is expected according to the shifting approximation (Scheer and Schock, 2011). Another violation occurs at higher bias voltage resulting in an intersection of the dark and light *J–V* characteristics, also known as the cross-over phenomenon commonly encountered in CIS devices. A set of solar cell parameters listed in Table 1 are extracted from the *J–V* measurements.

We see that the use of a *structured* instead of a *flat* window layer results in a gain of J_{sc} and a gain of efficiency at the expense of slightly reduced V_{oc} and somewhat lower *FF*. A low open circuit voltage is observed, an inherent shortcoming of the CIS absorber based solar cells (Scheer, 2012; Nadenau et al., 2000). The use of a *structured* instead of a *flat* window layer in the cell decreases the fill factor from 62% to 58%. An increase of the series resistance R_S (discussed further below, Fig. 5) from about 2.0 Ω cm^2 up to 2.2 Ω cm^2 at 1 sun illumination is too low to produce a loss of 4% in *FF*. Instead, the loss of the *FF* is attributed to the decrease of V_{oc} from 497 mV to 430 mV. The decrease of the V_{oc} is caused by a lowered bandgap from 1.5 eV to 1.3 eV (Fig. 1b) and an increase of the interface recombination discussed further below.

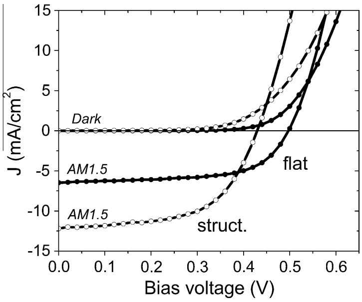

Fig. 2. *J–V* characteristics in dark and under solar simulator conditions (AM.1.5) measured at $T = 300$ K of the *structured* (open symbols) and the *flat* (solid symbols) ZnO/In_2S_3/$CuInS_2$ solar cell. Violation of the shifting approximation and cross-over phenomena is evident for both cells.

Table 1
Parameters of the *structured* and the *flat* ZnO/In_2S_3/$CuInS_2$ solar cell. The V_{oc}, J_{sc}, *FF* and η are extracted from *J–V* characteristics under 1 sun illumination at standard test conditions (Fig. 2), E_A is obtained from $V_{oc}(T)$ extrapolation to 0 K (Fig. 4) and E_g is obtained from *EQE* measurements (Fig. 1b).

Property		Units	Structured	Flat
Open-circuit voltage	V_{oc}	mV	430	497
Short-circuit current	J_{sc}	mA/cm^2	12.2	6.4
Fill factor	FF	%	58	62
Efficiency	η	%	3	2
Activation energy	E_A	eV	0.74 … 0.83	0.95 … 0.99
Bandgap of absorber	E_g	eV	1.3	1.5

The analysis of the *J–V* characteristics of the solar cell is based on the following, commonly used diode model:

$$J = J_0\left[\exp\left(\frac{qV^*}{nkT}\right) - 1\right] + G_{sh}V^* - J_L \qquad (1)$$

where J_0 is the saturation current at reverse bias, J_L is the light current generated in the cell under illumination, $V^* = V - JAR_S$ is the voltage across the *pn* junction of the cell where *A* is the back contact area. The non-idealities in the model are the series resistance R_S, shunt-conductance G_{sh} and diode ideality factor $n > 1$.

The diode ideality factor *n* when measured as a function of temperature can provide information about the dominating recombination mechanism in the solar cell (Verschraegen et al., 2005; Scheer and Schock, 2011). In principle, solar cell parameters should be derived from an illuminated *J–V* curve. Still, provided that the recombination mechanisms are identical in dark and at illuminated conditions, evaluation of the dark current would be preferable (Scheer and Schock, 2011). However, we have no grounds to believe that the dominant recombination mechanism is identical in dark and at illumination due to significant cross-over effect and violation of the shifting approximation of the *J–V* curves, see Fig. 2. Therefore both dark and light current are evaluated.

The temperature dependent ideality factors in dark and at illumination are extracted from *J–V* curves using the model above at relatively high bias voltage in the range of 0.35–0.5 V. As a first observation, values of *n* in the dark are above 2 and are temperature dependent, see Fig. 3. Both signatures are an indication of tunneling mechanism of the recombination current (Verschraegen et al., 2005; Nadenau et al., 2000). The origin of the tunneling currents is not clear, and not treated in this paper. In the case of the *flat* solar cell in dark, the best fit of the ideality factor as a function of temperature is obtained using the relation $n = E_{00}/kT$ or equivalently $n = T^*/T$, where $T^* = E_{00}/k$ (Verschraegen et al., 2005) suggesting that tunneling enhanced interface recombination is the dominating recombination mechanism in dark conditions. A characteristic tunneling energy E_{00} of 36.4 meV corresponding to characteristic

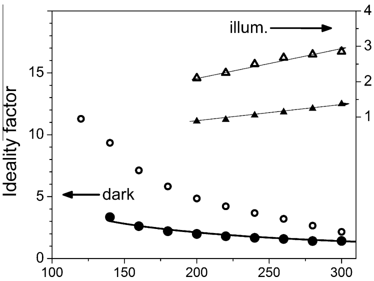

Fig. 3. The temperature dependent ideality factor of the *structured* (open symbols) and the *flat* (solid symbols) ZnO/In_2S_3/$CuInS_2$ solar cell. In dark (indicated by circles) the ideality factor of the *flat* cell is fitted to the model of tunneling enhanced interface recombination. At illuminated condition (indicated by triangles), visual guidelines are used to indicate linear behavior of the ideality factor as a function of temperature.

temperature of $T^* = 422$ K is extracted from fitting of $n(T)$ using the relations above. An even steeper upward slope of the $n(T)$ can be observed in the case of the *structured* cell. However, none of the models found in literature (Scheer and Schock, 2011; Rau, 1999; Rau et al., 2000) yield an acceptable fit in our case. Since higher $n(T)$ values suggest increased tunneling recombination (Reiβ et al., 2001), it could be speculated that the contribution of tunneling recombination is even more pronounced in the *structured* cell. A deeper insight to solve this issue is needed. However, it is not considered at this stage of our studies.

At illumination, the temperature dependent ideality factor of the *flat* cell does not yield similar results with values obtained from the dark *J–V* curves, see Fig. 3. In the case of the *flat* cell, an opposite trend, a weak temperature dependence and the ideality factor values smaller than 2 are observed, indicating thermal activation of the saturation current, while the cell is illuminated (Reiβ et al., 2001). Such a disagreement suggests that a different recombination mechanism is limiting the diode current in dark and at illumination. A mechanism where the tunneling-enhanced recombination in dark changes to thermally activated interface recombination upon light exposure, could be considered (Scheer, 2012). Similar results were published for substrate type solar cells using a CdS buffer layer, whereas such behavior was identified in $CuInS_2$ cells only and was not observed in substrate type cells using $CuInSe_2$ or $CuGaSe_2$ absorber prepared by sequential Cu/In precursor evaporation or sputtering, followed by selenization (Reiβ et al., 2001; Siebentritt, 2002). In contrast, the *structured* cell shows $n > 2$ and n increases with temperature, see Fig. 3. We do not have a suitable model explaining this behavior. However, when estimated from the $V_{oc} - J_{sc}$ plot (not shown) the ideality factor of the *structured* cell remains below 2 while increasing with the temperature, similar to $n(T)$ of the *flat* cell.

The temperature dependence of the V_{oc} of the sprayed ETA CIS cells is used to extract the activation energy E_A of the saturation current J_0 (Scheer, 2012), as presented in Fig. 4. The extrapolation of $V_{oc}(T)$ to the temperature of 0 K yields E_A values of 950–990 meV and 740–830 meV, for the *flat* and the *structured* cell, respectively, at illumination intensities of 0.5–100 mW/cm^2. The fact that the extrapolation of V_{oc} at different illumination intensities does not converge at 0 K, in particular lowering of illumination intensity yields a lower E_A (Fig. 4), is implying on illumination dependent cell properties. In addition, the temperature dependent ideality factor (Fig. 3) might render E_A values less accurate (Nadenau et al., 2000).

The activation energy E_A should approximately equal the minimum bandgap in the absorber including the interfaces (Scheer and Schock, 2011) and gives knowledge about the main recombination mechanism. Comparing the values of E_A to the bandgap values E_g obtained from *EQE* study (Fig. 1b), we recognize that $E_A < E_g$. Such a variance between E_A and E_g is generally ascribed to the effect of recombination at the absorber/buffer interface (Scheer, 2012; Scheer and Schock, 2011; Nadenau et al., 2000; Reiβ et al., 2001). In particular, a lowered V_{oc} of 430 mV (*structured* cell) instead of 497 mV (*flat* cell), see Fig. 2, could be explained by enhanced interface recombination when using the cell with the *structured* ZnO_{rod} window layer instead of a compact ZnO layer. Thus, we assume that the interface states will form the main recombination channel.

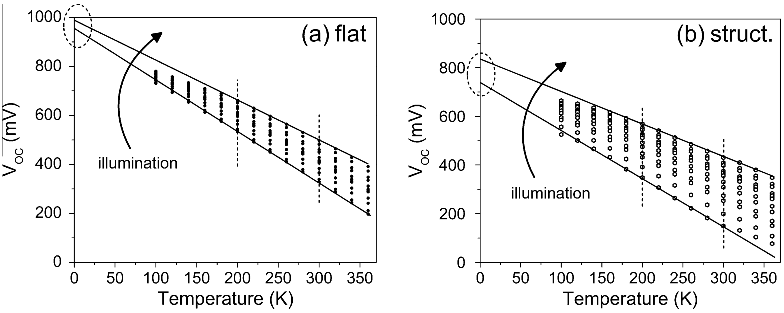

Fig. 4. Temperature dependence of the open circuit voltage V_{oc} of the *flat* (a) and the *structured* (b) ZnO/In_2S_3/$CuInS_2$ solar cell. The extrapolation of V_{oc} to 0 K yields an activation energy E_A of 950–990 meV and 740–830 meV for the *flat* and *structured* cell, respectively, at illumination intensities around 0.5–100 mW/cm^2. The vertical dashed lines indicate the region used for extrapolation (200–300 K).

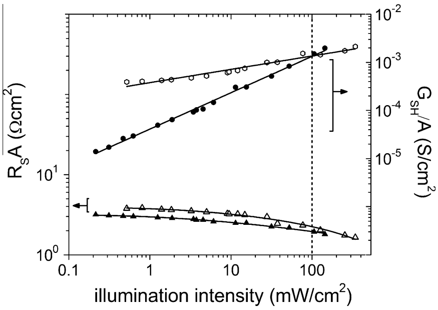

Fig. 5. Series resistance R_S (left scale, triangles) and shunt-conductance G_{sh} (right scale, circles) dependent on illumination intensity, of the *structured* (open symbols) and the *flat* (solid symbols) ZnO/In_2S_3/$CuInS_2$ solar cell.

A tentative solution to reduce the interface recombination in cells with a CIS absorber by varying the window layer instead of the buffer layer is proposed in Scheer (2012). Additionally, it has been reported that the saturation current activation energy of $CuInS_2$/CdS/ZnO cells of substrate type increased close to E_g values by using Ag added to precursor of $CuInS_2$ or, alternatively, by rapid thermal processing in H_2S environment (Reiβ et al., 2001).

The physical cause of the illumination dependency of the CSP deposited solar cells, which manifest itself most prominently in the cross-over of the dark and illuminated *J–V* curves, is still unclear. To look into this, non-idealities like series resistance R_S and shunt conductance G_{sh} of the cells are evaluated at varied illumination conditions. The R_S and G_{sh} values extracted from the *J–V* data at varied illumination intensities are presented in Fig. 5. One can see that R_S values above 2 Ω cm^2 at $T = 300$ K are present at varied illumination, which can be considered detrimental to the output of a solar cell. Series resistance of 0.7 Ω cm^2 has been reported as acceptable for devices with reasonable open-circuit voltage (Khelifi et al., 2010).

Another concern is the large photo-sensitivity of G_s (*photoconductance* of the shunt-path) while increasing the illumination intensity, especially conspicuous for the *flat* cell. Values of G_{sh} at the highest used illumination intensity, see Fig. 5, reach as much as ~100 times or ~5 times the values of G_{sh} when measured at low illumination, for the *flat* and the *structured* cell, respectively. This behavior can be explained as discussed further below.

Additionally, the G_{sh} of the *structured* cell, although showing less *photoconductance* while varying the illumination intensity in the range of 0.5–100 mW/cm^2, remains higher from G_{sh} of the *flat* cell at illumination intensities below 100 mW/cm^2. Such discrepancy is most likely a result of a higher absorption ability in the *structured* solar cell, as seen from *EQE* spectra (Fig. 1a), thus from a higher photodoping effect at similar illumination intensities when compared to the *flat* cell, however, valid at illumination intensities below 100 mW/cm^2. The circumstances do change at illumination intensities >100 mW/cm^2, where G_{sh} of the *structured* cell remains lower than G_{sh} of the *flat* cell. Despite all, the absolute values of the G_{sh} seem not to be a major disadvantage of the CSP deposited solar cell because G_{sh} remains below 10^{-3} S/cm^2 (Scheer and Schock, 2011) at varied illumination, see Fig. 5.

Interestingly, the *structured* cell performs better than the *flat* cell only at illumination intensities >2 mW/cm^2, see Fig. 6d. Although the J_{sc} of the *structured* cell remains higher at >2 mW/cm^2 illumination, a significant deterioration of the V_{oc}, *FF* and, as a result, a lower conversion efficiency η is measured at illumination intensities lower than 2 mW/cm^2, as compared to the *flat* reference cell. Comparing the tendency of V_{oc}, *FF* and η to illumination dependent G_{sh} values, see Fig. 5, a causality could be proposed. We see that a much higher G_{sh} is present at low illumination intensity with the *structured* solar cell compared to that of the *flat* cell. However, at higher illumination intensity, G_{sh} is comparable with that of the *flat* cell. Thus, the shunt-conductance limits the performance of the chemically sprayed *structured* solar cell at low illumination intensity.

At significant photodoping, the dominant recombination mechanism of a solar cell can be changed due to changes in the band diagram (Scheer and Schock, 2011). This could already be predicted from the comparison of the ideality factors in dark and at illumination, see Fig. 3. In other words, the ideality factor, in addition to G_{sh} and R_S (Fig. 5), is expected to be illumination dependent. This is indeed the case, see Fig. 7. The *structured* cell shows a stronger evolution of the ideality factor under varied illumination, compared to the *flat* cell. A higher sensitivity of the *structured* cell V_{oc} upon varied illumination can also be observed, compare Fig. 4a and b. Thus, it could be speculated that due to the ideality factors photosensitivity, the extrapolation of V_{oc} to 0 K does not yield a single value but rather an interval of activation energies E_A at varied illumination for both cells (Fig. 4a and b). In the *structured* cell, a higher photodoping effect is inflicted from higher absorption (Fig. 1a), higher currents (Fig. 6a), and a rougher window layer of the *structured* solar cell.

In the *structured* cell, the illumination dependence of G_{sh} and ideality factor *n* seems to be in correlation, see Figs. 5 and 7. However, when we include the *flat* cell, such an inference is not so clear. In order to clarify if the photosensitivity of the ideality factor (Fig. 7) is influenced by the photosensitive shunt-conductance (Fig. 5), we should elucidate the physical location of the shunts. In literature, the diffusion of Cu from CIS layer into the In_2S_3 layer is experimentally shown by X-ray photoelectron spectroscopy (XPS) measurements for substrate configuration type $CuInS_2$/In_2S_3 solar cells deposited by CSP (Theresa John et al., 2005). The fact that In_2S_3 buffer layer might be unintentionally doped with Cu during preparation of the solar cell suggests that the behavior of the G_{sh} and R_S (Fig. 5) is due to the photoconductivity of In_2S_3:Cu layer (Gilles et al., 1962). Based on the assumption of the existence of a In_2S_3:Cu interface layer, the cross-over effect observed

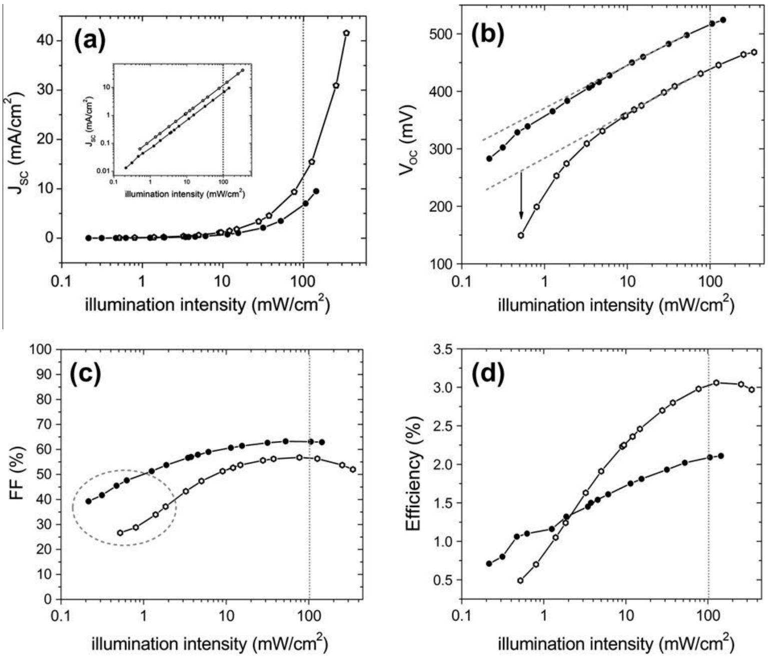

Fig. 6. Illumination dependence at $T = 300$ K of the J_{sc} (a), V_{oc} (b), FF (c) and conversion efficiency η (d) of the *structured* (open symbols) and the *flat* (solid symbols) ZnO/In_2S_3/$CuInS_2$ solar cell. The in-set of (a) shows J_{sc} in a logarithmic scale. From (d) it is clear that the *structured* solar cell performs better at higher illumination intensities.

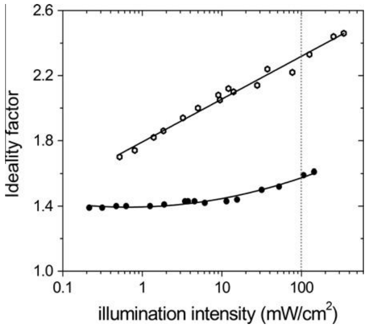

Fig. 7. Illumination dependence at $T = 300$ K of the ideality factor of the *structured* (open symbols) and the *flat* (solid symbols) ZnO/In_2S_3/$CuInS_2$ solar cell.

in our cells (Fig. 2) could be explained. In this view, the photodoping of the buffer layer increases the potential drop over the buffer, thus reducing an existing electron barrier in the conduction band and increasing diode current under illumination (Scheer and Schock, 2011). Similarly, the violation of the shifting approximation (Fig. 2) could be explained based on an illumination dependent shunt path (most likely in the buffer) which, at illumination, would drain a higher current (see Fig. 5) Scheer and Schock, 2011. Furthermore, as speculated in Section 3.1 (Analysis of the *EQE*), a lower growth temperature could be expected for the absorber deposited on top of the *structured* window/buffer layer. A lower growth temperature, which retards the Cu diffusion into In_2S_3, could serve as an explanation to a lowered photosensitivity of the shunt conductance of the *structured* cell, see Fig. 5. Ultimately, the diffusion of Cu from the absorber layer to the buffer is a factor which, according to our assumption, hinders the cell performance and obstructs characterization.

In order to hold back Cu-diffusion into the In_2S_3 buffer, a double-layer CIS structure has been proposed to improve performance of In_2S_3/$CuInS_2$ type substrate configuration solar cells deposited by the CSP method (Cherian et al., 2012). Recently, we showed (Katerski et al., 2012) that lowering the CIS growth temperature of the *flat* superstrate cell from 320 °C to 250 °C results in the following changes: increase of the V_{OC} extrapolated to 0 K from 960 meV up to 1170 meV, increase of V_{oc} from 370 meV to 570 meV, increase FF from 38% to 58%. As a drawback, J_{sc} was reduced from 7.2 mA/cm^2 to 3.5 mA/cm^2. Although the resulting efficiency gain was moderate, from 1% to 1.2%, the cross-over effect was reduced with decreasing the absorber growth temperature. Finally, for solar cells with CIS grown at 250 °C, no cross-over was observed. Possibly, diffusion of Cu into the buffer layer is significantly reduced at lower CIS deposition temperatures. Likewise, Cu diffusion restricts us to apply rapid thermal processing (RTP) technique (Reiβ et al., 2001) for the CIS absorber in a superstrate configuration. In addition, the suggested In_2S_3:Cu photosensitive interface layer (as speculated above) can tentatively be proposed to be responsible for the different dominating recombination mechanism in dark and at illuminated conditions (Fig. 3). To eliminate problems associated with Cu diffusion into the buffer layer, Cu-free absorbers, e.g. binary compounds like Sb_2S_3 (Dittrich et al., 2011; Hodes and Cahen, 2012) or SnS (Ramakrishna Reddy et al., 2006; Ristov et al., 2001; Ghosh et al., 2010), are considered for further developing the low-cost superstrate type solar cell deposited by the CSP method.

3.3. Analysis of the C–f characteristics

The admittance spectroscopy provides valuable insight to evaluate energy distibution of defect levels in a semiconductor bandgap. Admittance spectroscopy measurements were interpreted using theory given by Walter (Walter et al., 1996). The *C–f* characteristics of the cells are presented in Fig. 8. The *flat* cell (Fig. 8a) features a capacitance plateau at ca 20 nF/cm^2 obtained at the lowest used temperatures 100–140 K at frequencies 10^3–10^4 Hz. The plateau is referred to as high frequency capacitance (C_{HF}) Scheer and Schock, 2011; Khelifi et al., 2011. A further capacitance drop below C_{HF} to around 10 nF/cm^2 could be assigned to the freeze-out of the majority carriers at low-temperature, high-frequency regime (Khelifi et al., 2011; Herberholz et al., 1998; Bayhan and Sertap Kavasoğlu, 2006). Similar *C–f* features of the *structured* cell (Fig. 8b) are not so evident. For both cells, inductance cannot be identified in the capacitance spectra (Scofield, 1995), however the parasitic effect due to series resistance is visible at frequencies >10^6 Hz, where spectra tend to converge towards 0 F/cm^2 (Lauwaert et al., 2010).

The low-frequency capacitance C_{LF} is a sum of C_{HF} and contribution of electronically active traps in the depletion region of the *pn*-junction (Khelifi et al., 2011; Bayhan and Sertap Kavasoğlu, 2003). A relatively slow but distinctive capacitance decay from C_{LF} to C_{HF} at varied temperatures over several frequency magnitudes indicates a band of defects (Walter et al., 1996; Marlein et al., 2009) for both the *flat* and the *structured* cell. The appearance of the capacitance step is due to charging and discharging of deep levels in the bandgap. The position of the capacitance step is expected to shift towards higher frequencies when increasing the cell temperature (Bayhan and Sertap Kavasoğlu, 2006). At the highest measurement temperature used $T = 360$ K, roughly a step of 120 nF/cm^2 for the *structured* and 60 nF/cm^2 for the *flat* cell, was observed from the C_{LF} transition to C_{HF}, indicating a higher defect concentration in the relevant component material of the *structured* cell, compared to the *flat* cell (Bayhan and Sertap Kavasoğlu, 2006). At the C_{LF} regime, however, capacitance is not frequency independent in the studied temperature range for either of the cells, indicating a tail-like defect distribution (Walter et al., 1996).

The energetic distribution of defect states in the bandgap is evaluated from the temperature dependent admittance spectroscopy using the method proposed by Walter et al. (1996). The frequency ω is converted to the energetic distance E_ω from the respective band edge

$$E_\omega = kT \ln \frac{2\nu_0}{\omega} \tag{2}$$

where ν_0 is the attempt-to-escape frequency, and ω is the angular frequency $\omega = 2\pi f$. The calculation of absolute values of defect density $N_t(E_\omega)$ is omitted. Instead, a *scaled derivative* (Decock et al., 2011), which is independent of band-bending assumptions and proportional to N_t, is calculated. The scaled derivative is defined as (Decock et al., 2011):

$$-\frac{1}{w}\frac{dC}{d\omega}\frac{\omega}{kT} \tag{3}$$

Thus, the energetic distribution of defects is determined using the derivative of the junction capacitance C_p. The *scaled derivative* of C_p was plotted at varied temperatures, followed by proper choice of the attempt-to-escape fre-

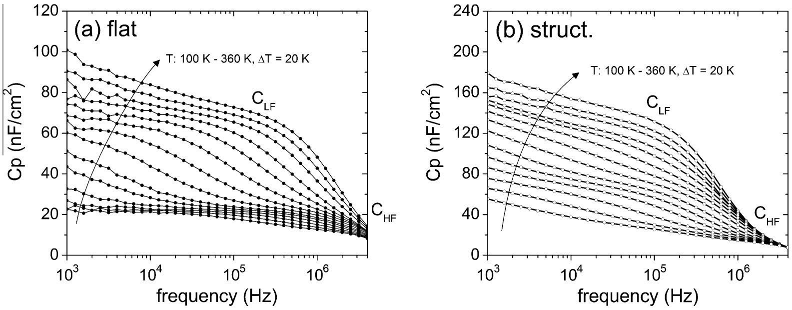

Fig. 8. *C–f* characteristics temperature dependence in steps of 20 K, of the *flat* (a) and the *structured* (b) $ZnO/In_2S_3/CuInS_2$ solar cell, at 0 V bias. One significant drop of capacitance can be distinguished at the studied temperature and frequency range for both solar cells. Notice the different scale height of the vertical axis.

quency, as stipulated by Walter et al. (1996). The results are presented in Fig. 9, whereas both graphs are a composed of the *scaled derivatives* at different temperatures, merged and smoothed with a specially designed algorithm (Decock et al., 2011). The *scaled derivative* when evaluated for the *flat* cell yields a relatively wide band of states centered at 200 meV. High temperature measurements indicate a tail of states reaching from 270 meV towards the midgap. We see much difference in the defect energy distribution of the *flat* and the *structured* cell. The *structured* cell has a distinct lower energy defect band around 100 meV which is not present in the *flat* cell. The peak around 220 meV of the *structured* cell is close to the peak around 200 meV of the *flat* cell, implying that these two peaks may have common origin which is inherent in the relevant material. We also expect a broad defect band in the *structured* cell that extends to its midgap. In general, the deep level defects in the *structured* cell appear to be more broadband than in the *flat* cell.

In addition, the *structured* cell shows higher values of the *scaled derivative*. Assuming that the built-in voltage and the Fermi level of the cells are comparable to each other, it follows that the *structured* cell has a higher defect concentration than the *flat* cell because its *scaled derivative* is higher. A higher content of Cu_XS, as speculated in Section 3.1 (Analysis of the *EQE* spectra), is likely to cause a higher density of defects in the absorber of the *structured* cell. Furthermore, the higher concentration of defects and a broader defect distribution with an additional band of defects in the *structured* cell are likely to cause the lower V_{oc} (Fig. 2), as compared to the *flat* cell, in addition to the effect of increased interface recombination.

At this stage of analysis, the model will not reveal whether the defect bands are near the conduction or valence band edge. Furthermore, the spacial location of these defect bands is still unclear. It is known that capacitance measurements are characteristic of the least doped side of a *pn* junction (Verschraegen et al., 2005). We rely on the standard Mott–Schottky analysis of the *C–V* measurements (not shown), which indicate that the capacitance originates from a *p*-type material. That is, a negative slope of the $d(C^{-2})/dV$ curve was observed. Thus, $CuInS_2$ absorber bulk or buffer/absorber interface will be considered, because In_2S_3 and In_2S_3:Cu are of *n*-type conductivity.

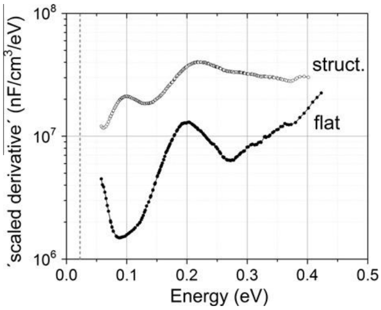

Fig. 9. The *scaled derivative* of the capacitance C_p spectra (at 3×10^2–5×10^5 Hz) of the *flat* and the *structured* $ZnO/In_2S_3/CuInS_2$ solar cell at 0 V bias. The bands centered at ca 220 meV (*structured*) and 200 meV (*flat*) correspond to the distinctive capacitance steps in Fig. 8. The parameters used are: attempt-to-escape frequency $\nu_0 = 2.88 \times 10^9$ Hz and relative dielectric permittivity $\varepsilon = 10$ (for both cells). The dashed line at ca 26 meV indicates *kT* at room temperature.

Evidently, wide defect bands are present in both cells (Fig. 9). The *J–V* study shows rather clearly that recombination at the interface is predominant. However, if one assumes that the Fermi level is fixed at the interface with respect to the bands, a broad defect distribution should be of bulk origin and cannot be attributed to the interface (Walter et al., 1996). Thus, the admittance spectroscopy analysis here only confirms the existence of other non-interface defects but this does not necessarily negate the existence of interface states. Ultimately, at predominant tunneling contribution to the recombination (Fig. 3), there may be no sense to distinguish between interface and bulk recombination (Nadenau et al., 2000).

Identification of defect levels in chalcopyrite type solar cells has attracted considerable interest, see for example DLTS studies on CdS/CIS cells (Siemer et al., 2001b), photoluminescence studies on chalcopyrites (Siebentritt et al., 2010), and references within. In this work, identification of the defect bands is omitted due to possibly ambiguous CIS phase composition. To further investigate the possible physical origin of the detected defect levels in the cells, measurements of $N_t(V)$ should be evaluated using an extended model (Decock et al., 2011) for clarifying the origin of the distinguished steps in the *C–f* plots and to improve accuracy.

4. Conclusions

The results of *J–V* measurements show that the diode ideality factors of the *structured* and the *flat* $ZnO/In_2S_3/CuInS_2$ cells prepared by CSP have a significant temperature and illumination dependence. The current in dark and at illumination of the ETA CIS cells is controlled by interface recombination. The cells have a saturation current that is mostly thermally activated at illuminated conditions, while tunneling enhanced interface recombination is deduced from measurements in dark. Relatively large series resistance above $2\ \Omega\ cm^2$ is characteristic of both cell types and the shunt-conductances obtain highest values of 10^{-3} S/cm^2 at 1 sun illumination due to photosensitivity. Although light absorption ability increases, we are faced with a less effective carrier collection when using a cell with a nanostructured window layer instead of an all-*flat*-layers inorganic $ZnO/In_2S_3/CuInS_2$ solar cell. The latter is attributed to two effects. In addition to increased interface recombination, there are more defects in the *structured* cell which are broader in energy and suspectedly higher in concentration when compared to the *flat* cell as shown by admittance spectroscopy. However, due to higher light absorption ability, the efficiency of the *structured* cell at 1 sun is higher than that of the *flat* cell. We recognized that the diffusion of copper from the absorber to the buffer layer is likely to cause the illumination dependent properties of the cell materials. Thus, for further development of the low-cost superstrate type solar cell deposited by the CSP method, binary compounds like Sb_2S_3 or SnS for use as absorber material are considered.

Acknowledgements

Financial support by Estonian Ministry of Education and Research (SF0140092s08); Estonian Science Foundation (ETF9081 and ETF8509) and European Union through the European Regional Development Fund (Centre of Excellence "Mesosystems: Theory and Applications", TK114) is gratefully acknowledged; E.K. acknowledges graduate school "Functional materials and technologies" receiving funding from the European Social Fund under Project 1.2.0401.09-0079 in Estonia; and European Social Fund's Doctoral Studies and Internationalisation Programme DoRa for supporting the research stay at Gent University. Dr. Arvo Mere, Dr. Jüri Krustok and Dr. Koen Decock are thanked for valuable discussions.

References

Antony, A., Asha, A.S., Yoosuf, R., Manoj, R., Jayaraj, M.K., 2004. Growth of $CuInS_2$ thin films by sulphurisation of Cu–In alloys. Sol. Energy Mater. Sol. Cells 81, 407–417.

Bayhan, H., Sertap Kavasoğlu, A., 2003. Admittance and impedance spectroscopy on Cu(In, Ga)Se_2 solar cells. Turk. J. Phys. 27, 529–535.

Bayhan, H., Sertap Kavasoğlu, A., 2006. Study of CdS/Cu(In, Ga)Se_2 heterojunction interface using admittance and impedance spectroscopy. Sol. Energy 80, 1160–1164.

Camus, C., Allsop, N.A., Gledhill, S.E., Bohne, W., Röhrich, J., Lauermann, I., Lux-Steiner, M.C., Fischer, C.H., 2008. Properties of Spray ILGAR $CuInS_2$ thin films. Thin Solid Films 516, 7026–7030.

Cherian, A.S., Jinesh, K.B., Kashiwaba, Y., Abe, T., Balamurugan, A.K., Dash, S., Tyagi, A.K., Sudha Kartha, C., Vijayakumar, K.P., 2012. Double layer $CuInS_2$ absorber using spray pyrolysis: a better candidate for $CuInS_2/In_2S_3$ thin film solar cells. Sol. Energy 86, 1872–1879.

Decock, K., Khelifi, S., Buecheler, S., Pianezzi, F., Tiwari, A.N., Burgelman, M., 2011. Defect distributions in thin film solar cells deduced from admittance measurements under different bias voltages. J. Appl. Phys. 110, 063722.

Dittrich, T., Belaidi, A., Ennaoui, A., 2011. Concepts of inorganic solid-state nanostructured solar cells. Sol. Energy Mater. Sol. Cells 95, 1527–1536.

Ernst, K., Belaidi, A., Könenkamp, R., 2003. Solar cell with extremely thin absorber on highly structured substrate. Semicond. Sci. Technol. 18, 475–479.

Ghosh, B., Roy, R., Chowdhury, S., Banerjee, P., Das, S., 2010. Synthesis of SnS thin films via galvanostatic electrodeposition and fabrication of CdS/SnS heterostructure for photovoltaic applications. Appl. Surf. Sci. 256, 4328–4333.

Gilles, J.M., Hatwell, H., Offergeld, G., van Cakenberghe, J., 1962. Photoconductivity in indium sulfide. Phys. Status Solidi B 2, K73–K77.

Goossens, A., Hofhuis, J., 2008. Spray-deposited $CuInS_2$ solar cells. Nanotechnology 19, 424018.

Herberholz, R., Igalson, M., Schock, H.W., 1998. Distinction between bulk and interface states in $CuInSe_2$/Cd/ZnO by space charge spectroscopy. J. Appl. Phys. 83, 318–325.

Herzog, C., Belaidi, A., Ogacho, A., Dittrich, T., 2009. Inorganic solid state solar cell with ultra-thin nanocomposite absorber based on nanoporous TiO_2 and In_2S_3. Energy Environ. Sci. 2, 962–964.

Hodes, G., Cahen, D., 2012. All-Solid-State, Semiconductor-Sensitized Nanoporous Solar Cells. Acc. Chem. Res. 45, 705–713.

Kaiser, I., Ernst, K., Fischer, C.H., Könenkamp, R., Rost, C., Sieber, I., Lux-Steiner, M.C., 2001. The eta-solar cell with $CuInS_2$: a photovoltaic cell concept using an extremely thin absorber (eta). Sol. Energy Mater. Sol. Cells 67, 89–96.

Kärber, E., Katerski, A., Oja Acik, I., Mikli, V., Mere, A., Krunks, M., 2011. Effect of H_2S treatment on properties of $CuInS_2$ thin films deposited by chemical spray pyrolysis at low temperature. Thin Solid Films 519, 7180–7183.

Katerski, A., Kärber, E., Krunks, M., Mikli, V., Mere, A., 2012. Development of sprayed $CuInS_2$ thin film absorber for nanostructured solar cell. In: MRS Proceedings, 1447, mrss12-1447-w10-47, <http://dx.doi.org/10.1557/opl.2012.1511>.

Khelifi, S., Belghachi, A., Lauwaert, J., Decock, K., Wienke, J., Caballero, R., Kaufmann, C.A., Burgelman, M., 2010. Characterization of flexible thin film CIGSe solar cells grown on different metallic foil substrates. Energy Procedia 2, 109–117.

Khelifi, S., Decock, K., Lauwaert, J., Vrielinck, H., Spoltore, D., Piersimoni, F., Manca, J., Belghachi, A., Burgelman, M., 2011. Investigation of defects by admittance spectroscopy measurements in poly (3-hexylthiophene):(6,6)-phenyl C_{61}-butyric acid methyl ester organic solar cells degraded under air exposure. J. Appl. Phys. 110, 094509.

Kieven, D., Dittrich, T., Belaidi, A., Tornow, J., Schwarzburg, K., Allsop, N., Lux-Steiner, M., 2008. Effect of internal surface area on the performance of ZnO/In_2S_3/CuSCN solar cells with extremely thin absorber. Appl. Phys. Lett. 92, 153107.

Klaer, J., Bruns, J., Henninger, R., Siemer, K., Klenk, R., Ellmer, K., Bräunig, D., 1998. Efficient $CuInS_2$ thin-film solar cells prepared by a sequential process. Semicond. Sci. Technol. 13, 1456.

Krunks, M., Mellikov, E., Bijakina, O., 1997. Copper sulfides by chemical spray pyrolysis process. Phys. Scr. T69, 189–192.

Krunks, M., Kijatkina, O., Rebane, H., Oja, I., Mikli, V., Mere, A., 2002. Composition of $CuInS_2$ thin films prepared by spray pyrolysis. Thin Solid Films 403–404, 71–75.

Krunks, M., Katerski, A., Dedova, T., Oja Acik, I., Mere, A., 2008. Nanostructured solar cell based on spray pyrolysis deposited ZnO nanorod array. Sol. Energy Mater. Sol. Cells 92, 1016–1019.

Krunks, M., Kärber, E., Katerski, A., Otto, K., Oja Acik, I., Dedova, T., Mere, A., 2010. Extremely thin absorber layer solar cells on zinc oxide nanorods by chemical spray. Sol. Energy Mater. Sol. Cells 94, 1191–1195.

Krustok, J., Josepson, R., Raadik, T., Danilson, M., 2010. Potential fluctuations in $Cu_2ZnSnSe_4$ solar cells studied by temperature dependence of quantum efficiency curves. Phys. B 405, 3186–3189.

Lauwaert, J., Decock, K., Khelifi, S., Burgelman, M., 2010. A simple correction method for series resistance and inductance on solar cell admittance spectroscopy. Sol. Energy Mater. Sol. Cells 94, 966–970.

Lévy-Clément, C., Tena-Zaera, R., Ryan, M.A., Katty, A., Hodes, G., 2005. CdSe-Sensitized p-CuSCN/Nanowire n-ZnO Heterojunctions. Adv. Mater. 17, 1512–1515.

Marlein, J., Decock, K., Burgelman, M., 2009. Analysis of electrical properties of CIGSSe and Cd-free buffer CIGSSe solar cells. Thin Solid Films 517, 2353–2356.

Muffler, H.J., Fischer, C.H., Diesner, K., Lux-Steiner, M.C., 2001. ILGAR – a novel thin-film technology for sulfides. Sol. Energy Mater. Sol. Cells 67, 121–127.

Nadenau, V., Rau, U., Jasenek, A., Schock, H.W., 2000. Electronic properties of $CuGaSe_2$-based heterojunction solar cells. Part I: Transport analysis. J. Appl. Phys. 87, 584–593.

Otto, K., Oja Acik, I., Tõnsuaadu, K., Mere, A., Krunks, M., 2011. Thermoanalytical study of precursors for In_2S_3 thin films deposited by spray pyrolysis. J. Therm. Anal. Calorim. 105, 615–623, and references [9, 10, 12] therein.

Page, M., Niitsoo, O., Itzhaik, Y., Cahen, D., Hodes, G., 2009. Copper sulfide as a light absorber in wet-chemical synthesized extremely thin absorber (ETA) solar cells. Energy Environ. Sci. 2, 220–223.

Qasrawi, A.F., Gasanly, N.M., 2003. Photoelectronic and electrical properties of $CuIn_5S_8$ single crystals. Cryst. Res. Technol. 38, 1063–1070.

Ramakrishna Reddy, K.T., Koteswara Reddy, N., Miles, R.W., 2006. Photovoltaic properties of SnS based solar cells. Sol. Energy Mater. Sol. Cells 90, 3041–3046.

Rau, U., 1999. Tunneling-enhanced recombination in Cu(In, Ga)Se_2 heterojunction solar cells. Appl. Phys. Lett. 74, 111–113.

Rau, U., Jasenek, A., Schock, H.W., Engelhardt, F., Meyer, T., 2000. Electronic loss mechanisms in chalcopyrite based heterojunction solar cells. Thin Solid Films 361–362, 298–302.

Reiβ, J., Malmström, J., Werner, A., Henge, I., Klenk, R., Lux-Steiner, M.C., 2001. Current transport in $CuInS_2$ solar cells depending on absorber preparation. In: MRS Proceedings, 668, H9.4, Spring Meeting of the Materials Research Society, San Francisco.

Ristov, M., Sinadinovski, G., Mitreski, M., Ristova, M., 2001. Photovoltaic cells based on chemically deposited *p*-type SnS. Sol. Energy Mater. Sol. Cells 69, 17–24.

Scheer, R., 2012. Open questions after 20 years of $CuInS_2$ research. Prog. Photovolt: Res. Appl. 20, 507–511.

Scheer, R., Schock, H.W., 2011. Chalcogenide Photovoltaics: Physics Technologies, and Thin Film Devices. Wiley-VCH, Weinheim.

Scheer, R., Klenk, R., Klaer, J., Luck, I., 2004. $CuInS_2$ based thin film photovoltaics. Sol. Energy 77, 777–784.

Scofield, J.H., 1995. Effects of series resistance and inductance on solar cell admittance measurements. Sol. Energy Mater. Sol. Cells 37, 217–233.

Siebentritt, S., 2002. Wide gap chalcopyrites: material properties and solar cells. Thin Solid Films 403–404, 1–8.

Siebentritt, S., Igalson, M., Persson, C., Lany, S., 2010. The electronic structure of chalcopyrites – bands, point defects and grain boundaries. Prog. Photovolt: Res. Appl. 18, 390–410.

Siemer, K., Klaer, J., Luck, I., Bruns, J., Klenk, R., Bräunig, D., 2001a. Efficient $CuInS_2$ solar cells from a rapid thermal process (RTP). Sol. Energy Mater. Sol. Cells 67, 159–166.

Siemer, K., Klaer, J., Luck, I., Bräunig, D., 2001b. DLTS measurements on $CuInS_2$ solar cells. Thin Solid Films 387, 222–224.

Theresa John, T., Mathew, M., Sudha Kartha, C., Vijayakumar, K.P., Abe, T., Kashiwaba, Y., 2005. $CuInS_2/In_2S_3$ thin film solar cell using spray pyrolysis technique having 9.5% efficiency. Sol. Energy Mater. Sol. Cells 89, 27–36.

Verschraegen, J., Burgelman, M., Penndorf, J., 2005. Temperature dependence of the diode ideality factor in $CuInS_2$-on-Cu-tape solar cells. Thin Solid Films 480–481, 307–311.

Walter, T., Herberholz, R., Muller, C., Schock, H.W., 1996. Determination of defect distributions from admittance measurements and application to Cu(In, Ga)Se_2 based heterojunctions. J. Appl. Phys. 80, 4411–4420.

Winkler, M., Tober, O., Penndorf, J., Szulzewsky, K., Röser, D., Lippold, G., Otte, K., 2000. Phase constitution and element distribution in Cu–In–S based absorber layers grown by the CISCuT-process. Thin Solid Films 361–362, 273–277.

Winkler, M., Griesche, J., Konovalov, I., Penndorf, J., Wienke, J., Tober, O., 2004. CISCuT – solar cells and modules on the basis of $CuInS_2$ on Cu-tape. Sol. Energy 77, 705–716.

Wu, Y., Wadia, C., Ma, W., Sadtler, B., Alivisatos, A.P., 2008. Synthesis and photovoltaic application of copper(I) sulfide nanocrystals. Nano Lett. 8, 2551–2555.

Appendix A

Article III

E.Kärber, T.Raadik, T.Dedova, J.Krustok, A.Mere, V.Mikli, M.Krunks. (2011). „Photoluminescence of spray pyrolysis deposited ZnO nanorods“. Nanoscale Research Letters, 6(359), 1–7.

Kärber *et al. Nanoscale Research Letters* 2011, **6**:359
http://www.nanoscalereslett.com/content/6/1/359

Nanoscale Research Letters
a SpringerOpen Journal

NANO EXPRESS **Open Access**

Photoluminescence of spray pyrolysis deposited ZnO nanorods

Erki Kärber[1], Taavi Raadik[1], Tatjana Dedova[1], Jüri Krustok[1], Arvo Mere[1], Valdek Mikli[2] and Malle Krunks[1*]

Abstract

Photoluminescence of highly structured ZnO layers comprising well-shaped hexagonal rods is presented. The ZnO rods (length 500-1,000 nm, diameter 100-300 nm) were grown in air onto a preheated soda-lime glass (SGL) or ITO/SGL substrate by low-cost chemical spray pyrolysis method using zinc chloride precursor solutions and growth temperatures in the range of 450-550°C. We report the effect of the variation in deposition parameters (substrate type, growth temperature, spray rate, solvent type) on the photoluminescence properties of the spray-deposited ZnO nanorods. A dominant near band edge (NBE) emission is observed at 300 K and at 10 K. High-resolution photoluminescence measurements at 10 K reveal fine structure of the NBE band with the dominant peaks related to the bound exciton transitions. It is found that all studied technological parameters affect the excitonic photoluminescence in ZnO nanorods.

PACS: 78.55.Et, 81.15.Rs, 61.46.Km

Introduction

ZnO is a semiconductor material for various photonic and electrical applications. ZnO shows a unique set of physical and chemical properties, such as a wide band gap (3.37 eV), large exciton binding energy (60 meV) at room temperature, radiation hardness [1], piezoelectricity and photoelasticity [2] and surface chemistry sensitive to environment. Zinc oxide nanostructured layer comprizing nanorods, further denoted as ZnO nanorod layer (ZnO_{NRL}), is a material with large effective surface area, suitable for short-wavelength devices, such as ultraviolet (UV) light-emitting diodes (LED) [3,4], UV nanolaser arrays [5], UV photodetectors [6], field emitters [7], UV protectors-filters [8], and chemical sensors [9,10]. As a passive layer with light-trapping properties, ZnO_{NRL} can be used as an antireflection coating on silicon solar cells [11], surface-enhancing window layer in the second generation solar cells with extremely thin inorganic absorber layer (ETA) [12] or with dye-sensitized solar cells (DSSC) [13]. The chemical spray pyrolysis (CSP)-deposited ZnO_{NRL} was used in ETA solar cells showing energy conversion efficiency of 4.2% [14].

For many of such devices, a large-scale, low-cost fabrication of high optical and crystalline quality ZnO is desirable. Low-temperature chemical synthesis methods can provide large scale and low-cost fabrication. Photoluminescence (PL) is a very sensitive and an effective method to identify the dominant recombination mechanism and defects in materials. However, according to PL study, the as-deposited ZnO_{NRL} grown via a low-temperature wet-chemical methods (chemical bath, electrodeposition, hydrothermal growth) do not show a high excitonic to visible emission intensity ratio at 300 K (room temperature), indicating a high defect concentration in these samples [15-21]. The PL properties of ZnO_{NRL} deposited by the wet-chemical methods can be improved by post-growth annealing at high temperatures of 200-850°C in forming gas or vacuum environment [15,17-19,21].

In this study, strong excitonic PL is observed in the as-deposited ZnO_{NRL}, grown via CSP at growth temperatures up to 550°C from zinc chloride ($ZnCl_2$) solutions. CSP technique is a template- and catalyst-free method, allowing fast and low-cost deposition of ZnO_{NRL} [22]. According to XRD, ZnO_{NRL} comprise *c*-axis (002)-oriented, hexagonal rods of pure ZnO wurtzite phase with aspect ratio up to 30 [23,24]. The aim of this work is to study the variation in the PL response due to different growth parameters used for the CSP-deposited ZnO_{NRL}.

---

* Correspondence: malle@staff.ttu.ee
[1] Department of Materials Science, Tallinn University of Technology, Ehitajate tee 5, 19086 Tallinn, Estonia
Full list of author information is available at the end of the article

As a result, the PL properties were found to depend on the growth temperature, substrate type, spray rate, and the solvent type. The correlation between the electrical and the photoluminescence properties of the CSP-deposited ZnO_{NRL} were reported earlier [25]. Our previous studies on the CSP-deposited ZnO_{NRL} were focused on the development of the ZnO_{NRL} [22-24], no specific study on the PL of the CSP-deposited ZnO_{NRL} was reported until now.

Experimental

The ZnO_{NRL} were deposited by pneumatic CSP method in air at growth temperatures (T_G) of 480°C, 530°C, 550°C using zinc chloride ($ZnCl_2$) precursor solutions. Two kind of substrates were used: soda-lime glass (SGL) and commercial indium tin oxide-covered glass (ITO/SGL). The growth temperature T_G was controlled through the temperature of a molten tin bath used to obtain uniform heating of the substrate. Other deposition parameters were varied in the following: Three discrete values were used for the spray rate (v): 1.2, 2.2, and 6.2 ml/min. Two kinds of solvents for $ZnCl_2$ were used: H_2O and alcoholic solvent (H_2O + ethanol, in ratio of 2:3 by volume), the volume of spray solution was 50 ml. The concentration of $ZnCl_2$ in the spray solution was kept constant in the presented series ranging from 0.05 mol/L (Effect of the substrate on PL properties of ZnO_{NRL} and Effect of the spray rate on PL properties of ZnO_{NRL} sections) to 0.1 mol/L (General properties of ZnO_{NRL}, Effect of the growth temperature on PL properties of ZnO_{NRL}, and Effect of solvent type on PL properties of ZnO_{NRL} sections). The acidity of the solution was kept at pH = 5. The studied samples were as grown. XRD measurements were performed on a Rigaku Ultima IV diffractometer with Cu K_α radiation (λ = 1.5406 Å) using the silicon strip detector D/teX Ultra.

The photoluminescence (PL) measurements of ZnO_{NRL} were made at room temperature (T = 300 K) and at T = 10 K in a closed-cycle He cryostat (Janis). He-Cd laser (325 nm) was used as an excitation source, the excitation intensity was approximately 0.5 mW/mm^2. The luminescence emission in the energy region of 1.45-3.45 eV was dispersed by a computer-controlled Carl Zeiss SPM-2 monochromator (f = 0.4 m) equipped with a prism and detected by FEU-79 photomultiplier with a lock-in amplifier. High-resolution LabRam Horiba Yvon HR 800 spectrometer and CCD-detector were used in the region of 3.30-3.40 eV for a closer study of the PL of ZnO_{NRL} in UV-region. The same apparatus was used for the Raman spectroscopic studies. Zeiss EVO-MA15 apparatus was used for the scanning electron microscopic (SEM) and the energy dispersive spectroscopic (EDS) study of the ZnO_{NRL}. The apparatus was equipped with the Oxford Instruments PentaFet x3 spectrometer using the INCA Energy EDS system at accelerating voltage of 7 kV.

Results and discussion

General properties of ZnO_{NRL}

Typical XRD pattern of sprayed ZnO_{NRL} is presented in Figure 1. According to XRD, the as-grown ZnO_{NRL} are highly *c*-axis-oriented hexagonal (wurtzite) ZnO structures. The Raman spectrum of as-deposited ZnO_{NRL} is presented in Figure 2. Raman peaks located at 99 and 438 cm^{-1} with a fitted excitonic peak widths (FWHM) of 1.2 and 6.1 cm^{-1}, respectively, are dominant ones. Raman peaks at 99, 438, and 379 cm^{-1} are attributed to the E_2(low), E_2(high), and A_1(TO) Raman modes of wurtzite phase of ZnO, respectively [26]. The Raman peak at approximately 580 cm^{-1} which is correlated to V_O and/or Zn_i defects [27] is not observed. The peaks at 128, 330, and 1,153 cm^{-1} are due to the second order or multiple phonon scattering of the Raman modes of the ZnO wurtzite structure, observed by other authors as well [28]. The sharp Raman peaks characteristic of the wurtzite phase and the absence of defect-induced Raman peaks is an indication of a high-quality crystalline material. According to EDS analysis, the O/Zn atomic ratio in ZnO_{NRL} is ca. 1.5. The excess of oxygen (compared to the stoichiometric ZnO) as well as the presence of In, Sn, and Si signal in the EDS spectra (not presented), originates from the ITO/SGL substrate. Other elements are not detected by the EDS.

SEM surface images of ZnO_{NRL} grown onto ITO/SGL substrate are presented as Figure 3. The ZnO_{NRL} deposited from aqueous solution of $ZnCl_2$ (0.1 mol/L) at T_G =

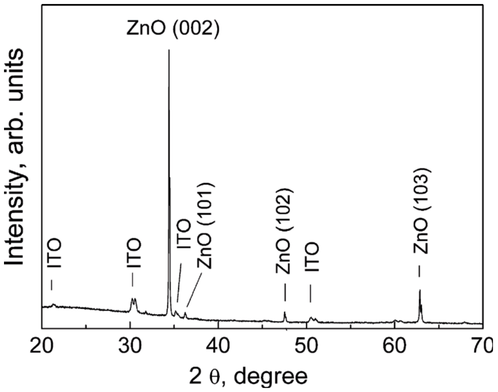

Figure 1 XRD pattern of ZnO nanorod layer deposited by chemical spray pyrolysis. The layer was deposited onto ITO/SGL substrate at growth temperature of 550°C, using aqueous solution. SEM image of the corresponding ZnO nanorod sample is presented in Figure 3a.

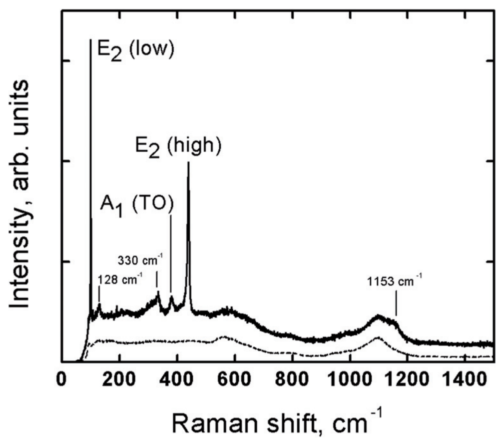

Figure 2 Raman spectrum of ZnO nanorod layer deposited by chemical spray pyrolysis. The layer was deposited onto ITO/SGL substrate at growth temperature of 550°C, using aqueous solvent. SEM image of the corresponding ZnO nanorod sample is presented in Figure 3a. The Raman spectrum of the ITO/SGL substrate is shown with the dashed line.

550°C is composed of separately standing ZnO crystals with a diameter of 100-300 nm and length of ca. 800 nm, see Figure 3a. When grown at a lower temperature of T_G = 480°C using aqueous solutions, the rod-like shape of the crystals is not well-developed (Figure 3b) as also shown in our earlier study [22]. However, the deposition of an alcoholic solution at T_G = 480°C results in well-developed hexagonal rods with a diameter of ca. 100-200 nm and length of ca. 700-800 nm (see Figure 3c). This result indicates that the spray of an alcoholic solution allows to obtain ZnO_{NRL} composed of rods with high aspect ratio at lower substrate temperature compared to the spray of aqueous solution.

The PL spectra of the best ZnO_{NRL} samples show a dominant near band edge (NBE) emission at T = 10 K and at T = 300 K, see Figure 4 (further discussion in Effect of the substrate on PL properties of ZnO_{NRL}, Effect of the growth temperature on PL properties of ZnO_{NRL}, Effect of the spray rate on PL properties of ZnO_{NRL}, and Effect of solvent type on PL properties of ZnO_{NRL} sections). The NBE peak positions were determined by fitting the spectra with the Lorentz distribution using the Fityk curve-fitting freeware. The NBE peak measured at T = 300 K is due to free exciton transition. High-resolution PL measurements at T = 10 K reveal four transitions due to bound excitons: a prevailing exciton peak at 3.358-3.360 eV, two other exciton peaks at 3.363 eV and 3.368-3.370 eV, a peak of the two electron transition at 3.334-3.335 eV and the free exciton peak at 3.378 eV [26,29-32]. The exciton peak at ca. 3.360 eV, which is attributed to a donor-related transition by many authors [26,29-32], is present as the dominant transition, irrespective of the deposition conditions.

Effect of the substrate on PL properties of ZnO_{NRL}

The PL spectra of ZnO_{NRL} deposited at T_G of 550°C onto the SGL and the ITO/SGL substrates, are presented as Figure 4. We can see a drastic reduction of the red band intensity at 10 K in case of ZnO_{NRL} on ITO/SGL substrate. In addition, the green PL emission band in the region of 2.2-2.8 eV is not present at T = 10 K and at T = 300 K in case of the ITO/SGL substrate used. This could be expected because strong red and green bands do not tend to co-exist [26,33].

The broad and structureless green luminescent band is mostly reported as an intrinsic defect level due to V_O [34,35] or V_{Zn} [36] or both, acting as a donor-deep-acceptor pair [37]. Although controversial, the band is most likely a native complex defect of zinc vacancy involving Zn_i, O_{Zn}, and V_O [26]. The origin of another visible Gaussian band, the red band in region of 1.5-2.0 eV, is attributed to interstitial-type defects like Zn_i, O_i [15,18] while PL bands between the red and the green

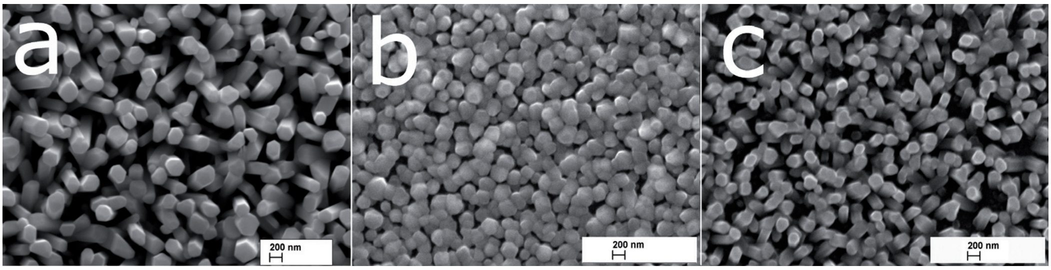

Figure 3 SEM images of ZnO nanorod layers deposited by chemical spray pyrolysis. The layers (**a**, **b**, **c**) were deposited onto ITO/SGL substrate at growth temperature of 550°C (a) or 480°C (b, c) using aqueous (a, b) or alcoholic solutions (c) at similar spray rate (2.2 ml/min).

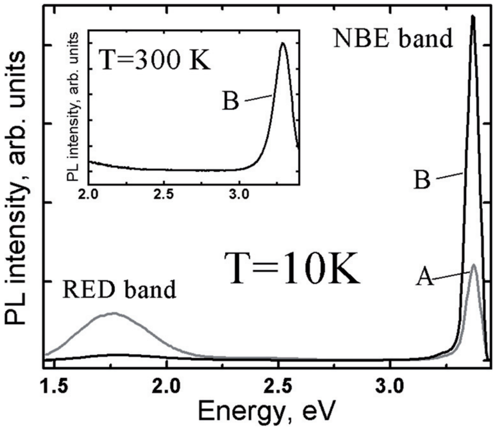

Figure 4 Photoluminescence spectra at 10 K of the spray pyrolysis-deposited ZnO nanorod layers. The layers were deposited from aqueous solution onto SGL or ITO/SGL substrates, illustrated by spectrum A and B, respectively. The growth temperature (550°C) and spray rate (6.2 ml/min) were kept similar. The inset shows the photoluminescence spectrum at 300 K in region of 2.0-3.4 eV, characteristic of ZnO nanorods deposited onto ITO/SGL substrate at temperature of 550°C.

band are commonly attributed to O_i [18,38-40]. Without a comprehensive study additional to PL spectroscopy, the defect identification remains speculative [15].

At room temperature (T = 300 K), for the ZnO_{NRL} grown at 550°C onto ITO/SGL, no green emission is detected, see Figure 4 inset. Therefore, we conclude that ZnO_{NRL} with a lower content of defects can be deposited using the ITO instead of SGL substrates, however, such a growth mechanism of the ZnO_{NRL} onto the ITO remains unclear. It may be speculated that a more homogenious lateral heat distribution may be responsible for the significant improvement of the NBE to red band intensity ratio (I_{NBE}/I_{RED}) in the case of using the ITO/SGL substrate for deposition of ZnO_{NR}. Another speculation may be that ITO acts as a barrier, restraining the diffusion of some elements, *e. g.*, sodium from the SGL glass during high-temperature spray process as it has been recorded by X-ray photoelectron spectroscopy for the CSP-deposited $CuInS_2$ films [41]. In such a case, borosilicate glass could be a suitable replacement for the SGL substrate. Whatever the reason might be, ITO-covered substrates are preferred in order to achieve ZnO_{NRL} with high crystal quality during the CSP process. This observation is of significant importance due to the fact that for many electronic applications including solar cells, a conductive and transparent material, such as ITO, is required as the substrate material.

Effect of the growth temperature on PL properties of ZnO_{NRL}

From our previous study, it is known that the increase of T_G from 480°C up to 550°C minimizes the intensity of the green PL band at 300 K [25]. The spectra recorded at T = 10 K (Figure 5) reveal that an increase of T_G from 480°C up to 550°C results in a PL spectra with significantly increased excitonic intensity, showing FWHM of 4.5 meV for ZnO_{NRL} grown at T_G = 550°C onto ITO/SGL substrate. Such low values of FWHM (4.5 meV) can be correlated to a very low concentration of defects [42]. In addition, the increase of the growth temperature of ZnO_{NRL} results in an increase of the ratio of NBE to red band intensity (the red band is not shown in Figure 5). The I_{NBE}/I_{RED} emission ratio increases as follows: 34, 39, and 160, illustrated by spectrum A, B, and C (in Figure 5), respectively. This is an indication of significant change in the defect composition in the ZnO_{NRL} and an increase of the crystal quality due to an increase of the growth temperature of ZnO_{NRL}. According to SEM study, the characteristic morphology of the samples changes with different T_G. The SEM image in Figure 3a is a characteristic of ZnO_{NRL} grown at T_G = 550°C. A significantly lower surface-to-volume area (no quantitative calculations were made) could be estimated from Figure 3b, presenting the SEM image of ZnO_{NRL} deposited at T_G = 480°C. At the same time, an increase of the excitonic PL band was

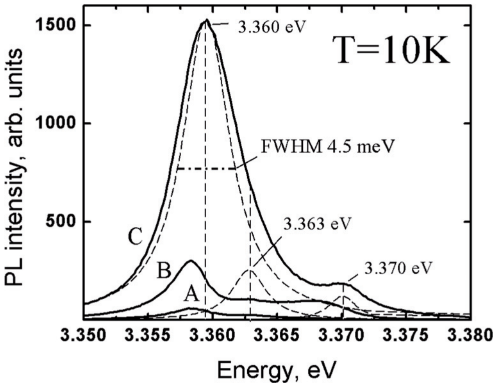

Figure 5 Excitonic photoluminescence spectra at 10 K of ZnO nanorod layers deposited at different growth temperatures. The growth temperature is kept at 480°C, 530°C, or 550°C, illustrated by spectrum A, B, and C, respectively. The ZnO nanorod layers are deposited onto ITO/SGL substrates from aqueous solution at similar spray rate (2.2 ml/min). Spectrum C is shown with fitting results, Raman spectrum of the corresponding ZnO nanorod sample is presented in Figure 1 and the SEM image is presented in Figure 3a. The SEM image of the sample corresponding to spectrum A is presented in Figure 3b.

registered without a decrease of the FWHM of the fitted peaks (Figure 5, spectra A-C). Therefore, the increase of the intensity of the excitonic band could be due to a higher surface-to-volume ratio of the ZnO_{NRL}, in addition to an increased crystal quality. A similar effect was described for the electrochemically synthesized ZnO nanowires [20].

In connection with the results in the Effect of the substrate on PL properties of ZnO_{NRL} section, higher T_G of 550°C and the ITO/SGL substrates are preferred for the deposition of ZnO_{NRL} in order to achieve high optical quality by the CSP method. The best samples were grown at 550°C onto ITO/SGL substrate, showing NBE emission only. Although, no significant reduction in FWHM is observed while using a higher growth temperature of 550°C, an apparent shift of the main NBE peak at approximately 3.360 eV towards higher energy could be an indicator of additional transitions. The high ratio of I_{NBE} to $I_{VISIBLE}$ emissions alone, although widely reported as an indication of good [43] or even excellent optical quality [7,44], may not be enough to characterize the purity of ZnO_{NRL} [15,43]. However, the resolvable fine structure of the excitonic PL emission could be taken as an indication of a relatively high crystal quality of the CSP deposited ZnO_{NRL}.

Effect of the spray rate on PL properties of ZnO_{NRL}

The effect of the variation in the spray rate on PL properties of ZnO_{NRL} is presented as Figure 6. A decrease in the spray rate from 6.2 ml/min down to 1.2 ml/min increases the intensity of the exciton peak at 3.358-3.360 eV.

The rise in the intensity of the peaks could be correlated to a longer deposition period, hence, a lower growth rate. In addition, the FWHM of the main peak decreases from 4.0 meV down to 2.2 meV, accompanied by a small shift from 3.360 eV to 3.358 eV in the exciton peak position. A shift in the position of a defect-bound exciton is a clear indication of a change in the type of the dominant impurity in the ZnO_{NRL}, while a smaller FWHM is a sign of increased crystal quality. For comparison, peak widths of 6-9 meV and 4.7 meV are reported for ZnO_{NRL} grown by hydrothermal method with post-deposition annealing [15] and thermal evaporation and vapor-phase transport [7], respectively. A FWHM of 1 meV is characteristic of the excitonic peak at 3.360 eV reported for a single crystal MOCVD-deposited ZnO_{NRL}, measured at 3.4 K [31]. The PL intensity in a log-scale reveals a free exciton peak at 3.378 eV appearing only at a spray rate of 1.2 ml/min (see Figure 6 inset), providing confirmation that a low defect density is obtained in ZnO_{NRL} [45]. Thus, in addition to high growth temperatures, low spray rates are preferred for CSP deposition of ZnO_{NRL} in case aqueous solutions are used.

Effect of solvent type on PL properties of ZnO_{NRL}

The effect of the use of different solvents on the PL properties of ZnO_{NRL} is presented as Figure 7. An exciton peak at 3.363 eV is observed only when aqueous

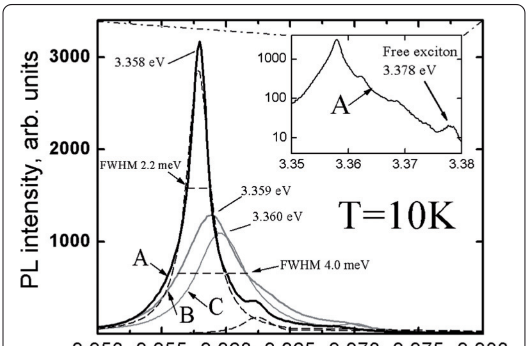

Figure 6 Excitonic photoluminescence spectra at *T* = 10 K of ZnO nanorod layers deposited at different spray rates. The layers are deposited from aqueous solutions onto ITO/SGL substrates at 550°C with spray rate of 1.2, 2.2, and 6.2 ml/min, illustrated by spectrum A, B, and C, respectively. Spectrum A is shown with fitting results. The inset in the Figure 6 shows spectrum A in logarithmic scale.

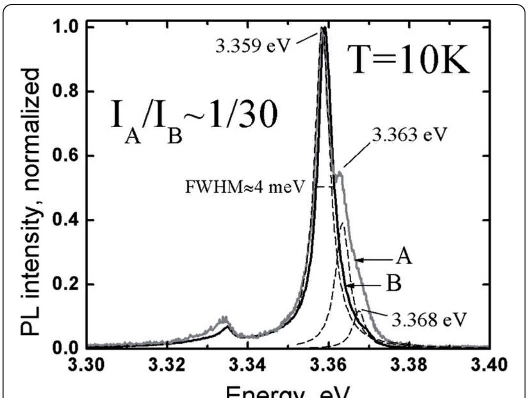

Figure 7 Normalized photoluminescence spectra of ZnO nanorod layers deposited using different solvents. The layers are deposited onto ITO/SGL substrate at 480°C from aqueous or alcoholic solution, illustrated by spectrum A and B, respectively. Spray rate is kept similar (2.2 ml/min). Spectrum A is shown with fitting results. SEM image of the sample corresponding to spectrum B is presented in Figure 3c.

solutions are used for deposition of ZnO_{NRL}. A shallow donor impurity corresponding to an excitonic peak at approximately 3.363 eV has been correlated to hydrogen impurity by many authors, see for example [29]. However, we can present no proof for hydrogen incorporation in this study, thus, it will not be considered further.

In case the alcoholic solvent is used, the excitonic band intensity increases approximately 30 times. The PL intensity ratio I_{NBE}/I_{RED} increases from 34 in case of aqueous up to 294 in case alcoholic solution is used. This observation could be explained taking into account a similar observation from the effect of the T_G (Effect of the growth temperature on PL properties of ZnO_{NRL} section). The use of an alcoholic solution results in a smaller spray droplet size, leading to a more homogeneous distribution of the sprayed solution over the substrate, compared to an aqueous solution. In addition to a smaller droplet size, the high volatility of the alcoholic solvent is very likely to cause a lower rate of the substrate cooling. Thus, a higher value of the effective growth temperature is expected in the reaction zone of pyrolysis, resulting in a somewhat higher growth temperature than the stated T_G. This can be discussed in the following.

Due to the fact that the PL spectrum A in Figure 7 coincides with spectrum A in Figure 5, we can see that the use of an alcoholic solution instead of an aqueous solution increases the NBE band intensity (approximately × 30) in ZnO_{NRL} deposited at 480°C (Figure 7). Similar effect has been observed while increasing the T_G from 480°C up to 550°C (Figure 5). In Effect of the growth temperature on PL properties of ZnO_{NRL} section, we tentatively attributed this effect to an increased surface-to-volume ratio of the ZnO_{NRL}. Similarly, the ZnO_{NRL} grown at 480°C from alcoholic solution (see SEM image in Figure 3c) shows a significantly increased surface-to-volume ratio compared to ZnO_{NRL} grown at 480°C from aqueous solution (see Figure 3b). Therefore, one possible cause of a higher NBE intensity of spectrum B compared to spectrum A in Figure 7, could be a higher surface-to-volume ratio, in addition to improved crystal quality.

Although the density of rods and the aspect ratio is known to increase when deposited from alcoholic solutions [46], the effect of the temperature cannot be overlooked either in the sense of an increased NBE intensity. As a result, it can be concluded that a lower T_G or a higher spray rate is acceptable for the CSP deposition of the ZnO_{NRL} in case an alcoholic solution is used, compared to the T_G and spray rates used for aqueous solutions (Effect of the growth temperature on PL properties of ZnO_{NRL} and Effect of the spray rate on PL properties of ZnO_{NRL} sections). The use of an alcoholic instead of aqueous solution could be applied in order to achieve a higher surface-to-volume ratio at a similar T_G. It must be pointed out, however, that the PL of the ZnO_{NRL} deposited at a low spray rate (1.2 ml/min) from aqueous solution was superior to all considered samples in sense of narrow NBE peaks (Effect of the spray rate on PL properties of ZnO_{NRL} section).

Conclusions

We report photoluminescence properties in as-deposited ZnO nanorod layers (ZnO_{NRL}), grown via fast and low-cost pneumatic CSP method in air. The results indicate that a good crystal quality can be achieved, while ZnO_{NRL} with the best optical quality were deposited at a growth temperature of 550°C using ITO/SGL substrate. No green or red emission was detected for these samples, measured at 10 K. In addition, green emission is absent at 300 K for the best samples. The prevalence of the bound exciton transitions suggests a low defect density in our best ZnO_{NRL}. Low spray rates (1.2 ml/min) are recommended in case aqueous solution is sprayed, otherwise alcoholic solution is preferred for the deposition of ZnO_{NRL}. Lower substrate temperature is acceptable in case alcoholic solution is used, in order to achieve comparable crystal quality, compared to the use of aqueous solution. At T = 10 K, fitted excitonic peak widths (FWHM) are 2-5 meV. For comparison, peak widths of 6-9 meV are reported for ZnO_{NRL} grown by hydrothermal method with post-deposition annealing [15]. These results indicate that the quality of the spray-deposited ZnO_{NRL} is superior compared to other solution-based methods in the sense of photoluminescence properties. The results of this study imply that the spray-deposited ZnO_{NRL} is sufficient for the use as a transparent window layer in an ETA solar cell and for applications to other low-cost photonic devices at room temperature.

Acknowledgements
The study is financially supported by: Estonian Ministry of Education and Research (SF0140092s08) and Estonian Science Foundation grants: ETF8509, ETF6954, and ETF8282.

Author details
[1]Department of Materials Science, Tallinn University of Technology, Ehitajate tee 5, 19086 Tallinn, Estonia [2]Centre for Materials Research, Tallinn University of Technology, Ehitajate tee 5, 19086 Tallinn, Estonia

Authors' contributions
EK carried out photoluminescence experiments, analysis, and interpretation of experimental results and writing of major part of paper, TR carried out photoluminescence experiments, TD designed and deposited ZnO nanorods, JK provided valuable theoretical discussions, AM provided valuable experimental discussions, VM carried out SEM study, MK designed the study, revised the manuscript, provided motivation and discussions. All authors read and approved the final version of the manuscript.

Competing interests
The authors declare that they have no competing interests.

Received: 26 January 2011 Accepted: 21 April 2011
Published: 21 April 2011

References

1. Look DC, Coskun C, Claflin B, Farlow GC: **Electrical and optical properties of defects and impurities in ZnO.** *Physica B: Condensed Matter* 2003, **340-342**:32-38.
2. Chen TT, Cheng CL, Fu SP, Chen YF: **Photoelastic effect in ZnO nanorods.** *Nanotechnology* 2007, **18**:225705.
3. Könenkamp R, Word RC, Godinez M: **Ultraviolet electroluminescence from ZnO/polymer heterojunction light-emitting diodes.** *Nano Lett* 2005, **5**:2005-2008.
4. Kim DC, Han WS, Cho HK, Kong BH, Kim HS: **Multidimensional ZnO light-emitting diode structures grown by metal organic chemical vapor deposition on p-Si.** *Appl Phys Lett* 2007, **91**:231901.
5. Zhou H, Wissinger M, Fallert J, Hauschild R, Stelzl F, Klingshirn C, Kalt H: **Ordered, uniform-sized ZnO nanolaser arrays.** *Appl Phys Lett* 2007, **91**:181112.
6. Ji LW, Peng SM, Su YK, Young SJ, Wu CZ, Cheng WB: **Ultraviolet photodetectors based on selectively grown ZnO nanorod arrays.** *Appl Phys Lett* 2009, **94**:203106.
7. Li C, Fang GJ, Liu NH, Li J, Liao L, Su FH, Li GH, Wu XG, Zhao XZ: **Structural, photoluminescence, and field emission properties of vertically well-aligned ZnO nanorod arrays.** *J Phys Chem C* 2007, **111**:12566-12571.
8. Wang RH, Xin JH, Tao XM, Daoud WA: **ZnO nanorods grown on cotton fabrics at low temperature.** *Chem Phys Lett* 2004, **398**:250-255.
9. Yang Z, Li LM, Wan Q, Liu QH, Wang TH: **High-performance ethanol sensing based on an aligned assembly of ZnO nanorods.** *Sensors and Actuators B-Chemical* 2008, **135**:57-60.
10. Liu FT, Gao SF, Pei SK, Tseng SC, Liu CHJ: **ZnO nanorod gas sensor for NO2 detection.** *J Taiwan Inst Chem Eng* 2009, **40**:528-532.
11. Chen JY, Sun KW: **Growth of vertically aligned ZnO nanorod arrays as antireflection layer on silicon solar cells.** *Sol Energy Mater Sol Cells* 2010, **94**:930-934.
12. Tena-Zaera R, Ryan MA, Katty A, Hodes G, Bastide S, Lévy-Clément C: **Fabrication and characterization of ZnO nanowires/CdSe/CuSCN eta-solar cell.** *C R Chim* 2006, **9**:717-729.
13. Baxter JB, Aydil ES: **Dye-sensitized solar cells based on semiconductor morphologies with ZnO nanowires.** *Sol Energy Mater Sol Cells* 2006, **90**:607-622.
14. Krunks M, Kärber E, Katerski A, Otto K, Acik IO, Dedova T, Mere A: **Extremely thin absorber layer solar cells on zinc oxide nanorods by chemical spray.** *Sol Energy Mater Sol Cells* 2010, **94**:1191-1195.
15. Tam KH, Cheung CK, Leung YH, Djurišić AB, Ling CC, Beling CD, Fung S, Kwok WM, Chan WK, Phillips DL, Ding L, Ge WK: **Defects in ZnO nanorods prepared by a hydrothermal method.** *J Phys Chem B* 2006, **110**:20865-20871.
16. Bekeny C, Voss T, Gafsi H, Gutowski J, Postels B, Kreye M, Waag A: **Origin of the near-band-edge photoluminescence emission in aqueous chemically grown ZnO nanorods.** *J Appl Phys* 2006, **100**:104317.
17. Wu LL, Wu YS, Pan XR, Kong FY: **Synthesis of ZnO nanorod and the annealing effect on its photoluuminescence property.** *Optical Materials* 2006, **28**:418-422.
18. Cross RBM, De Souza MM, Narayanan EMS: **A low temperature combination method for the production of ZnO nanowires.** *Nanotechnology* 2005, **16**:2188-2192.
19. Xiang B, Wang PW, Zhang XZ, Dayeh SA, Aplin DPR, Soci C, Yu DP, Wang DL: **Rational synthesis of p-type zinc oxide nanowire arrays using simple chemical vapor deposition.** *Nano Lett* 2007, **7**:323-328.
20. Voss T, Bekeny C, Gutowski J, Tena-Zaera R, Elias J, Lévy-Clément C, Mora-Sero I, Bisquert J: **Localized versus delocalized states: Photoluminescence from electrochemically synthesized ZnO nanowires.** *J Appl Phys* 2009, **106**:054304.
21. Hung CH, Whang WT: **A novel low-temperature growth and characterization of single crystal ZnO nanorods.** *Mater Chem Phys* 2003, **82**:705-710.
22. Dedova T, Krunks M, Grossberg M, Volobujeva O, Acik IO: **A novel deposition method to grow ZnO nanorods: Spray pyrolysis.** *Superlattices Microstruct* 2007, **42**:444-450.
23. Dedova T, Volobujeva O, Klauson J, Mere A, Krunks M: **ZnO nanorods via spray deposition of solutions containing zinc chloride and thiocarbamide.** *Nanoscale Res Lett* 2007, **2**:391-396.
24. Krunks M, Dedova T, Oja Açik I: **Spray pyrolysis deposition of zinc oxide nanostructured layers.** *Thin Solid Films* 2006, **515**:1157-1160.
25. Krunks M, Dedova T, Kärber E, Mikli V, Oja Acik I, Grossberg M, Mere A: **Growth and electrical properties of ZnO nanorod arrays prepared by chemical spray pyrolysis.** *Physica B* 2009, **404**:4422-4425.
26. Özgür Ü, Alivov YI, Liu C, Teke A, Reshchikov MA, Dogan S, Avrutin V, Cho SJ, Morkoc H: **A comprehensive review of ZnO materials and devices.** *J Appl Phys* 2005, **98**:041301.
27. Chen SJ, Liu YC, Lu YM, Zhang JY, Shen DZ, Fan XW: **Photoluminescence and Raman behaviors of ZnO nanostructures with different morphologies.** *J Cryst Growth* 2006, **289**:55-58.
28. Zhang R, Yin PG, Wang N, Guo L: **Photoluminescence and Raman scattering of ZnO nanorods.** *Solid State Sciences* 2009, **11**:865-869.
29. Meyer BK, Alves H, Hofmann DM, Kriegseis W, Forster D, Bertram F, Christen J, Hoffmann A, Strassburg M, Dworzak M, Haboeck U, Rodina AV: **Bound exciton and donor-acceptor pair recombinations in ZnO.** *Physica Status Solidi B-Basic Research* 2004, **241**:231-260.
30. Teke A, Özgür Ü, Doğan S, Gu X, Morkoç H, Nemeth B, Nause J, Everitt HO: **Excitonic fine structure and recombination dynamics in single-crystalline ZnO.** *Phys Rev B* 2004, **70**:195207.
31. Zhang BP, Binh NT, Wakatsuki K, Segawa Y, Kashiwaba Y, Haga K: **Synthesis and optical properties of single crystal ZnO nanorods.** *Nanotechnology* 2004, **15**:S382-S388.
32. Liu YL, Liu YC, Feng W, Zhang JY, Lu YM, Shen DZ, Fan XW, Wang DJ, Zhao QD: **The optical properties of ZnO hexagonal prisms grown from poly (vinylpyrrolidone)-assisted electrochemical assembly onto Si(111) substrate.** *J Chem Phys* 2005, **122**:174703.
33. Studenikin SA, Golego N, Cocivera M: **Fabrication of green and orange photoluminescent, undoped ZnO films using spray pyrolysis.** *J Appl Phys* 1998, **84**:2287-2294.
34. Leiter FH, Alves HR, Hofstaetter A, Hofmann DM, Meyer BK: **The oxygen vacancy as the origin of a green emission in undoped ZnO.** *Physica Status Solidi B-Basic Research* 2001, **226**:R4-R5.
35. Leiter F, Alves H, Pfisterer D, Romanov NG, Hofmann DM, Meyer BK: **Oxygen vacancies in ZnO.** *Physica B: Condensed Matter* 2003, **340-342**:201-204.
36. Kohan AF, Ceder G, Morgan D, Van de Walle CG: **First-principles study of native point defects in ZnO.** *Phys Rev B* 2000, **61**:15019-15027.
37. Guo B, Qiu ZR, Wong KS: **Intensity dependence and transient dynamics of donor-acceptor pair recombination in ZnO thin films grown on (001) silicon.** *Appl Phys Lett* 2003, **82**:2290-2292.
38. Du G, Yang Y, Li T, Xu B: **Preparation of polymorphic ZnO with strong orange luminescence.** *J Mater Sci* 2010, **45**:1464-1468.
39. Kim YJ, Shang HM, Cao GZ: **Growth and characterization of 001 ZnO nanorod array on ITO substrate with electric field assisted nucleation.** *J Sol-Gel Sci Technol* 2006, **38**:79-84.
40. Chandrinou C, Boukos N, Stogios C, Travlos A: **PL study of oxygen defect formation in ZnO nanorods.** *Microelectron J* 2009, **40**:296-298.
41. Katerski A, Mere A, Kazlauskiene V, Miskinis J, Saar A, Matisen L, Kikas A, Krunks M: **Surface analysis of spray deposited copper indium disulfide films.** *Thin Solid Films* 2008, **516**:7110-7115.
42. Tena-Zaera R, Elias J, Lévy-Clément C, Bekeny C, Voss T, Mora-Sero I, Bisquert J: **Influence of the Potassium Chloride Concentration on the Physical Properties of Electrodeposited ZnO Nanowire Arrays.** *J Phys Chem C* 2008, **112**:16318-16323.
43. Ghosh R, Fujihara S, Basak D: **Studies of the optoelectronic properties of ZnO thin films.** *J Electron Mater* 2006, **35**:1728-1733.
44. Park WI, Kim DH, Jung SW, Yi GC: **Metalorganic vapor-phase epitaxial growth of vertically well-aligned ZnO nanorods.** *Appl Phys Lett* 2002, **80**:4232-4234.
45. Zhou HJ, Fallert J, Sartor J, Dietz RJB, Klingshirn C, Kalt H, Weissenberger D, Gerthsen D, Zeng HB, Cai WP: **Ordered n-type ZnO nanorod arrays.** *Appl Phys Lett* 2008, **92**:132112.
46. Dedova T, Krunks M, Mere A, Klauson J, Volobujeva O: **Preparation of shape and size-controlled zinc oxide nanostructures by chemical spray pyrolysis technique.** In *Zinc Oxide and Related Materials; Warrendale.* Edited by: Christen J, Jagadish C, Look DC, Yao T, Bertram F. Materials Research Society; 2007:359-365.

doi:10.1186/1556-276X-6-359
Cite this article as: Kärber *et al.*: **Photoluminescence of spray pyrolysis deposited ZnO nanorods.** *Nanoscale Research Letters* 2011 **6**:359.

Appendix A

Article IV

E.Kärber, A.Katerski, I.Oja Acik, V.Mikli, A.Mere, M.Krunks. (2011). „Effect of H_2S treatment on properties of $CuInS_2$ thin films deposited by chemical spray pyrolysis at low temperature“. Thin Solid Films, 519, 7180 – 7183.

Thin Solid Films 519 (2011) 7180–7183

Contents lists available at ScienceDirect

Thin Solid Films

journal homepage: www.elsevier.com/locate/tsf

Effect of H_2S treatment on properties of $CuInS_2$ thin films deposited by chemical spray pyrolysis at low temperature

E. Kärber [a], A. Katerski [a], I. Oja Acik [a], V. Mikli [b], A. Mere [a], M. Krunks [a,*]

[a] Department of Materials Science, Tallinn University of Technology, Ehitajate tee 5, 19086 Tallinn, Estonia
[b] Centre for Materials Research, Tallinn University of Technology, Ehitajate tee 5, 19086 Tallinn, Estonia

ARTICLE INFO

Available online 31 December 2010

Keywords:
$CuInS_2$
Thin film
Chemical spray pyrolysis
Thermal treatment
Chalcopyrite
XRD
XPS
Raman spectroscopy

ABSTRACT

$CuInS_2$ thin films were deposited by chemical spray of aqueous solutions containing $CuCl_2$, $InCl_3$ and thiourea at substrate temperature of 250 °C in air and subjected to annealing at 530 °C in H_2S atmosphere. Structure and composition before and after annealing were studied by XRD, EDS, XPS and Raman spectroscopy. As-sprayed films were low-crystalline, showed uniform distribution of elements in film thickness and no oxygen content. For the $CuInS_2$ films deposited from the solutions with $[Cu^{2+}]/[In^{3+}]=1.0$ and 1.1, H_2S treatment for 30 min increased the chalcopyrite content up to 73% and 51%, respectively. Cu_xS phase in sprayed CIS films promotes the crystallite growth but retards the formation of chalcopyrite phase during H_2S treatment.

1. Introduction

Copper indium disulphide, $CuInS_2$ (CIS) is a promising absorber material for photovoltaic applications because of its direct bandgap energy of 1.5 eV and high absorption coefficient. This material has been successfully used for thin film solar cells with conversion efficiency of 11.4% [1].

The success of photovoltaic devices in energy production market largely depends also on their cost. Hence, low-cost non-vacuum material deposition technologies should be further developed. One of them is the chemical spray pyrolysis (CSP) method. Here the solution of appropriate precursor materials is deposited in the form of fine droplets onto the preheated substrate where the growth of thin film takes place. CSP deposited CIS films have been successfully used as a thin absorber layer in nanostructured solar cells based either on TiO_2 nanoparticle [2] or ZnO nanorod layer [3,4] and have reached light-to-electricity conversion efficiencies of ~7% [2] and ~4% [4], respectively.

As-sprayed CIS films deposited at low temperatures (around 300 °C) have been found to be not well-crystallized, especially when using $[Cu^{2+}]/[In^{3+}]\leq 1$ in the spray solution, and contain residues originated from the precursors [5]. However, deposition at temperatures above 350 °C has led to the formation of polycrystalline film containing metal oxide phase [6–8]. Post-deposition treatment in hydrogen sulphide atmosphere of CIS films grown by various techniques such as vacuum evaporation [9], RF reactive sputtering [10], ILGAR-spray [11] has been found to improve the composition and structure of the films. In our earlier reports [12,13] on thermal treatment of CSP deposited CIS films in H_2S atmosphere we showed that the treatment is effective to improve the film crystallinity and purity, increase chalcopyrite ordering and optical band gap value, and reduce sulphur deficiency originally characteristic of the CIS films grown at 350–370 °C. By H_2S treatment, metal oxide phase (probably In-oxide) present in as-sprayed film was converted into metal sulphide [6,7]. This secondary phase in annealed films, obviously present on grain boundaries [6], could be responsible for worsening of the electrical transport properties compared to as-deposited films [13].

In this paper, we present the results of the studies on the effect of H_2S treatment on the elemental and phase composition, and structural properties of CIS films grown by CSP at ca. 250 °C in air. The growth temperature of 250 °C used in this study is close to the lowest temperature where CIS could be obtained by CSP of the solution containing $InCl_3$, $CuCl_2$ and thiourea as starting chemicals [14].

2. Experimental

$CuInS_2$ (CIS) films were deposited by spray of an aqueous solution containing $CuCl_2$, $InCl_3$ and $SC(NH_2)_2$ at precursors molar ratio of Cu:In:S = 1:1:3 ($[Cu^{2+}]/[In^{3+}]=1.0$) and 1.1:1:3.1 ($[Cu^{2+}]/[In^{3+}]=1.1$) onto the preheated borosilicate glass substrates placed onto a molten Sn bath, the films deposited were named “CIS-1.0” and “CIS-1.1”, respectively. The films were deposited at the substrate temperature of 250 °C, the substrate temperature was kept with

---

[*] Corresponding author. Tel.: +372 6203363; fax: +372 6202020.
E-mail address: malle@staff.ttu.ee (M. Krunks).

0040-6090/$ – see front matter © 2010 Elsevier B.V. All rights reserved.
doi:10.1016/j.tsf.2010.12.185

accuracy of ± 5 °C with the help of the feedback control system for the heater supply. Deposition parameters such as spray solution volume of 50 ml, precursor salt concentration ($[In^{3+}] = 2$ mmol/l) and feeding rate of 1 ml/min were kept constant for all samples. As-deposited films were etched in KCN solution for 5 min (called 'as-deposited' films) in order to remove Cu_XS phase. Post-deposition heat treatments were performed for KCN etched films in flowing $N_2 + H_2S$ atmosphere. The samples were inserted into the quartz tube, tube was purged with N_2, then H_2S gas was included in proportion of ca. 95% N_2 (99.5% purity) and 5% H_2S (99.99% purity). After that quartz tube was inserted into the preheated oven. The samples were heated up to 530 °C within 5 min, the duration of the treatments was varied between 5 and 60 min, and were cooled down with the cooling rate of ca 25 °C/min.

The films were characterized by the X-ray diffraction (XRD) patterns in the 2θ range of 10–60 deg, recorded by a Rigaku Ultima IV diffractometer (Cu Kα radiation) equipped with line detector DtexUltra. The average crystallite size was calculated from the FWHM of the (112) diffraction peak of the $CuInS_2$ (PDF 27-0159) using the Scherrer's formula and the Sherrer constant of 0.94. Raman spectra of the layers were recorded in the backscattering non-polarized mode at room temperature using confocal micro-Raman spectrometer HORIBA Jobin Yvon Model HR 800. The excitation radiation wavelength was 532.0 nm and the intensity was 10^7 W/m^2. The elemental composition of the films was studied by the energy dispersive spectroscopy (EDS) on an Oxford Instruments PentaFet x3 spectrometer using an INCA Energy EDS system at accelerating voltage of 7 kV and the XPP (modified Phi–Rho–Z) correction program for quantification of the elements. Data were collected from four different regions with area of 50 μm^2. Single crystalline $CuInS_2$ was used as a standard. Concentration of the elements in the films was determined with uncertainty of ±0.3 at%.

X-ray photoelectron spectroscopic (XPS) measurements were performed using a Kratos AXIS Ultra DLD X-ray Photoelectron Spectrometer. Analysis was carried out with monochromatic Al Kα X-rays (1486.6 eV) operating at 15 kV and 225 W. Energy calibrations were performed taking the C1s line at 284.6 eV as a reference. The atomic concentrations were determined from Cu2p$_{3/2}$, In3d$_{5/2}$, O1s, S2p, Cl2p and Si2p core level peak areas using sensitivity factors and analyzer transmission function of the spectrometer provided by the Vision 2.2.8 analysis software. Ar^+ ion sputtering (4 kV, 20 mA) was used for the depth profiling in order to obtain information of the film bulk composition.

3. Results and discussion

3.1. XRD study

XRD patterns of as-deposited at 250 °C and H_2S-treated at 530 °C for 5 min CIS-1.0 film are presented in Fig. 1. XRD patterns of CIS-1.1 film are shown in inset. As-deposited CIS-1.0 film shows very low crystallinity and may contain another phase (peak marked by "x' in Fig.1). As this 'x' peak appears only when the solution with $[Cu^{2+}]/[In^{3+}] \leq 1.0$ is sprayed, then it is believed that this extra reflection could belong to an other phase such as In-rich ternary or an In-S phase as discussed in earlier studies [12,13,15].

In this study, annealing in H_2S atmosphere at 530 °C was performed using relatively short treatment duration of 5, 10 and 30 min. It could be seen that annealing time of 5 min is already sufficient to obtain well-crystallized CIS-1.0 film. An extra reflection ('x' peak) is disappeared on the XRD pattern of the CIS-1.0 film and crystallite size is increased from 8 nm up to 50 nm (Table 1). Short-term annealing has been found to be effective also to increase the crystallinity of the CIS-1.1 film (Fig.1, inset). Independent of the $[Cu^{2+}]/[In^{3+}]$ molar ratio in the spray solution, the annealed films are composed of highly (112) orientated $CuInS_2$ (JCPDS 00-027-0159) according to XRD. Effect of annealing time on the development of the crystallite size is presented in Table 1. It can be seen that by annealing for 10 min at 530 °C in H_2S atmosphere the crystallites in CIS-1.0 film reach an average size of ca 70 nm and prolonged treatment has insignificant effect. Crystallite size of ca. 80 nm in CIS-1.1 film is obtained already by annealing for 5 min. Although the CIS-1.1 as-deposited and annealed films show better crystallinity, it should be noticed here that irregular surface morphology accompanied by the composition differences in flat and rough area [16] could be limiting factors for a device. Contrarily, the CIS-1.0 films from solutions with the $[Cu^{2+}]/[In^{3+}] = 1.0$ possess uniform morphology and composition (not presented, see for example, Fig. 2 in [13]).

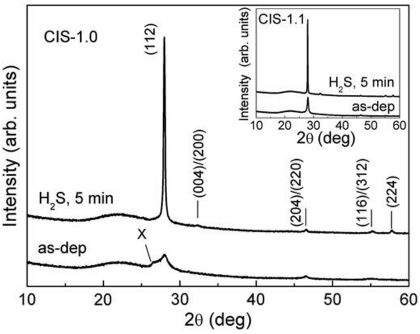

Fig. 1. XRD patterns of as-deposited and annealed for 5 min at 530 °C in H_2S atmosphere CIS-1.0 and CIS-1.1 films (in inset).

3.2. Elemental composition: EDS and XPS study

Elemental composition of as-deposited and H_2S-treated CIS-1.0 and CIS-1.1 films by EDS study is presented in Table 2. According to EDS, the as-deposited at 250 °C CIS-1.0 and CIS 1.1 are sulphur-deficient and contain chlorine residues up to 4 at%. This result corresponds to that reported for CSP deposited CIS films elsewhere, see for example [5,8]. As-deposited CIS-1.0 film is slightly Cu-rich, while the ratio of atomic concentrations ([Cu]/[In]) is higher in CIS-1.1 films. H_2S treatment removes chlorine residues and increases sulphur content. CIS-1.0 films annealed for 5 up to 30 min exhibit $[S]/([Cu] + [In]) \cong 1.0$. Thus, the elemental composition is close to that of stoichiometric $CuInS_2$. However, CIS-1.0 films with the treatment time of 60 min and CIS-1.1 films independent of the treatment time

Table 1

Crystallite size, FWHM of A_1 Raman bands of Chalcopyrite (CH) and Cu–Au (CA) ordered phases, and quality factor (QF) of as-deposited and annealed in H_2S atmosphere CIS-1.0 and CIS-1.1 films. Annealing temperature was 530 °C, duration was varied between 5 and 60 min.

Sample	Annealing time (min)		FWHM (cm^{-1})		QF (%)
		Crystallite size (nm)	A1 (CH)	A1 (CA)	
CIS-1.0	As-dep.	8	19	23	29
	5	50	9.6	11	46
	10	69	8.9	13	57
	30	71	7.8	15	73
	60	73	6.2	13	76
CIS-1.1	As-dep.	19	14	24	31
	5	80	9.5	11	49
	10	84	8.2	10	51
	30	92	9.3	12	51

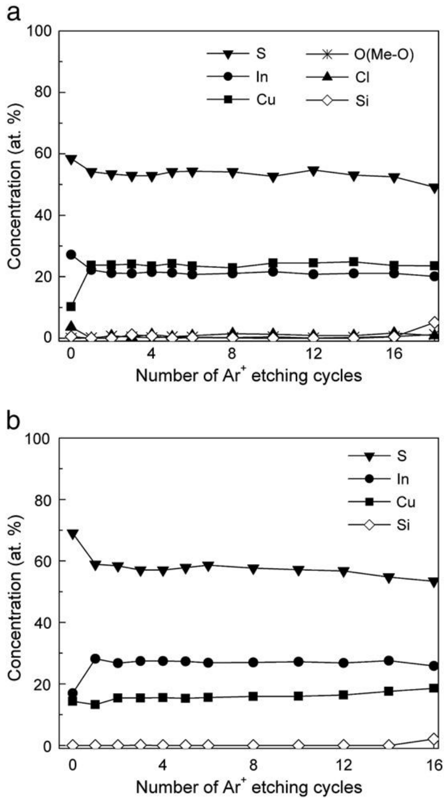

Fig. 2. XPS composition profiles of (a) as-deposited CIS-1.0 film and (b) after H_2S treatment for 60 min. The depth of the Ar$^+$ etching cycle is ca. 13 nm.

show $[S]/([Cu]+[In])<1.0$, which indicates deviation from the stoichiometry of $CuInS_2$.

According to the XPS spectra (spectra are not presented) of as-deposited and treated in H_2S atmosphere at 530 °C CIS-1.0 films, the binding energies (BE) of Cu2$p_{3/2}$, In3$d_{5/2}$, S2p core levels are placed at 932.5 eV, 445.0 eV, 162.0 eV, respectively. The binding energies recorded correspond to that of copper, indium and sulphur in spray-deposited CIS films [6,8]. The O1s core level peaks at BE of 532.0 and 530.0 eV, characteristic of oxygen in adsorbed $(OH)^-$ groups and oxygen bonded to metal (Me–O) [17], respectively, were present in the XPS spectrum recorded from the un-cleaned surface of as-deposited film. Also weak response from Cl2p at BE = 198.7 eV has been detected in the XPS spectrum of as-deposited CIS due to contamination originated from the metal chloride precursors. This result is in correspondence with the EDS results (Table 2). XPS peaks of O (Me–O) and Cl were absent in the spectrum of H_2S-treated film.

Table 2
Composition of as-sprayed at 250 °C and treated for 5, 10 and 30 min at 530 °C in H_2S atmosphere CIS-1.0 and CIS-1.1 films according to EDS.

Sample type	Treatment time (min)	S (at%)	Cu (at%)	In (at%)	Cl, (at%)	S/(Cu + In)
CIS-1.0	As-dep.	45.3	25.9	25.0	3.4	0.89
	5	49.5	25.6	24.8	0	0.98
	10	49.4	25.9	24.6	0	0.98
	30	50.3	25.4	24.3	0	1.01
	60	48.1	25.7	24.7	0	0.95
CIS-1.1	As-dep.	43.6	27.0	24.0	4.0	0.85
	5	48.1	27.0	23.9	0	0.94
	10	47.3	27.5	24.2	0	0.91
	30	47.5	27.4	23.9	0	0.93

Ar$^+$ ion sputtering was applied to study the film composition in depth. No shift in the positions of Cu2$p_{3/2}$, In3$d_{5/2}$, S2p core level peaks was detected. The atomic concentrations of the elements vs. the number of Ar$^+$ ion sputtering cycles are presented in Fig. 2. According to XPS, deposition at 250 °C results in CIS films with content of oxygen (Me–O, BE = 530.0 eV) of ca. 1 at%, and almost uniform distribution of the elements in the film depth (Fig. 2a). For comparison, CIS films deposited by CSP at 350–370 °C showed oxygen (Me–O) content up to 16 at% and graded distribution of the elements and phases from the film surface to depth [7,8]. By H_2S treatment for 60 min, nearly uniform distribution of the elements in the CIS-1.0 film thickness is preserved (Fig. 2b). Interestingly, the [Cu]/[In] ratio in the bulk region of H_2S-treated film (Fig. 2b) is lower compared to that in as-deposited film (Fig. 2a). It refers that the annealed film may have In-rich composition in the bulk region being in variance with the EDS data. Further studies are needed to explain this phenomenon. In the surface region, contrarily, the [Cu]/[In] is higher for H_2S-treated film (Fig. 2b). It is possible that Cu_XS phase is segregated from the bulk to the surface as detected by Raman for 60 min H_2S-treated film (See Section 3.3). Segregation of Cu_XS phase has been observed during post-deposition annealing of ILGAR-sprayed CIS film [11].

3.3. Raman study

Raman scattering spectroscopy studies were performed in order to estimate the phase composition of CIS films. For the CIS-1.0 films, the Raman measurements (Fig. 3a) revealed four peaks of the chalcopyrite (CH) ordered CIS at 240, 292, 320, and 337 cm^{-1}, attributed to E_3TO/B_2^2TO, A_1, B_2^1TO/E^1TO, and E_1LO scattering modes, respectively [18]. Raman peak centered at 303 cm^{-1} belongs to A_1 mode of the Cu–Au ordered (CA) phase (Fig. 3a, 3b) [18]. The peak at 470 cm^{-1} was observed for the CIS-1.0 film with 60 min of H_2S-treatment (Fig. 3a) and for the H_2S-treated CIS-1.1 films (Fig. 3b). This peak corresponds to A_1 mode of the Cu_XS phase [19].

The as-deposited CIS-1.1 film does not exhibit the peak at 470 cm^{-1} because KCN etching was made in order to remove Cu_XS residues prior to thermal treatment. According to Raman study, Cu_XS phase was detected only in H_2S-treated samples. This refers that Cu_XS phase was initially present in as-deposited samples, while KCN etching removed Cu_XS only from the surface. During the thermal treatment Cu_XS segregates towards the surface region as also has been observed for ILGAR-spray deposited CIS films [11,20].

Heat treatment in the H_2S environment resulted in narrowing of the A_1(CH) Raman peaks (Fig. 3, Table 1), which according to [21], is an evidence of increased crystal quality. The quality factor (QF) determined as $QF = I(CH)/(I(CH)+I(CA))$ [21], where I is the intensity of the corresponding peak obtained from the Lorentzian-fitted Raman spectra, was used to evaluate the percentage of CH ordered phase in the film (Table 1). Heat treatment results in the increase of QF in CIS-1.0 and CIS-1.1 films. After 30 min of annealing, QF of 73% was obtained for CIS-1.0 films and 51% for CIS-1.1 films. The maximum QF value of 51% for CIS-1.1 films was obtained within 5 to 10 min of annealing time. CIS-1.0 films exhibited further improvement up to 60 min of heat treatment, resulting in CH content in CIS of 76% and A_1 peak width of 6.2 cm^{-1}. This result is comparable with the results reported for CIS films deposited by co-evaporation process [21]. For comparison, CIS-1.0 films deposited by CSP at higher temperature of 370 °C, containing In-oxide phase according to XPS [7], reached QF of 62% by H_2S treatment for 2 h [12].

A saturation of the QF in CIS-1.0 film, achieved within 30 to 60 min of H_2S treatment (Table 1), occurred with appearance of the Cu_XS peak in the Raman spectrum. This finding is supported by the XPS data

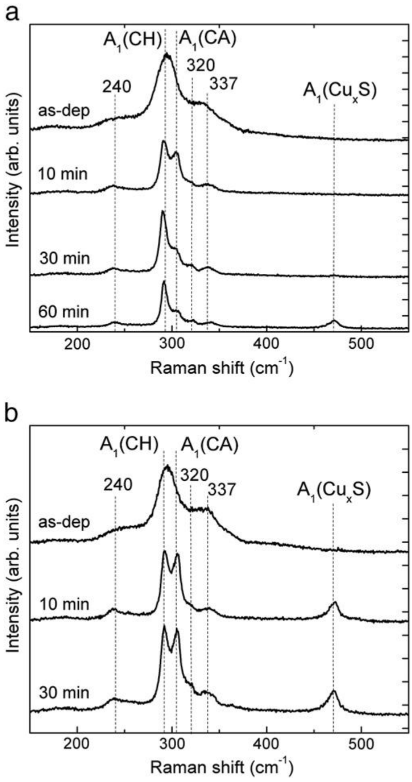

Fig. 3. Raman spectra of (a) CIS-1.0 and (b) CIS-1.1 films, deposited onto borosilicate substrate. Different annealing durations are shown (10 min, 30 min for CIS-1.0 and CIS-1.1, 60 min for CIS-1.0).

(Fig. 2b) showing higher [Cu]/[In] ratio on the surface of the H_2S-treated CIS-1.0 film compared to the bulk. It could be speculated that Cu_XS phase, detected by Raman spectroscopy in CIS-1.0 film surface after prolonged annealing (60 min) and in CIS-1.1 films independent of the annealing time (5–30 min), retards the development of the CH ordered $CuInS_2$ in spray-deposited CIS films.

4. Conclusions

In this study we showed that $CuInS_2$ films grown by chemical spray at 250 °C, which is close to the lowest applicable temperature for this process, do not contain oxygen. Oxygen contamination is unavoidable using film growth temperatures above 300 °C in air. Short-term treatment of as-deposited low crystalline films in flowing $N_2 + H_2S$ atmosphere at 530 °C effectively removes chlorine residues, increases sulphur content and, as a result, well-crystallized $CuInS_2$ films with nearly stoichiometric composition were obtained.

For the $CuInS_2$ films, obtained by spray of the solutions with $[Cu^{2+}]/[In^{3+}] = 1.0$ and $[Cu^{2+}]/[In^{3+}] = 1.1$ in spray solutions, H_2S treatment for 30 min increased the chalcopyrite (CH) content up to 73% and 51%, respectively. The results of this study show that presence of Cu_XS phase in sprayed CIS films promotes the crystallite growth but retards the formation of chalcopyrite phase during post-deposition annealing.

Acknowledgements

Financing by the Estonian Ministry of Education and Research under the project SF0140092s08 and the Estonian Science Foundation under the grant ETF6954 are gratefully acknowledged. The authors thank Mr. M. Danilson for assistance with the XPS measurements.

References

[1] R. Klenk, K. Klaer, R. Scheer, M.Ch. Lux-Steiner, I. Luck, N. Meyer, U. Rühle, Thin Solid Films 480–481 (2005) 509.
[2] A. Goossens, J. Hofhuis, Nanotechnology 19 (2008) 424018.
[3] I. Oja Acik, A. Katerski, A. Mere, J. Aarik, A. Aidla, T. Dedova, M. Krunks, Thin Solid Films 517 (2009) 2443.
[4] M. Krunks, E. Kärber, A. Katerski, K. Otto, I. Oja Acik, T. Dedova, A. Mere, Sol. Energy Mater. Sol. Cell 94 (2010) 1191.
[5] M. Krunks, O. Kijatkina, H. Rebane, I. Oja, V. Mikli, A. Mere, Thin Solid Films 403–404 (2002) 71.
[6] S. Marsillac, M.C. Zouaghi, J.C. Bernède, T. Ben Nasrallah, S. Belgacem, Sol. Energy Mater. Sol. Cell 76 (2003) 125.
[7] A. Katerski, A. Mere, V. Kazlauskiene, J. Miskinis, A. Saar, L. Matisen, A. Kikas, M. Krunks, Thin Solid Films 516 (2008) 7110.
[8] T. Sebastian, M. Gopinath, C. Sudha Kartha, K.P. Vijayakumar, T. Abe, Y. Kashiwaba, Sol. Energy 83 (2009) 1683.
[9] Y. Akaki, K. Nomoto, S. Nakamura, T. Yoshitake, K. Yoshino, J. Phys.: Conf. Ser. 100 (2008) 082022.
[10] Y.B. He, T. Krämer, I. Österreicher, A. Polity, B.K. Meyer, M. Hardt, Semicond. Sci. Technol. 20 (2005) 685.
[11] C. Camus, N.A. Allsop, S.E. Gledhill, W. Bohne, J. Röhrich, I. Lauermann, M.C. Lux-Steiner, Ch.-H. Fisher, Thin Solid Films 516 (2008) 7026.
[12] I. Oja, M. Nanu, A. Katerski, M. Krunks, A. Mere, J. Raudoja, A. Goossens, Thin Solid Films 480–481 (2005) 82.
[13] M. Krunks, A. Mere, A. Katerski, V. Mikli, J. Krustok, Thin Solid Films 511–512 (2006) 434.
[14] M. Krunks, E. Mellikov, O. Bijakina, Phys. Scripta T69 (1997) 189.
[15] J.D. Harris, K.K. Banger, D.A. Scheiman, M.A. Smith, M.H.-C. Jin, A.F. Hepp, Mater. Sci. Eng. B98 (2003) 150.
[16] M. Krunks, O. Kijatkina, A. Mere, T. Varema, I. Oja, V. Mikli, Sol. Energy Mater. Sol. Cell 87 (2005) 207.
[17] C.D. Wagner, A.V. Naumkin, A. Kraut-Vass, J.W. Allison, C.J. Powell, J.R. Rumble Jr., NIST Standard Ref. Database 20, Ver. 3.4 (2006) (Web Version at http://www.srdata.nist.gov/xps/index.htm).
[18] C. Camus, Ph.D thesis, Freie Universität Berlin, Berlin, Germany, 2008.
[19] E. Rudigier, B. Barcones, I. Luck, T. Jawhari-Colin, A. Pèrez-Rodríguez, R. Scheer, J. Appl. Phys. 95 (2004) 5153.
[20] T. Schmid, C. Camus, S. Lehmann, D. Abou-Ras, Ch.-H. Fischer, M.C. Lux-Steiner, R. Zenobi, Phys. Status Solidi A 206 (2009) 1013.
[21] J. Alvarez-García, E. Rudigier, N. Rega, B. Barcones, R. Scheer, A. Pérez-Rodríguez, A. Romano-Rodríguez, J. R. Morante. Thin solid Films 431–432 (2003) 122.

Appendix A

Article V

M.Krunks, **E.Kärber**, A.Katerski, K.Otto, I.Oja Acik, T.Dedova, A.Mere. (2010). „Extremely thin absorber layer solar cells on zinc oxide nanorods by chemical spray“. Solar Energy Materials and Solar Cells, 94(7), 1191–1195.

Solar Energy Materials & Solar Cells 94 (2010) 1191–1195

Contents lists available at ScienceDirect

Solar Energy Materials & Solar Cells

journal homepage: www.elsevier.com/locate/solmat

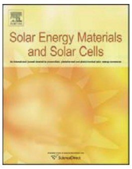

Extremely thin absorber layer solar cells on zinc oxide nanorods by chemical spray

M. Krunks*, E. Kärber, A. Katerski, K. Otto, I. Oja Acik, T. Dedova, A. Mere

Department of Materials Science, Tallinn University of Technology, Ehitajate tee 5, Tallinn 19086, Estonia

A R T I C L E   I N F O

Article history:
Received 21 December 2009
Received in revised form
22 February 2010
Accepted 22 February 2010
Available online 10 April 2010

Keywords:
ETA-cell
Chemical spray pyrolysis
ZnO nanorods
Indium sulfide
Copper indium disulfide

A B S T R A C T

$ZnO_{rod}/In_2S_3/CuInS_2$ type ETA-cells were prepared by in-line chemical spray pyrolysis method. Effects of buffer layer thickness and ZnO nanorod length (500–1000 nm) were studied by means of SEM, *I–V* dependencies and EQE spectra. Conformal layer of In_2S_3, obtained by spray of solution with pH = 4.8, effectively protects ZnO nanorods from dissolution during the spray of acidic solutions. Increasing In_2S_3 layer thickness reduces fluctuations of the cell output parameters, and increases V_{OC} and FF; however, at certain thickness induces losses due to light absorption. The highest conversion efficiency 4.17% at AM1.5 was recorded from small contact area of the cell based on rods with length of 600 nm. Perspectives for further development are discussed.

1. Introduction

ZnO nanorods as photoactive material and an electrode in photovoltaic cells have been launched few years ago and have been extensively studied thereafter. The most widely used designs of ZnO nanowire based PV cells include addition of a light harvesting material such as organic dyes, polymers or inorganic extremely thin absorbers (ETA). According to the theoretical model, conversion efficiencies of 10–15% are predicted for ETA solar cells [1]. ETA-cells with the structure components such as ZnO compact layer on TCO, ZnO nanorod layer on compact ZnO and CdSe absorber on ZnO rods, all produced by wet chemical methods, have reached the efficiency of 2.3% [2]. The use of ion layer gas reaction (ILGAR) technique for preparation of In_2S_3 layer onto ZnO rods, and applying CuSCN as a p-conductor, ETA-cells with conversion efficiencies of 2.5–3.4% have been obtained [3,4]. Recently our group presented the technology of preparation of ZnO nanorod arrays by a simple chemical spray method [5,6]. Conversion efficiencies in the order of 2.5% have been recorded for ETA-cells, where both ZnO rods and $CuInS_2$ absorber were prepared by chemical spray [7,8].

In this study, we present the results on development of ETA-cells produced by in-line chemical spray process using two-layer buffer of In_2S_3 on ZnO nanorods and $CuInS_2$ as absorber layer. We focus on the effect of buffer layer thickness on solar cell output characteristics, and discuss the problems arising from varying the length of ZnO rods to increase the internal surface area.

2. Experimental

ZnO structured layers composed of ZnO nanocolumns with diameters of 200–300 nm and lengths of ~500–1000 nm were deposited by the chemical spray method onto transparent conductive oxide (TCO) covered glass substrates. $ZnCl_2$ was used as a zinc source [5,6]. In_2S_3 was deposited onto the ZnO nanostructured window as a two-layer buffer. First, a dense 'In-S' layer was deposited onto the ZnO nanorod layer using diluted aqueous precursor solution ($InCl_3$:$SC(NH_2)_2 = 1{:}3$) with pH = 4.8 in order to avoid chemical dissolution of ZnO nanocrystals. Thereafter, the layers of In_2S_3 and $CuInS_2$ as a buffer and an absorber, respectively, were deposited by spray of acidic precursor solutions with pH = 3.0. Buffer and absorber layers were deposited onto the substrate kept at 300 °C. Thus, the formed solar cell structure is as follows: $TCO/ZnO_{rod}/In_2S_3/CuInS_2$.

ZnO nanorod arrays and solar cell structures were characterized by high resolution scanning electron microscopy (SEM) images recorded on Zeiss HR FESEM Ultra 55 and Zeiss EVO-MA15. Current–voltage (*I–V*) characteristics of solar cells in dark and under halogen lamp illumination (intensity 100 W/cm^2) were recorded using AUTOLAB PGSTAT 30 system. *I–V* curves of the best cell were recorded in a sun simulator (Class A) at AM1.5. Carbon contacts with determined area (scribed when CuSCN was applied) were used as back contacts. For some cells CuSCN was

---

* Corresponding author. Tel.: +372 620 3363. fax: +372 620 3367.
E-mail address: malle@staff.ttu.ee (M. Krunks).

0927-0248/$ - see front matter © 2010 Elsevier B.V. All rights reserved.
doi:10.1016/j.solmat.2010.02.036

applied as p-conductor following the recipe given in [9]. External quantum efficiency (EQE) spectra were recorded in the spectral region of 1.0–3.5 eV (1240–355 nm) using a computer-controlled SPM-2 monochromator (Carl Zeiss-Jena, $f=40$ cm) and l00 W halogen lamp with calibrated spectral intensity as excitation light source.

3. Results and discussion

3.1. Chemical spray deposition of ZnO nanostructured layers and In_2S_3 buffer layer

ZnO nanostructured layers composed of elongated crystals with the length of about 500, 700 and 1000 nm, further named as type A, B and C, respectively, were deposited onto TCO covered glass substrates. SEM micrographs of the layers are presented in Fig. 1. The length and thickness of the rods were adjusted by changing the concentration of $ZnCl_2$ in an aqueous spray solution from 0.05 mol/l up to 0.1 mol/l.

In our previous study, thin layer of TiO_2 was deposited onto the ZnO nanocrystals to avoid their chemical dissolution during the deposition of the following layers of solar cell from acidic spray solutions [7,8]. Despite the fact that TiO_2 layer protects ZnO rods from chemical dissolution, its thickness is a critical parameter affecting the cell output characteristics as starting from a certain thickness it can block the charge carrier transport in the device.

In this study we omitted TiO_2 layer in the structure as it is extremely difficult to control the conformity of sprayed TiO_2 layer at low thicknesses [10]. In order to maintain the simplicity of solar cell preparation, a very thin layer of 'In–S' was deposited instead of TiO_2 using low spray rate and diluted precursor solution with pH ~4.8. SEM studies (Fig. 2a) indicate the formation of a dense and smooth layer of 'In–S', which uniformly covers ZnO crystals.

The deposition of the In_2S_3 buffer was proceeded by spray of 25 ml of more concentrated solutions using three times higher deposition rate. SEM micrograph of ZnO nanocrystals after deposition of In_2S_3 layer is presented in Fig. 2b. As can be seen, the In_2S_3 layer shows more rough coverage than 'In–S' layer on ZnO crystals. According to XPS and optical measurements, both 'In–S' and In_2S_3 layers show similar composition and optical band gap values of ca. 2.2 eV for indirect transitions.

3.2. Effect of indium sulfide buffer layer thickness on I–V characteristics of solar cells

I–V curves of solar cells on ZnO rods of type A (Fig. 1a), depending on thickness of the indium sulfide layer, are presented in Fig. 3. It can be seen that the cell with thin 'In–S' buffer layer (Fig. 2a) results in very low open circuit voltage (V_{OC}) of ca. 100 mV and fill factor (FF) of 30%, although short circuit current density (j_{SC}) in the order of 10 mA/cm^2 has been recorded (Fig. 3, curve 1). Solar cell with thicker buffer of In_2S_3 (see Fig. 2b) shows V_{OC} of 463 mV and FF of 54% (Fig. 3, curve 2). Including both 'In-S' and In_2S_3 layers into the solar cell structure increases FF up to 62% (Fig. 3, curve 3). Thus, applying dense and conformal layer of 'In–S' as a part of In_2S_3 buffer improves the cell output characteristics.

Solar cell output parameters depending on the 'In–S' layer thickness (given by amount of the solution sprayed as a technological parameter) deposited onto ZnO structured layers of type A are presented in Fig. 4. It can be seen that deposition of 'In–S' layer from both 25 and 250 ml solution decreases the fluctuations of the cell output parameters compared to the cells without 'In-S' layer. Slight increase in V_{OC}, FF and, as a result, the cell conversion efficiency was observed while including 2-layer buffer into the cell. However, some decrease in j_{SC} was observed, which could be explained by increased serial resistance of the cell with a thicker buffer layer. Consequently, the application of 'In–S' layer has similar effect as TiO_2 layer on ZnO nanorods [8]. According to *I–V* curves, the thickness of 'In–S' layer is much less critical compared to TiO_2.

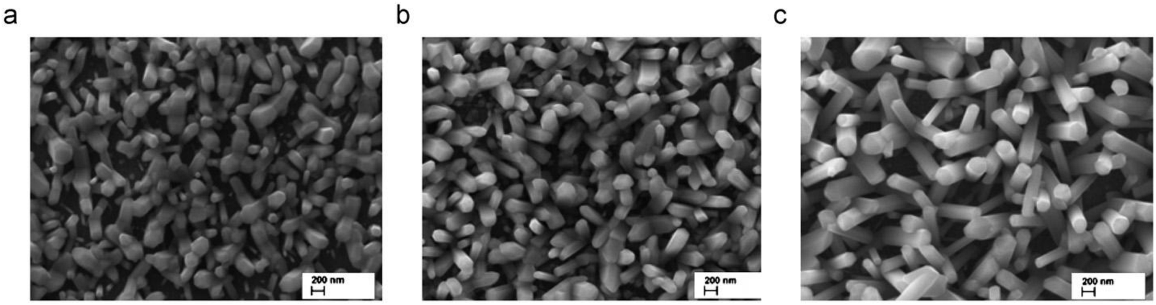

Fig. 1. SEM micrographs of spray deposited ZnO nanorod arrays with different lengths (L) of rods: (a) $L\sim500$ nm (type A); (b) $L\sim700$ nm (type B); (c) $L\sim1000$ nm (type C).

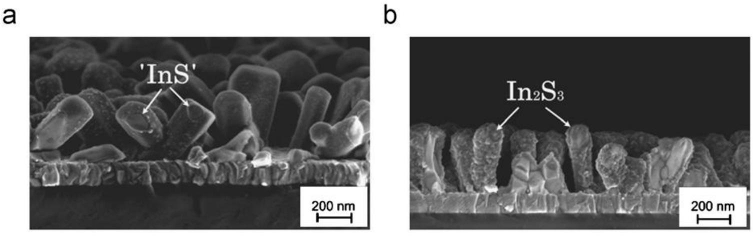

Fig. 2. SEM micrographs of ZnO nanorods covered with (a) 'In–S' and (b) In_2S_3 layers.

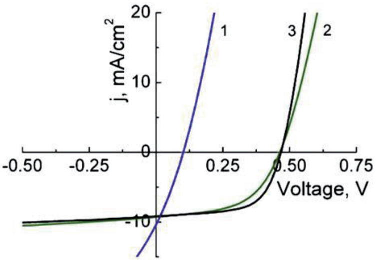

Fig. 3. *I–V* curves of solar cells on ZnO nanorods (type A) with different thickness of the indium sulfide buffer layer. Buffer layers: 'In–S' (1), In_2S_3 (2), 'In–S'+ In_2S_3 (3). *I–V* curves were recorded under halogen lamp illumination (100 mW/cm^2).

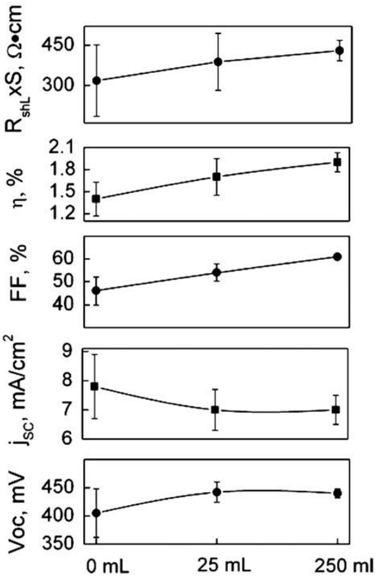

Fig. 4. Effect of 'In–S' layer thickness on solar cell output parameters (Voc, *j*, FF, *η* and light shunt resistance, R_{shL} *S*) of structured cells. Solar cell structures are based on ZnO layers of type A. Thickness of 'In–S' layer was varied by volume of spray solution.

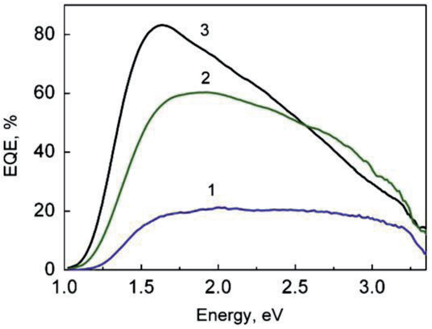

Fig. 5. EQE spectra of spray pyrolysis deposited solar cells depending on thickness of indium sulfide buffer layer. Local thickness of In_2S_3 buffer layer increases from cell 1 to cell 3. Buffer layers: 'In–S'(25 ml) (1), 'In–S'(25 ml)+In_2S_3 (2), 'In-S'(250 ml)+In_2S_3 (3) . Local thickness of $CuInS_2$ absorber layer was closely similar for all samples. The cells were made on ZnO rods of type A.

Table 1
Output parameters of the solar cells depending on the length (*L*) of ZnO crystals.

Type	*L*, nm	V_{OC}, mV	J_{SC}, mA/cm^2	FF,%	*η*,%	R_{shL} *S*, Ω cm^2
FLAT	0	463	5.2	61	1.5	660
A	~500	428	11.4	60	2.9	284
B	~700	334	13.0	43	1.9	168
C	~1000	265	10.5	33	0.95	58

3.3. *Effect of indium sulfide buffer layer thickness on EQE of solar cells*

External quantum efficiency (EQE) spectra were recorded in order to evaluate the influence of buffer layer thickness on collection of carriers. EQE spectra show that increase in buffer layer thickness (from curve 1 to curve 3 in Fig. 5) increases the losses in the high energy region of the spectrum (2.0–3.2 eV). Losses above 2.0 eV are obviously due to increased absorption in the thicker buffer layer. At the same time the EQE as high as 80% has been recorded in the low energy region around 1.5 eV for the cell with the thickest buffer layer ('In–S' from 250 ml+In_2S_3, curve 3 in Fig. 5). EQE value recorded in the low energy region is comparable with external quantum efficiencies of Sb_2S_3 sensitized TiO_2 nanoporous cells where, contrariwise, high efficiencies were recorded between 450 and 520 nm [11]. Similar to Ref. [11], high quantum efficiencies were measured at wavelengths between 400 and 500 nm also for $ZnO_{rod}/In_2S_3/CuSCN$ type of ETA-cell [4].

Although collection of carriers at 2.0–3.2 eV is lowered for the cell with the thickest buffer layer, this cell shows the highest shunt resistance, fill factor and efficiency (Fig. 4). Use of thinner buffer layer results in an improvement of EQE curve shape (Fig. 5), however, accompanied with a decrease in EQE absolute values, which is in correlation with lower efficiencies of these cells (Figs. 3 and 4). EQE study shows that buffer layer thickness should be optimized in order to reduce losses caused by absorption in buffer layer.

3.4. *Effect of ZnO nanorod length on solar cell output parameters*

In order to study the effect of ZnO nanorod length on solar cell output characteristics, solar cell structures were prepared onto ZnO layers of type A, B, C (Fig. 1a–c). Buffer layer was prepared as bi-layer ('In-S'+In_2S_3), where 'In-S' layer was deposited from 25 ml of precursor solution. Other deposition parameters such as concentration and volume of spray solutions for In_2S_3 and $CuInS_2$ layers were kept constant throughout the series. Table 1 summarizes the output parameters of the solar cells.

As can be seen, the j_{SC} increases by increasing the ZnO layer roughness (from flat up to structured ZnO with the rods *L*~700 nm). The current density of the structured cell with rods *L*~700 nm is nearly three times higher compared to a flat sample. At the same time, *V*oc decreases with the increase in length of the rods. Similar trend has been observed earlier [3,7] and was explained by increased recombination due to increased internal surface area.

In this set of samples the highest efficiency of 2.9% has been recorded for the cell based on the rods with *L*~500 nm showing only slightly lower *V*oc (428 mV), similar FF (60%) and more than

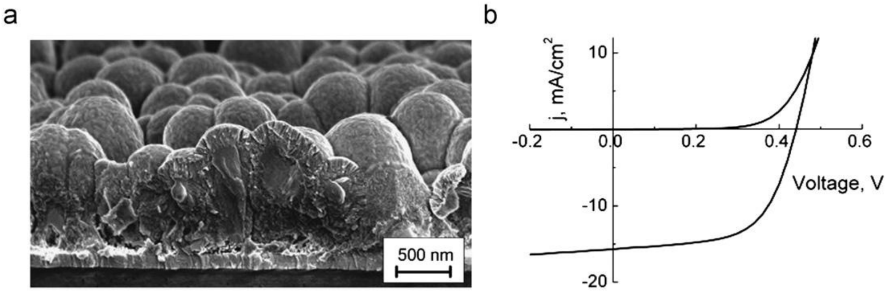

Fig. 6. SEM cross-sectional micrograph (a) before applying back contact, and current–voltage characteristics (b) of the best solar cell $ZnO_{rod}/In_2S_3/CuInS_2$. Light *I–V* characteristic is measured under illumination with the sun simulator.

two times higher j_{SC} (11.4 mA/cm^2) compared to the planar cell (V_{OC}=463 mV, FF=61%, j_{SC}=5.2 mA/cm^2). Shunt resistance characteristic of structured cell (284 Ω cm^2) is about twice lower than that of planar device (660 Ω cm^2) and corresponds to an increased junction area.

Solar cells based on ZnO rods of type B (L~700 nm) show higher current density than the cell comprising shorter crystals, but significantly reduced V_{OC} and FF (Table 1). As a result, the conversion efficiency drops to 1.9%. The cell based on rods of type C (L~1000 nm) results in much lower current density than expected, accompanied by a decrease in V_{OC}, FF and shunt resistance.

In our case, no change of the cell characteristics was observed when CuSCN as hole conductor was applied onto the cells based on ZnO rods of type A, B, and C. Probably, roughness of our structures was too low to detect the effect of CuSCN.

It could be speculated that increased recombination losses together with enhanced leakage, including tunnelling, in the case of significantly lower local thicknesses of component layers on longer rods, as also shown in [4,12], are responsible for lower performance of the cell. It is obvious that local thickness of the component layers decreases with increase in the length of the ZnO nanorods while keeping deposition conditions such as amount and concentration of spray solution unchanged. Additionally, in our type of solar cell, where ZnO nanorod layer is directly deposited onto TCO, there is a high probability for short circuiting between back and front contacts, particularly in the case of longer rods.

All these speculations should be controlled in further studies in order to make an efficient cell on long ZnO nanorods.

In current stage of studies conversion efficiencies ca. 4.0% from relatively small contact area of 1.0–1.5 mm^2 were achieved for several cells based on ZnO nanorods with length of ca. 600 nm. SEM cross-sectional micrograph and current–voltage characteristic of the best cell are presented in Fig. 6. The highest conversion efficiency 4.17% (Voc=441 mV, j_{SC}=15.7 mA/cm^2, FF=60.4%) was measured under illumination with the sun simulator (AM1.5) from the contact with area 1.50 mm^2. Increasing the contact area to 2.54 mm^2 and 3.14 mm^2 decreases the efficiency to 3.0% and 2.8%, respectively, mainly due to decrease in FF. As the efficiency from contact area of 10 mm^2 is only 1.8%, being also induced by decreased j_{SC}, then further optimization of the solar cell structure, especially of homogeneity and thickness of component layers, is obligatory in order to obtain higher efficiencies over the larger back contact area.

It is worth to mention that output characteristics of the nanostructured cells obtained by in-line spray pyrolysis process within a short preparation time in the order of 100 min did not show any degradation upon storage in laboratory conditions during eleven months.

4. Conclusions

In this study, ETA-cells with the structure of $TCO/ZnO_{rod}/In_2S_3/CuInS_2$ were prepared by in-line chemical spray pyrolysis technique. It was shown that thin and conformal layer of In_2S_3 ('In–S'), deposited by spray of diluted precursor solutions with pH=4.8, effectively prevents, analogous to TiO_2 [8], ZnO rods from chemical dissolution in acidic media. An increase in buffer layer ('In–S') thickness on ZnO rods with length of ca. 500 nm reduces fluctuations of the cell output parameters and contributes to higher V_{OC}, FF and conversion efficiency.

The cells with thick 'In–S'+In_2S_3 buffer layer show external quantum efficiencies as high as 80% in the spectral region around 1.5 eV. However, EQE is significantly lower in high energy spectral region above 2.0 eV due to absorption in relatively thick buffer. Thus, the optimization of the buffer layer thickness is essential to attain higher efficiencies.

The increase in internal surface area of the solar cell by varying the length of ZnO rods up to 700 nm increases j_{SC}, but leads to decrease in V_{OC} and FF obviously due to increased recombination at higher interface area, favoured conditions for short circuiting and non-optimal thicknesses of the component layers.

At present stage of studies the highest conversion efficiencies of 4.0%, recorded from relatively small contact area of 1.0–1.5 mm^2, were attained for several cells based on ZnO nanorods with length of ca. 600 nm. We believe that conversion efficiencies above 5% can be reached on ZnO rods with a higher aspect ratio by adjustment of thickness and uniformity of the component layers.

Acknowledgements

Financial support by the Estonian Ministry of Education and Research under target financing project SF0140092s08 and the Estonian Science Foundation under grant ETF6954 are gratefully acknowledged. The authors thank Dr. O. Volobujeva and Dr. V. Mikli for SEM microphotos.

References

[1] K. Taretto, U. Rau, Modeling extremely thin absorber solar cells for optimized design, Progress in Photovoltaics 12 (2004) 573–591.

[2] C. Lévy-Clément, R. Tena-Zaera, M.A. Ryan, A. Katty, G. Hodes, CdSe-sensitized p-CuSCN/nanowire n-ZnO heterojunctions, Advanced Materials 17 (2005) 1512–1515.

[3] D. Kievan, T. Dittrich, A. Belaidi, J. Tornow, K. Schwarzburg, N. Allsop, M. Lux-Steiner, Effect of internal surface area on the performance of $ZnO/In_2S_3/CuSCN$ solar cells with extremely thin absorber, Applied Physics Letters 92 (2008) 153107.

[4] A. Belaidi, T. Dittrich, D. Kieven, J. Tornow, K. Schwarzburg, M. Lux-Steiner, Influence of the local absorber layer thickness on the performance of ZnO

nanorod solar cells, Physica Status Solidi—Rapid Reseach Letters 2 (2008) 172–174.

[5] M. Krunks, T. Dedova, I. Oja Açik, Spray pyrolysis deposition of zinc oxide nanostructured layers, Thin Solid Films 515 (2006) 1157–1160.

[6] T. Dedova, O. Volobujeva, J. Klauson, A. Mere, M. Krunks, ZnO nanostructures via spray deposition of solutions containing zinc chloride and thiocarbamide, Nanoscale Research Letters 2 (8) (2007) 391–396.

[7] M. Krunks, A. Katerski, T. Dedova, I. Oja Acik, A. Mere, Nanostructured solar cell based on spray pyrolysis deposited ZnO nanorod array, Solar Energy Materials and Solar Cells 92 (2008) 1016–1019.

[8] I. Oja Acik, A. Katerski, A. Mere, J. Aarik, A. Aidla, T. Dedova, M. Krunks, Nanostructured solar cell by spray pyrolysis: effect of titania barrier layer on the cell performance, Thin Solid Films 517 (2009) 2443–2447.

[9] B. O'Regan, F. Lenzmann, R. Muis, J. Wienke, A solid-state dye-sensitized solar cell fabricated with pressure-treated P25–TiO_2 and CuSCN: analysis of pore filling and IV characteristics, Chemistry of Materials 14 (2002) 5023–5029.

[10] I. Oja Acik, A. Junolainen, V. Mikli, M. Danilson, M. Krunks, Growth of ultra-thin TiO_2 films by spray pyrolysis on different substrates, Applied Surface Science 256 (2009) 1391–1394.

[11] Y. Itzhaik, O. Niitsoo, M. Page, G. Hodes, Sb_2S_3-sensitized nanoporous TiO_2 solar cells, Journal of Physical Chemistry C 113 (2009) 4254–4256.

[12] R. O'Hayre, M. Nanu, J. Schoonman, A. Goossens, A parametric study of TiO_2/$CuInS_2$ nanocomposite solar cells: how cell thickness, buffer layer thickness, and TiO_2 particle size affect performance, Nanotechnology 18 (2007) 055702.

Appendix A

Article VI

M.Krunks, T.Dedova, **E.Kärber**, V.Mikli, I.Oja Acik, M.Grossberg, A.Mere. (2009). „Growth and electrical properties of ZnO nanorod arrays prepared by chemical spray pyrolysis”. Physica B: Physics of Condensed Matter, 404(22), 4422–4425.

Physica B 404 (2009) 4422–4425

Contents lists available at ScienceDirect

Physica B

journal homepage: www.elsevier.com/locate/physb

Growth and electrical properties of ZnO nanorod arrays prepared by chemical spray pyrolysis

M. Krunks [a,*], T. Dedova [a], E. Kärber [a], V. Mikli [b], I. Oja Acik [a], M. Grossberg [a], A. Mere [a]

[a] Department of Materials Science, Tallinn University of Technology, Estonia
[b] Centre for Materials Research, Tallinn University of Technology, Estonia

A R T I C L E I N F O

PACS:
81.05.Dz
81.15.Rs
61.46.Km
73.63.−b
78.55.−m
68.37.Hk

Keywords:
Zinc oxide
Nanorods
Chemical spray pyrolysis
Electronic properties
Photoluminescence

A B S T R A C T

Chemical spray pyrolysis was applied to grow ZnO nanorod arrays from zinc chloride solutions with pH=2 and 5 on glass/ITO substrate at 480 and 550 °C. The obtained structures were characterized by their morphological, electrical and PL properties. According to SEM, deposition of acidic solutions retards coalescence of the growing crystals. The charge carrier density in ZnO nanorods was determined from the *C–V* characteristics of ZnO/Hg Schottky barrier. Carrier densities $\sim 10^{15}\,cm^{-3}$ and slightly above $10^{16}\,cm^{-3}$ were recorded for ZnO deposited at 550 and 480 °C, respectively. According to PL studies, intense UV-emission is characteristic of ZnO independent of growth temperature, the concentration of oxygen vacancy related defects is lower in ZnO nanorods deposited at 550 °C. Solution pH has no influence on carrier density and PL properties.

1. Introduction

Zinc oxide nanostructured layers comprising nanorods are very attractive for various applications such as new generation solar cells with different sensitizers [1–4], high efficient gas sensors [5], ultraviolet detectors [6], etc.

Wet-chemical methods such as growth in the solution [1,2,7] or electrochemical deposition [3] have been mainly used to produce ZnO nanorod layers for photovoltaic applications. We recently reported that nanostructured cells with conversion efficiency of 2.5–3.9% could be prepared on spray deposited ZnO nanorods using thin $CuInS_2$ absorber layer [4,8,9].

Development of ZnO nanorods by spray technique is controlled by the growth temperature, precursor concentration in spray solution, type of solvent and surface morphology of the substrate [10–13]. It has been shown that in the case of high density of nuclei on the substrate, ZnO crystals tend to grow together and a rough layer composed of fat and short crystals is formed [11]. Additives in spray solution, for instance thiocarbamide, can lead to retarded lateral growth of crystals and support in this manner the formation of ZnO nanorods with higher aspect ratio [12]. In this paper we report on the effect of spray solution acidity on morphology of ZnO layers.

Furthermore, not only morphology but also the optical and electrical properties of ZnO nanorods are highly important for different applications. Contrarily to optical properties, electrical properties of ZnO nanorods (ZnO_{NR}) are not intensively studied as particular morphology of ZnO nanorod arrays makes their electrical characterization difficult. The electrical measurements of field effect transistors (FET) based on an individual ZnO nanocrystal have been applied to characterize the properties of ZnO_{NR} [14,15]. Using this kind of technique, the ZnO nanocrystal should be detached from the substrate and time consuming manipulation is needed to fabricate single nanowire FETs. In addition, AFM measurements in cantilever contact mode have been carried out on an individual nanorod grown on a conductive substrate [16–18]. Electrical properties of ZnO in nanorod arrays have been investigated by means of impedance spectroscopy of n-ZnO_{NR}/liquid junction [19] or ZnO_{NR}/p-Si heterojunction [20]. In this paper we present the first results on evaluation of concentration of carriers in sprayed ZnO nanorods as determined from *C–V* measurements of ZnO_{NR}/Hg Schottky barrier. According to our best knowledge, the electrical properties of spray-deposited ZnO nanocrystals have not been studied yet.

2. Experimental

Pneumatic spray set-up as described elsewhere [10] was used to grow ZnO nanorod layers on indium tin oxide (ITO) covered

---

[*] Corresponding author.
E-mail address: malle@staff.ttu.ee (M. Krunks).

0921-4526/$ - see front matter © 2009 Elsevier B.V. All rights reserved.
doi:10.1016/j.physb.2009.09.014

glass substrates with size of $25 \times 25 \times 1\,mm^3$. ZnO nanostructured layers were deposited by varying technological parameters such as growth temperature (480 and 550 °C), concentration of $ZnCl_2$ in spray solution (0.05, 0.1, 0.2 mol/l) and acidity of spray solution (pH of 5 and 2). Solution pH of 2 was adjusted by addition of HCl. The growth temperature was controlled through the temperature of the soldered tin bath used to obtain uniform heating of the substrate. The spray rate was maintained at 2.5 ml/min.

The surface morphology and cross-section views of ZnO nanostructured layers were examined by scanning electron microscopy (SEM) using a Zeiss EVO-MA15 apparatus.

Electrical characterization of ZnO nanocrystals was carried out using mercury (Hg) probe to form the ZnO/Hg Schottky barrier. The mercury drop with the area of $7\,mm^2$ was applied to contact ZnO nanorods. Due to the high surface tension of Hg, the contact forms only with the top of the ZnO nanorods. Thus, the short circuit with the back contact (ITO) could be avoided without using any special treatment, for example, filling the gaps between the rods with a resist [18]. Electrically effective contact area was calculated from constant part of the $1/C^2$ vs. voltage curve in reverse biased region (see below, part 3). C–V curves were recorded at AC testing voltage of 20 mV and frequency of 10 kHz on Autolab PGSTAT-30. The concentration of charge carriers in ZnO nanorods was calculated from the C–V characteristics applying the Mott–Schottky model.

The optical properties were investigated by photoluminescence (PL) measurements at room temperature (300 K) using a He–Cd laser (325 nm) as an excitation source.

3. Results and discussion

Fig. 1 demonstrates SEM micrographs of ZnO nanorods obtained by spray of $ZnCl_2$ aqueous solution (0.1 mol/l) with pH of 5 and 2 at substrate temperature of 550 °C. The effect of the spray solution acidity on the morphology of ZnO nanorod layer can be observed. According to the image analysis of SEM microphotos carried out by the Media Cybernethics Image-Pro 3 system, the spray of the solution with pH = 5 results in ZnO layer with density of crystals (mean diameter of ZnO crystals ~200 nm) as high as 212 per analyzed area of $24\,\mu m^2$ ($\sim 9 \times 10^6\,mm^{-2}$). Deposition of the solution with pH = 2 results in ZnO layer showing larger deviation in diameter of crystals (Fig. 1b). According to the image analysis of SEM microphotos in Fig. 1b, the number of crystals is lower – 166 per the area analyzed ($\sim 7 \times 10^6\,mm^{-2}$). The effect of the solution pH on the layer morphology is clearly apparent if more concentrated solution (c = 0.2 mol/l) was sprayed (Fig. 1c and d). Deposition of the 0.2 mol/l solution with pH = 5 results in the layer composed of ZnO fat crystals with low aspect ratio (Fig. 1c). Addition of HCl into the spray solution results in the layer with drastically changed morphology (Fig. 1d). Under this condition separately standing ZnO rods with significantly higher aspect ratio (L = 1.6 μm, d = 100–500 nm) are formed.

Nevertheless not directly proved, the changes in the layer morphology depending on the solution pH refer to the possibility that partial dissolution of initially formed seed crystals occurs in the nucleation stage due to spray of an acidic solution. As a result, the number of growing crystals is reduced and their coalescence can also be avoided. It is not excluded as well that solution pH has effect via controlling the hydrolysis of $ZnCl_2$ precursor in spray solution. The use of acidic solutions offers an alternative way besides thiocarbamide containing solutions [12] for obtaining separately standing ZnO nanorod layers on ITO electrode by spray pyrolysis method.

Electrical characterization of ZnO nanocrystals in spray-deposited ZnO_{NR} array was carried out using mercury (Hg) probe to form the ZnO/Hg Schottky barrier as shown in Fig. 2.

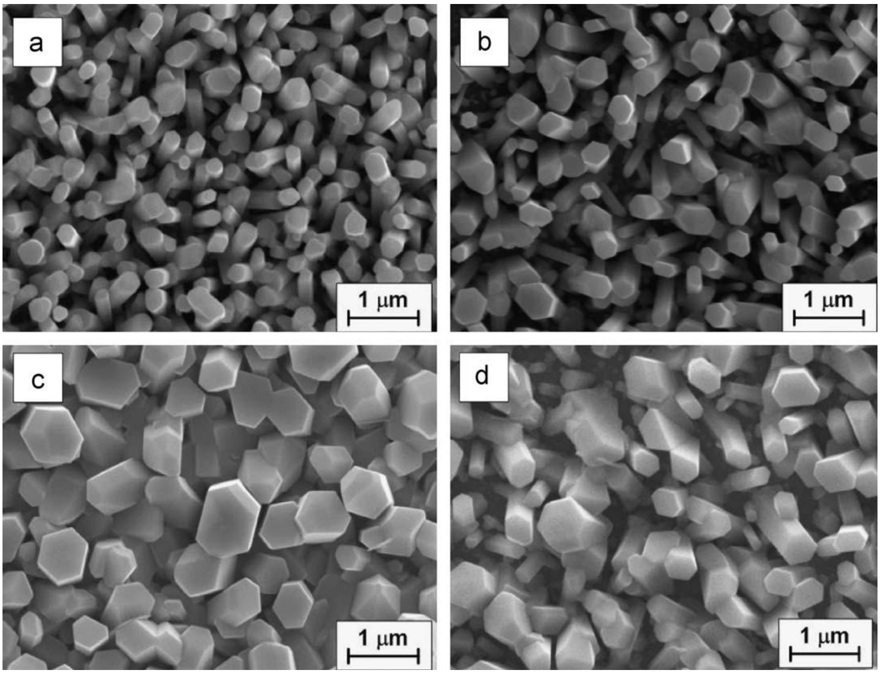

Fig. 1. SEM micrographs of ZnO nanorod layers deposited from the solution with pH = 5 (a and c) and pH = 2 (b and d). $[ZnCl_2]$ = 0.1 mol/l (a and b); $[ZnCl_2]$ = 0.2 mol/l (c and d). Substrate temperature 550 °C.

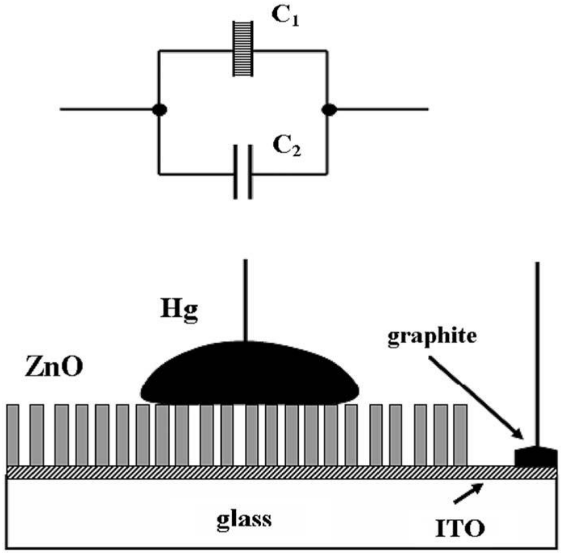

Fig. 2. A sketch of the Hg contact applied to the ZnO nanorod array and a model of capacitance for fully depleted nanorods. C_1 is the capacitance caused by the active area and C_2 is the capacitance caused by an air gap.

Current–voltage (*I–V*) characteristics were recorded to confirm the formation of a rectifying contact. Capacitance–voltage (*C–V*) characteristics of the rectifying contact were used to calculate the concentration of carriers in ZnO nanorods according to the Mott–Schottky model.

Using Hg probe for making Shottky barrier to the ZnO nanorod layer, the main problem is the determination of the electrically active ZnO/Hg contact area (from now on: active area). In this paper we propose a method for valuation of the active area from *C–V* measurements.

A model in Fig. 2 is used to represent the total capacitance C_0 of ZnO nanorod array between ITO layer and Hg contact. C_0 can be determined from the horizontal part of $1/C^2$ vs. V plot at reverse bias region (Fig. 3). If this occurs, then the depletion layer width is equal to the length of ZnO nanorods and C_0 can be expressed as

$$C_0 = C_1 + C_2, \tag{1}$$

where parallel capacitance C_1 is caused by the active area, acting as a Schottky barrier capacitor, and C_2 is caused by the air gap, partially filled with ZnO nanorods which do not take part of the Schottky barrier capacitance. Thus, C_2 is considered as an air gap with relative permittivity $\varepsilon \approx 1$, and Eq. (1) can be represented as

$$C_0 = \frac{\varepsilon_0 \cdot \varepsilon_1 \cdot A_1}{L} + \frac{\varepsilon_0 \cdot (A - A_1)}{L}, \tag{2}$$

where A is the area of the Hg drop, ε_1 is the relative permittivity of ZnO (ε_1=8.5), ε_0 is the electric constant (8.85×10^{-12} F/m), L is the length of the ZnO nanorod obtained from the SEM study.

From Eq. (2), the active area A_1 can be calculated as

$$A_1 = \frac{C_0 \cdot L - \varepsilon_0 \cdot A}{\varepsilon_0 (\varepsilon_1 - 1)}. \tag{3}$$

This calculation is valid only if the depletion layer width is equal to the length of ZnO nanorod. In case this requirement is not fulfilled, the model is inapplicable and active area was estimated from the SEM microphotos.

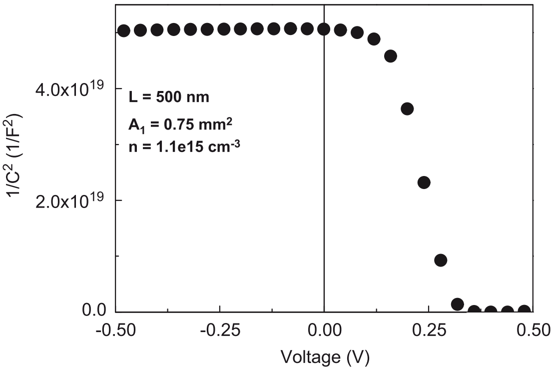

Fig. 3. Mott–Schottky plot of ZnO/Hg contact, *C–V* characteristic was recorded at 10 kHz.

Table 1
Effect of the growth temperature (T_s), concentration of $ZnCl_2$ in spray solution (c) and solution pH on the concentration of carriers (n) in spray deposited ZnO nanorods.

Sample	c (mol/l)	T_s (°C)	Solvent	pH	A_1 (cm^2)	n (cm^{-3})
1	0.1	550	H_2O	5	5.7×10^{-3}	1.3×10^{15}
2	0.1	550	H_2O	2	2.4×10^{-2}	1.1×10^{15}
3	0.2	550	H_2O	5	2.7×10^{-2}	2.0×10^{14}
4	0.2	550	H_2O	2	1.4×10^{-2}	2.7×10^{14}
5	0.1	480	EtOH	5	2.3×10^{-3}	9.8×10^{16}
6	0.1	480	EtOH	2	8.3×10^{-3}	2.2×10^{16}

A_1—active area of Hg/ZnO contact.

Concentration of charge carriers (n) is calculated according to the conventional Mott–Schottky model using

$$n = \frac{2}{q\varepsilon_0\varepsilon_1 A_1^2} \frac{dV}{d\left(\frac{1}{C^2}\right)}, \tag{4}$$

where q is the electron charge. The concentration of charge carriers in spray deposited ZnO nanorods depending on the substrate temperature and solution pH are summarized in Table 1.

As it can be seen, ZnO nanorods deposited at substrate temperature of 550 °C indicate relatively low density of carriers close to 10^{15} cm^{-3} irrespective of the solution pH. Interestingly, even lower concentration of carriers was recorded in ZnO nanorods deposited from more concentrated solution (0.2 mol/l). Further studies are needed to describe this phenomenon.

However, lowering the substrate temperature from 550 to 480 °C resulted in ZnO nanorods with higher concentration of carriers in the range of 10^{16}–10^{17} cm^{-3} (Table 1). Concentration of carriers in spray-deposited ZnO is close to that reported for the ZnO rods obtained by MOCVD technique [20,21] and are characteristic of nominally undoped ZnO [14]. In general, low temperature solution based deposition techniques yield ZnO nanorods with relatively high carrier concentration of 10^{19}–10^{20} cm^{-3} [18,19]. Our results are in correspondence with that reported for electrodeposited ZnO nanorods where concentration of carriers higher than 10^{19} cm^{-3} in as-grown ZnO is reduced by two orders of magnitude after the annealing in air at 450 °C [19].

The room-temperature PL spectrum of ZnO nanorod layer deposited at 480 °C (Fig. 4) shows a broad emission band centered

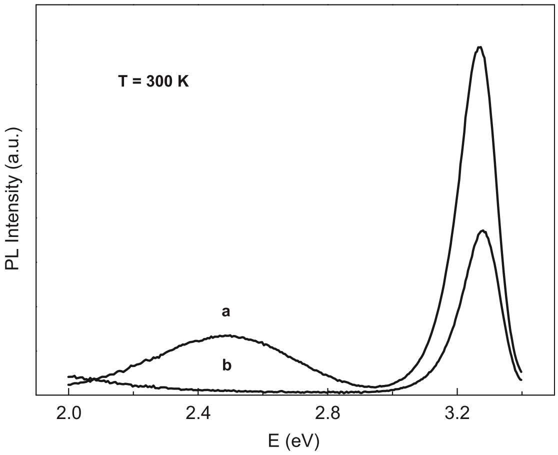

Fig. 4. Photoluminescence (PL) spectra of ZnO nanorod layers deposited at substrate temperature of 480 °C (a) and 550 °C (b). PL spectra are recorded at room temperature.

around 2.5 eV in the visible spectral region and an intense UV-emission band centered around 3.27 eV. The green PL emission band is not present in the spectrum of the sample prepared at 550 °C (Fig. 4). Instead, a rise of the PL signal in the low-energy range of the spectrum is observed. It is generally accepted that UV-emission band is mainly due to the recombination of bound excitons in ZnO. The green PL emission band is assigned to the oxygen vacancies in ZnO, this luminescence being due to the recombination of photogenerated hole with singly ionized oxygen vacancies [22]. While the green emission band is being observed in oxygen deficient samples, the orange PL emission is seen in oxygen rich samples [23]. Correlation between the green and orange PL emission intensity and free-carrier density has been established—the green PL emission decreases and the orange PL emission increases while increasing the annealing temperature in oxidative conditions [22]. Thus, it can be concluded that the concentration of oxygen vacancies related defects is lower in the material deposited at higher temperature being also expressed in lower density of carriers.

However, to obtain ZnO nanorod layers with concentration of carriers above $10^{16}\,cm^{-3}$ the deposition should be made by keeping the substrate temperatures below 500 °C. In this case alcohol based solutions should be sprayed instead of aqueous ones. According to the SEM study, the deposition of an aqueous solution does not result in a nanorod layer at this substrate temperature, as also reported in our earlier studies [10,11]. Using an alcohol based solution, ZnO nanorod layer is formed as cooling of the substrate is less intense and the substrate temperature of 480 °C is sufficient to grow ZnO crystals.

It seems that deposition at temperatures below 500 °C is not the solution to obtain the material for electronic applications where carrier concentrations higher than $10^{18}\,cm^{-3}$ are required. To attain this goal, the doping with donor impurities as reported for ZnO nanorod arrays prepared by vapor phase transport technique [14], seems to be more reasonable approach.

4. Conclusions

According to SEM study, spray pyrolysis deposition of acidic zinc chloride solutions (pH = 2) instead of those with pH = 5 offers a new approach to grow ZnO nanorod layer with separately standing crystals on ITO substrate where, ordinarily, coalescence of growing crystals occurs easily. As a result, the density of ZnO crystals on the substrate is decreased, however, their size distribution is broadened.

A model for electrical characterization of ZnO nanorods using Hg probe to form ZnO_{NR}/Hg Schottky barrier is presented and applied to calculate the concentration of charge carriers. Due to high surface tension of Hg there is no need for filling the gaps between the rods with a resist to avoid short circuiting between the front and back contact. Furthermore, the electrically active contact area can also be determined from *C–V* measurements.

ZnO nanorods deposited at substrate temperature of 550 °C from aqueous solutions indicate concentration of carriers in the range of 10^{14}–$10^{15}\,cm^{-3}$ irrespective of the spray solution acidity. Carrier concentrations of $\sim 10^{16}\,cm^{-3}$ are characteristic of ZnO obtained at temperatures below 500 °C. However, alcohol based solutions should be sprayed in this case to obtain ZnO nanorod layers.

According to PL studies, the concentration of oxygen vacancy related defects is lower in ZnO nanorods deposited at 550 °C compared to those deposited at 480 °C. Intensive UV-emission prevails in PL spectra independent of the growth temperature or solution pH and refers that spray deposited ZnO has relatively high crystal quality.

Acknowledgments

Financial support by the Estonian Ministry of Education and Research (Target Financing Project SF0140092s08), Estonian Science Foundation (Grant ETF6954) and European Social Fund's Doctoral Studies and Internationalization Program DoRa is gratefully acknowledged.

References

[1] J.B. Baxter, E.S. Aydil, Sol. Energy Mater. Solar Cells 90 (2006) 607.
[2] L.E. Greene, M. Law, B.D. Yuhas, P.D. Yang, J. Phys. Chem. C 111 (2007) 18451.
[3] R. Tena-Zaera, M.A. Ryan, A. Katty, G. Hodes, S. Bastide, C. Lévy-Clément, C. R. Chim. 9 (2006) 717.
[4] M. Krunks, A. Katerski, T. Dedova, I. Oja Acik, A. Mere, Sol. Energy Mater. Solar Cells 92 (2008) 1016.
[5] Z. Yang, L.-M. Li, Q. Wan, Q.-H. Liu, T.-H. Wang, Sensors Actuators B 135 (2008) 57.
[6] O. Lupan, L. Chow, G. Chai, L. Chernyak, O. Lopatiuk-Tirpak, H. Heinrich, Phys. Stat. Sol. (a) 205 (2008) 2673.
[7] D. Kieven, T. Dittrich, A. Belaidi, J. Tornow, K. Schwarzburg, N. Allsop, M. Lux-Steiner, Appl. Phys. Lett. 92 (2008) 153107.
[8] I. Oja Acik, A. Katerski, A. Mere, J. Aarik, A. Aidla, T. Dedova, M. Krunks, Thin Solid Films 517 (2009) 2443.
[9] A. Mere, A. Katerski, T. Dedova, I. Oja Acik, M. Krunks, in: Proceedings of the 23rd EUPVSEC, Valencia, Spain, 3.DO.5.1, 2147, 1–5 September 2008.
[10] M. Krunks, T. Dedova, I. Oja Açik, Thin Solid Films 515 (2006) 1157.
[11] T. Dedova, M. Krunks, M. Grossberg, O. Volobujeva, I. Oja Acik, Superlatt. Microstruct. 42 (2007) 444.
[12] T. Dedova, O. Volobujeva, J. Klauson, A. Mere, M. Krunks, Nanoscale Res. Lett. 2 (2007) 391.
[13] U. Alver, T. Kılınç, E. Bacaksız, S. Nezir, Mater. Chem. Phys. 106 (2007) 227.
[14] H. Zhou, J. Fallert, J. Sartor, R.J.B. Dietz, C. Klingshirn, H. Kalt, D. Weissenberger, D. Gerthsen, H. Zeng, W. Cai, Appl. Phys. Lett. 92 (2008) 132112.
[15] Th. Weimann, P. Hinze, E. Schlenker, A. Bakin, A.C. Mofor, A. Behrends, A. Waag, Microelectr. Eng. 85 (2008) 1248.
[16] W.I. Park, G.-C. Yi, J.-W. Kim, S.-M. Park, Appl. Phys. Lett. 82 (2003) 4358.
[17] J. Nayak, J. Kasuya, A. Watanabe, S. Nozaki, J. Phys.: Condens. Matter 20 (2008) 195222.
[18] E. Schlenker, A. Bakin, B. Postels, A.C. Mofor, H.-H. Wehmann, T. Weimann, P. Hinze, A. Waag, Phys. Stat. Sol. (b) 244 (2007) 1473.
[19] I. Mora-Seró, F. Fabregat-Santiago, B. Denier, J. Bisquert, R. Tena-Zaera, J. Elias, C. Lévy-Clément, Appl. Phys. Lett. 89 (2006) 203117.
[20] J.-J. Wu, D.K.-P. Wong, Adv. Mater. 19 (2007) 2015.
[21] J.Y. Park, H. Oh, J.-J. Kim, S.S. Kim, J. Cryst. Growth 287 (2006) 145.
[22] K. Vanheusden, W.L. Warren, C.H. Seager, D.R. Tallant, J.A. Voigt, B.E. Gnade, J. Appl. Phys. 79 (1996) 7983.
[23] S.A. Studenikin, N. Golegu, M. Cocivera, J. Appl. Phys. 84 (1998) 2287.

Appendix B

Curriculum Vitae

Ees- ja perekonnanimi	Erki Kärber
Sünniaeg ja -koht	16 aprill 1984, Tallinn
E-post	erki.karber@ttu.ee
Haridus	2009– . . . Tallinna Tehnikaülikool, doktorantuur, keemia- ja materjalitehnoloogia õppekava. 2007–2009 Tallinna Tehnikaülikool, loodusteaduse magister, *Cum Laude*, tehnilise füüsika õppekava. 2004–2007 Tallinna Tehnikaülikool, loodusteaduse bakalaureus, tehnilise füüsika õppekava. 2003–2004 Eesti Merevägi, ajateenistus. 2000–2003 Tallinna Väike-Õismäe gümnaasium, keskharidus.
Teenistuskäik	2013– ... Tallinna Tehnikaülikool, Keemia ja materjaliteaduse instituut, insener (0.50) 2011– 2013 ... Tallinna Tehnikaülikool, Keemia ja materjaliteaduse instituut, insener (0.25)
Osalemine projektides	2014– . . . Õhukesed kiled ja nanomaterjalid keemilistel vedeliksadestusmeetoditel uue põlvkonna fotovoltseadistele (IUT19-4), täitja. 2011–. . . Tippkeskus Mesosüsteemid – teooria ja rakendused (TK114), töörühma „Funktsionaalstruktuuride süntees” täitja. 2012– . . . Efektiivsed plasmoonilised absorberid päikesepatareidele (AR12118), põhitäitja.

2008–2013 Õhukesekilelised ja nanostruktuursed materjalid keemilistel meetoditel (SF0140092s08), täitja.

2010–2013 Absorberkihid keemilise pihustuspürolüüsi meetodil nanostruktuursetele päikesepatareidele (ETF9081), põhitäitja.

2010–2013 Keemilise pihustuspürolüüsi meetodil kasvatatud ZnO nanovarraste areng (ETF8509), põhitäitja.

2007–2010 Õhukesed kiled ja fotovoltstruktuurid keemilistel vedeliksadestusmeetoditel (ETF6954), põhitäitja.

Täiendusõpe

2009–2014 TÜ ja TTÜ doktorikool „Funktsionaalsed materjalid ja tehnoloogiad" (FMTDK). Osalemine suvekoolides, ettekanded konverentsidel. Stipendiumid rahvusvahelistel konverentsidel, suvekoolides ja töötubades osalemiseks.

2011 kevadsemester, Electronics and Information Systems Department (ELIS), Ghent University, Belgium. Päikesepatareide elektrilised mõõtmised, kursused pooljuhtmaterjalide ning päikesepatarei omadustest ja iseloomustamisest.

2011–... Tippkeskuse „Mesosüsteemide teooria ja rakendused" raames: ettekanded konverentsidel.

Osalemine rahvusvahelistel konverentsidel suuliste ettekannetega (Solar Energy for World Peace 2013, QUANTSOL Winter workshop 2010, Cyseni 2010) ja posterettekannetega (NextGen NanoPV 2013, XXI IMRS 2012, E-MRS 2010 Fall Meeting, E-MRS 2010 Spring Meeting).

Osalemine suvekoolides (ISUenergy 2012, QUANTSOL 2010) ja koolitustel (3rd Impedance Spectroscopy School 2011).

Tunnustus

2012 3. preemia üliõpilaste teadustööde riiklikul konkursil, doktoriõppe astmes. Konkursitöö: *Kärber et. al. (2011) Nanoscale Res. Lett. 6:359.*

	2011 Äramärgitud töö (*Krunks et. al. (2013) Sol. Energy Mater. Sol. Cells 94, 1191-95*) tehnika ja tehnoloogia valdkonnas „TTÜ parim teadusartikkel 2010“ konkursil.
	2008 Eesti Energia Stipendium, SA Tallinna Tehnikaülikooli Arengufondi sügiskonkurss.
Kaitstud lõputööd	2009 Õhukeste kilede elektriliste parameetrite mõõtmine Van der Pauw ja Halli ühildatud meetodil ning Kelvini sondi meetodil, magistritöö, juhendaja dotsent Arvo Mere.
	2007 Elektron paramagnetiline resonants (EPR): põhimõtted, aparatuur ja rakendused, bakalaureusetöö, juhendaja dotsent Kalju Lott.

Appendix B

Curriculum Vitae

First name and surname	Erki Kärber
Date and place of birth	16 April 1984, Tallinn
E-mail	erki.karber@ttu.ee
Education	2009– . . . Tallinn University of Technology, doctoral studies, Chemical and Materials Technology curriculum.
	2007–2009, Tallinn University of Technology, Master of Science in Natural Sciences (Applied Physics), *Cum Laude*, Engineering Physics curriculum.
	2004–2007, Tallinn University of Technology, Bachelor of Science in Natural Sciences, Engineering Physics curriculum.
	2003–2004, Estonian Navy, military service.
	2000–2003, Tallinn Väike-Õismäe high school, secondary education.
Employment	2013– . . . Tallinn University of Technology, Department of Materials Science, Engineer (0.50)
	2011– 2013, Tallinn University of Technology, Department of Materials Science, Engineer (0.25)
Projects	2014– . . . Thin films and nanomaterials by wet-chemical methods for next-generation photovoltaics (IUT19-4).
	2011– . . . Centre of Excellence: Mesosystems, Theory and applications (TK114), in workgroup Synthesis of Functional Structures.
	2012– . . . Efficient plasmonic absorbers for solar cells. (AR12118).

	2008–2013, Thin film and nanostructured materials by chemical methods (SF0140092s08).
	2010–2013, Absorber layers by chemical spray pyrolysis for nanostructured solar cells (ETF9081)
	2010–2013, Development of ZnO nanorods by chemical spray (ETF8509).
	2007–2010, Thin films and structures for photovoltaics by wet chemical deposition techniques (ETF6954).
Training	2009–2014 Graduate school „Functional materials and technologies“. Participation at summer schools, presentations at conferences. Scholarships to international conferences, summer schools and workshops.
	2011 spring semester, Electronics and Information Systems department (ELIS), Ghent University, Belgium. Admittance spectroscopy. Solar cell measurements. Courses on principles and characterization of semiconductors and solar cells.
	2011– . . . Centre of Excellence: ´Mesosystems, Theory and applications´. Presentations at conferences.
	Participation at international conferences with oral presentations (Solar Energy for World Peace 2013, QUANTSOL Winter workshop 2010, Cyseni 2010) and poster-presentations (NextGen NanoPV 2013, XXI IMRS 2012, E-MRS 2010 Fall Meeting, E-MRS 2010 Spring Meeting)
	Participation at international summer schools (ISUenergy 2012, QUANTSOL 2010) and workshops (3rd Impedance Spectroscopy School 2011).
Recognition	2012, 3. prize, at National Students' Research Contest (by Estonian Ministry of Education and Research), for *Kärber et. al. (2011) Nanoscale Res. Lett. 6:359.*

	2011, Noted in the field of science and technology articles (*Krunks et. al. (2013) Sol. Energy Mater. Sol. Cells 94, 1191-95*) at Tallinn University of Technology contest for best scientific article 2010. 2008, Eesti Energia Scholarship. Tallinn University of Technology Development Fund autumn scholarship.
Defended dissertations	2009 Electrical parameters of thin films by Van der Pauw - Hall and Kelvin probe methods, master´s thesis, supervisor - Associate Professor Arvo Mere. 2007 Electron paramagnetic resonance (EPR): principles, apparatus and applications, bachelor´s thesis, supervisor - Associate Professor Kalju Lott.

List of publications

1. **E. Kärber**, K. Otto, A. Katerski, A. Mere, M. Krunks. (2014). Raman spectroscopic study of In_2S_3 films prepared by spray pyrolysis. Materials Science in Semiconductor Processing, *in press*.

2. M. Kriisa, **E. Kärber**, M. Krunks, V. Mikli, T. Unt, M. Kukk, Arvo Mere. (2014). Growth and properties of ZnO films on polymeric substrate by spray pyrolysis method. Thin Solid Films, 555, 87–92.

3. O. Budarnaja, D. Klauson, T. Dedova, **E. Kärber**, M.Viljus, S. Preis. (2014). Template synthesis of titanium dioxide coatings and determination of their photocatalytic activity by aqueous oxidation of humic acid. Kinetics and Catalysis, *accepted*.

4. **E. Kärber,** A. Abass, S. Khelifi, M. Burgelman, A. Katerski, M. Krunks. (2013). Electrical characterization of all-layers-sprayed solar cell based on ZnO nanorods and extremely thin CIS absorber. Solar Energy, 91, 48 - 58.

5. M. Kriisa, M. Krunks, **E. Kärber**, M. Kukk, V. Mikli, A. Mere. (2013). Effect of Solution Spray Rate on the Properties of Chemically Sprayed ZnO:In Thin Films. Journal of Nanomaterials, 423632.

6. M. Vent, **E. Kärber,** T. Unt, A. Mere, M. Krunks. (2012). The effect of growth temperature and spraying rate on properties of ZnO:In films. physica status solidi (c), 9, 1604 – 1606.

7. A. Katerski, **E. Kärber**, M. Krunks, V. Mikli, A. Mere (2012). Development of sprayed $CuInS_2$ thin film absorber for nanostructured solar cell. MRS Proceedings, 1447, mrss12-1447-w10-47.

8. **E.Kärber**, T.Raadik, T.Dedova, J.Krustok, A.Mere, V.Mikli, M.Krunks. (2011). Photoluminescence of spray pyrolysis deposited ZnO nanorods. Nanoscale Research Letters, 6(359), 1 - 7.

9. **E. Kärber**, A. Katerski, I. Oja Acik, V. Mikli, A. Mere, M. Krunks. (2011). Effect of H_2S treatment on properties of $CuInS_2$ thin films deposited by chemical spray pyrolysis at low temperature. Thin Solid Films, 519, 7180 – 7183.

10. M. Krunks, **E. Kärber**, A. Katerski, K. Otto, I. Oja Acik, T. Dedova, A. Mere. (2010). Extremely thin absorber layer solar cells on zinc oxide nanorods by chemical spray. Solar Energy Materials and Solar Cells, 94(7), 1191 - 1195.

11. **E. Kärber**, I.Oja Acik, A.Katerski, A. Mere, M. Krunks. (2010). Nanostructured solar cell prepared by chemical spray pyrolysis method. Extended abstract of the QUANTSOL 2010 Winter workshop, 7-12 March, Breil/Brigels, Switzerland. Available: http://www.quantsol.org/qu10_pub.htm

12. **E. Kärber**, T. Dedova, I. Oja Acik, M. Krunks, A. Mere (2010). Determination of charge carrier density in zinc oxide nanorods prepared by chemical spray pyrolysis. Proceedings of Cyseni 2010, May 27-28, Kaunas, Lithuania. ISSN 1822-7554, p. 340-344.

13. M. Vent, K. Annert, **E. Kärber,** M. Krunks (2010). ZnO thin films as transparent conductive oxides by chemical spray pyrolysis. Proceedings of Cyseni 2010, May 27-28, Kaunas, Lithuania. ISSN 1822-7554, p. 399-407.

14. K. Annert, M. Vent, T. Dedova, **E. Kärber**, I. Oja Acik, O. Volobujeva, A.Mere, M. Krunks (2010). Impacts of different solvents and substrates on properties of zinc oxide nanorod layers prepared by chemical spray pyrolysis. Proceedings of Cyseni 2010, May 27-28, Kaunas, Lithuania. ISSN 1822-7554, p. 301-309.

15. M. Krunks, T. Dedova, **E. Kärber**, V. Mikli, I. Oja Acik, M. Grossberg, A. Mere. (2009). Growth and electrical properties of ZnO nanorod arrays prepared by chemical spray pyrolysis. Physica B: Physics of Condensed Matter, 404(22), 4422 - 4425.

16. J. Hiie, F. Quinci, V. Lughi, V. Sergo, V. Valdna, V. Mikli, **E. Kärber**, T. Raadik. (2009). Chlorine Doping of Cadmium Sulfide on the Example of CBD CdS. Thin-Film Compound Semiconductor Photovoltaics. Proceedings of MRS Spring Meeting, San Francisco USA, 13-17.04.2009.

DISSERTATIONS DEFENDED AT TALLINN UNIVERSITY OF TECHNOLOGY ON *NATURAL AND EXACT SCIENCES*

1. **Olav Kongas**. Nonlinear Dynamics in Modeling Cardiac Arrhytmias. 1998.

2. **Kalju Vanatalu**. Optimization of Processes of Microbial Biosynthesis of Isotopically Labeled Biomolecules and Their Complexes. 1999.

3. **Ahto Buldas**. An Algebraic Approach to the Structure of Graphs. 1999.

4. **Monika Drews**. A Metabolic Study of Insect Cells in Batch and Continuous Culture: Application of Chemostat and Turbidostat to the Production of Recombinant Proteins. 1999.

5. **Eola Valdre**. Endothelial-Specific Regulation of Vessel Formation: Role of Receptor Tyrosine Kinases. 2000.

6. **Kalju Lott**. Doping and Defect Thermodynamic Equilibrium in ZnS. 2000.

7. **Reet Koljak**. Novel Fatty Acid Dioxygenases from the Corals *Plexaura homomalla* and *Gersemia fruticosa*. 2001.

8. **Anne Paju**. Asymmetric oxidation of Prochiral and Racemic Ketones by Using Sharpless Catalyst. 2001.

9. **Marko Vendelin**. Cardiac Mechanoenergetics *in silico*. 2001.

10. **Pearu Peterson**. Multi-Soliton Interactions and the Inverse Problem of Wave Crest. 2001.

11. **Anne Menert**. Microcalorimetry of Anaerobic Digestion. 2001.

12. **Toomas Tiivel**. The Role of the Mitochondrial Outer Membrane in *in vivo* Regulation of Respiration in Normal Heart and Skeletal Muscle Cell. 2002.

13. **Olle Hints**. Ordovician Scolecodonts of Estonia and Neighbouring Areas: Taxonomy, Distribution, Palaeoecology, and Application. 2002.

14. **Jaak Nõlvak**. Chitinozoan Biostratigrapy in the Ordovician of Baltoscandia. 2002.

15. **Liivi Kluge**. On Algebraic Structure of Pre-Operad. 2002.

16. **Jaanus Lass**. Biosignal Interpretation: Study of Cardiac Arrhytmias and Electromagnetic Field Effects on Human Nervous System. 2002.

17. **Janek Peterson**. Synthesis, Structural Characterization and Modification of PAMAM Dendrimers. 2002.

18. **Merike Vaher**. Room Temperature Ionic Liquids as Background Electrolyte Additives in Capillary Electrophoresis. 2002.

19. **Valdek Mikli**. Electron Microscopy and Image Analysis Study of Powdered Hardmetal Materials and Optoelectronic Thin Films. 2003.

20. **Mart Viljus**. The Microstructure and Properties of Fine-Grained Cermets. 2003.

21. **Signe Kask**. Identification and Characterization of Dairy-Related *Lactobacillus*. 2003

22. **Tiiu-Mai Laht**. Influence of Microstructure of the Curd on Enzymatic and Microbiological Processes in Swiss-Type Cheese. 2003.

23. **Anne Kuusksalu**. 2–5A Synthetase in the Marine Sponge *Geodia cydonium*. 2003.

24. **Sergei Bereznev**. Solar Cells Based on Polycristalline Copper-Indium Chalcogenides and Conductive Polymers. 2003.

25. **Kadri Kriis**. Asymmetric Synthesis of C_2-Symmetric Bimorpholines and Their Application as Chiral Ligands in the Transfer Hydrogenation of Aromatic Ketones. 2004.

26. **Jekaterina Reut**. Polypyrrole Coatings on Conducting and Insulating Substracts. 2004.

27. **Sven Nõmm**. Realization and Identification of Discrete-Time Nonlinear Systems. 2004.

28. **Olga Kijatkina**. Deposition of Copper Indium Disulphide Films by Chemical Spray Pyrolysis. 2004.

29. **Gert Tamberg**. On Sampling Operators Defined by Rogosinski, Hann and Blackman Windows. 2004.

30. **Monika Übner**. Interaction of Humic Substances with Metal Cations. 2004.

31. **Kaarel Adamberg**. Growth Characteristics of Non-Starter Lactic Acid Bacteria from Cheese. 2004.

32. **Imre Vallikivi**. Lipase-Catalysed Reactions of Prostaglandins. 2004.

33. **Merike Peld**. Substituted Apatites as Sorbents for Heavy Metals. 2005.

34. **Vitali Syritski**. Study of Synthesis and Redox Switching of Polypyrrole and Poly(3,4-ethylenedioxythiophene) by Using *in-situ* Techniques. 2004.

35. **Lee Põllumaa**. Evaluation of Ecotoxicological Effects Related to Oil Shale Industry. 2004.

36. **Riina Aav**. Synthesis of 9,11-Secosterols Intermediates. 2005.

37. **Andres Braunbrück**. Wave Interaction in Weakly Inhomogeneous Materials. 2005.

38. **Robert Kitt**. Generalised Scale-Invariance in Financial Time Series. 2005.

39. **Juss Pavelson**. Mesoscale Physical Processes and the Related Impact on the Summer Nutrient Fields and Phytoplankton Blooms in the Western Gulf of Finland. 2005.

40. **Olari Ilison**. Solitons and Solitary Waves in Media with Higher Order Dispersive and Nonlinear Effects. 2005.

41. **Maksim Säkki**. Intermittency and Long-Range Structurization of Heart Rate. 2005.

42. **Enli Kiipli**. Modelling Seawater Chemistry of the East Baltic Basin in the Late Ordovician–Early Silurian. 2005.

43. **Igor Golovtsov**. Modification of Conductive Properties and Processability of Polyparaphenylene, Polypyrrole and polyaniline. 2005.

44. **Katrin Laos**. Interaction Between Furcellaran and the Globular Proteins (Bovine Serum Albumin β-Lactoglobulin). 2005.

45. **Arvo Mere**. Structural and Electrical Properties of Spray Deposited Copper Indium Disulphide Films for Solar Cells. 2006.

46. **Sille Ehala**. Development and Application of Various On- and Off-Line Analytical Methods for the Analysis of Bioactive Compounds. 2006.

47. **Maria Kulp**. Capillary Electrophoretic Monitoring of Biochemical Reaction Kinetics. 2006.

48. **Anu Aaspõllu.** Proteinases from *Vipera lebetina* Snake Venom Affecting Hemostasis. 2006.

49. **Lyudmila Chekulayeva**. Photosensitized Inactivation of Tumor Cells by Porphyrins and Chlorins. 2006.

50. **Merle Uudsemaa**. Quantum-Chemical Modeling of Solvated First Row Transition Metal Ions. 2006.

51. **Tagli Pitsi**. Nutrition Situation of Pre-School Children in Estonia from 1995 to 2004. 2006.

52. **Angela Ivask**. Luminescent Recombinant Sensor Bacteria for the Analysis of Bioavailable Heavy Metals. 2006.

53. **Tiina Lõugas**. Study on Physico-Chemical Properties and Some Bioactive Compounds of Sea Buckthorn (*Hippophae rhamnoides* L.). 2006.

54. **Kaja Kasemets**. Effect of Changing Environmental Conditions on the Fermentative Growth of *Saccharomyces cerevisae* S288C: Auxo-accelerostat Study. 2006.

55. **Ildar Nisamedtinov**. Application of ^{13}C and Fluorescence Labeling in Metabolic Studies of *Saccharomyces* spp. 2006.

56. **Alar Leibak**. On Additive Generalisation of Voronoï's Theory of Perfect Forms over Algebraic Number Fields. 2006.

57. **Andri Jagomägi**. Photoluminescence of Chalcopyrite Tellurides. 2006.

58. **Tõnu Martma**. Application of Carbon Isotopes to the Study of the Ordovician and Silurian of the Baltic. 2006.

59. **Marit Kauk**. Chemical Composition of $CuInSe_2$ Monograin Powders for Solar Cell Application. 2006.

60. **Julia Kois**. Electrochemical Deposition of $CuInSe_2$ Thin Films for Photovoltaic Applications. 2006.

61. **Ilona Oja Açik**. Sol-Gel Deposition of Titanium Dioxide Films. 2007.

62. **Tiia Anmann**. Integrated and Organized Cellular Bioenergetic Systems in Heart and Brain. 2007.

63. **Katrin Trummal**. Purification, Characterization and Specificity Studies of Metalloproteinases from *Vipera lebetina* Snake Venom. 2007.

64. **Gennadi Lessin**. Biochemical Definition of Coastal Zone Using Numerical Modeling and Measurement Data. 2007.

65. **Enno Pais**. Inverse problems to determine non-homogeneous degenerate memory kernels in heat flow. 2007.

66. **Maria Borissova**. Capillary Electrophoresis on Alkylimidazolium Salts. 2007.

67. **Karin Valmsen**. Prostaglandin Synthesis in the Coral *Plexaura homomalla*: Control of Prostaglandin Stereochemistry at Carbon 15 by Cyclooxygenases. 2007.

68. **Kristjan Piirimäe**. Long-Term Changes of Nutrient Fluxes in the Drainage Basin of the Gulf of Finland – Application of the PolFlow Model. 2007.

69. **Tatjana Dedova**. Chemical Spray Pyrolysis Deposition of Zinc Sulfide Thin Films and Zinc Oxide Nanostructured Layers. 2007.

70. **Katrin Tomson**. Production of Labelled Recombinant Proteins in Fed-Batch Systems in *Escherichia coli*. 2007.

71. **Cecilia Sarmiento**. Suppressors of RNA Silencing in Plants. 2008.

72. **Vilja Mardla**. Inhibition of Platelet Aggregation with Combination of Antiplatelet Agents. 2008.

73. **Maie Bachmann**. Effect of Modulated Microwave Radiation on Human Resting Electroencephalographic Signal. 2008.

74. **Dan Hüvonen**. Terahertz Spectroscopy of Low-Dimensional Spin Systems. 2008.

75. **Ly Villo**. Stereoselective Chemoenzymatic Synthesis of Deoxy Sugar Esters Involving *Candida antarctica* Lipase B. 2008.

76. **Johan Anton**. Technology of Integrated Photoelasticity for Residual Stress Measurement in Glass Articles of Axisymmetric Shape. 2008.

77. **Olga Volobujeva**. SEM Study of Selenization of Different Thin Metallic Films. 2008.

78. **Artur Jõgi**. Synthesis of 4’-Substituted 2,3’-dideoxynucleoside Analogues. 2008.

79. **Mario Kadastik**. Doubly Charged Higgs Boson Decays and Implications on Neutrino Physics. 2008.

80. **Fernando Pérez-Caballero**. Carbon Aerogels from 5-Methylresorcinol-Formaldehyde Gels. 2008.

81. **Sirje Vaask**. The Comparability, Reproducibility and Validity of Estonian Food Consumption Surveys. 2008.

82. **Anna Menaker**. Electrosynthesized Conducting Polymers, Polypyrrole and Poly(3,4-ethylenedioxythiophene), for Molecular Imprinting. 2009.

83. **Lauri Ilison**. Solitons and Solitary Waves in Hierarchical Korteweg-de Vries Type Systems. 2009.

84. **Kaia Ernits**. Study of In_2S_3 and ZnS Thin Films Deposited by Ultrasonic Spray Pyrolysis and Chemical Deposition. 2009.

85. **Veljo Sinivee**. Portable Spectrometer for Ionizing Radiation “Gammamapper”. 2009.

86. **Jüri Virkepu**. On Lagrange Formalism for Lie Theory and Operadic Harmonic Oscillator in Low Dimensions. 2009.

87. **Marko Piirsoo**. Deciphering Molecular Basis of Schwann Cell Development. 2009.
88. **Kati Helmja**. Determination of Phenolic Compounds and Their Antioxidative Capability in Plant Extracts. 2010.
89. **Merike Sõmera**. Sobemoviruses: Genomic Organization, Potential for Recombination and Necessity of P1 in Systemic Infection. 2010.
90. **Kristjan Laes**. Preparation and Impedance Spectroscopy of Hybrid Structures Based on $CuIn_3Se_5$ Photoabsorber. 2010.
91. **Kristin Lippur**. Asymmetric Synthesis of 2,2'-Bimorpholine and its 5,5'-Substituted Derivatives. 2010.
92. **Merike Luman**. Dialysis Dose and Nutrition Assessment by an Optical Method. 2010.
93. **Mihhail Berezovski**. Numerical Simulation of Wave Propagation in Heterogeneous and Microstructured Materials. 2010.
94. **Tamara Aid-Pavlidis**. Structure and Regulation of BDNF Gene. 2010.
95. **Olga Bragina**. The Role of Sonic Hedgehog Pathway in Neuro- and Tumorigenesis. 2010.
96. **Merle Randrüüt**. Wave Propagation in Microstructured Solids: Solitary and Periodic Waves. 2010.
97. **Marju Laars**. Asymmetric Organocatalytic Michael and Aldol Reactions Mediated by Cyclic Amines. 2010.
98. **Maarja Grossberg**. Optical Properties of Multinary Semiconductor Compounds for Photovoltaic Applications. 2010.
99. **Alla Maloverjan**. Vertebrate Homologues of Drosophila Fused Kinase and Their Role in Sonic Hedgehog Signalling Pathway. 2010.
100. **Priit Pruunsild**. Neuronal Activity-Dependent Transcription Factors and Regulation of Human *BDNF* Gene. 2010.
101. **Tatjana Knjazeva**. New Approaches in Capillary Electrophoresis for Separation and Study of Proteins. 2011.
102. **Atanas Katerski**. Chemical Composition of Sprayed Copper Indium Disulfide Films for Nanostructured Solar Cells. 2011.
103. **Kristi Timmo.** Formation of Properties of $CuInSe_2$ and $Cu_2ZnSn(S,Se)_4$ Monograin Powders Synthesized in Molten KI. 2011.
104. **Kert Tamm**. Wave Propagation and Interaction in Mindlin-Type Microstructured Solids: Numerical Simulation. 2011.
105. **Adrian Popp**. Ordovician Proetid Trilobites in Baltoscandia and Germany. 2011.
106. **Ove Pärn**. Sea Ice Deformation Events in the Gulf of Finland and This Impact on Shipping. 2011.
107. **Germo Väli**. Numerical Experiments on Matter Transport in the Baltic Sea. 2011.
108. **Andrus Seiman**. Point-of-Care Analyser Based on Capillary Electrophoresis. 2011.

109. **Olga Katargina**. Tick-Borne Pathogens Circulating in Estonia (Tick-Borne Encephalitis Virus, *Anaplasma phagocytophilum*, *Babesia* Species): Their Prevalence and Genetic Characterization. 2011.
110. **Ingrid Sumeri**. The Study of Probiotic Bacteria in Human Gastrointestinal Tract Simulator. 2011.
111. **Kairit Zovo**. Functional Characterization of Cellular Copper Proteome. 2011.
112. **Natalja Makarytsheva**. Analysis of Organic Species in Sediments and Soil by High Performance Separation Methods. 2011.
113. **Monika Mortimer**. Evaluation of the Biological Effects of Engineered Nanoparticles on Unicellular Pro- and Eukaryotic Organisms. 2011.
114. **Kersti Tepp**. Molecular System Bioenergetics of Cardiac Cells: Quantitative Analysis of Structure-Function Relationship. 2011.
115. **Anna-Liisa Peikolainen**. Organic Aerogels Based on 5-Methylresorcinol. 2011.
116. **Leeli Amon**. Palaeoecological Reconstruction of Late-Glacial Vegetation Dynamics in Eastern Baltic Area: A View Based on Plant Macrofossil Analysis. 2011.
117. **Tanel Peets**. Dispersion Analysis of Wave Motion in Microstructured Solids. 2011.
118. **Liina Kaupmees**. Selenization of Molybdenum as Contact Material in Solar Cells. 2011.
119. **Allan Olspert**. Properties of VPg and Coat Protein of Sobemoviruses. 2011.
120. **Kadri Koppel**. Food Category Appraisal Using Sensory Methods. 2011.
121. **Jelena Gorbatšova**. Development of Methods for CE Analysis of Plant Phenolics and Vitamins. 2011.
122. **Karin Viipsi**. Impact of EDTA and Humic Substances on the Removal of Cd and Zn from Aqueous Solutions by Apatite. 2012.
123. **David Schryer**. Metabolic Flux Analysis of Compartmentalized Systems Using Dynamic Isotopologue Modeling. 2012.
124. **Ardo Illaste**. Analysis of Molecular Movements in Cardiac Myocytes. 2012.
125. **Indrek Reile**. 3-Alkylcyclopentane-1,2-Diones in Asymmetric Oxidation and Alkylation Reactions. 2012.
126. **Tatjana Tamberg**. Some Classes of Finite 2-Groups and Their Endomorphism Semigroups. 2012.
127. **Taavi Liblik**. Variability of Thermohaline Structure in the Gulf of Finland in Summer. 2012.
128. **Priidik Lagemaa**. Operational Forecasting in Estonian Marine Waters. 2012.
129. **Andrei Errapart**. Photoelastic Tomography in Linear and Non-linear Approximation. 2012.
130. **Külliki Krabbi**. Biochemical Diagnosis of Classical Galactosemia and Mucopolysaccharidoses in Estonia. 2012.

131. **Kristel Kaseleht**. Identification of Aroma Compounds in Food using SPME-GC/MS and GC-Olfactometry. 2012.

132. **Kristel Kodar**. Immunoglobulin G Glycosylation Profiling in Patients with Gastric Cancer. 2012.

133. **Kai Rosin**. Solar Radiation and Wind as Agents of the Formation of the Radiation Regime in Water Bodies. 2012.

134. **Ann Tiiman**. Interactions of Alzheimer's Amyloid-Beta Peptides with Zn(II) and Cu(II) Ions. 2012.

135. **Olga Gavrilova**. Application and Elaboration of Accounting Approaches for Sustainable Development. 2012.

136. **Olesja Bondarenko**. Development of Bacterial Biosensors and Human Stem Cell-Based *In Vitro* Assays for the Toxicological Profiling of Synthetic Nanoparticles. 2012.

137. **Katri Muska**. Study of Composition and Thermal Treatments of Quaternary Compounds for Monograin Layer Solar Cells. 2012.

138. **Ranno Nahku**. Validation of Critical Factors for the Quantitative Characterization of Bacterial Physiology in Accelerostat Cultures. 2012.

139. **Petri-Jaan Lahtvee**. Quantitative Omics-level Analysis of Growth Rate Dependent Energy Metabolism in *Lactococcus lactis*. 2012.

140. **Kerti Orumets**. Molecular Mechanisms Controlling Intracellular Glutathione Levels in Baker's Yeast *Saccharomyces cerevisiae* and its Random Mutagenized Gluthatione Over-Accumulating Isolate. 2012.

141. **Loreida Timberg**. Spice-Cured Sprats Ripening, Sensory Parameters Development, and Quality Indicators. 2012.

142. **Anna Mihhalevski**. Rye Sourdough Fermentation and Bread Stability. 2012.

143. **Liisa Arike**. Quantitative Proteomics of *Escherichia coli*: From Relative to Absolute Scale. 2012.

144. **Kairi Otto**. Deposition of In_2S_3 Thin Films by Chemical Spray Pyrolysis. 2012.

145. **Mari Sepp**. Functions of the Basic Helix-Loop-Helix Transcription Factor TCF4 in Health and Disease. 2012.

146. **Anna Suhhova**. Detection of the Effect of Weak Stressors on Human Resting Electroencephalographic Signal. 2012.

147. **Aram Kazarjan**. Development and Production of Extruded Food and Feed Products Containing Probiotic Microorganisms. 2012.

148. **Rivo Uiboupin**. Application of Remote Sensing Methods for the Investigation of Spatio-Temporal Variability of Sea Surface Temperature and Chlorophyll Fields in the Gulf of Finland. 2013.

149. **Tiina Kriščiunaite**. A Study of Milk Coagulability. 2013.

150. **Tuuli Levandi**. Comparative Study of Cereal Varieties by Analytical Separation Methods and Chemometrics. 2013.

151. **Natalja Kabanova**. Development of a Microcalorimetric Method for the Study of Fermentation Processes. 2013.

152. **Himani Khanduri**. Magnetic Properties of Functional Oxides. 2013.

153. **Julia Smirnova**. Investigation of Properties and Reaction Mechanisms of Redox-Active Proteins by ESI MS. 2013.

154. **Mervi Sepp**. Estimation of Diffusion Restrictions in Cardiomyocytes Using Kinetic Measurements. 2013.

155. **Kersti Jääger**. Differentiation and Heterogeneity of Mesenchymal Stem Cells. 2013.

156. **Victor Alari**. Multi-Scale Wind Wave Modeling in the Baltic Sea. 2013.

157. **Taavi Päll**. Studies of CD44 Hyaluronan Binding Domain as Novel Angiogenesis Inhibitor. 2013.

158. **Allan Niidu**. Synthesis of Cyclopentane and Tetrahydrofuran Derivatives. 2013.

159. **Julia Geller**. Detection and Genetic Characterization of *Borrelia* Species Circulating in Tick Population in Estonia. 2013.

160. **Irina Stulova**. The Effects of Milk Composition and Treatment on the Growth of Lactic Acid Bacteria. 2013.

161. **Jana Holmar**. Optical Method for Uric Acid Removal Assessment During Dialysis. 2013.

162. **Kerti Ausmees**. Synthesis of Heterobicyclo[3.2.0]heptane Derivatives *via* Multicomponent Cascade Reaction. 2013.

163. **Minna Varikmaa**. Structural and Functional Studies of Mitochondrial Respiration Regulation in Muscle Cells. 2013.

164. **Indrek Koppel**. Transcriptional Mechanisms of BDNF Gene Regulation. 2014.

165. **Kristjan Pilt**. Optical Pulse Wave Signal Analysis for Determination of Early Arterial Ageing in Diabetic Patients. 2014.

166. **Andres Anier**. Estimation of the Complexity of the Electroencephalogram for Brain Monitoring in Intensive Care. 2014.

167. **Toivo Kallaste**. Pyroclastic Sanidine in the Lower Palaeozoic Bentonites – A Tool for Regional Geological Correlations. 2014.